AN ABSTRACT OF THE THESIS OF

Lance Parson for the degree of Master of Science in Civil Engineering presented on July 12, 2022.

Title: Seismic Performance of Retrofitted Reinforced Concrete Columns Including Soil-Structure Interaction

Abstract approved:

____

Christopher C. Higgins

There are many existing bridges around the world that were designed without consideration for seismic effects. Many of these bridges were designed before modern earthquake engineering design standards and practices existed and thus are expected to perform poorly during strong ground shaking. Common structural deficiencies are found in their reinforced concrete (RC) substructures, including columns and footings. The most common deficiencies include reinforcing steel lap-splices within the plastic hinge region, insufficient lap-splice length, and poor lateral confinement due to insufficient transverse reinforcement. The effect of these details results in non-ductile response of the member that produces damage, residual drift, and can lead to bridge failure. Recent research has demonstrated the effectiveness of a novel retrofit method that uses titanium alloy bar (TiAB) ligaments and continuous spirals that provide both confinement and an alternative flexural load path that enables the retrofitted column to endure large drifts with sustained and predictable ductile response, high energy dissipation, reduced residual drift due to self-centering capacity, and no loss of axial load capacity. Although the retrofit is a viable option for improving seismic performance of columns, there are limited data that consider or incorporate the effects of soil-structure interactions on retrofit performance and design.

An experimental program was executed to evaluate reverse-cyclic performance of square RC columns retrofitted with TiABs on simulated soil. All specimens were designed and constructed to be representative of full-scale column-footings identified within the Oregon Department of Transportation bridge inventory. Eight (8) tests were conducted on three (3) specimens under sustained axial load and applied lateral loading. Different soil simulant constraints were used to isolate and quantify their effects on the structural performance. An analytical model of the soil subgrade and embedment was developed to predict the global response of the specimens under different boundary conditions.

Retrofitted columns exhibited either no damage or very minor damage due to activation of rocking foundation conditions with soft soil conditions. Higher column bar flexural stresses were observed in the case of stiffer soil conditions. In all cases, inelastic response of the soil simulant was observed. A single specimen that was unretrofitted was observed to fail with the soil simulant and then retrofitted with the TiABs. It was evident in subsequent tests that the retrofitted column possessed sufficient flexural strength and stiffness to activate the rocking foundation mechanism which thereby limited demands in the structural elements. The findings of this study demonstrate that interactions between the column-footing-soil should be properly accounted for to ensure the desired design outcome when considering and implementing seismic retrofit strategies on bridge substructures.

Seismic Performance of Retrofitted Reinforced Concrete Columns Including Soil-Structure Interaction

by
Lance Parson

A THESIS

submitted to

Oregon State University

in partial fulfillment of
the requirements for the
degree of

Master of Science

Presented July 12, 2022
Commencement June 2023

Master of Science thesis of Lance Parson presented on July 12, 2022.

APPROVED:

Major Professor, representing Civil Engineering

Head of the School of Civil and Construction Engineering

Dean of the Graduate School

I understand that my thesis will become part of the permanent collection of Oregon State University libraries. My signature below authorizes release of my thesis to any reader upon request.

Lance Parson, Author

ACKNOWLEDGEMENTS

First, I would like to thank my loving wife for her unconditional love and support and her dedication to our family during this time.

I would like to express my gratitude to my advisor Dr. Christopher Higgins for his mentorship and guidance in my professional and academic career. His contribution to my professional growth is invaluable to my future work.

I would also like to thank Dr. Armin Stuedlein, Dr. Erica Fischer, and Dr. Abigail Tomasek for their service and participation on my graduate committee. They have provided valuable insight for my current and future academic goals.

Special thanks to Dr. Andre Barbosa for his encouragement and guidance during my undergraduate work, Dr. Sharoo Shrestha for the work in this research and guidance, and Dr. Ali Khosravi for his work and advice in writing, numerical modeling, and being handy with a shovel. I would also like to extend a special thanks to Dr. Yasmeen Al-Sakin for her guidance and expertise.

I would also like to the Mr. Jeff Gent for his technical support during the experiments, and I am grateful to the following graduate students that helped me throughout the project: Madison Hall, Julie Lie, Christopher Neumann, Ian Morrell and Aaron Reedus. Thank you to the undergraduate students that worked on the project as well.

I would also like to thank the Oregon Department of Transportation and the Federal Highway Administration for funding this research.

CONTRIBUTION OF AUTHORS

Dr. Armin Stuedlein is the principal investigator of this research project. Dr. Christopher Higgins is the co-principal investigator of this research project. Dr. Higgins is the co-author of this thesis.

TABLE OF CONTENTS

TABLE OF CONTENTS (Continued)

TABLE OF CONTENTS (Continued)

Page

TABLE OF CONTENTS (Continued)

Page

TABLE OF CONTENTS (Continued)

Page

LIST OF FIGURES

LIST OF FIGURES (Continued)

LIST OF FIGURES (Continued)

LIST OF FIGURES (Continued)

Figure Page

LIST OF TABLES

LIST OF APPENDICES

LIST OF APPENDIX FIGURES

LIST OF APPENDIX FIGURES (Continued)

LIST OF APPENDIX FIGURES (Continued)

LIST OF APPENDIX FIGURES (Continued)

LIST OF APPENDIX FIGURES (Continued)

LIST OF APPENDIX FIGURES (Continued)

Figure Page

LIST OF APPENDIX FIGURES (Continued)

LIST OF APPENDIX FIGURES (Continued)

LIST OF APPENDIX TABLES

DEDICATION

I would like to dedicate this thesis to my wife, Ning An. Without your patience, and strength I would not have gotten this far. You’re amazing.

I. INTRODUCTION

Bridges in the United States built prior to the 1970's contain poorly detailed reinforced concrete (RC) substructure components that have inadequate seismic resistance. This was recognized after the 1971 San Fernando earthquake where many bridges performed poorly and resulted in changes to seismic design specifications. Deficient reinforcing details are concentrated in the column-footing substructure that supports the superstructure. Column details that contribute to these deficiencies include short lap-splices located in plastic hinge regions, widely spaced ties that provide inadequate confinement and diagonal-tension capacity in critical regions. Footing details can also be insufficient to resist flexure due to soil bearing pressures generated during a seismic event and commonly only a single mesh of reinforcing steel is located at the bottom of the footing. These factors coupled with stiff soils and low soil moisture content can result in damage leading to non-ductile failures of the substructure and foundation that could result in bridge failure. The Oregon Department of Transportation (ODOT) has previously funded research that led to the development of a novel titanium retrofit technique that improves the seismic performance of deficient RC columns. This new technique allows the column to achieve high seismic performance (excellent ductility, force protection, reduced strength degradation, and reduced residual drift) but does not address soil-structure interactions (SSI). This gap led to development of an experimental program focused on SSI of column-footing specimens retrofitted with a novel design using titanium alloy bars (TiABs). Full-scale column-footing specimens were designed to have similar properties and details to older in-service RC columns with poor seismic detailing. Experimental tests were conducted in the laboratory using a soil simulant to evaluate the interactions between specimens and "soil." The soil simulant exhibited reasonable compressive strength and behavior consistent with constitutive properties of native soils found in Oregon.

1.1 Background

The Cascadia Subduction Zone is formed by the Juan De Fuca Plate being forced below the North American Plate. This Cascadia Subduction Zone exists just off the coast of Oregon and has generated significant earthquakes with estimated moment magnitudes exceeding 9.0. The ODOT Bridge inventory includes hundreds of bridges that were built before the adoption of seismic codes and were not designed to resist strong ground shaking. Many of these bridges lie along vital routes for evacuation and emergency relief efforts including I-5, US97, and OR58. Square RC columns with seismically deficient details support a large number of these bridges.

To assess the inventory of bridge substructures along these critical access routes, Shrestha (2019) reviewed, cataloged, and statistically quantified the different column-foundation details based on original ODOT bridge drawings. Shrestha (2019) reported typical square RC bridge columns in Oregon are 61 cm x 61 cm (24 in. x 24 in.) and have a clear height between 4.57 m to 5.49 m (15 ft. to 18 ft.). The concrete was designed to have a nominal compressive strength of 22.8 MPa (3.3 ksi). Vintage columns have 4-#36M (#11) bars equivalent to ASTM Gr.40 steel at the corners as longitudinal reinforcement. To satisfy transverse reinforcement requirements #10M (#3) hoops with 90˚ hooks were placed 30.5 cm (12in.) on center. Longitudinal column bars were spliced at the base with starter bars that extended into the footing with no additional confinement of column ties. This lap-splice length was approximately 29 times the bar diameter (d_b) leaving the longitudinal reinforcing steel bars unable to develop the required tension forces. To achieve equivalent properties through detailing, #32M (#10) Gr. 60 bars were used with a lap-splice length of approximately 28 times d_b, or 914 mm (36 in.). Based on a statistical review of vintage RC columns along Oregon I-5, the axial load specified was 667 kN (150 kips) for each specimen. Furthermore, 71% of the square columns were found to rest on spread footings having a single reinforcing steel mesh located at the bottom with 7.6 cm. (3 in.) concrete cover limiting the capacity for the footing to resist soil bearing pressures.

Failure mechanisms that typically develop in pre-1971 bridges arise from common detailing deficiencies from original design. These structural deficiencies include: inadequate lap-splice detailing, insufficient confinement and ductility in the plastic hinge regions, low grade concrete, insufficient footing area, and inadequate shear and flexural strength to resist soil pressures caused by seismic activity (Priestly 1996; Xiao et al. 1996; Saiidi et al. 2001; Krish et al. 2018; Shrestha 2019). There are currently several successful seismic retrofitting strategies that effectively increase the seismic performance of RC columns during an earthquake. The retrofit strategies for RC columns are split into two categories; passive and active confinement.

Passive confinement is characterized by jacketing a column using steel or a fiber-reinforced polymer (FRP). This is the most common type of method used to provide effective confinement and shear strength, especially in areas with poor lap splice performance. Jacketing also offers a minimal increase in column diameter. Carbon fiber reinforced polymers (CFRP) or glass fiber reinforced polymer (GFRP), for short square RC columns, have been found to not only increase their shear strength but also energy dissipation capacity (Mirmiran et al. 1998; Haroun and Elsanadedy 2005; Galal et al. 2005). Additionally, steel jacketing provides confinement of the RC column due to the transverse steel along the height of the jacket, and prevents spalling that leads to the deterioration of the bond of longitudinal bars.

Active confinement provides another approach for retrofitting RC columns. The primary method for accomplishing this is by applying external lateral prestress using metal hoops. Tension in the metal hoops provides uniform lateral pressure that increases the shear resistance in the concrete. This technique is effective in improving ductility and limits the development of diagonal tension cracks (Saatcioglu & Yalcin 2003).

While these strategies represent effective methods for providing confinement and flexural resistance in response to a seismic event, each technique exhibits deficiencies. FRP techniques require a complicated installation method and proprietary anchors to achieve effective anchorage; furthermore, the bonding agents are limited by environmental factors and FRP materials are often unable to provide adequate ductility without confinement (Mirmiran et al. 1998; Galal et al. 2005; ACI 440.2R-17, ACI Committee 440 2017). In addition to adding to the effective seismic weight of the system, steel jacketing can also produce inelastic strain penetration into footings cause brittle shear failures from grouting. Additionally, retrofitting a square RC column with a rectangular jacket prevents adequate confinement over the retrofitted area due to bulging (Chai et al. 2008; Bournas & Triantafillou 2009). Lastly, wire prestressing requires a complex construction process that includes fixing anchors into existing members (Zong-Cai et al. 2014). These deficiencies led to the development of a novel titanium retrofit technique for square RC columns that combines

TiABs and conventional concrete to satisfy the requirements of a passive confinement strategy. By implementing supplemental TiAB ligaments, a redundant flexural load path is provided for unbroken columns. Furthermore, a TiAB spiral is also installed over the lap splice region and over the anchor points of the supplemental ligaments to provide lateral confinement by casting an unbonded concrete shell between the TiAB spiral and the column. The novel retrofit using the TiAB produced seismic performance that was equivalent or greater than modern seismic designs (Shrestha 2019). The ease of installation and performance makes the TiAB retrofit technique ideal for square RC columns in high seismic regions.

1.2 Motivation

The proposed retrofit not only successfully improves strength, ductility, and energy dissipation, but is corrosion resistant and easy to fabricate and install. However, the previous study by Shrestha (2019) had limited considerations for soil-structure-interaction (SSI) and exhibited sustainably good performance on only half of the loading cycle due to rigid body translation of the column across the top of the footing.

All but two (2) specimens were modeled with a fixed base; one (1) specimen was supported on timber piles and the other specimen was used to evaluate the influence of SSI and the nonlinear soil bearing pressure-displacement response which used a soil simulant which yielded smaller demands in the column throughout the height. It was observed that SSI can strongly influence overall seismic performance and more study was needed to assess the impact on retrofit techniques for the bridge substructure. Mitigation of collapse for seismic events throughout the ODOT bridge inventory relies on efficiently improving seismic resilience through either bridge replacement or retrofit. To develop comprehensive retrofit design guidance, the potential benefit or detriment of SSI needs to be incorporated within ODOT Bridge Design and Drafting and Geotechnical Design Manuals (BDDM and GDM). This guideance needs be based on empirical evidence developed from the evaluation of full-scale specimens and structural models for spread footings that enable estimates of capacities and demands for the seismic performance of the system. This will maximize efficiencies for costly foundation retrofits.

As part of the study by Shrestha (2019), short columns exhibited sliding of the column at the footing interface due to higher shear demands, insufficient dowel action, and/or insufficient interface friction. This occurs as the column concrete at the interface of the footing begins to break down inside the TiAB reinforced shell, and the spiral, being anchored on only one side, begins to open thereby removing the beneficial confinement. The results of the study suggest that the addition of a second spiral anchored on the opposite side of the retrofit would prevent the shell from opening and eliminate the associated loss of confinement. Unretrofitted columns fail due to bond slip of the lapped longitudinal reinforcing bars before the core concrete is pulverized and sliding can occur. Effectively preventing sliding and bond slip regardless of the direction of loading would improve the retrofit performance.

1.3 Research Scope

Research compiled in this thesis accomplishes three objectives; 1) investigation of soil-structure interaction (SSI) effects on square RC columns with a new TiAB retrofit, 2) characterization of column behavior with a TiAB retrofit after prior failure of the column without retrofit 3) development of footing analysis methods using strut and tie methods that include SSI.

To fulfill the requirements of the first objective, seven quasi-static cyclic tests were carried out using full-scale short square RC columns on a soil simulant. Two (2) specimens were retrofitted with both TiAB ligaments and two (2) TiAB spirals, and one (1) specimen was a vintage column with no retrofit. One (1) retrofitted specimen was tested on the soil simulant with an embedment depth of 0.61 m (2 ft.) and a 0.203 m (8 in.) subgrade. The second retrofit was tested without embedment. The third specimen consisted of a vintage column with no retrofit. This column was tested first with both a soil simulant embedment and subgrade under an axial load of 667 kN (150 kips), and then again with axial load of 445 kN (100 kips). The embedment was then stiffened, by removing the soil simulant and replacing it with steel springs, to eventually fail the vintage column without retrofit. The last two (2) tests consisted of a TiAB ligament retrofit applied to the previously failed column tested under the same soil conditions used during the vintage column failure.

To characterize the behavior of a column retrofitted after failure, five (5) of the previously described seven (7) tests were conducted on a vintage column. After the retrofit using only TiAB ligaments was completed, the specimen was tested in the elastic range to see how the response changed due to addition of only the titanium ligaments at deflections sufficiently large enough for comparison with the results at column failure but without producing further damage to the specimen. TiAB spiral was then installed and the shell was cast before the final test on soil simulant for the rehabilitated column was completed.

Characterizing vintage footing behavior included recording visual damage during the seven (7) experimental tests on the soil simulant and one (1) test in which the footing was held down with beams anchored into the strong floor. For this test, a hole was cored through the center of the foundation face 165 mm (6.5 in.) down from the top of the footing and a 34.9 mm (1-3/8 in.) diameter Dywidag bar was placed through the footing because there was no steel reinforcement at the top of the footing. The test was intended to fail the column; however, the lack of reinforcing at the top of the footing resulted in failure of the footing. Lastly, a strut and tie model was developed to analyze the footing including SSI .

1.4 Thesis Organization

This thesis consists of seven main chapters which are organized as follows:

Chapter 2 is a thorough review of literature relevant to the research reported herein.

Chapter 3 presents the experimental plan and procedures used to accomplish the research objectives.

Chapter 4 presents a summary of empirical results, analysis, and observations from the tests performed.

Chapter 5 provides a validation of the foam as a soil simulant.

Chapter 6 presents a summary of conclusions from the experimental and modeling results.

Appendices provide all of the results and supplementary data and information not provided in the main body of the thesis.

II. LITERATURE REVIEW

Research of a novel retrofit using TiABs for poorly detailed RC bridge columnsto improve their seismic performance was undertaken.. The technical development requires review of relevant literature that addresses the main research topics including (1) Contributing factors to column failure during earthquakes, (2) Alternative retrofit strategies, (3) Titanium Alloy Bar (TiAB) retrofit approaches, (4) Soil-Structure Interaction (SSI).

2.1 Contributing Factors to Column Failure

Early design philosophies implemented in engineering practice neglected possible lateral demands due to earthquakes. Such designs contain poor reinforcement details the can result in damage, nonductile response of members and/or connections that can lead to bridge failure during or after an earthquake. Failure often occurs due to insufficient shear resistance and flexural ductility in the bridge columns. There are three significant sources responsible for the column failure; (1) Lap-splice behavior, (2) Confinement and ductility in the plastic hinge region, and (3) The effect of axial load and lateral load direction on lateral load capacity.

2.1.1 Lap-splice Behavior

Lap-splices in bridge substructures are located at the base of reinforced concrete (RC) columns above the footing. This is the region of highest flexural demand and a probable source of poor performance in a structure when there is a bond failure. Bridge columns historically have longitudinal bars spliced with starter bars in the footing for ease of construction above the foundation. Studies by Cairns and Arthur (1979), Lukose et al. (1982), Girard and Bastien (2002), Melek and Wallace (2004), and ElGawady et al. (2010) observed that short lap splice lengths and inadequate transverse reinforcement were accountable for the poor performance in bridge columns. Therefore, researchers have concluded that lap-splices should not be used in the plastic hinge regions unless proper detailing, confinement, and adequate development length are ensured for lateral load capacity and ductility (Paulay 1982; Chai et al. 1994; Lynn et al. 1996).

The primary factors in detailing lap-splices are applied axial load, bar size, lateral confinement, longitudinal reinforcement ratio, spacing between vertical bars, splice length, and yield strength of longitudinal reinforcing steel (Priestly et al. 1996). Secondary factors that have been considered but were found to have little influence on the ultimate lap-splice bond failure due to concrete cracking include the distance between spliced bars, the strength of the concrete, and the thickness of the concrete cover (Paulay 1982).

Melek and Wallace (2004) tested six (6) full-scale RC columns under different axial loads, loading history, and shear demands to understand the effect insufficient lap splices have on column behavior. Specimens were first loaded axially and then tested laterally under reversed cyclic loading. They were able to draw several conclusions from the tests in relation to the primary factors of lap-splice detailing. The study found that ACI 381-02 (ACI Committee 318 2014) underestimates the bond stresses in lap-spliced bars, which may result in column failures in structures designed using this code. Melek and Wallace (2004) also found that the effect of axial load magnitude was negligible when considered in relation to a normalized moment and the lateral drift behavior of the column. The column lateral strength degraded faster with higher shear magnitude despite the increase in lateral load capacity when the axial load was higher. The most important indication from the tests' results was that inadequate lap-splice lengths may cause lateral strength degradation. The study specimens were constructed using a deficient lap-splice length of $20d_b$, where d_b is equal to the longitudinal reinforcing bar diameter. This resulted in large rigid body rotation of the column due to bond deterioration that allowed the longitudinal bars to slip. This failure highlights the importance of characterizing the rigid body rotation due to slip over the lap-splice length, which would help to standardize the moment versus slip-rotation springs in modeling lap-splice behavior.

The importance of lateral load magnitude and direction were found to also be important by Lukose et al. (1982). In their study, the researchers found that reversed cyclic loading was more deleterious to the performance of the spliced bars than monotonic loading. This was observed as crossing concrete cracks and damage penetration. While there were observed higher bond stresses on the tension side and there was greater relative bar-slip under tension, bar-slip on the compression side did increase as the concrete cover spalled off from longitudinal splitting of the concrete. This lead Lukose et al. (1982) to conclude that well-distributed, adequate transverse reinforcement along the splice length and beyond the development length of the bars to control bond deterioration and increase the strength and ductility of the lap-splice region. Furthermore, based on the results of the study, lap-splice lengths of 20 to 30 times the diameter of the longitudinal bars (d_b) were used in bridge columns as compression lap-splices and became characteristic of columns with large diameter longitudinal reinforcing bars. However, several studies by Chai et al. (1994), Xiao and Ma (1997), Breña and Schlick (2007), Harajli (2008), and Chai et al. (2008) discovered that this range of lap-splice lengths may be inadequate to completely transfer the tensile forces from the column bars to the starter bars resulting in rapid degradation of flexural strength.

Valluvan et al. (1993) tested 12 columns with the intent to examine retrofitted splice behavior. All of the specimens had a lap-splice 24 times the length of the longitudinal bar diameter. One specimen was a control, two strengthened the lap-splice by welding the bars together, one with an additional tie at the end of the spliced region and one without, and the remaining nine specimens were retrofitted the splice region by using additional confinement. There were three methods used to obtain additional confinement; (1) steel angles and straps along the splice region, (2) external steel reinforcing bar ties, and (3) additional internal ties in the splice region. The results indicated that welding the spliced bars provided continuity in the load path and allowed the bars to yield during cyclic loading when adequate transverse reinforcement was added over the spliced region. However, welding can significantly change the chemical properties of the bars causing brittle failures. The study also found that external confinement was effective in increasing the strength of the lap-splice given that steel ties were added along with grout. Lastly, the study found that removing concrete cover to insert internal ties caused micro-cracking in the core concrete creating stress concentrations.

Another study by Harries et al. (2006) explored the effect external confinement had on the performance of the splice region. The retrofit used carbon fiber-reinforced polymer (CFRP) composite jacketing to add external confinement of square RC columns. The retrofit resulted in allowing the column to develop the same nominal flexural capacity of columns with continuous longitudinal reinforcing steel bars. This also limited transverse strains and delayed bond slip in the spliced region; however, after slipping occurred the residual splice capacity and column ductility no longer benefit from the additional confinement. This led to three significant conclusions; (1) alternate load paths or other measures should be used to control the slip in spliced bars once significant slipping has occurred, (2) reinforced platting (e.g. CFRP composite jacketing) is inefficient confinement on square RC columns, and (3) proper detailing of the lap-splice in plastic hinge regions should include sufficient confinement and an alternate load path after the splice fails.

The research thus far has stressed the importance of proper detailing of lap splices that fall within potential plastic hinge regions. This includes proper confinement and an alternate load path or measure after splice failure. Therefore, the retrofit used in this study not only offers an alternate load path using external TiAB ligaments to support the poor reinforcing steel bar lap-splice but also offers a load path for columns that have failed due to bond slip. Additionally, the retrofit offers true circular confinement for square columns that provides a more uniform confining pressure throughout the section.

2.1.2 Confinement and Ductility

Inelastic cyclic loading leads to a decrease in the shear capacity in a plastic hinge region due to the degradation of the concrete in the column. Researchers Daudey and Filiatrault (2000) have concluded that in the plastic hinge regions the available ductility in RC columns is directly related to the longitudinal and transverse reinforcing steel details. Further studies have found that inadequate confinement limits the ultimate curvature corresponding to a compressive strain around 0.005 and a low ductility capacity, which leads to bond failure between reinforcing steel bars and brittle concrete splitting (Chai et al. 1994; Harajli 2009). Therefore it is important to detail sufficiently for ductility with effective confinement in the plastic hinge regions to withstand the displacements caused by inelastic loading without significant degradation of strength.

In 1987 Ozcebe & Saatcioglu studied the behavior of four (4) full-scale square RC columns with different confinement configurations under constant axial load and reverse cyclic loading. Each column had the same cross-section and longitudinal reinforcing steel details where the 8- #25M (#8) diameter bars were uniformly distributed. Two (2) of the specimens were confined using square hoops with 135˚ hooks with specimen two having 2/3 the spacing of transverse reinforcement as first. The second two had additional cross-ties and use the same larger spacing as the first column. The third specimen had 135˚ hooks and the last specimen had both 90˚ and 135˚ hooks. While the smaller spacing did improve the confinement in the second specimen it still did not perform as well as the last two specimens with the cross-ties. The results showed that cross-ties were superior in providing confinement to square ties. The researchers further validated their results by comparing the performance with an analytical prediction using the "Kent & Park model" (Kent & Park 1971) and the "Sheikh and Uzumeri model" (Sheikh & Uzumeri 1982). Based on the results, the analytical prediction underestimated the performance when the unconfined concrete model was used and strain hardening of the reinforcing steel was not considered. The researchers concluded that proper confinement configurations were the most efficient at improving the confinement, and increasing the transverse reinforcing ratio fails to engage the unsupported longitudinal reinforcing steel bars.

Early research by Mander et al. (1988) successfully developed an equation for confined compressive strength for both tied and continuously confined sections. They accomplished this by first developing a theoretical stress-strain model for confined concrete with different transverse reinforcing steel bars; then validated their model by correlating it with 31 experimental tests of near full-scale column specimens. The equation uses an effective confinement coefficient, k_e, based on the type of transverse reinforcing steel bars used. The value of k_e lies between 0.6 for tied sections with large aspect ratios and 0.95 for sections confined by spirals. The higher end of the scale reflects the greater efficiency of circular transverse reinforcement in providing adequate confinement. Furthermore, the effective lateral confining stress, f_1 (a function of k_e), that can be developed at yield of the transverse reinforcing steel and the compressive strength of the confined concrete are directly related by the equation. The resulting expression for f_1 illustrates an inversely proportional relationship with the longitudinal spacing of the ties or spiral.

Following up on their initial research, Saatcioglu & Ozcebe (1989) studied the effect of confinement through the response of the transverse reinforcing steel of fourteen full-scale square RC columns. The specimens were all built with the same transverse reinforcing steel layout with varying spacing. The specimen with the smallest spacing was the most effective in enhancing the confinement of the core concrete than any other specimen. The results were analyzed adjacent to the previous tests leading researchers to conclude that with the same level of confinement, the transverse steel arrangement could be more viable than reducing the tie spacing. In1994 Watson et al. developed design charts from the previously derived stress-strain relationships that allow for the determination of the quantity of transverse reinforcing steel required for specific curvature-ductility factors in the potential plastic-hinge regions of RC columns.

Nine 1/3 scale square RC columns were tested by Razvi & Shaikh (2018) to study the efficiency of confinement provided by ferro-mesh jacketing. There were three types of confinement that varied among specimens: (1) stirrups, (2) stirrups and ferro-mesh jacketing, (3) only ferro-mesh jacketing. They subjected the specimens to a concentric compressive load and analyzed the performance in terms of axial load carrying capacity, energy dissipation, and ductility in relation to the lateral deformation. Specimens that used stirrups and the ferro-mesh jacketing performed better than specimens with only one type of confinement. These specimens had a 20% increase in their axial load capacity and showed higher energy dissipation compared to the RC columns that only used stirrups.

2.1.3 Effect of Axial and Lateral Load Direction on Lateral Load Capacity

There are two main concerns when designing to accommodate axial loads, the crushing force and additional overturning moments due to P-Delta effects. However, Priestly et al. (1995) discovered it can also be beneficial in increasing the shear strength by forming an inclined compression strut that resists the applied shear force directly through the horizontal component of the axial force. Saaticioglu & Ozcebe (1989) also tested the effect of varying axial loads in both tension and compression to simulate the axial load couple that results from the application of a lateral load on a bent frame. Their observed results of the tension load indicated an early inelastic response and a delay in strength degradation beyond the initial yield. For the opposing case, higher yield strength and earlier strength degradation were observed when a compression axial load was applied. The hysteretic responses indicated that the yield moment is affected by the level of concurrent axial load.

Earthquakes impose lateral loads that act in directions other than the principal axis that subject rectangular columns to biaxial bending (Zahn et al. 1989). Saatcioglu and Ozcebe (1989) included in their study the effect of simultaneously varying bidirectional load reversals, and they recorded a post-yield response that was characterized by relatively severe strength and stiffness degradation compared to unidirectional load response. The study by Zahn et al. included 400mm (15.7in) square RC columns with transverse reinforcement specified in the code, and subjected to lateral loads both diagonally at the corner of the column and parallel to the face of the column. Between both cases, there was no significant difference in flexural strength and ductility. Later, in 2018 Wang et al. performed a study on ten full-scale rectangular RC columns to better understand the effects of seismic events on CFRP retrofitted columns. Half of the columns were retrofitted with three layers of CFRP along the plastic hinge length and the other half were not. The lateral load was applied at varying angles in a range from the strong axis to the weak axis. The results of their study indicated that there was a general trend in capacity reduction of lateral drift, ductility, stiffness, and energy dissipation as the angle of loading changed from the strong axis to the weak axis. Furthermore, both retrofitted and unretrofitted columns exhibited the worst performance at 60˚ not along the weak axis. The CFRP did enhance the seismic performance of the columns regardless of the angle of loading. The failure varied in unretrofitted columns from a brittle shear failure mode to a ductile flexural failure mode. In the case of the retrofitted columns, a ductile failure mode controlled despite the change in the angle of lateral loading. The success of enhancing the seismic performance of columns leads to a review of alternative retrofit strategies.

2.2 Alternative Retrofit Strategies

The two principal strategies utilized in retrofitting RC columns are passive confinement and active confinement. Passive confinement is characterized by jacketing a column with either a steel or a composite material and relies on the material properties to provide lateral confinement. Active confinement actively prestresses the column by applying external lateral prestress using metal hoops.

2.2.1 Passive Confinement

There are two main techniques that provide passive confinement via retrofit. Those are steel jacketing and composite material jacketing. The use of steel jackets provides two advantages over conventional hoops or spirals, 1) significant confinement due to transverse steel along the length of the retrofit, and 2) the concrete encase in the retrofit is prevented from spalling. These two advantages prevent deterioration of the bond between the longitudinal bars and the concrete, and the longitudinal bars from buckling in columns that do not have sufficient confinement from conventional hoops.

Chai et al. (2008) investigated the behavior of a steel jacket retrofit on circular columns with insufficient flexural strength and ductility. They tested six (6) 0.4 scale column footing specimens with as-built details. Two of the columns were constructed to meet a 1960's era footing design that only used straight reinforcement in the bottom of the footing. The other four specimens had stronger reinforcing details in the footing. For the retrofit a 4.76 mm (3/16 in.) thick A36 hot-rolled steel jacket was used, and a gap of 6.35mm (1/4 in.) was provided between the column and the steel jacket. Five of the columns were fully grouted and one column has a partial retrofit with a thin Styrofoam sheet between the grout and the column, which allowed for a controlled dilation of the concrete cover at large lateral displacements to limit improvement in the flexural capacity; simulating a partially grouted case. The columns were subjected to a constant axial load of 1779 kN (400 kips, or 0.18$f'c\ Ag$), and lateral loading reversals. The control specimen was damaged and then repaired and tested again.

Results indicated that the lap-splice length of $20d_b$, where d_b is equal to the longitudinal reinforcing bar diameter, was insufficient to develop the yield stress in the longitudinal bars and they observed severe strength degradation due to bond failure in the control specimen. Fully-grouted steel jacketing was effective in increasing the lateral strength, stiffness, and ductility compared to the as-built columns. The partial retrofit provided for a more gradual strength degradation and exhibited bond failure at the initial stages of loading. Conclusions drawn from the results highlight several problems that come with steel jacketing. 1) poor footing strength may result in brittle footing shear failures as grouting can cause inelastic strain penetration into the footing. 2) Rectangular jackets are preferred in areas with limited spacing; however, out-of-plane bulging is a source of concern for the column's flexural capacity because adequate confinement can not be maintained.

El Gawady et al. (2010) tested eight 0.4-scale RC columns with rectangular cross-sections and examined their behavior considering deficient lap-splice details and different retrofit jacketing techniques. The columns were tested under $0.07f'cAg$, or 7% of the column axial load capacity. In this study, a lap-spliced length was 35 d_b, and performed better than any previously reported shorter lap-splices. In the control specimen, the failure mechanism consisted of lap-splice bond failure and low-cycle fatigue rupture of the longitudinal bars. The researchers observed worse behavior in the steel-jacketed columns than in the control specimens. The crushing of the concrete in the gap between the jacket in the footing was credited as the source of the failure as this led to the buckling of the longitudinal bars in the gap. Despite the failure, the retrofit did not change the initial stiffness of specimens and produced a more stable hysteretic response with reduced pinching. El Gawady et al. (2010) retrofitted four specimens with FRP and CFRP; these columns that used CFRP wraps had an increase in displacement ductility up to 14% and largely exhibited a low-cycle fatigue rupture of the longitudinal bars. Lastly, Axial strains observed in the rectangular CFRP jackets were significantly higher than in specimens where the oval-shaped CFRP jacket was implemented.

Composite material jacketing typically comes in the form of a type of fiber-reinforced polymer (FRP) jacket and is used to improve the confinement of concrete as a seismic upgrade or rehabilitation. Some of the earliest efforts to study this technique were done by Xiao and Ma (1997) in which they studied the behavior of RC circular columns with poor lap-splice details retrofitted with prefabricated composite jacketing. The results of their study returned significant improvements in the flexural capacity and ductility after repair. Further studies demonstrated that circular profiles performed better than square profiles (Mirmiran et al. 1998; Haroun and Elsandadey 2005; and Gosku et al. 2014).

Haroun and Elsansadedy (2005) investigated the effect of FRP jackets on the ductility of circular and rectangular columns by performing lateral cyclic loading tests on ½ scale RC bridge columns that had short lap-splice lengths. The circular columns were 609 mm (24 in.) in diameter and the square columns were 609 mm x 609 mm (24 in. x 24 in.). The square columns needed to have a 2 in. radius at the corner to fit the retrofit. Congruent with previous studies circular columns retrofitted with the FRP jackets exhibited better performance than the square columns. Furthermore, partial slippage of the lap splice was observed during loading on columns with FRP jackets that were designed for a larger jacket strain, but had lower lateral capacity. Only one square column that had pre-mold mortar blocks to create a quasi-circular section with continuous confinement improved performance but still failed to meet the target ductility demands.

That same year Galal et al. (2005) performed reversed cyclic lateral testing on 2/3 scale short square RC columns with different quantities of transverse reinforcement under constant axial load. The purpose of the study was to investigate the difference in response of columns retrofitted with CFRP, and glass fiber reinforced polymer (GFRP). One control specimen had a higher transverse reinforcement. Both FRP jackets performed better than the control specimen as indicated by the strains measured in the transverse reinforcement and the FRP layers. Results showed that CFRP was more effective than GFRP at both increasing shear strength and energy dissipation capacity. Moreover, columns with CFRP jackets exhibited ductile behavior plastically hinging at the top and bottom, unlike the control specimen that exhibited brittle shear failure.

A further study on the effectiveness of using CFRP to retrofit non-ductile square RC columns with low concrete strength and continuous longitudinal reinforcing steel bars was conducted by Ozcan et al. (2008). Five RC columns were tested under reversed cyclic lateral loading and the effect of axial load during the retrofit execution was examined. There was one control specimen, two with one layer of CFRP, and two with two layers of CFRP. One of each type of retrofitted column was under axial load from the time of retrofit until the end of the test. Conclusions drawn from the test were that increasing the number of CFRP layers improves the drift capacity regardless of the axial load during the retrofit application; this was also the case for the ultimate drift ratios. The CFRP improved the column ductility but not the lateral load-carrying capacity.

Similarly, Goksu et al. (2014) tested eight RC non-ductile rectangular columns with CFRP retrofits. Four of the specimens had continuous longitudinal reinforcement and four had lap-splices with a length of $40d_b$. All of the specimens had the same transverse reinforcement at 200 mm (7.9 in.) on center. Consistent with Ozcan et al. (2008), higher ductility was observed in the columns with continuous longitudinal reinforcement and CFRP jackets; however, this was not the case for the columns with lap-splices. Therefore, CFRP on rectangular RC columns can provide adequate confinement thereby preventing buckling in the longitudinal reinforcement. Contrary to this the columns with the lap-splices displayed bond-slip failure. Researchers concluded that an alternate load path is required along with effective confinement after the lap-splice fails.

2.2.2 Active Confinement

The alternative to a retrofit that provides passive confinement is a retrofit that provides active confinement. The technique used to accomplish this strategy is wire prestressing. Active confinement using external pressure on an RC column can enhance strength and stiffness more effectively than passive systems, as observed by Saatcioglu and Yalcin (2003), Andrawes et al. (2010), and Zong-Cai et al. (2014). Shear resistance in concrete comes from cracked concrete or uncracked concrete through aggregate interlock. These components are typically assessed using the 45˚ truss analogy as explained in the ACI design code (ACI 318 2002). If there is insufficient transverse reinforcement diagonal-tension failure can occur due to the inability of the concrete to carry shear across a crack. Therefore, during a seismic event if shear cannot be carried across a crack the only resistance comes from the transverse reinforcing steel. Prestressing overcomes the formation and propagation of diagonal shear cracks thereby improving the shear resistance.

Two studies that explored active confinement as a seismic retrofit technique were by Gamble et al. (1996) and Saatcioglu and Yalcin (2003) on square RC columns retrofitted with prestressed CFRP, and metal strips. Both studies found that prestressing provided a significant increase in the shear strength and ductility; more importantly, high-strength steel strips greatly reduced shear cracks and improved deformation capacity. Furthermore, Saatcioglu and Yalcin (2003) investigated prestressing hoops with specially designed anchors on circular, square, and rectangular columns that were deficient in shear resistance. Results indicated a lateral drift capacity increase of 4% in shear critical columns after retrofitting.

While prestressing with metal strips and hoops can enhance the performance by suppressing shear failure there are a few reasons why this technique may not be a viable option. Zong-Cai et al (2014). Highlights that the installation requires proper anchoring to an existing member and a feed-through tensile jack must be used to apply the tension for prestressing the wires or strips. Lastly, while this technique does increase shear capacity, enhanced flexural ductility is necessary to satisfy the demands imposed on the column during a seismic event. Columns that require a seismic retrofit often lack this characteristic.

2.3 Titanium Alloy Bar Retrofit Approach

Seismic retrofits currently available have successfully demonstrated their efficacy in improving lateral load capacity in stiffness, strength, and ductility for circular RC columns. Unfortunately, these effects have not been comparable in square RC columns. This is largely due to the inability of these techniques to provide effective confinement in areas critical to failure during lateral loading. Uniform stress around the column is necessary to provide effective confinement. In square columns, the edges of the section must be chamfered before the retrofit can be applied to obtain an improved stress profile that more closely resembles uniformity. Attempts to FRP circular or oval jackets have been reported; however, conclusions suggest they require sophisticated installation techniques and effective anchorage using proprietary anchors (Mirman et al. 1998; Galal et al. 2005). Furthermore, FRP materials are brittle, limited by environmental constraints, and the contribution to ductility is only noteworthy in relation to the increased confinement provided (ACI 440.2R-17, ACI Committee 440, 2017). In the case of steel jacketing, it is difficult to ensure proper grouting which may result in weak pockets similar to the partial retrofit observed in the study done by Chai et al. (2008). Inspection of these retrofits is difficult, especially in post-earthquake evaluations. Retrofitting techniques focus on ensuring confinement but have given little focus to improving flexural strength in columns that use lap-splices in the longitudinal reinforcing steel. Recently studies have been conducted by Shrestha (2019) on a novel retrofit approach using titanium alloy bars (TiABs) that is both economic and effective.

2.3.1 Titanium in Structural Engineering

There is a myriad of characteristics titanium alloys possess that make them popular in other engineering disciplines such as aerospace and aeronautics. The materials are lightweight, flexible, and thermally insensitive (Takahashi et al. 1994, Shrestha 2019). Properties that lend TiABs to use in structures are high tensile strength, ductility, environmental durability, high shear strength, high maximum service temperature, and thermal compatibility to concrete. ODOT has implemented the use of TiABs to rehabilitate damaged girders on Mosier Bridge over Oregon's main East-West highway, I-84, using a near-surface mounting (NSM) technique. The retrofit took only a couple of weeks to finish and saved more than 97% of the estimated cost to replace the bridge; furthermore, the cost was 30% less than using alternative retrofit methods and provided sufficient rehabilitation to the bridge performance (Higgins et al. 2017). These features suggest a TiAB retrofit is a viable option alternative and have provided the experimental and analytical basis for TiAB retrofit use on square RC bridge columns (Barker 2014; Amneus 2014; Knudtsen 2016; Vavra 2016; Higgins et al. 2017; Shrestha 2019).

2.3.2 Titanium Alloy Bar Retrofit on Square Reinforced Concrete Columns

The retrofit technique developed by Shrestha (2019) utilizes both TiAB ligaments, which are used to increase the flexural strength of columns with lap-splices by providing an additional flexural load path, and TiAB spirals to provide continuous confinement through hoop action. Anchoring the TiABs involves a simple process of drilling and epoxying the bars directly into the column and footing; the retrofit does not require any specialized construction practices. Lastly, a polycarbonate sheet is used as formwork for casting the concrete shell around the column. This formwork provides allows inspection of the concrete casting to ensure there are no pockets, and because of TiAB corrosion-resistant properties, no cover is necessary allowing for post-earthquake inspections.

Quasi-static cyclic load tests with constant axial load were performed on 14 full-scale square columns by Shrestha (2019). Specimens profiles measured 610 mm x 610 mm (24 in. x 24 in.) and were constructed with equivalent as-built details in the column. The retrofit details were designed following a review of the ODOT bridge inventory and include 4 - #10 (#32M) Gr. 60 longitudinal reinforcing steel bars, compared to the vintage detail of 4 - #11 (#36M) Gr. 40 longitudinal reinforcing steel bars. Transverse reinforcement consisted on #3(#10M) Gr. 40 square hoops with 90˚ hooks at 305 mm (12 in.) on center and 1.5 in. of concrete cover. Vintage lap-splice length for the columns was 914 mm (36 in.; approximately 28d_b. Five tall columns measuring 3.962 m (13ft.), and nine short columns measuring 2.743 m (9 ft.) were tested.

Shrestha (2019) examined the parameters of loading direction, retrofit details, column height, and rocking footings. Results were discussed in terms of global structural behavior, force-deformation response, strength degradation, displacement ductility, energy dissipation, equivalent viscous damping, and stiffness degradation. The strain response in the TiAB ligaments, TiAB spirals, column ties over the lap-splice length, starter bars, and column bars over the lap-splice length was also recorded. The study also presented the results of the shear deformation response and the average curvature of the system.

With respect to the direction of loading two control specimens were tested first as representative columns. The first column was tested at 0˚ at the face of the column and failed at a drift ratio of 0.87%. The second column was tested at 45˚ to investigate the effect of the lateral loading direction and failed at a drift ratio of 1.25%. Results indicated a brittle failure mode and no distinguishable displacement ductility in either column. The failure mechanism observed was bond failure between the longitudinal bars in the column and the starter bars extending from the foundation. The failure in the column loaded perpendicular to the face was characterized by vertical cracking and progressive splitting and spalling over the lap-splice region. Failure in the column loaded at 45˚ exhibited some 45˚ cracking across the face of the column.

A short column with both a TiAB spiral and 90˚ hook ligaments was laterally loaded under a constant axial load of 667 kN (150 kips). Results indicated that the retrofit was not able to prevent the lap-splice failure. However, when compared to the square control specimen, the ultimate lateral capacity had increased from approximately 165 kN (37 kips) to 409 kN (92 kips) and the specimen was able to maintain its strength at a drift ratio of 4% as the lap-splice failure was delayed successfully.

In relation to hook angle, a comparative study was done by Shrestha (2019) to examine the difference in the behavior of ligaments with a 90˚ hook and a 135˚ hook. While the 135˚ hooks were successful in suppressing the extraction of the ligament from the column, indicated by reduced cracking and smaller dilation of the concrete around the hook regions, the installation was more expensive and required special equipment to drill the anchor holes at the corresponding angle.

When comparing the effect of the ligaments used in conjunction with the spiral the specimen without ligaments had reduced energy dissipation and shallower hysteresis loops and lower equivalent viscous damping. Furthermore, the specimen without ligaments exhibited rigid body translation across the surface of the footing due to higher shear demands and insufficient dowel action or interface friction. Without ligaments, the specimen capacity dropped to 80% at approximately 3.3% drift on the pull cycle and 7.2% drift on the push cycle. The ability to maintain the higher drift ratio on the push cycle was attributed to the TiAB spiral anchorage that allowed for the continuous engagement of the flexural steel on one side. After testing the column, the retrofit shell was removed and the column was inspected for damage. Upon inspection, it was discovered that the column was pulverized and the start bars bent along the plane of rigid body translation in the direction of loading, and splice failure was evident from cracks that ran along the length of the lap-splice. Based on these results, a TiAB retrofit would benefit from a second spiral over the plastic hinge length, anchored opposite from the full-length spiral, to improve ductility regardless of the direction of loading and sustain the lateral load capacity for longer.

The last variable that was examined was the material of the ligaments. Another test was completed using stainless steel ligaments which exhibited a much less ductile response, and a plastic hinge formed above the retrofit shell resulting in rotation in the column above the retrofit shell and minimal movement below the retrofit. Using stainless steel ligaments increased the member strength which created a weak failure plane above the sprial.

Shrestha (2019) also developed a design guide for construction and recommendations, using the experimental validation as the basis, for the seismic retrofitting of columns that match the vintage column details. This includes square RC columns with footing starter bars and insufficient lap-splice length and inadequate transverse reinforcement. The guide uses a symmetric 4-span bridge constructed in the mid 20th century, considered a ‘standard bridge’ as classified by the ODOT bridge inventory review. The design does not include provisions for columns that have already exhibited damage or failure.

2.4 Soil-Structure Interaction

It is necessary to understand the role of soil-structure interaction (SSI) given that all structures are subject to soils acting on the footing that influences the overall structural response in a seismic event; however, studies that include the effects of both SSI and inelastic bridge substructures are limited. Studies typically model structures with either a fixed base and no SSI or with idealized soil behavior (Shrestha 2019). These studies do not reflect realistic foundation scenarios and often obscure the role of structural non-linearity in response to the seismic demands on the structure. For example, Ciampoli and Pinto (2005) and Chaudry et al. (2001) suggests that SSI does not have a significant effect on the inelastic demands of the structure. Contrary to Ciampoli and Pinto (2005) and Chaudry et al. (2001), researchers Mylonakis and Gazetas (2000), Gazetas and Mylonakis (2001), Fraino et al. (2010) reported SSI has a significant influence on the inelastic response of structures.

With a lack of consensus into SSI, plastic hinges in structural members are expected to provide ductility and achieve energy dissipation demands. The plastic hinge forms to limit additional material degradation and structural instability (Cheng and Mander 1997). Plastic hinges are typically designed in the column to retain elastic behavior in the foundation; however, conservative foundation design is inconsistent with findings in recent studies. Three of the most important findings are; 1) Moderate to severe seismic events will likely induce a nonlinear foundation response, 2) Strong ground motions are a source of concern for soil failure and permanent deformation, and 3) Rocking foundations may be a favorable solution for the overall system performance.

Stiff soils require a high moment capacity in the footing compared to the yield moment capacity of the column. Considering this, moderate excitation may cause brittle failure through the formation of a plastic hinge at the base of the column. A reported case by Gazetas (2019) and Sharma (2019), was of a one-story building that collapsed during the moderate 1999 Athens earthquake.

Kawashima and Nagai (2006) and Apostolou et al. (2007) reported uplift of spread footings after the following earthquakes; 1964 Good Friday (Alaska), 1971 San Fernando, 1999 Kocaeli, and 1999 Athens. The authors surmised that foundation rocking is inevitable for spread footings subjected to ground motions specifically when they are only loaded on the soil by gravity loading.

2.4.1 Rocking Foundations

The dynamic nature of seismic ground motions may not lead to structure collapse in the case of soil failure or foundation uplift caused by the moment shear and vertical loading (Gajan et al. 2005; Anastasopoulos et al. 2012; Hakhamaneshi 2014; and Kutter et al. 2016). Examples of structures with shallow foundations that have avoided severe damage from earthquakes due to rocking are as follows as reported by the researcher(s) listed: 1952 Arvin-Tehachapi (Housner 1956), 1960 Chili (Housner 1963), 1997 Tongan (Campbell 1977), 1989 Loma Prieta (Elghazouli 2009), 1993 Hokkaido Nansei-Oki and 1995 Kobe (NEHRP 2004), 1999 Kocaeli (Gazetas et al. 2003), and 2001 Christchurch (Storie et al. 2014).

Many researchers have proposed using foundation rocking as an effective method for seismic isolation (Housner 1963; Beck and Skinner 1973; Huckelbridge and Ferencz 1981; Preistley et al. 1996; Mergoas and Kawashima 2005; Chen et al. 2006; Sakellaraki and Kawashima 2006; Gajan and Kutter 2008; Anastasopoulos et al. 2010; Kutter et al. 2011; Deng et al. 2012; Hakhamaneshi 2014; Allmond et al. 2015). Furthermore, this has been utilized in designing bridges in-service today such as the Rio-Antirrio bridge in Greece and the Vasco de Gama bridge in Portugal (Pecker 2003). Rocking foundation systems have been described as a weak footing/ strong column system, in which the column is prevented from plastically hinging (Allmond 2014). This is due to the comparative low moment capacity of the footing in relation to the moment capacity of a traditional plastic hinging column design. Factors that contribute to a rocking foundation are footing width, soil density, soil type, embedment, suction, erosion, excess pore water pressure generation, and liquefaction. The factors important in this study are contact length, footing width, soil density, and embedment.

2.4.2 Estimation of Critical Contact Length

A rocking foundation alternates between contact at the base of the foundation against the subgrade and the uplift of the foundation, which creates a gap under the unloaded portion of the foundation. A curved surface at the soil-foundation interface forms as a result of this phenomenon (Rosebrook

2002; Gajan et al. 2005). As the magnitude of rotation increases the area under the foundation in contact becomes smaller and moves closer to the toe of the foundation. As this occurs bearing pressures increase along the contact length to satisfy equilibrium conditions. If sufficient rotation is achieved, bearing pressures become equal to the ultimate bearing resistance and no further reduction in area can occur. For rectangular spread footings the critical contact length is the length of the footing in contact with the subgrade and is defined by:

$$A_c = P/q_u$$

$$L_c = A_c/B$$

Where A_c is the critical contact area, P is the vertical load of the structure, q_u is the ultimate bearing resistance of the soil, and B is the width of the footing. After cyclic lateral loading, it is possible for gravity to close the gap created by the curved surface of the soil thereby providing a self-centering mechanism. Additionally, local bearing failure occurs at the edges of the curved soil-foundation interface (Allmond 2014; Hakhamaneshi 2014; Sharma 2019).

2.4.3 Effect of Soil Density

Denser granular materials exhibit a greater in-situ horizontal effective stress, larger dilatancy, and particle rotation frustration resulting in a larger mean effective stress during shearing. Additionally, for footings resting on this material, the normalized moment capacity is higher resulting in less energy dissipation (Allmond 2014).

Effects soil density and initial void ratio have on rocking foundations were investigated by Faccioli et al. (1999), Negro et al. (2000), and Anastasopoulos et al. (2011). Faccioli et al. (1999) specifically investigated the nonlinear interaction between shallow foundations and supporting soils and the effect soil density had on them, by doing cyclic loading experiments. Researchers observed that as the soil beneath the footing curved the rotational stiffness degraded and local bearing failure occurred along the soil footing interface. This varied with initial soil density. Results further indicated that on denser soils less energy was dissipated, and larger moment capacity than the loose soil. While large permanent settlements were observed in both cases, the footing on the dense sand experienced uplift in the initial cycles of loading and the footing on loose sands sank continuously with no sign of uplift.

2.4.4 Effect of Embedment

Studies on the effect of embedment suggest there is an increase in stiffness of the foundation and a reduction in the displacement amplitude during seismic events. Furthermore, as the embedment increases the soil provides additional confinement to the foundation which results in increased moment and bearing capacities. Passive earth pressures and bearing stresses are also affected by the amount of embedment resulting in a stiffer rotation and displacement response in the foundation (Lysmer and Kuhlemeyer 1969; Novak 1970; Novak and Beredugo 1972; Gupta 1972; Novak 1974; Lin and Jennings 1984; Gazetas and Stokoe 1991; Inukai and Imazawa 1992).

Hakhamaneshi (2014) evaluated the rocking performance of foundations in relation to their shape and embedment. It was observed that similar foundation superstructures reached the same final embedment indifferent of the initial embedment depth. Soil was also observed flowing into the gap formed during rocking. Results indicated a balanced rocking system due to the equality between the soil flowing into the game formed and the settlement caused by local bearing failure or sliding.

Sharma (2019) investigated the effect of embedment on the behavior of footings in clay materials during rocking. A series of quasi-static cyclic tests were performed on model footings placed in clay. Sharma (2019) found that the footing resting on the ground surface had lower initial rocking stiffness and moment capacity than the embedded footing. Additionally, the footing resting on the ground surface had a nearly linear stiffness during unloading. Clay embedment performed similarly to sand as footings exhibit uplift due to soil in-filling and dilatancy. However, the footing resting on the ground surface settled rather than uplift in relation to a footing on sand.

2.4.5 Effects of Rocking Foundation on Seismic Assessments of Retrofitted Bridge Columns Footing Systems

Before the 1970's footing reinforcement details did not include provisions for seismic input; therefore, it was typical to use only a single two-dimensional reinforcing mat at the bottom of the footing. Seismic forces acting on the footing, when the plastic hinge in the column forms, can be three to four times greater than elastic design magnitudes. Older bridge foundations may have the following inherent potential problems: 1) Inadequate tension capacity in the footing and pile cap connections, 2) Inadequate flexural and shear strength, 3) Large shear stresses in column-footing connections, 4) increases in demand to the footing and increases in premature footing failures due to column retrofitting, or increases in column flexural strength (Xiao et al. 1996; McLean and Marsh 1999; Shrestha 2019). A proposed solution to these potential problems are utilizing rocking foundations.

Hung et al. (2011) investigated the effect of rocking behavior in three columns. two RC circular columns with lap-splices in the longitudinal reinforcement and inefficient transverse confinement and one column with a steel jacket retrofit. All the specimens were built on spread footings. Hung et al. (2011) observed a reduction in the ductility demand of the columns supporting as long as the system has sufficient ductility for the rocking mechanism to occur.

Shrestha (2019) conducted an experimental study on two full-scale retrofitted RC columns; one with a fixed base and one with realistic footing details on a soil simulant, FOAMULAR 1000 Extruded Polystyrene (XPS). The soil was constructed of two 7.62 cm (3 in.) layers of XPS and 5.08 cm (2 in.) of concrete that measured 182.9 cm x 182.9 cm (72 in. x 72 in.) board meant to limit cutting of the foam. The column and footing tested on the soil simulant remained elastic. Minor cracks in the footing were observed after the test that divided the footing into four quadrants. These cracks likely formed due to an artificial increase in the footing size by the concrete board, which was an extra foot in both dimensions compared to the footing. Despite the cracking, the benefits of rocking mechanism to dissipate energy for seismically retrofitted bridge columns were clearly highlighted.

In summary contributing factors to column failure during a seismic event include insufficient lap-splice lengths, lap-splices in the plastic hinge length, poor confinement and ductility, and the flexural demands produced by axial and lateral loads. This has led to the development of column retrofits. Most of the retrofits do not include alternate flexural load paths, little to no increase in lateral load capacity, a way of inspection or post-earthquake evaluation, and inability to provide adequate confinement for square RC columns. The TiAB retrofit delays the failure of the lap-splice, and adequately confines the square RC column. The TiAB spiral anchor can engage the flexural steel on one side. Additionally, little SSI research has been conducted on retrofitted columns on shallow foundations. This study will investigate the soil-structure interaction of the TiAB retrofit applied to square RC columns while improving the new TiAB retrofit by adding a second spiral over the plastic hinge length to maintain more sustainable flexural capacity in all directions. Furthermore, this study investigates the ability to strengthen a column which has previously failed using the TiAB retrofit approach.

III. EXPERIMENTAL PROGRAM

An experimental program was developed to characterize the effects of SSI on square RC columns, constructed using vintage details with a new TiAB retrofit strategy. The program included an improvement on the original TiAB retrofit design developed by Shrestha (2019), by installing a second spiral over the plastic hinge length. Additionally, it included construction of three full-scale square RC column specimens and eight different tests on these specimens. Test variables included stages of axial load magnitude, with and without retrofit, soil simulant, embedment, and stiffness of passive pressure.

Specimen design and construction were based on bridge columns along the critical pathways, I-5, US-97, and OR-58. Their geometries, reinforcing details, retrofit details, and construction process are discussed below, followed by instrumentation, test setup, vertical loading, and lateral displacement protocol. Material properties can be found in Appendix A.

3.1 Specimen Design

Specimens were designed based on the ODOT bridge inventory review completed by Shrestha (2019). The review explains that 75% of columns were square and 32.9 % were between 4.57 m (15 ft.) and 5.49 m (18 ft.). Furthermore, longitudinal reinforcement for the columns was most commonly 1 % of the gross cross-sectional area, typically 4-#36M (#11) Grade 40 bars. Transverse reinforcement most commonly provided were #10M (#3) square ties, equivalent to Grade 40, at 305 mm (12 in.) on center with 38.1 mm (1.5 in.) clear cover. The average lap-splice for the typical longitudinal reinforcement was $29d_b$, where d_b is the diameter of the longitudinal bar.

Spread footings were used as the foundation for 79% of the columns. Footings were most commonly 1.52 m (5 ft.) square and reinforced with a steel mesh of #16M (#5) Grade 40 at the bottom of the footings with 76.2 mm (3 in.) clear cover.

The concrete mix-design used in the experimental program was provided by a local ready-mix supplier. The 28-day design compressive strength was 28 MPa (4 ksi) and the maximum aggregate size was 4.75 mm (3/8 in.). Three (3) specimens were constructed from the design and eight (8) tests were conducted. Specimen 1 and 2 were retrofitted with TiAB ligaments and TiAB spirals, and specimen three was first failed as an unretrofitted vintage column and then retrofitted in phases to achieve the second objective. Table 3.1 outlines test numbers and descriptions and matches them with the corresponding specimen.

Table 3.1 Specimen notation and test description.

Test ID	Specimen ID	Test Description
1	S.1	Complete Retrofit w/ Foam Embedment & Subgrade
2	S.2	Complete Retrofit w/ No Embedment & Foam Subgrade
3	S.3	Vintage w/ Foam Embedment, Subgrade, 150 kip axial
4	S.3	Vintage w/ Foam Embedment, Subgrade, 100 kip axial
5	S.3	Vintage Failure w/ Foam Subgrade and Steel Embedment
6	S.3	Vintage TiAB Ligaments w/ Foam Subgrade & Steel Embedment
7	S.3	Vintage Complete Retrofit w/ Foam Subgrade & Steel Embedment
8	S.2	Complete Retrofit w/ Tied Down Footing

Tests after column failure with subsequent stages of retrofit, T6 and T7, were intended to mimic conditions during an aftershock following a seismic event in which a damaged or failed column-footing would rest on adjacent soil that was also damaged during the initial earthquake.

3.1.1 Footing Details

Spread footing dimensions used in the experimental program were 1.52 m (5 ft.) square and 0.609 m (2 ft.) deep following the results of the bridge inventory review. A single mesh of reinforcement was used with 76.2 mm (3 in.) clear cover; however, Grade 40 reinforcing bars were not available. Therefore, an equivalent mesh of #13M (#4) Grade 60 bars was used. 18-#13M (#4) bars spaced 171 mm (6.75 in.) on center, and 4-#32M (#10) starter bars with a 559mm (22 in.) tail in accordance with ACI 318-02. Figure 3.1 illustrates the footing design for all specimens.

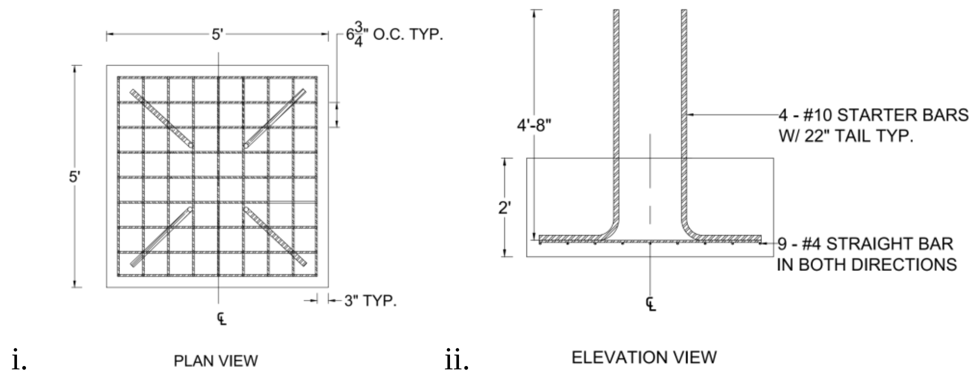

Figure 3.1. – Typical vintage footing details (all dimensions are inches). i) Plan view, ii) Elevation view.

3.1.2 Column Details

The overall height of the columns was 2.74 m. (9 ft.) above the top of the footing. The location of the lateral load was 2.438 m (8 ft.) above the top of the footing. The specimen represents the lower half of an actual bridge column whereby the point of inflection is assumed to occur at midheight. The column cross section was 609 mm (24 in.) square. Equivalent longitudinal reinforcement of 4-# 32M (#10) Grade 60 was used due to unavailability of #36M (#11) Grade 40. Transverse reinforcement included #10M (#3) Grade 40 square ties with 90˚ hooks spaced 305 mm (12 in.) on center starting at 152 mm (6 in.) from the top of the footing and clear cover measures 38 mm (1.5 in.) over the length of the column. The longitudinal reinforcing bars measured 2.62 m (8 ft.-7in.) and 2.67 m (8 ft. – 9 in.) to avoid clash of the hooks. To secure the point of loading #13M (#4) Grade 60 square ties with 90˚ hooks 122 mm (4 in.) on-center were used as reinforcement, and four 60.3 mm (2-3/8 in.) holes were blocked out. Lap-splice length chosen was $30d_b$ to achieve a comparable length to the average lap-splice of vintage columns. Figure 3.2 depicts column details for all specimens.

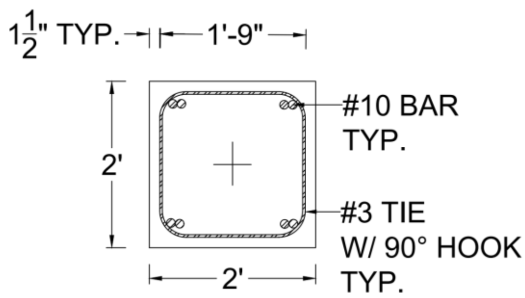

i. PLAN VIEW

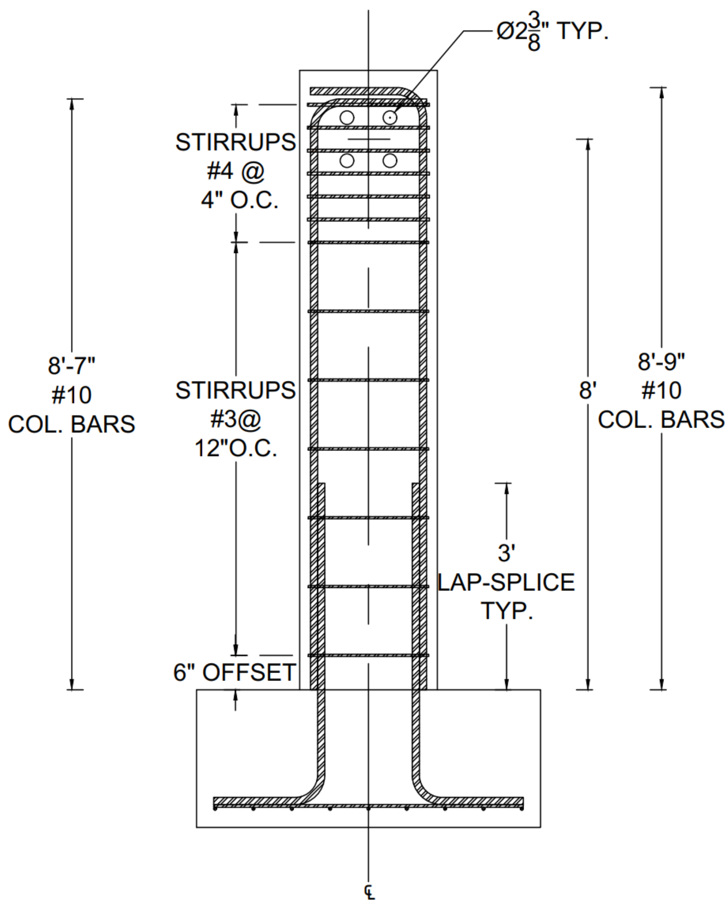

ii. ELEVATION E-W

Figure 3.2 - Vintage column details (all dimensions are feet and inches). i) Plan view, ii) Elevation view.

3.2 Retrofit Design

The retrofit design included two main TiAB components, ligaments and spirals. There were two ligaments placed on each face of the column anchored in the column and the footing. The rest of the ligament lengths were unbonded from the column. Confinement was provided by applying a TiAB spiral over the length of the ligaments. Formwork was placed over the spiral and infilled with concrete for form an reinforced shell over the square column. The retrofit shell was cast with a nominal 889 mm (35 in.) in diameter around the column, and 1.52 m (5 ft.) tall to prevent the extraction of the ligaments from the column face. A second spiral was installed over the plastic hinge length to improve the ductility of the retrofit designed by Shrestha (2019). No concrete cover was provided over the titanium spiral due to the inherent corrosion-resistant properties of the titanium.

3.2.1 TiAB Ligament

TiAB ligaments varied in length to prevent an abrupt change in stress that would occur if they all terminated at a single elevation. Three different lengths were used 1.93 m (6 ft.- 4 in.), 1.78 m (5ft.-10in.), and 1.63 m (5ft.-4in.). Shrestha (2019) determined the average ligament length by calculating the tension lap-splice length recommended for column longitudinal bars by AASHTO LRFD Bridge Design Specification (2017). The TiAB ligaments were fabricated with 254 mm (10 in.) 90˚ hook with a proprietary deformation machined 191 mm (7.5 in.) along the length of the hook tail. At the opposite end, the bars were smooth and had the proprietary deformation along the lowest 381 mm (15 in.) of the length. The deformations allow the TiABs to be anchored into the concrete using structural epoxy. TiAB ligaments had a nominal diameter of 15.9 mm (5/8 in.). The details of the TiAB ligaments are illustrated in Figure 3.3

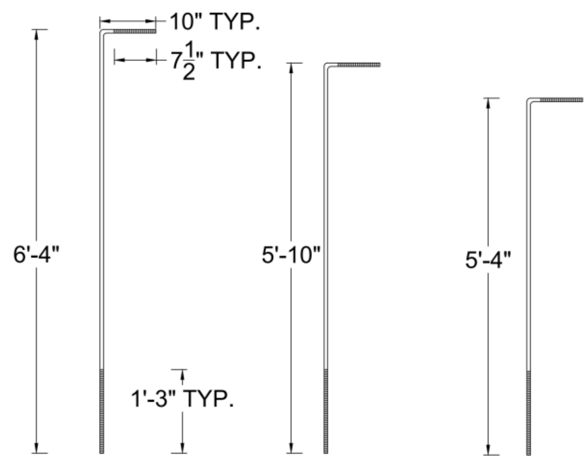

Figure 3.3 - TiAB ligament details (all dimensions are feet and inches).

3.2.2 TiAB Spiral

TiAB spirals are shipped from the manufacturer as a 9.52 mm (3/8 in.) diameter coil. There are no special instructions for fabrication. All cutting and bending of the TiAB spiral are completed during construction using conventional construction practices, and there are no proprietary deformations added to any part of the spiral. However, Shrestha (2019) used the following AASHTO LRFD design specifications (2017) recommendations for spirals as transverse reinforcement in the selection of size and spacing of the TiAB spirals.

- ❖ Minimum spiral diameter of 9.52 mm (3/8 in.)
- ❖ Maximum center to center spacing of spirals should be the smaller of $6.0d_b$ or 152 mm (6 in.)
- ❖ Minimum clear spacing between the spirals should be the greater of 1.33 max aggregate size or 25.4 mm (1 in.)

Based on a sensitivity analysis, guidelines from Priestly et al. (1996) and Mander et al. (1988), and the recommendations from AASHTO LRFD, Shrestha (2019) chose a 9.52 mm (3/8 in) diameter for the TiAB spiral with a 63.5 mm (2.5 in.) pitch over the majority of the height allowing at least 2.2 MPa (0.32 ksi) lateral pressure and uniform confinement to develop. To allow space for installation of a second spiral, the pitch was extend to 127 mm (5 in.) over the plastic hinge length of the column so that the total pitch was 63.5 mm (2.5 in.). A tighter pitch of 38.1 mm (1.5 in.)

was used over the length of ligament hooks, and extended 152 mm (6 in.) below the lowest TiAB hook installed. A completed specimen design is shown in Figure 3.4.

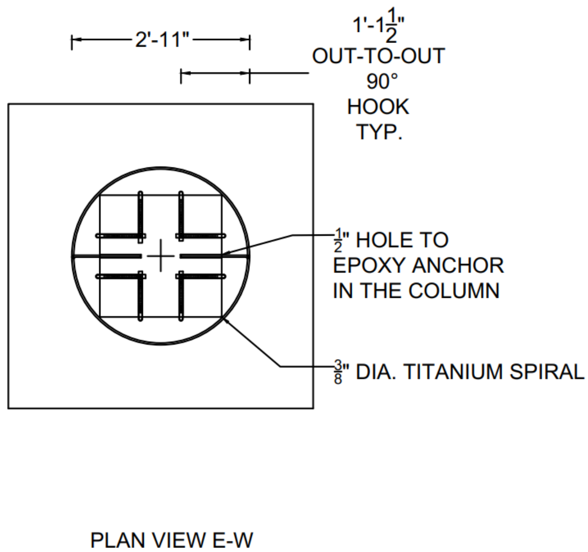

i.

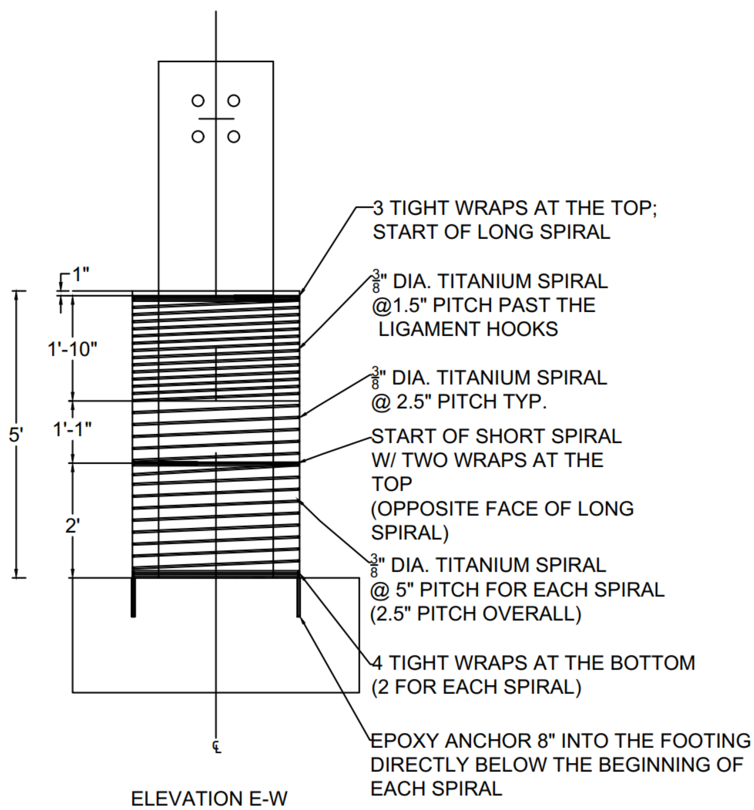

ii.

Figure 3.4 – Complete specimen design with TiAB spiral details (all dimensions are feet and inches). i) Plan view, ii) Elevation view.

3.3 Specimen Construction

Specimen construction was completed in the Large Scale Structural Engineering Laboratory at Oregon State University. The following section describes the sequential construction process in detail.

3.3.1 Footing Construction

The footings were constructed of a mesh grid of 18-#13M (#4) Grade 60 reinforcing steel with 7.62cm. (3 in.) of cover from the bottom and faces of the footing, 4-#32M (#10) starter bars, and the ready-mix concrete previously described in the specimen design. Reinforcing steel was laid out in a grid with bars at 171.5 mm. (6-3/4 in.) on-center and tied together using conventional tie wire. The bars in the North-South (N-S) direction were on the bottom to correspond with the lateral loading direction. Concrete dobies were 7.62 mm (3 in.) and were tied to the reinforcing mesh to maintain cover. Starter bars used in the connection to the column had a 0.914 m. (3 ft.) lap-splice length above the top of the footing and had a standard 90˚ hook with a length of 559 mm. (22 in.). The start bars were oriented 45˚ toward the corner of the formwork to accommodate the footing geometry, and a plywood jig was cut and tied to the bars to maintain the geometry of the starter bars during concrete placement. After placing the concrete, lifting hooks were inserted into the footing to facilitate moving specimens around the laboratory and the surface coincident with the column was raked to roughen the cold joint. Footing construction stages can be viewed in Fig 3.4.

i. 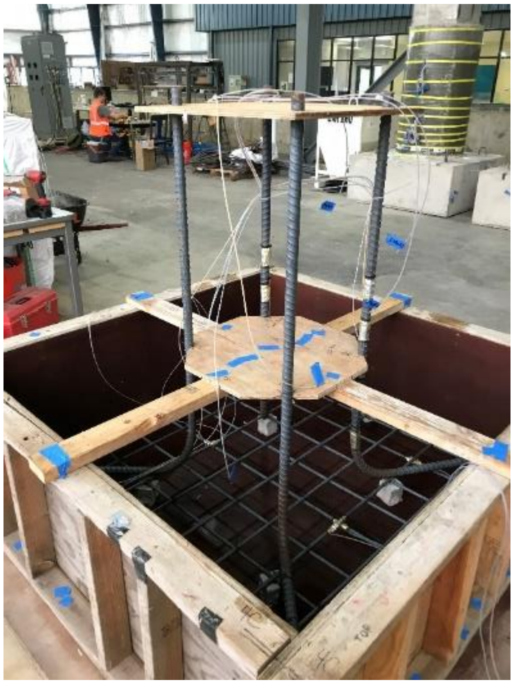 ii. 

Figure 3.5 - Stages of construction for vintage spread footings. i) Specimen geometry and formwork prior to casting. ii) Spread footing after concrete casting.

3.3.2 Column Construction

The columns were constructed using 4-#32M (#10) bars, 2.616 m. (8ft-7in.) and 2.667 m. (8ft-9in.) in length. The 50.8 mm. (2 in.) offset allowed the geometry of the column to be maintained for the standard 55.9 cm. (22 in.) hook length and the 3.81 cm. (1-1/2 in.) cover for the column. The longitudinal reinforcing steel was laid on its side using stands. Transverse reinforcement locations were marked and then tied to the longitudinal bars to complete the cage. A crane was used to lift the cage into place over the footing. After the formwork was assembled holes were blocked out for actuator attachment. The formwork was then tied down to keep it from moving during casting. Concrete was then pumped from the bottom by a local concrete pumping company. Columns were cast at 2.74 m. (9 ft.) tall to accommodate the loading setup. Figure 3.5 provides a images for different stages of column construction.

i. 

ii. 

iii. 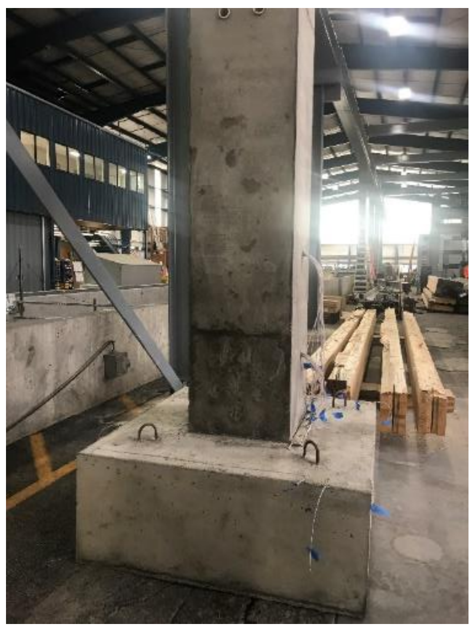

Figure 3.6 – Stages of construction for the vintage column. i) Column cage attached to the footing. ii) Tied down formwork with pump valve. iii) Completed vintage column on the spread footing.

3.3.3 TiAB Installation & Shell Construction

Ligaments were installed by first drilling 559 mm (22 in.) deep holes, 19 mm (3/4 in.), into the footing at 102 mm (4 in.) from the center of the column, and directly against the column face. The actual embedment depth into the footing was 508 mm (20 in.). The 50.8 mm (2 in.) extension of the hole allows TiAB ligaments to sit flush against the column by first placing the bar all the way down into the hole and then bending it back to align with the anchor hole in the column. Furthermore, the top 127 mm (5 in.) of the embedment depth were left undeformed to increase the anchorage strength and enlarge the cone of concrete developed during pullout. Because ligament heights were staggered, 238 mm (9-3/8 in.) anchor holes were drilled into the column at either 1.11m (3ft. – 7-3/4 in.), 1.26 m (4 ft. – 1-3/4in.), or 1.42m (4ft. - 7-3/4in.) and holes were rounded out to accommodate the radius of the ligament hooks. All holes were cleaned thoroughly using a vacuum and bottle brush and epoxy was injected into the holes so that when ligaments were installed the epoxy was flush with the surface of the specimen. Columns were then wrapped in plastic sheathing to prevent the shell from bonding to the column, ensuring a clear characterization of the retrofit behavior without contamination from composite action. After TiAB ligament installation a strap was used to hold the ligaments tight against the face of the column as the epoxy cured, and TiAB spiral installation began. Figures 3.7 and 3.8 display the ligament installation dimensions and process. Installation of the second spiral was as straightforward as that for a single long spiral and was completed using the conventional placement practice.

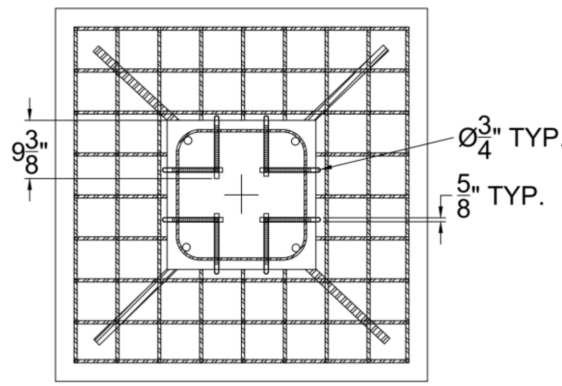

i. PLAN VIEW E-W

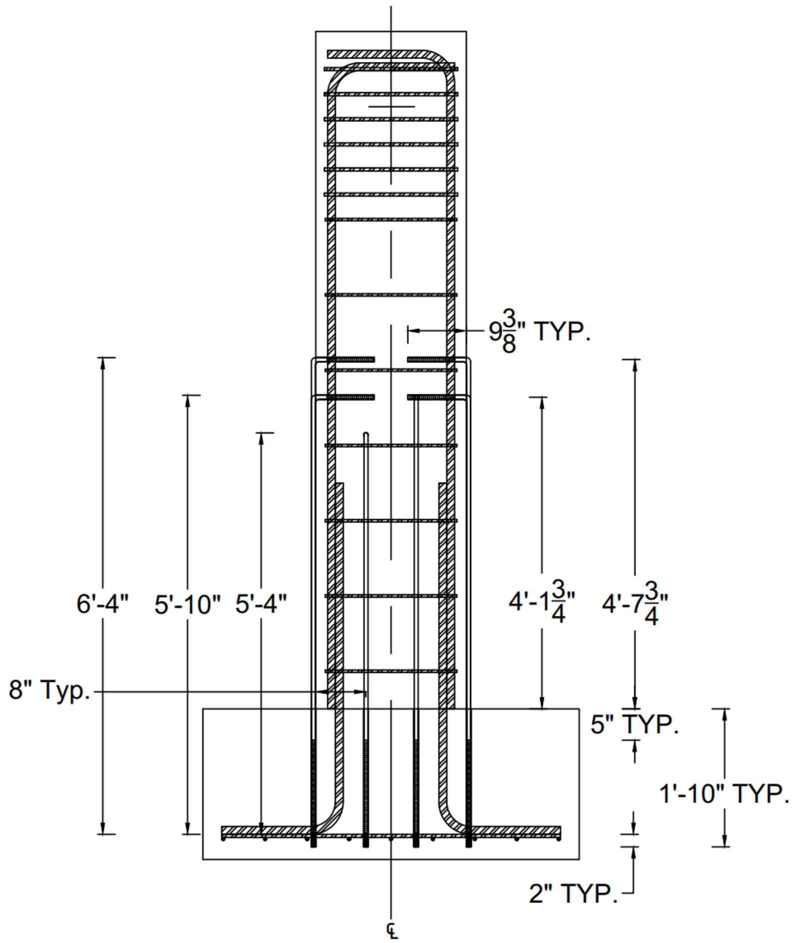

ii. ELEVATION N-S

Figure 3.7– Specimen with a ligament installation (all dimensions are feet and inches). i) Plan view, ii) Elevation view.

i.  ii. 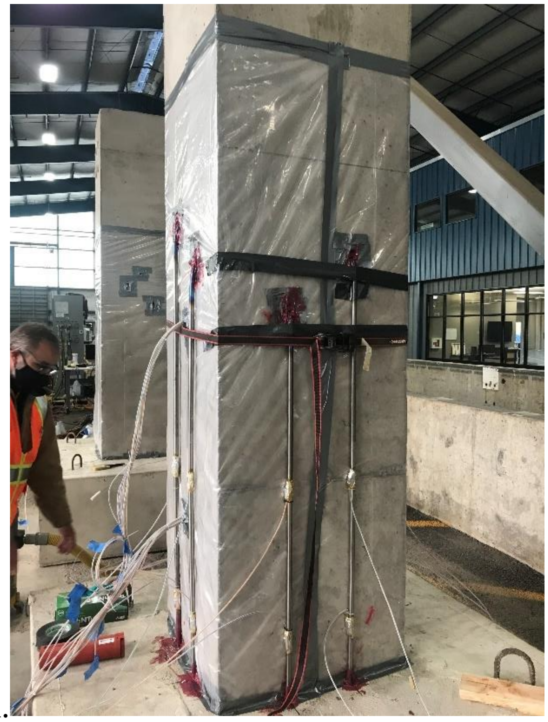

Figure 3.8 – Construction sequence of TiAB ligament installation. i) Drilled holes and plastic sheathing. ii) Complete installation of staggered ligaments.

TiAB spirals required 90˚ hooks to be bent to anchor the TiAB spirals into the column and footing, and an oxyacetylene torch was used to accomplish this. Anchor depth into the concrete for the spirals were 203 mm (8 in.) following design guidance given by Shrestha (2019). While the length of the hooks for the footing could be bent to the 203 mm (8 in.) depth, hooks in the column needed to be 343 mm (13.5 in.) to account for the column geometry. 12.7 mm (1/2 in.) holes, 203 mm (8 in.) deep, in the column were drilled in the center of the column on opposite faces, except for the vintage column. Holes in the vintage column were drilled in adjacent faces due to the lack of material on the North and South face after failure. For a flat concrete surface at the top of the shell, the top spiral was anchored 25.4 mm (1 in.) below the height of the shell at 1.5 m (4 ft. – 11 in.). The second spiral was anchored into the column at the height of the plastic hinge length 0.61 m (2 ft.). Hooks were then anchored into the column with the same method used on the ligaments. Three tight wraps were pulled around the column for the first spiral and two were used for the second spiral to prevent pullout of the hooks. Spirals were tied with mild steel to keep the geometry in place. At the bottom of the column two tight wraps for each spiral were used to prevent pullout of the hooks in the footing. Once the wraps were complete the holes were measured, drilled, cleaned, and hooks were bonded into the footing with structural epoxy. In the case of specimen 3, small PVC, pipe insulation foam, and duct tape were used to cover threaded rods installed for instrumentation required for testing the vintage column. Furthermore, because there was material missing from the bottom of the column a straight edge and a level were used to maintain the diameter of the TiAB spiral around the bottom portion of the column. Spray foam was used to dam the bottom of the formwork to prevent concrete from flowing out of the bottom. Concrete infill was cast by wrapping a polycarbonate sheet around the TiAB spiral and held in place with ratchet straps. TiAB spiral installation for specimens 1 and 2 are shown in Figure 3.9, and Figure3.10 shows TiAB spiral installation for specimen 3.

i. 

ii. 

Figure 3.9 – Specimen 1 and 2 TiAB spiral construction sequence. A) Spiral installation, B) Formwork for infill.

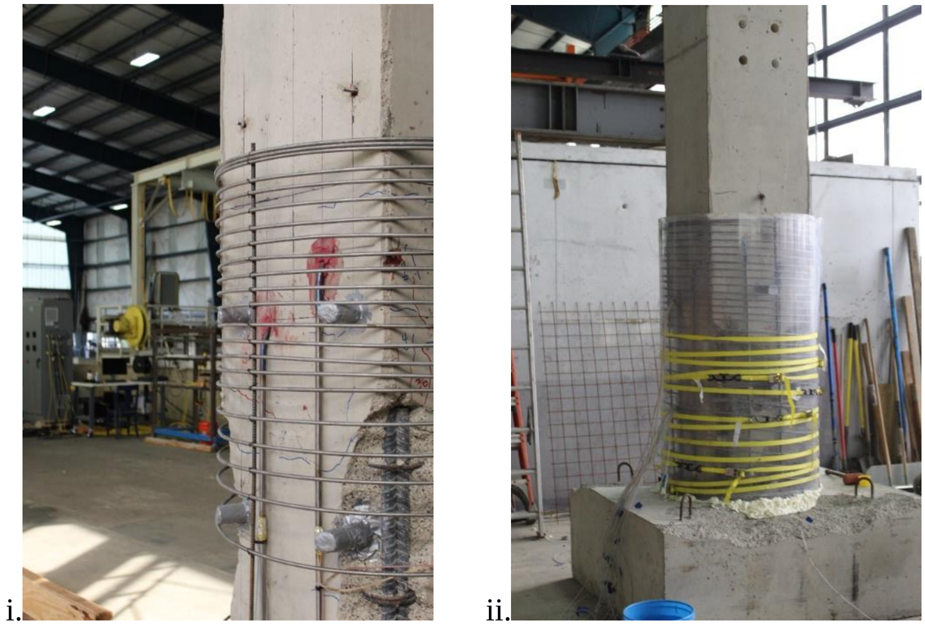

Figure 3.10 – TiAB spiral installation. i) threaded rod covers, ii) Shell casting formwork.

3.4 Material Properties

The material properties of the reinforcement were tested at a nearby qualified testing facility. The titanium mill certs were used without additional testing, and the concrete compressive and tensile tests were completed for day of test strength and 28-day strength. The results of these tests can be viewed in Tables 3.2 – 3.6. A comprehensive description of material properties can be found in Appendix B.

Table 3.2 - 28 Day Concrete Compressive Strength.

Specimen ID	Specimen Component	Compressive Strength, MPa (psi)	Standard Deviation	Coefficient of Variation
S.1	Footing	27.07 (3926)	238	6
S.1	Column	27.06 (3924)	181	4.6
S.1	Shell	35.07 (5086)	160	3.1
S.2	Footing	27.07 (3926)	238	6
S.2	Column	27.06 (3924)	181	4.6
S.2	Shell	35.07 (5086)	160	3.1
S.3	Footing	38.90 (5647)	161	2.9
S.3	Column	30.86 (4476)	141	3.1

Table 3.3 - Day of Test Concrete Compressive Strength.

Specimen ID	Test ID	Test Date	S.C.	Compressive Strength, MPa (psi)	Standard Deviation	Coefficient of Variation
S.1	1	11/17/2021	Footing	39.70 (5757)	77.9	1.4
S.1	1	11/17/2021	Column	46.24 (6707)	216	3.2
S.1	1	11/17/2021	Shell	39.0 (5655)	132	2.3
S.3	3,4	12/17/2021	Footing	47.39 (6873)	179	2.6
S.3	3,4	12/17/2021	Column	36.59 (5307)	277	5.2
S.3	7	4/20/2022	Shell	24.35 (3532)	109	3.1
S.2	8	6/1/2022	Footing	39.84 (5778)	124	2.1

Table 3.4 - Day of Test Concrete Tensile Strength.

Specimen ID	Test ID	Test Date	S.C.	Compressive Strength, MPa (psi)	Standard Deviation	Coefficient of Variation
S.2	8	6/1/2022	Footing	2.68 (389)	66.1	17

Table 3.5 - Tensile Test Results of Reinforcing Steel.

Bar Size	Bar Type	Tensile Strength, MPa (ksi)	Yield Strength, MPa (ksi)	Elongation in 4D (%)	Reduction of Area (%)	Original Gauge Diameter, mm
#10M, #3	Tie	583 (86)	386 (56)	27.78	-	-
#13M, #4	Footing	614 (89)	372 (54)	28	56	6.4 (0.252)
#32M, #10	Column/ Starter	758 (110)	490 (71)	21	49	12.8 (0.503)

Table 3.6 - Tensile Test Results of TiABs.

TiAB Bar Type	Tensile Strength, MPa (ksi)	Yield Strength, MPa (ksi)	Elongation 4D (%)	Reduction of Area (%)
Ligament	1126 (163.3)	1037 (150.4)	21	55
Spiral	1010 (146.5)	920 (133.4)	19	50

3.5 Instrumentation

The global and local response of the specimens during testing were captured using strain gauges, string potentiometers, spring return linear position sensors (LPS), and load cells. Commercially available strain gauges, with a gauge resistance of 120±0.3 Ω, were bonded to the footing bars, starter bars, column bars, column ties, TiAB ligaments, and TiAB spirals to capture strains. Axial load was measured with a 1335 kN (300 kip) load cell attached to a steel beam and connected to a pin and clevis, using Dywidag rods. A 31.7 mm (1-1/4 in.) LPS was hot glued in the center of the column above the shell to measure shell uplift during testing. A load cell attached to the lateral load hydraulic actuator was used to directly measure the applied column shear.

Four different lengths of string potentiometer were used; 50.8 mm (2 in.), 119 mm (4.7 in.), 254 mm (10 in.), and 1016 mm (40 in.). The global behaviors captured by these sensors were rigid body translation, rigid body rotation, column bending, and total column displacement. Measuring the rigid body rotation was accomplished by anchoring eight eye bolts into the footings, four at the corners 76.2 mm (3 in.) each face, and four in the center of the footings 76.2 mm (3 in.) from the face. String potentiometers were suspended from a instrumentation frame located above the specimen. Redundant sensors were added to the bottom of the footing by drilling a 15.9 mm (5/8 in.) diameter hole, 25.4 mm (1 in.) deep and adhering a stud using epoxy into the footings. Using a hole saw, 102 mm (4 in.) holes were drilled through the soil simulant subgrade and string potentiometers were placed on the strong floor. A magnet was then tied to the end to connect to the studs embedded in the footings. All string potentiometers used to measure rigid body rotation were 254 mm (10 in.) in length except for two in the center of the footing on the East and West faces, that were 119 mm (4.7 in.) in length.

Rigid body translation was measured using two 119 mm (4.7 in.) string potentiometers attached to the instrumentation frame 305 mm (12 in.) from the top of the footing on the East and West faces. These were attached to eye bolts anchored in the geometric center of the footing on the East and West face.

Total column displacement was measured by attaching a 1016 mm (40 in.) string potentiometer to fixed frame opposite the top of the column to measure the overall motion of the specimen at the point of loading. Using this and the previously mentioned string potentiometers the column bending could be derived.

Local responses including curvature, strain penetration, and shear strain of the column core were captured using string potentiometers. To capture these, threaded rods were bonded into the core of the column. This was achieved by drilling oversized holes through the cover and shell concrete and smaller holes into the core of the column. The threaded rod was then bonded into the column core. The purpose was to prevent contamination of the measurement from movement produced by the cover concrete and shell. String potentiometers were mounted to aluminum plates and bolted to the threaded rods. Strain penetration was captured by placing two 50.8 mm (2 in.) string potentiometers on the footing, at the center of the column on the North and South sides, and attaching the string to the lowest threaded rod embedded in the column. Three 254 mm (10 in.) string potentiometers were mounted in the center of the column along its height to capture column curvature. Shear strain was measured using three panels consisting of two horizontal, two diagonal, and two vertical string potentiometers bolted to threaded rod along the height of the column on the West face at 102 mm (4 in.) from the North and South faces. The top horizontal for the lowest panel acted as the bottom horizontal for the second lowest panel, this was also the case between the second and third panels. All string potentiometers in the panels measured 119 mm (4.7 in.), except the verticals which measured 254 mm (10 in.). Appendix B contains sensor naming conventions and sensor placement diagrams.

3.6 Test Setup

Two different setups were used to conduct the 8 tests. The first setup was designed to allow for rocking footing conditions to develop, and the second setup was designed to restrain the footing and produce column failure. Both setups required use of the laboratory strong wall and strong floor. The following section describes the test setup details and functions of the components.

3.6.1 Soil Simulant Layout

FOAMULAR® 1000 Extruded Polystyrene (XPS) was used as the soil simulant, material properties can be found in Appendix A. The soil simulant started as 50.8 mm (2 in.) thick sections that measured 0.61 m x 2.44 m (2 ft. x 8ft.). Sections were then cut to into several sections to provide the subgrade under the footing of the specimens and to provide the passive pressures on the North and South vertical faces of the footing. This also helped to preserve material. Holes were drilled into the soil simulant to accommodate the string potentiometers used to measure footing rotation as described previously. Figure 3.11 illustrates the soil simulant layout and the pieces cut to construct the soil simulant.

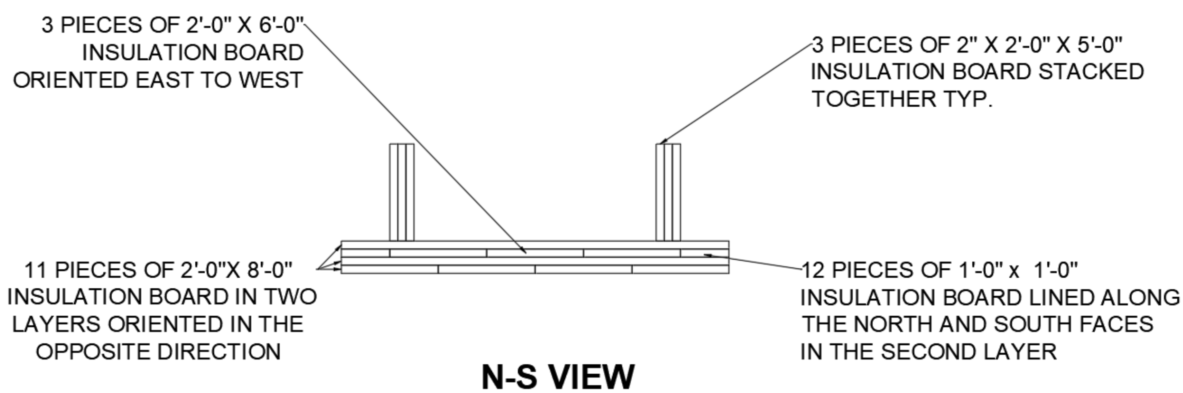

i.

ii. 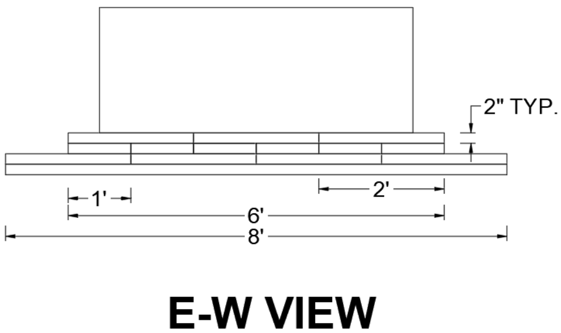

iii. 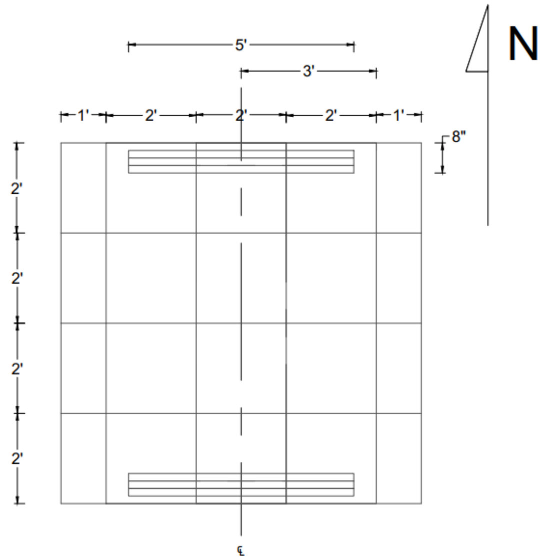

Figure 3.11 – Soil simulant layout (all dimensions are feet and inches). i) N-S elevation view and pieces used, ii) E-W Elevation view, iii) Plan view.

3.6.2 Soil-Structure Interaction Setup

Investigation of the soil-structure interaction (SSI) required a reaction frame to be built in the horizontal plane around the footing. This frame functioned to hold the soil simulant against the footing and to react the passive pressure generated as the footing rocked and pushed the simulant against it. Specimens were placed on a 203 mm (8 in.) subgrade of soil simulant, assuming a 2:1, vertical to horizontal, stress distribution (Figure 3.13) as defined by Budhu (2011), made up of 4 layers of soil simulant. The lateral resistance was provided by 3 layers of soil simulant to a total thickness of 152 mm (6 in.). It required two (2) sets of steel springs to be built to provide support for the soil simulant. The spring stiffnesses were designed based on the expected load at depth, using three different lengths of steel angle; 63.5 mm (2-1/2 in.), 82.5 mm (3-1/4 in.), and 85.7 mm (3-3/8 in.). Angles were welded on only one leg of a large base plate to provide the required stiffness variation with depth, and six steel plates measuring 102 mm (4 in.) were welded onto the apex of the angles to provide a uniform loading surface against the soil simulant. The top four springs had a stiffness of 20.15 kN/mm (115 kip/in.), the fifth spring stiffness was 30.13 kN/mm (172 kip/in.), and the bottom spring had a stiffness of 41.17 kN/mm (235 kip/in.). These stiffnesses were generated from numerical simulations completed using uniaxial compression test data in the analysis program FLAC3D from the previous study. Figure 3.12 illustrates the springs built and used in the test setup. On the North face of the footing a large reaction beam was used to support the spring and the reaction frame was anchored to the strong wall using 4 Dywidag bars.

Tests were performed using a servo-hydraulic control system that was used to impose predetermined displacements to the column at 3.25 m (128 in.) above the surface of the strong floor using a a hydraulic actuator with a 914 mm (36 in.) stroke. Tests were first initiated by applying a 667 kN (150 kip) axial load to the column top. The column load was resisted by a spreader beam that anchored to the strong floor at 1.22 m (4 ft) on both the East West sides of the specimen. A clevis and pin was used to prevent bending of the axial load anchor rods. A separate servo-hydraulic control system was used for the axial load. The axial load was controlled using load control to hold the force constant even as the column undergoes lateral drift. Attached to the beam was a 1335 kN (300 kip) load cell that measured the applied axial load. Figure 3.14 illustrates the test set up; however, minor changes to the test setup were made to accomplish particular test objectives.

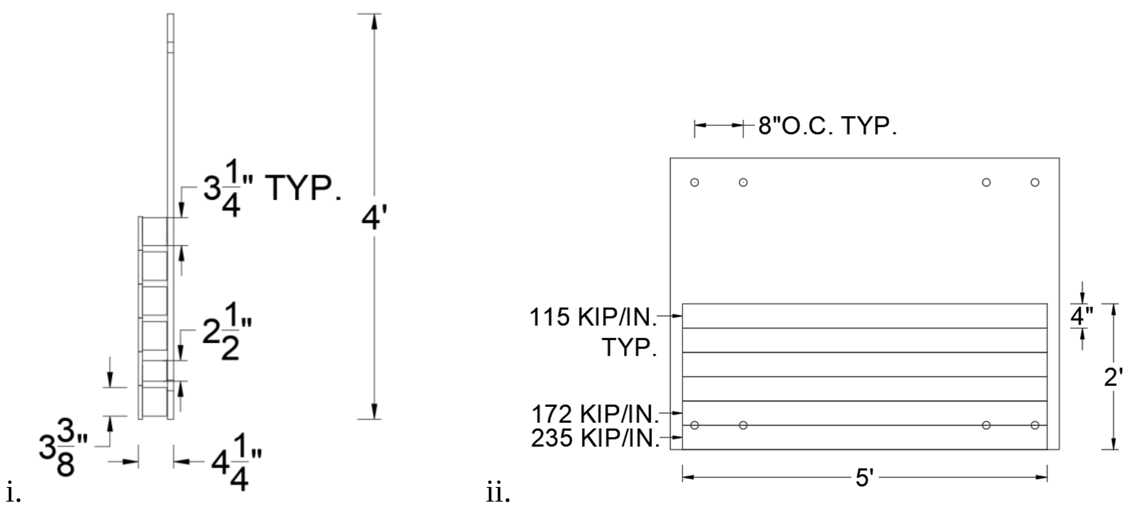

Figure 3.12 – Spring design for horizontal reaction frame. i) Angle dimensions, ii) Spring stiffness and bulk dimensions (all dimensions are feet and inches).

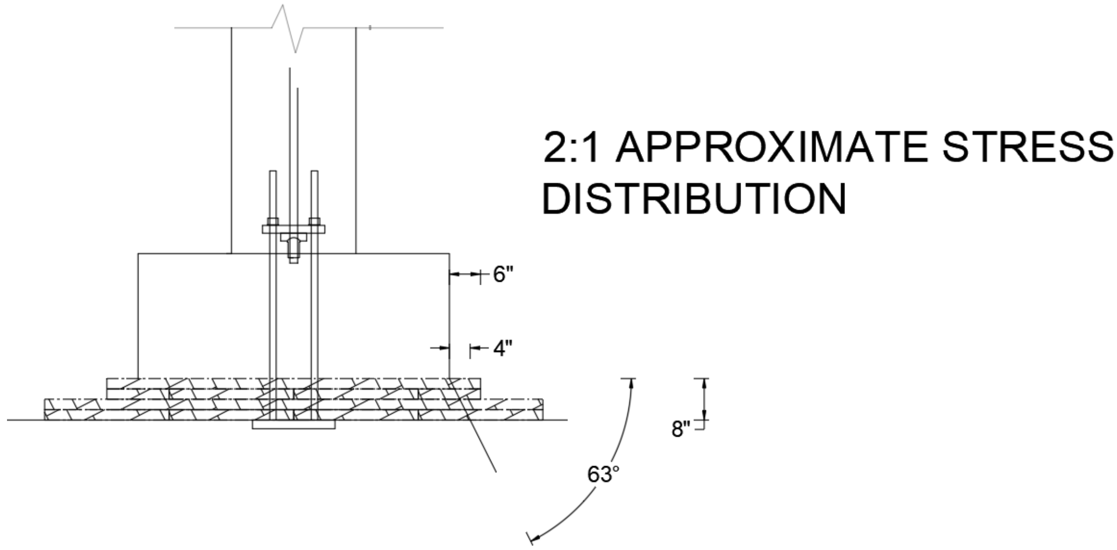

Figure 3.13 – Approximate stress distribution assumption to determine soil simulant layout (all dimensions are feet and inches).

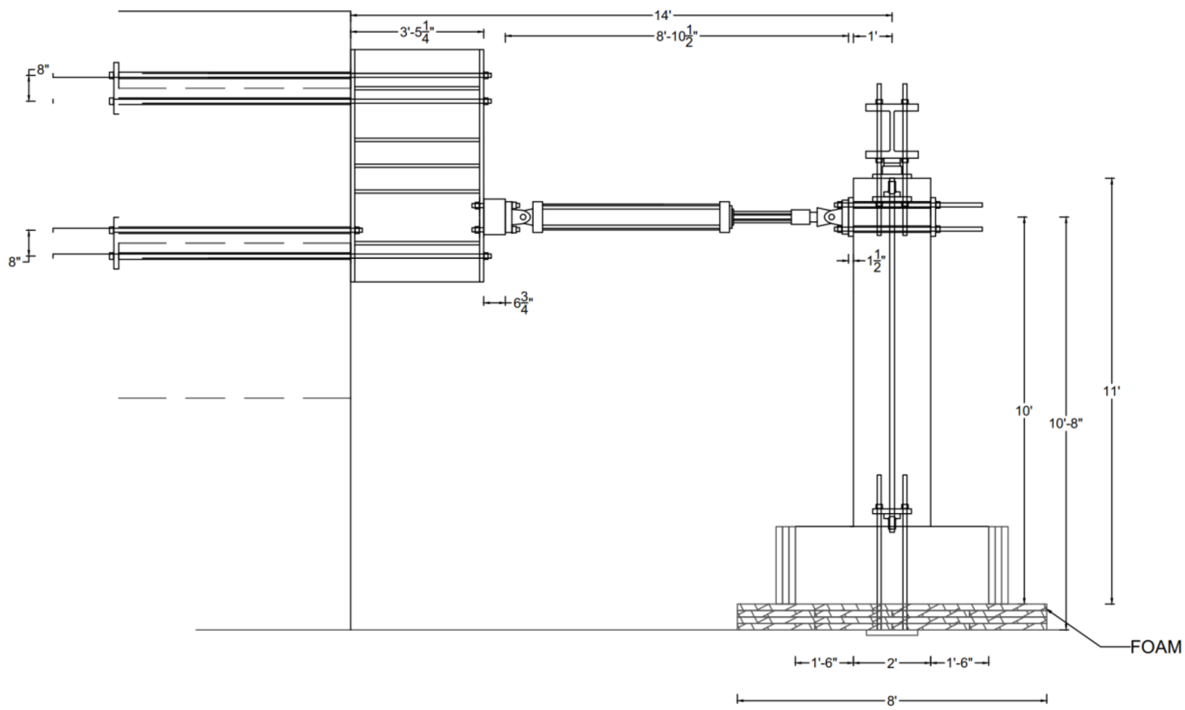

i.

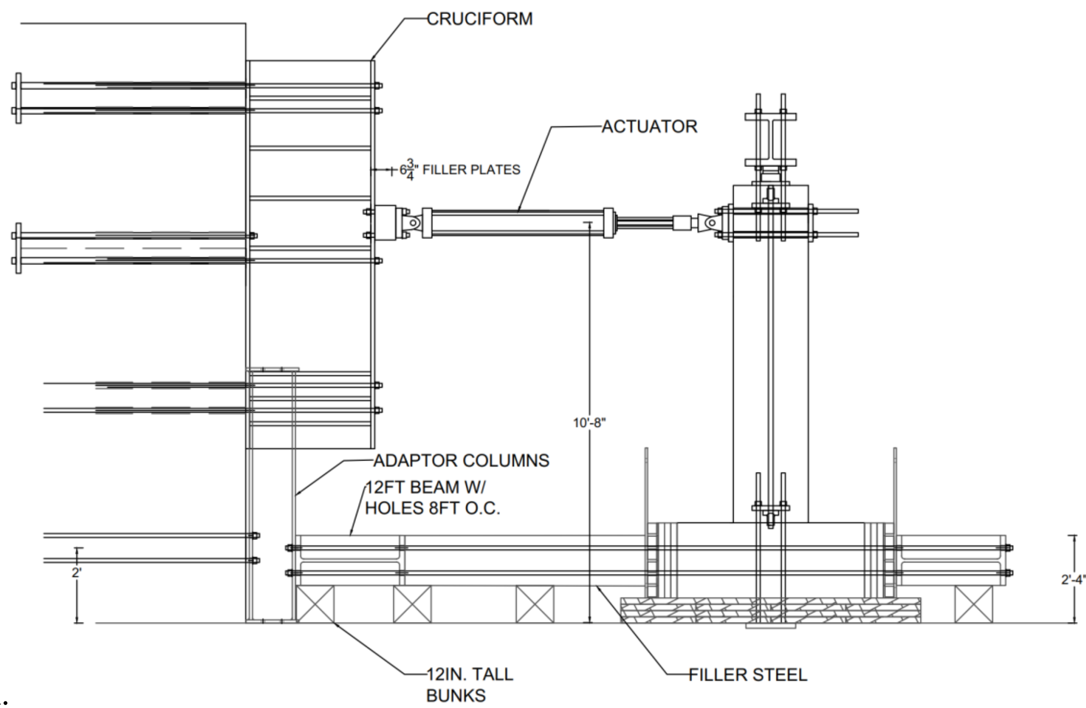

ii.

Figure 3.14 – SSI test setup design (all dimensions are feet and in). i) Specimen loading dimensions, ii) horizontal brace frame.

As previously mentioned the test setup was changed accordingly for each specific test. Figures 3.15 to 3.18 display the minor differences in each test setup.

Figure 3.15 – Test 1 (Specimen 1): Complete Retrofit with Soil Simulant Embedment and Subgrade. Standard SSI test setup.

Figure 3.16 – Test 2 (Specimen 2): Complete Restrofit with no embedment and a soil simulant subgrade

Figure 3.17 – Test 3 & 4 (Specimen 3): Vintage column with soil simulant embedment, subgrade, and axial load at 150kip and 100 kip.

Figure 3.18 – Test 5, 6, & 7 (Specimen 3): Vintage column failure, Vintage ligament retrofit, and Vintage complete retrofit. All three tests used a damaged soil simulant subgrade but steel springs for the embedment soil.

3.6.3 Experimental Setup for Failure Test of Retrofitted Column

To test the columns to failure required that the footing be restrained to force deformations and thus demands into the column. Because footing sizes are representative of old designs, they were too small to attach directly to the strong floor. An alternative vertical reaction system was devised with large beams to tie down the footing to restrict rotation and restrain rigid body motions. Further, more a reinforced concrete slab was cast and placed under the footing so that the horizontal actuator elevation could remain the same for all tests. Figure 3.19 displays the test setup used for specimen failure.

Figure 3.19 – Test 8 (Specimen 2): Complete retrofit with tied down footing test set up.

3.7 Loading Protocol

Specimens were subjected to both applied axial load and lateral displacement. Column axial load was derived from the work by Shrestha (2019) based on review of the ODOT bridge inventory. The most common column axial load observed in the bridge database was approximately 8% of the concrete compressive strength acting on the gross area of the column ($0.08f'_cA_g$). For the 24 in. square column the magnitude of the axial load was 677 kN (150 kip). This was used for all tests except for Test 4, in which the axial load was reduced to 100 kips to observe the influence of the axial load on the strength and response specimen of the specimen. The lateral displacement protocol impose on the specimens was derived by Shrestha (2019) in accordance with ACI 364.2R-13 based on the calculated yield displacement from moment-curvature analysis of the column. Table 3.2 shows the lateral displacement protocol imposed on the specimens for Tests 1-8.

Table 3.7 Lateral Displacement Protocol (Shrestha 2019).

Displacement cycle (in)	**Displacement cycle (% drift)**	**Loading rate (in/sec)**
0.10	0.10	0.005
0.19	0.20	0.01
0.29	0.30	0.02
0.40	0.42	0.03
0.80	0.83	0.04
1.20	1.25	0.04
1.60	1.67	0.08
2.00	2.08	0.08
2.40	2.50	0.1
2.80	2.92	0.1
3.20	3.33	0.12
3.60	3.75	0.12
4.00	4.17	0.12
4.40	4.58	0.12
4.80	5.00	0.12
5.20	5.42	0.12
5.60	5.83	0.12
6.00	6.25	0.12
6.80	7.08	0.12
7.60	7.92	0.12
8.00	8.33	0.12
9.60	10.00	0.12

IV. EXPERIMENTAL OBSERVATIONS AND ANALYSIS

The results of each reverse cyclic test on the full-scale square RC column-footing-soil specimens are presented in this chapter. Observations during tests are discussed to inform the analysis of results and are presented in terms of observed global structural behavior, force-displacement response, the evolution of stiffness degradation, strain magnitude and distribution, soil-structure interactions, post-failure retrofit analysis, and vintage footing behavior. Using the experimentally measured response, an analytical model of the synthetic soil was developed to predict the soil simulant pressures acting on the bottom and sign faces of the footing, and a strut and tie model was used to describe the performance of a footing containing as-built vintage details having only a single mat of reinforcing steel located at the bottom of the footing. A full archive of all experimentally measured data for each test is contained in Appendix C

4.1 Observed Global Structural Behavior

All tests were completed in accordance with the predetermined loading protocols discussed in Section 3.6. Observations were made during each test and formation and propagation of concrete cracking, or other visible distress were noted and photographed during each step of the proposed displacement history. The column portion of the specimens remained elastic in seven of the tests, even as the overall response was nonlinear. Non-linear behavior was due to plastic deformations observed in the soil-simulant. In one case, Test 8-Specimen 2, failure of the footing contributed to nonlinear response of the system. Test 5 was the only test in which the performance and failure were controlled by the column (unretrofitted column) as laps splice failure of the column flexural steel was observed above the footing. This was due to the use of steel springs as the embedment soil which generated higher pressures across the footing face compared to the soil simulant. Test 1 and Test 8 were the only tests in which damage to the footing was observed. The following sections describe the overall soil-structure response of the tested specimens based on the observations and data collected. Tests 1-3 were tested on new soil simulant each time, and Tests 4-7 were tested on soil simulant that had failed previously to mimic aftershock conditions. The strain rate for the axial loading on the soil simulant was 252 $\mu\varepsilon$/sec for the first test, and 49.6 $\mu\varepsilon$/sec for subsequent tests; soil stiffness is discussed in Section 4.5. It will be important to understand that the horizontal reaction frame was more flexible when push cycles were applied (North displacement of column) and relatively stiffer on pull cycles were applied (South displacement of column). This resulted in larger forces for the same actuator displacement amplitudes on the pull side of each cycle.

4.1.1 Test 1-Specimen 1: Complete Retrofit with New Soil Simulant Subgrade and Soil Simulant Embedment

This test was conducted over two days and data from both days were combined to provide a continuous record. On the first test day the imposed lateral displacements were half those of the predetermined loading protocol until a drift of 1.67%. To draw the horizontal reaction frame with the soil simulant, the connecting Dywidag rods were tightened. After applying the 667 kN (150 kip) axial load, the footing settlement was measured at approximately 2.54 mm (0.1 in.). During lateral loading, vertical cracks in the center of the footing on the West face were observed at a drift of 30.5 mm (1.2 in.). Offset of vertical cracks at the corners of the retrofit, indicating mobilization of the retrofit, were observed at a drift of 71.1 mm (2.8 in.). Footing cracking continued on the corners of the west face and minor horizontal cracks appeared on the NW corner of the column above the retrofit. At a drift of 81.3 mm (3.2 in.), additional flexural cracks formed in the footing, and the total lateral force acting on the vertical face of the footing were measured and observed to remain in the range of 182 kN (41 kips) on the push cycle. At a drift of 122 mm (4.8 in.), the second layer of foam on each face started to fail, and punching began to occur in the first layer of the subgrade. The center footing bar at the bottom of the footing mat in the direction of loading yielded at a drift of 132 mm (5.2 in.). The lateral pressure increased to 5.52 MPa (800 psi) at 203 mm (8 in.), and 6.21 MPa (900 psi) at 244 mm (9.6 in.). The lateral force increased to 200 kN (45 kips) and remained stable as the specimen underwent inelastic deformations. Upon the force reaching and maintaining 200 kN (45 kips), no other damage was observed in the specimen. After testing was complete and the specimen was removed from the test setup vertical cracks near the center of the footing were also observed and the cracks coalesced under the footing. Figure 4.1.A and Figure 4.1.B display the progression damage in Specimen 1 during Test 1.

i. 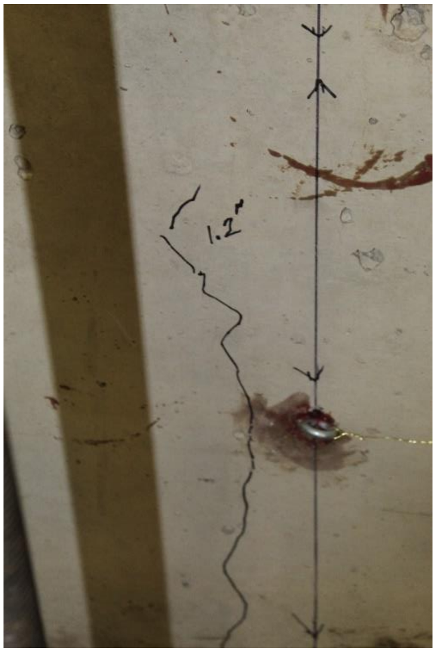

ii. 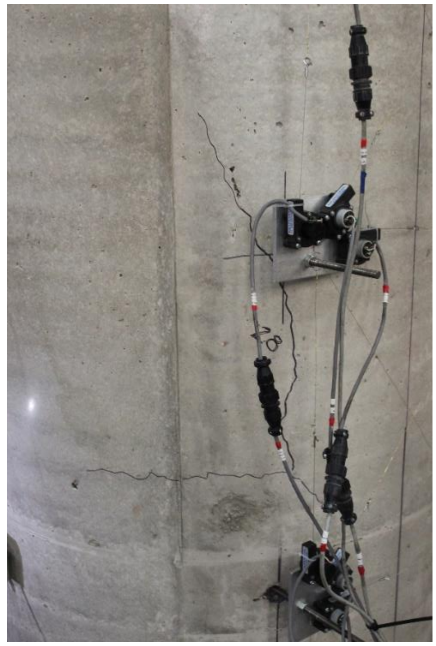

iii. 

Figure 4.1.A –Observed damage to Specimen 1 during Test 1. i) First cracks observed in the center of the footing on the west face, ii) Cracking of the retrofit shell indicating mobilization of the retrofit, iii) Cracking of the column above the retrofit.

Figure 4.1.B –Observed damage on the West face of the footing of Specimen 1 after testing.

4.1.2 Test 2-Specimen 2: Complete Retrofit with New Soil Simulant Subgrade and No Embedment

Prior to testing, shrinkage cracks were observed and marked to distinguish them from cracks that might emerge during testing. The axial load was then applied and an initial settlement distortion of 2.92 mm (0.115 in.) was recorded. During lateral loading, the specimen initially behaved elastically followed by inelastic behavior initiating a drift of 20.3 mm (0.8 in.). At a drift of 40.6 mm (1.6 in.) in the North direction, the footing on the South side lifted approximately 4.76 mm (3/16 in.) up from the soil simulant and 11.1 mm (7/16 in.) into the soil simulant on the North side. At 2% drift, the overall load-deformation response began to flatten out and the footing punched into the soil simulant 12.7 mm (1/2 in.). The soil simulant began curling up and moving with the footing, and at 71.1 mm (2.8 in.) of drift, the footing punched into the soil simulant 19 mm (3/4 in.). The footing punched into the soil simulant approximately 25.4 mm (1 in.) at a displacement of 102 mm (4 in.), which was the last drift cycle imposed during the test. While there was minor concrete cracking near the toe of the footing, there was no other observable damage to the footing, column, or retrofit. The bottom of the footing had no observable damage. The cracks on the side of the footing did not appear to propagate to the bottom surface of the footing. Figure 4.2 displays the progression of punching into the soil simulant and Figure 4.3.A – Figure 4.3.B shows the soil simulant damage by layer.

i. 

ii. 

iii. 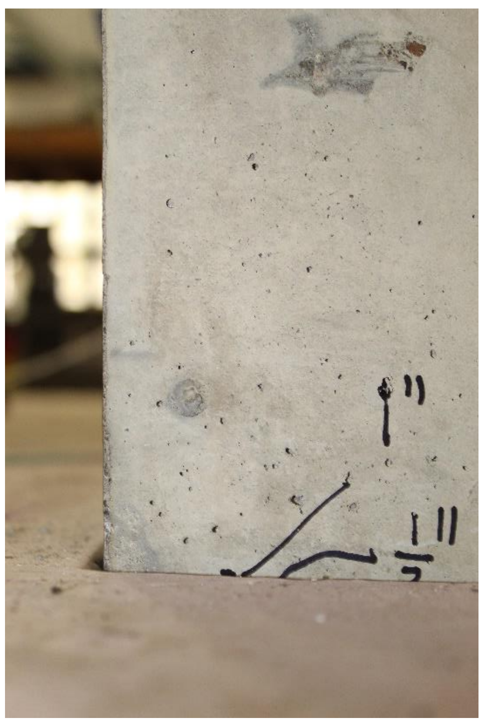

Figure 4.2 – Crushing of the footing into the soil simulant at drifts of i) 40.6 mm (1.6 in.), ii) 50.8 mm (2 in.), iii) 102 mm (4 in.).

i. 

ii. 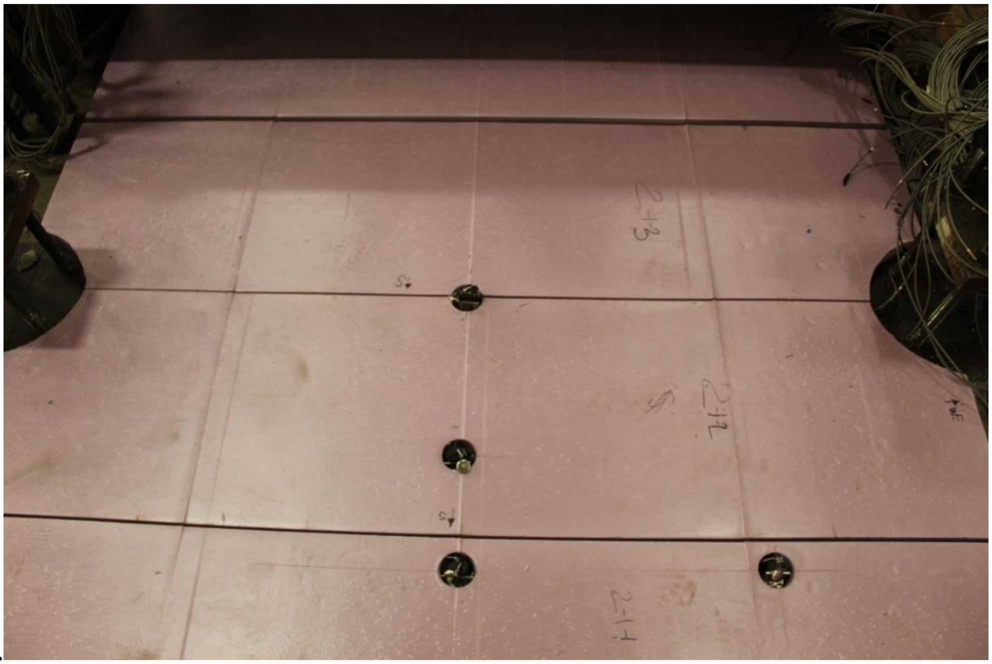

Figure 4.3.A – Soil simulant damage by layer. Layers are counted from closest to the floor up. i) Layer 4, directly underneath the footing. ii) Layer 3.

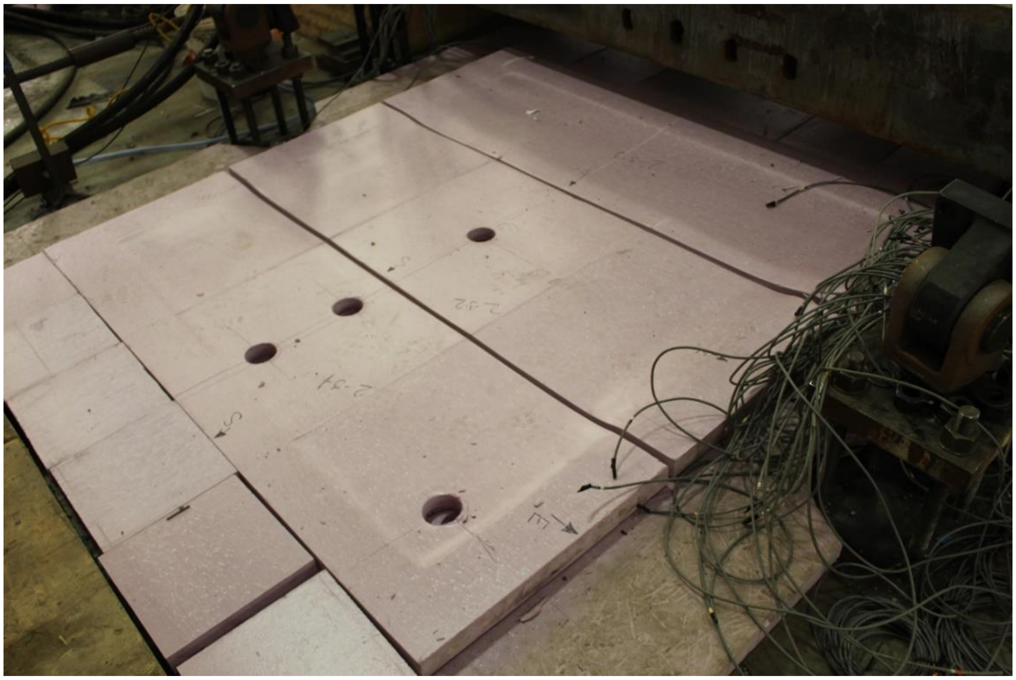

i.

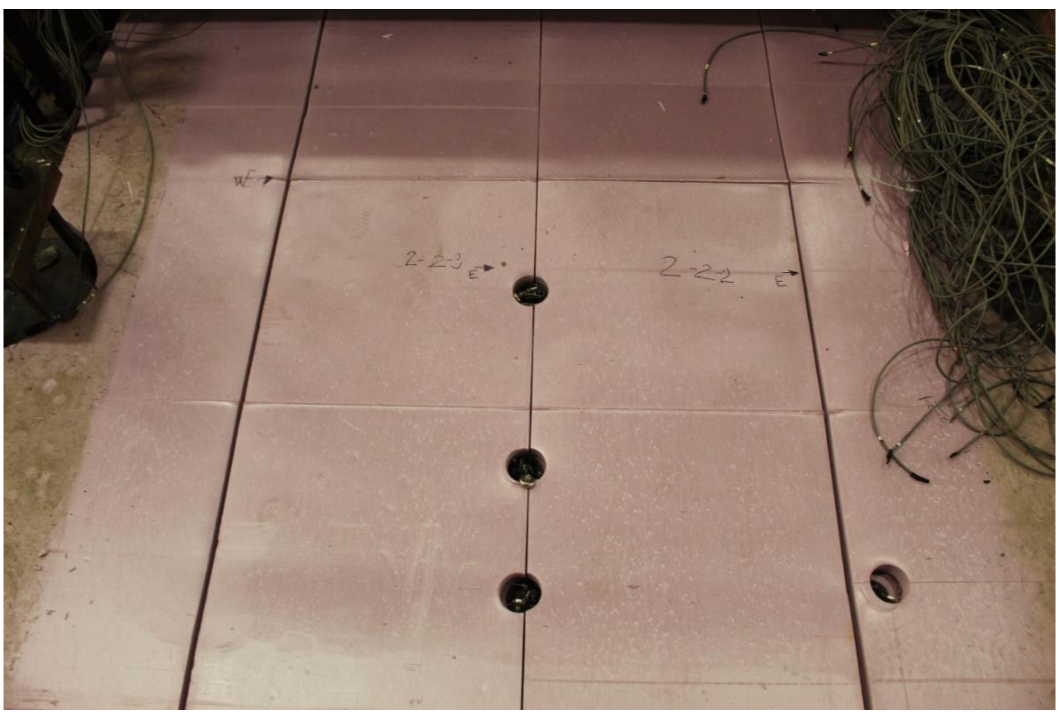

ii.

Figure 4.3.B – Soil simulant damage by layer. Layers are counted from closest to the floor up. i) Layer 2, ii) Layer 1 on the floor.

4.1.3 Test 3-Specimen 3: Vintage Column with New Soil Simulant Subgrade, Soil Simulant Embedment, 150-kip Axial Load

The specified axial load was first applied and an average initial settlement distortion of 2.79 mm (0.11 in.) was recorded. Lateral displacements were imposed and no damage occurred until a drift of 50.8 mm (2 in.). Visual rocking of the footing was observed at a drift of 20.3 mm (0.8 in.). Flexural cracking on the column along the lap-splice length on the second cycle of 50.8 mm (2 in.) displacement. At 61 mm (2.4 in.) of displacement vertical cracking along the bars continued to propagate, cracks began to form at the bottom of the column, and permanent deformations in the soil occurred. Horizontal cracking along the faces of the column also occurred at 61 mm (2.4 in.). Vertical cracking emerged of the lap-splice in the SW corner at 91.4 mm (3.6 in.) of displacement. The expected moment capacity, at 667 kN (150 kips) axial load, based on actual material properties is 579.5 kN*m (427 kip*ft); however, the soil began to fail first. At 102 mm (4 in.) of displacement cracks on the NW corner were a little wide near the bottom of the column. The column was tested to 152 mm (6 in.) of displacement and column failure did not occur. The soil simulant continued to plastically deform at subsequent displacements and the cracking observed at the end of the test on the face of the column is shown in Figure 4.4. The specimen axial load was unloaded by 1/3 and then the specimen was retested as detailed in the next section.

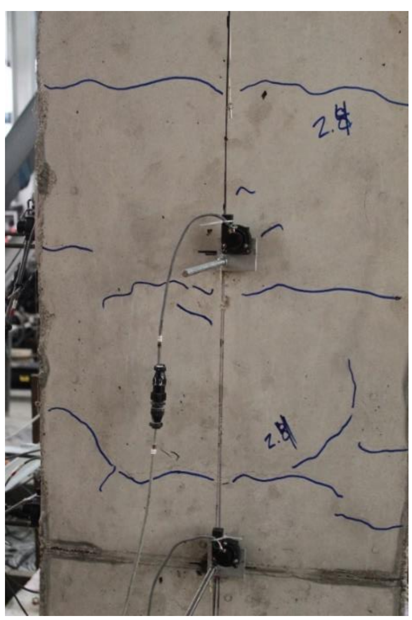

Figure 4.4 – Cracking distribution on the face of the vintage column.

4.1.4 Test 4-Specimen 3: Vintage Column with Damaged Soil Simulant Subgrade, Soil Simulant Embedment, 100-kip Axial Load

This test was a repeat of the prior test of Specimen 3 but with the reduced column axial load. The column was moved back to zero drift and 222 kN (50 kips) was removed from the axial load to a lower value of 445 kN (100 kips). This was done to lower the moment capacity in an attempt to produce failure of the column. Based on the actual column properties, the moment capacity with a 445 kN (100 kips) axial load was 526.6 kN*m (388 kip*ft). A 445 kN (100 kips) axial load is at the lower end of likely service levels in this size bridge column. Lateral displacements were applied using only one cycle at each interval until the column began to pick up load when the drift displacement was 91.4 mm (3.6 in.). This was due to nonparticipation of the soil simulant in lower displacements from prior permanent deformations under the footing and at the vertical faces of the footing. Vertical cracks began to appear at this displacement on the face of the column over the lap-splice length at a drift of 152 mm (6 in.) and 173 mm (6.8 in.). . The furthest displacement imposed on t specimen was 193 mm (7.6 in.) but the lateral forces did not increase substantially as the soil simulant plastically deformed under and at the faces of the footing. The specimen was unloaded and changes to the soil simulant were made as detailed in the next section.

i. 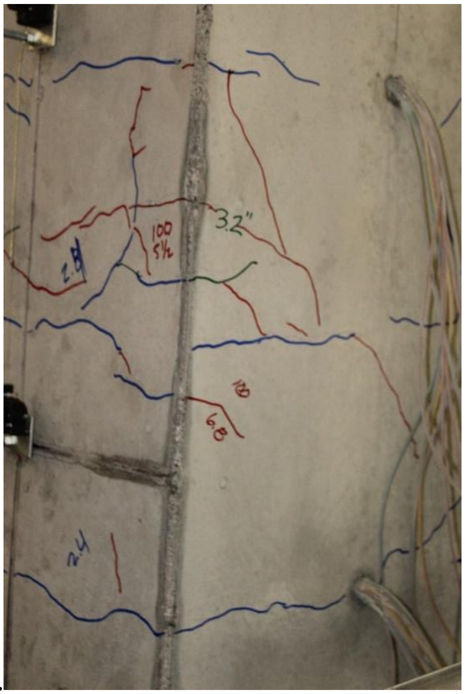

ii. 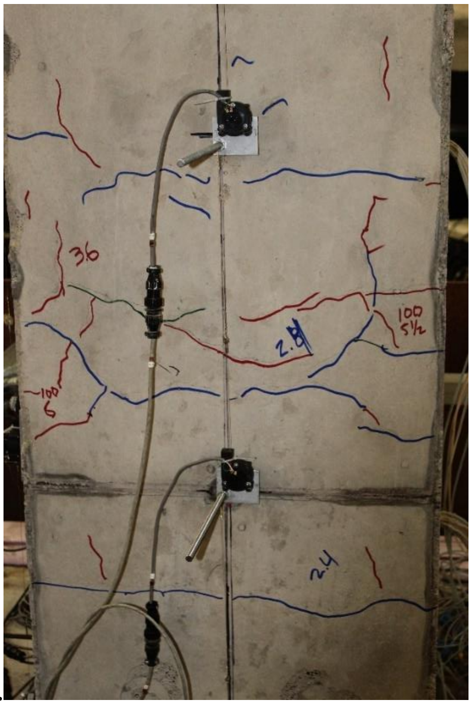

Figure 4.5 – Crack progression at 445 kN (100 kips) axial load. i) Cracks on the East face, ii) cracks on the South face.

4.1.5 Test 5-Specimen 3: Vintage Column Failure with Damaged Soil Simulant Subgrade and Steel Embedment

This test was a repeat of the prior test of Specimen 3 but with column axial load increased back to 667kN (150 kip) and with removal of the soil simulant foam at the footing faces only the steel springs provided the lateral resistance across the footing faces. After the 667kN (150 kips) of axial compression was applied, the lateral drift protocol was imposed. The top of the footing began spalling at a drift 40.6 mm (1.6 in) along the top of the North and South face. The starter bar on the NE corner yielded in the push side at approximately 76.2 mm (3 in.). At 81.3 mm (3.2 in.) the top SE corner of the footing broke off contaminating subsequent displacement measurements of the footing. At a drift of 102 mm (4 in.), a large concrete wedge on the top of the footing on the South face broke off, and the starter bar on the North side yielded. The top of the footing continued to exhibit progressive damage on both faces as the test continued. At a drift of 107 mm (4.2 in.), the column bar on the SE corner yielded. Local bearing on the steel soil springs caused damage to the face of the footing from the broken concrete that fell in between the steel springs and the footing at 122 mm (4.8 in.). Vertical cracks also occurred at this displacement along the lap-splice on the South face of the column, and further yielding occurred in the starter bars on the North side. Flexural cracks were observed at a drift of 132 mm (5.2 in.) on the South face of the column. Progressively larger strains occurred in the NE starter bar, while the SE starter bar did not yield. The column tie closest to the end of the lap-splice length, at 762 mm (30 in.) exhibited yield. Failure of the lap splice on the South face of the column occurred at a drift of 152 mm (6 in.). The test continued to a drift of 173 mm (6.8 in.) when the lap splice failed on the North face of the column. Settlement of the soil at the end of the test was approximately 31.7 mm (1-1/4 in.). Column and footing damage can be seen in Figure 4.6 and Figure 4.7.

i.

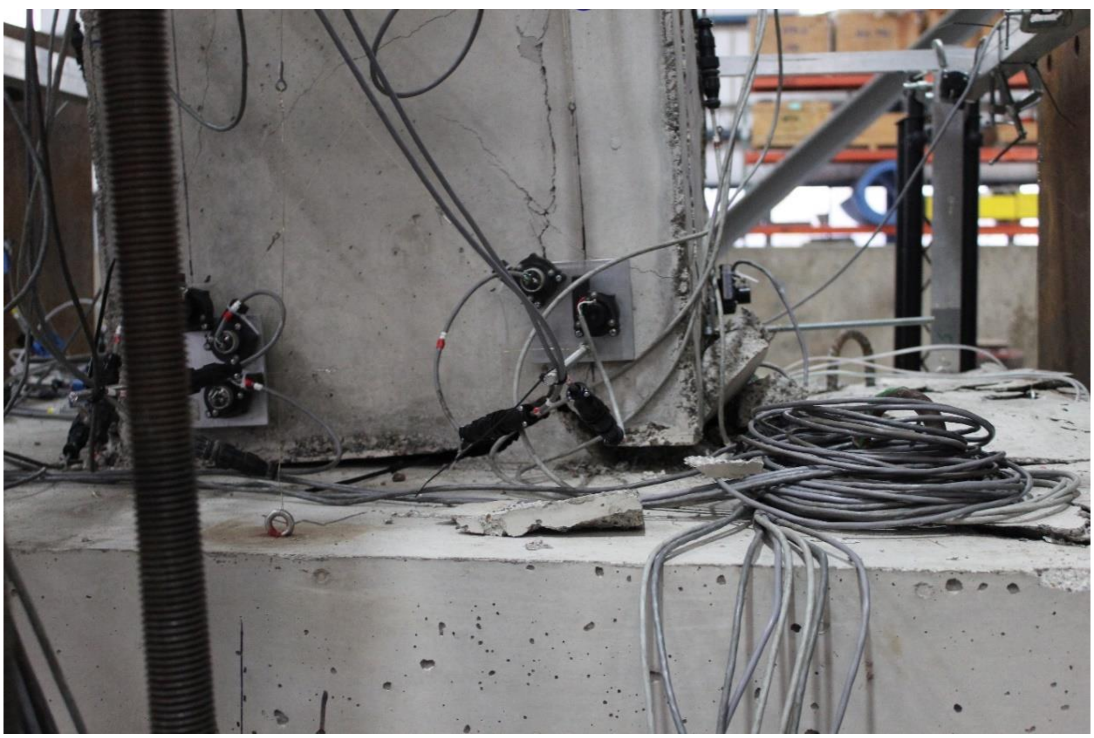

ii.

Figure 4.6 – Footing and column damage prior to spalling of the concrete around the lap-splice. i) SE corner of the column, ii) SW corner of the column.

i. 

ii. 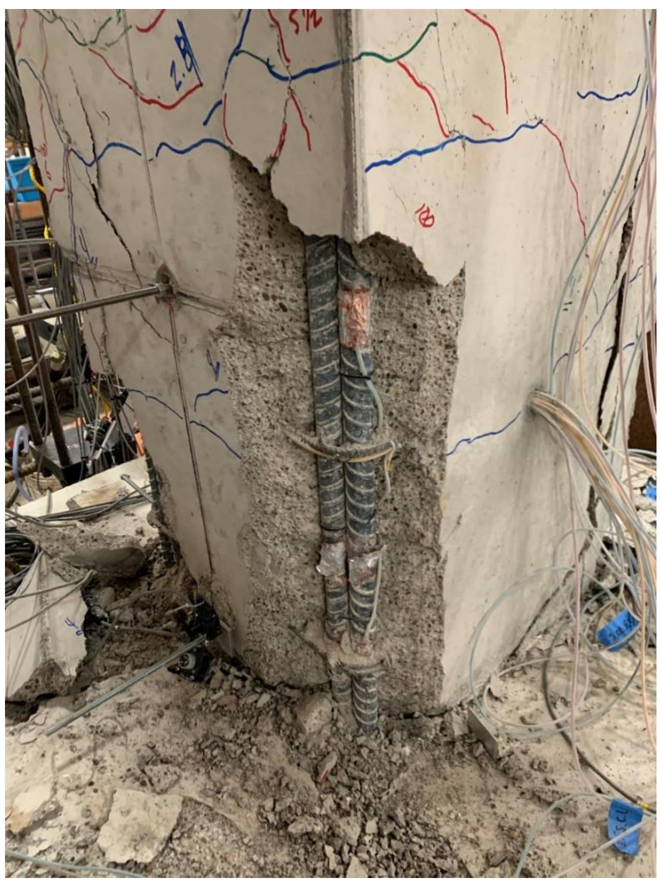

Figure 4.7 – Spalling of concrete from the column over the lap-splice length. i) Initial spalling on the SW corner, ii) Column damage after testing.

4.1.6 Test 6-Specimen 3: Failed Vintage Column with Ligament Retrofit, Damaged Soil Simulant Subgrade, and Steel Embedment

The test was conducted after the TiAB ligaments were installed to observe how the behavior changes when only ligaments are in place prior to placement of the spiral shell. This test and Test 7 represent the substructure of a bridge that has experienced a damaging seismic event and the retrofit has been installed to allow the column to remain in service even while subjected to aftershocks. Thus, the subgrade was damaged but the column remains in service following the retrofit. Because the retrofit was installed without axial load in the laboratory, this test is more representative of the case where the bridge is shored during retrofit installation. The test was kept well within the elastic range to avoid yielding the ligaments. Because the ligaments were installed before the axial load was applied they exhibited elastic buckling of approximately 500 $\mu\varepsilon$ as seen in Figures 4.8 and 4.9. The column axial precompression of produced stiffened initial response since the compressive strain must be overcome before flexural tension in eventually produced by application of the lateral load. The force-displacement plot was compared to the post-failure response of the column in Test 5, and stiffening response was observed after the lateral force resulted in overcoming the column axial pre-compression. This shows the TiAB ligaments provide flexural tension to enable the column to carry additional overturning moment as also seen in Figure 4.14. The difference in the capacity on the push and pull cycles, as seen in Figure 4.8 and 4.10, is a result of the difference between when the axial pre-compression was overcome, and the elastic losses due to the different horizontal reaction from stiffnesses in the test setup. Figure 4.10 shows the difference between the response of the column after failure and the column response after only the TiAB ligaments were installed. This demonstrates that the ligaments provide flexural tension, enabling the column to carry additional overturning moment. For clarity, the sensor naming conventions are reported in Appendix B as previously stated in Section 3.4.

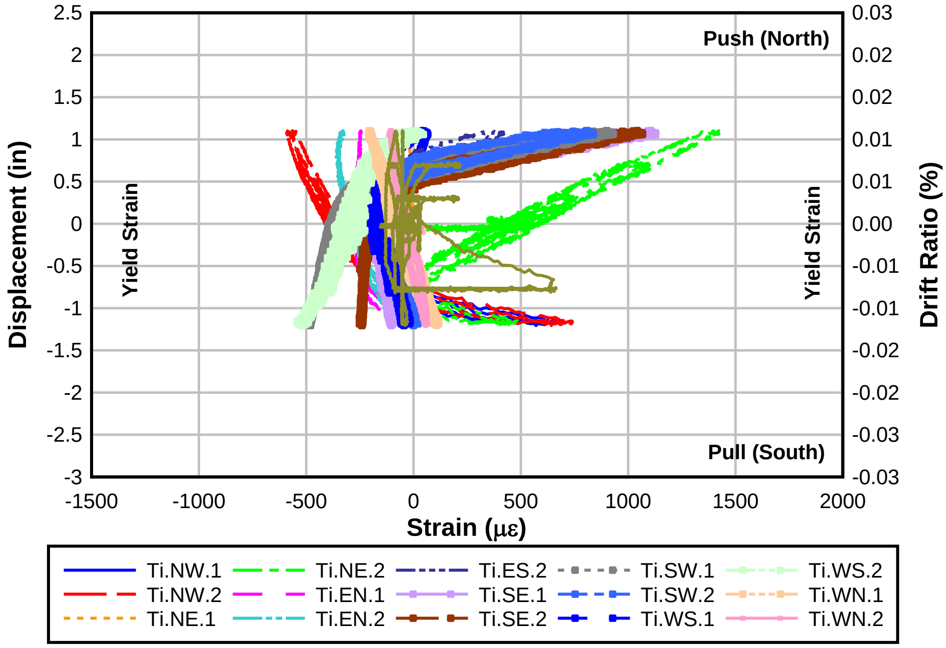

Figure 4.8 – TiAB ligament strain profile up-close.

Figure 4.9 – Elastic buckling of the TiAB ligaments during axial load application.

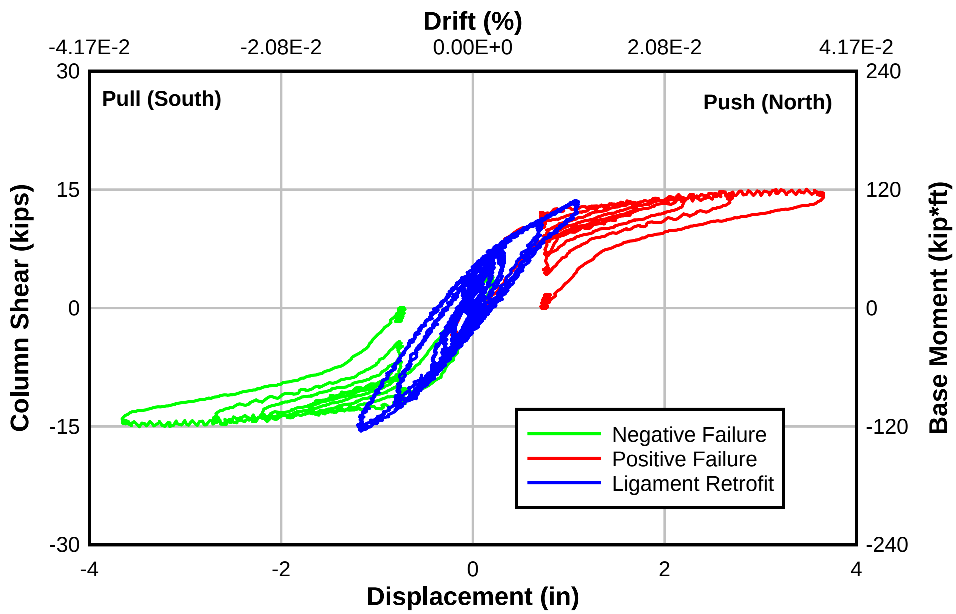

Figure 4.10 – Force displacement responses of specimen with TiAB ligament retrofit only compared to residual response of unretrofitted column after failure.

4.1.7 Test 7-Specimen 3: Failed Vintage Column with Complete Retrofit, Damaged Soil Simulant Subgrade, and Steel Embedment

After the failed vintage column (Specimen 3) was fully retrofitted, it was tested again on the same soil simulant that was previously damaged during Tests 3-6. The axial load was applied and the specimen subjected the lateral displacement protocol. The specimen exhibited softening at a drift of 71.1 mm (2.8 in.) and at 81.3 mm (3.2 in.) on pull cycles. The footing began to exhibit spalling on the South face. On the second cycle of the 91.4 mm (3.6 in.) displacement amplitude, the string potentiometer on the NE corner became contaminated because the footing spalled further. The soil simulant steel springs plastically deformed at 122 mm (4.8 in.) and a single new crack on the NE corner of the footing formed. The footing continued to spall on the North and South face. The sensor used to capture horizontal sliding of the footing on the East face was contaminated by the spalling concrete at a drift of 173 mm (6.8 in.). All of the visual distress was occurred in the footing or the steel springs, and the springs were pushed into the soil simulant as the damaged concrete on the footing became in contact with the steel springs at a drift of173 mm (6.8 in.) through the rest of the test. Strains in the starter bars could not be measured because the strain gauges were damaged in the previous tests; however, the TiAB ligaments exhibited a maximum strain in the range of 1400 με. Footing and soil simulant damage is shown in Figure 4.11.A and Figure 4.11.B.

Figure 4.11.A – Footing damage on the face of the footing after Test 7.

Figure 4.11.B – Condition of the soil simulant after Test 3 – Test 7.

4.1.8 Test 8-Specimen 2: Completely Retrofitted Column without Simulated Soil and Tied Down Footing

The last test was the first attempt to fail a retrofitted column. Because the vintage designed footing had no reinforcing steel in the top, a 44.4 mm (1-3/4 in.) diameter hole, 165 mm (6-1/2 in.) from the top of the footing was cored through the center of the footing. A 41.3 mm (1-5/8 in.) diameter Dywidag bar was placed through the hole and tightened against two (2) 190 mm (7-1/2 in.) square anchor plates to provide passive confinement at the top of the footing. To maintain the geometry of the test setup, a 203 mm (8 in.) thick reinforced concrete slab was constructed that took the place of the soil simulant, and two W12x136 beams were used to anchor the footing to the strong floor to prevent footing rotation and translation. Prior to testing, shrinkage cracks were marked to distinguish them from any subsequent load-induced cracks. The axial load was applied and the lateral displacement protocol imposed on the specimen. The SE starter bar was observed to yield at a drift of16.5 mm (0.65 in.) on the push side; however, a significant drop in the resisting force was observed at a drift of 20.3 mm (0.8 in.) of displacement. At this displacement cracks were observed in the footing, and the footing began to separate into four (4) sections. Due to the enlargement of the footing, the string potentiometers measuring sliding and rotation were contaminated. Therefore, the responses were considered separately pre- and post-footing damage. At 30.5 mm (1.2 in.) of drift on the push cycle, both North transverse footing bars yielded, as did the North side of the column tie located 762 mm (30 in.) above the top of the footing. Cracks then propagate into four quadrants at 40.6 mm (1.6 in.) of drift, and horizontal cracks opened across the lower portion of the footing at the North face. The test was terminated as the footing continued to fail at a peak drift of 61 mm (2.4 in.). At this displacement, horizontal cracks on both the North and South faces of the footing were very wide. The anchor rods used to tie down the footing were observed to be bent out of the vertical plane because the footing spread approximately 12.7 mm (1/2 in.) on the North face and slightly less on the South face. This spreading of the footing is attributed to the axial load pushing the column into the footing after the footing cracked and the lack of reinforcing steel at the top of the footing to restrain the cracks. Figure 4.12 shows the footing failure progression.

i. 

ii. 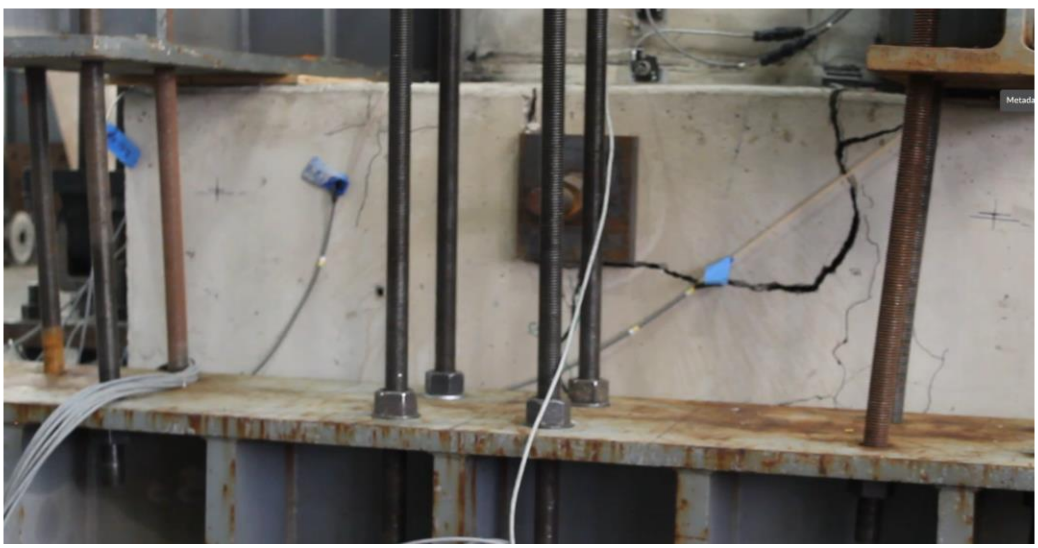

Figure 4.12 – Failure of footing on Specimen 2. i) Cracks formed at 20.3 mm (0.8 in.), ii) footing failure after testing.

4.2 Force Displacement Responses

The displacement response was recorded using a string potentiometer located on the column at the lateral loading point, and the applied load was recorded from the load cell attached to the lateral load actuator. These sensor data were used to characterize the overall specimen force-displacement response. The column moment from the applied lateral force was computed at the column at the top of the footing. Responses are reported in terms of column shear and drift ratio. The drift ratio is calculated by dividing the column displacement by the distance from this location to the top of the footing. Inherent in the experimental setup is a restoring force that comes from the horizontal component of the axial load as the specimen undergoes lateral displacement. The internal column shear was computed as the equivalent lateral load at the base of the column after removing the horizontal component of the axial load as detailed in the subsequent section.

4.2.1 Data Processing for Column Shear Force

The horizontal restoring force due to axial load setup was removed from the applied lateral load to computed the internal column shears during post-processing of the test data. The correction is a function of the drift magnitude, axial force, and geometry. Shrestha (2019) illustrated the components of the axial load and the applied load as shown in Figure 4.13. In Figure 4.13, Δ_T is the drift at the top of the column, $\Delta_{Measured}$ is the measured displacement, Δ' is the additional drift, H' is the distance from the top of the column to the point of rotation, and H_L is the height of loading measured from the column footing interface to the point of loading. The point of rotation for the axial load remains same throughout all tests because it is fixed at the pins anchored into the strong floor. The horizontal and vertical components of the axial load were determined for any given drift by utilizing equations E4.1-E4.5:

$$\tan(\beta) = \Delta_{Measured} / H' \qquad \text{E4.1}$$

$$\operatorname{atan}(\beta) = \beta \qquad \text{E4.2}$$

$$P_H = P \sin(\beta) \qquad \text{E4.3}$$

$$P_V = P \cos(\beta) \qquad \text{E4.4}$$

$$\Delta_T = \Delta_{Measured} + \mathrm{Sin}(\beta) \qquad \text{E4.5}$$

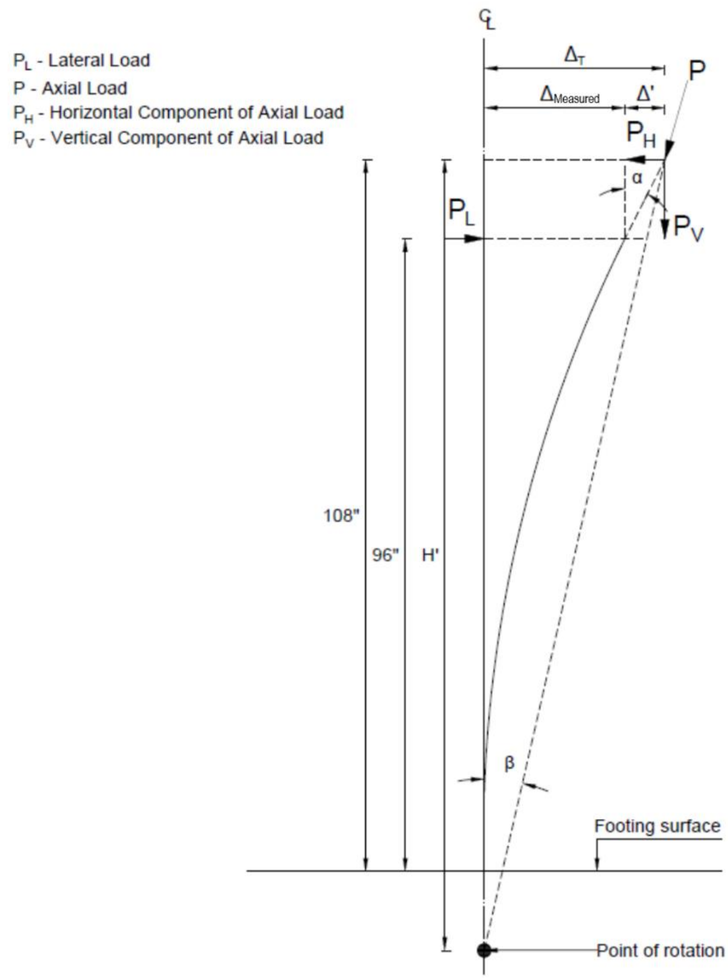

Figure 4.13 – Shrestha (2019) illustration of geometric factors influencing the additional drift.

In the present set of tests, axial load was applied 0.305 m (1 ft.) above the point of lateral loading. Because this is located higher up the column, additional horizontal deflection occurs at this point that is dependent on angle α, the angle change at the point of loading due to the column deformation, and angle β, the angle of the applied axial load. Because angle α is small over the 0.305 m (1 ft.) length, it is considered negligible. However, angle β was measured from the point of rotation of the axial load setup. This was measured by taking the average height of the pin joints on the strong floor, 3026 mm (119.125 in.) from the top of the column. The moment on the column was summed at the column footing interface, including effects from P-Delta as seen in equation E4.6:

$$M_{base} = P_L H_L + P_V \Delta_T - P_H H' \qquad \text{E4.6}$$

The equivalent lateral load, or column shear, was computed using equation E4.7:

$$V = M_{base}/H_L \qquad \text{E4.7}$$

Using the post-processed experimental data, the overall force-displacement responses for each test were determined and are shown in Figures 4.15 to 4.23. Horizontal dotted reference lines in these figures represents 80% of the measured peak capacity during the tests, commonly taken as the threshold for determining ductility. The expected yield moment was plotted as horizontal dashed lines and represents the required shear to produce flexural yielding in the column. The expected yield moment was determined using as-built and measured mechanical properties of the materials used to construct the specimens; concrete strength, steel yield strength. Test 6 had an expected yield moment that also included the TiAB ligament contribution assuming these to be fully bonded to the column without longitudinal steel reinforcing bars. Axial load- moment interactions were used to determine the expected yield moment as shown in Figure 4.14. A summary of key values is tabulated in Table 4.1.

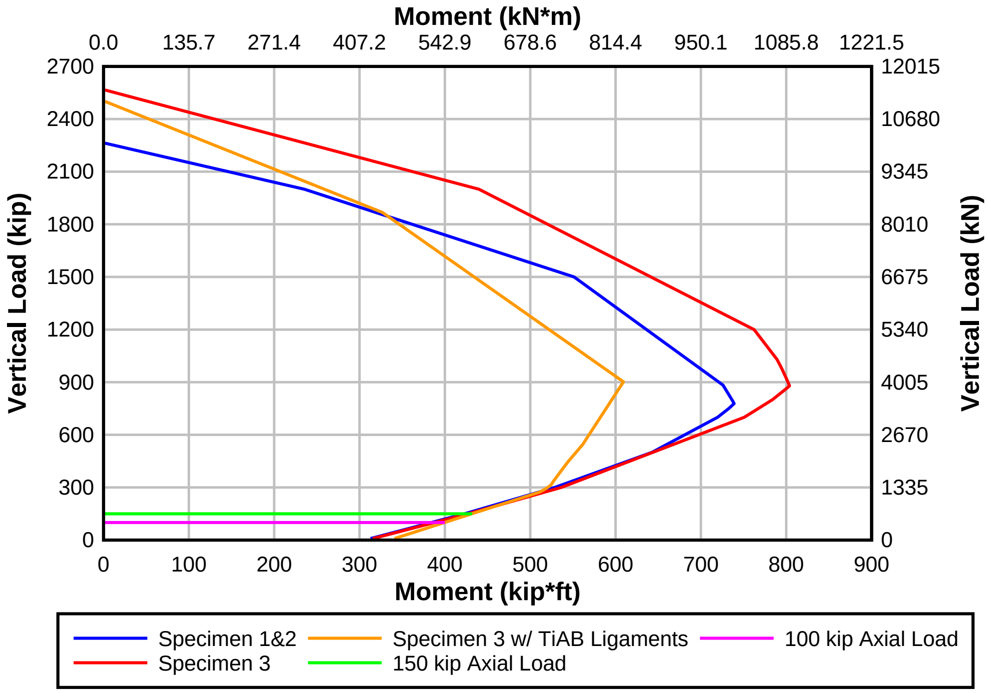

Figure 4.14 – P-M interaction diagrams considering as-built specimen material properties.

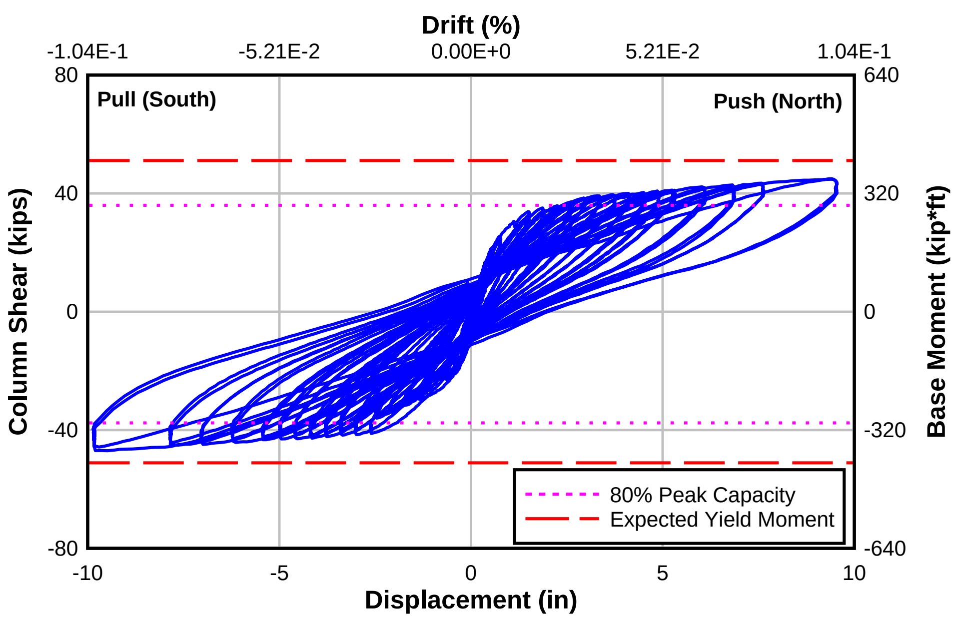

Figure 4.15 – Overall force-displacement response of Test 1, Specimen 1.

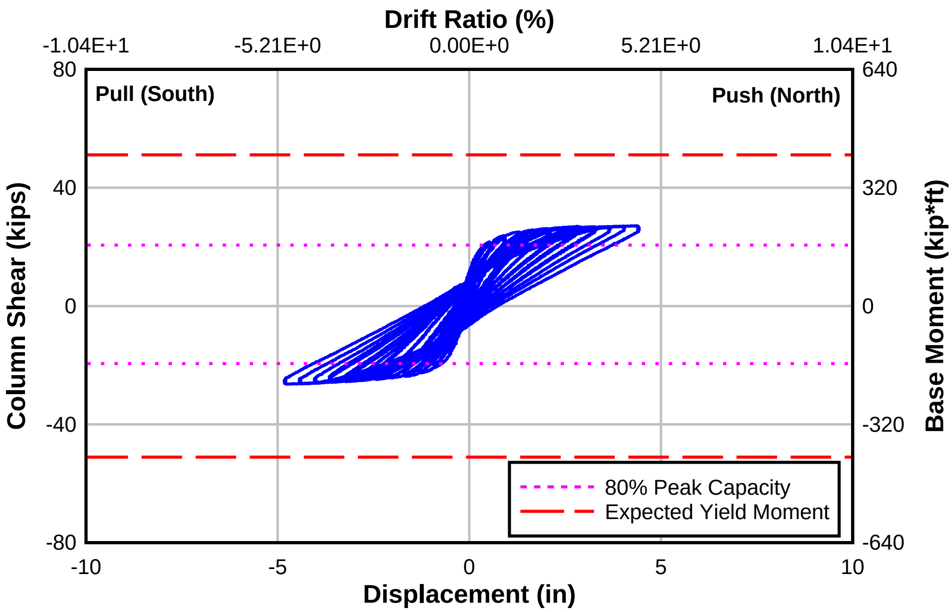

Figure 4.16 – Overall force-displacement response of Test 2, Specimen 2.

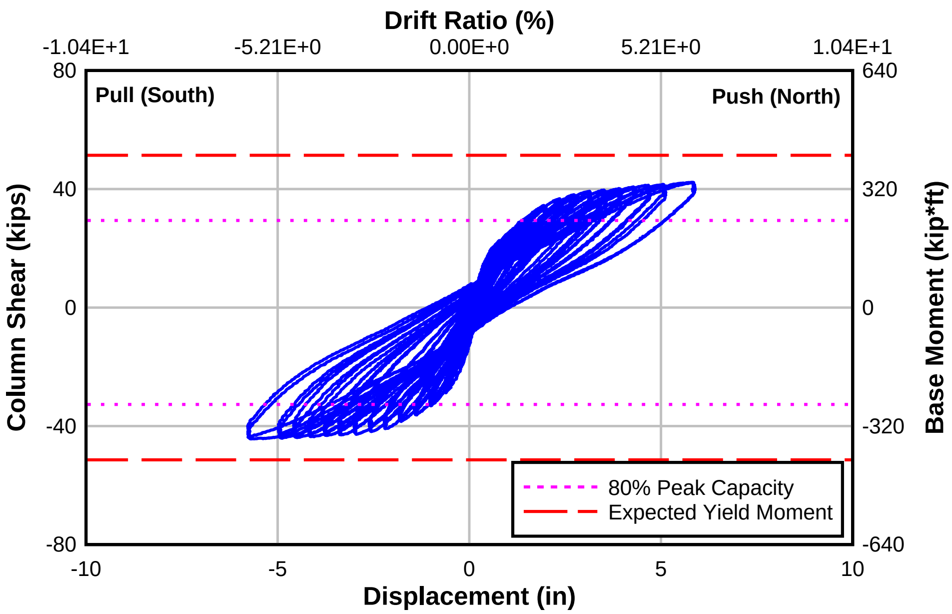

Figure 4.17 – Overall force-displacement response of Test 3, Specimen 3.

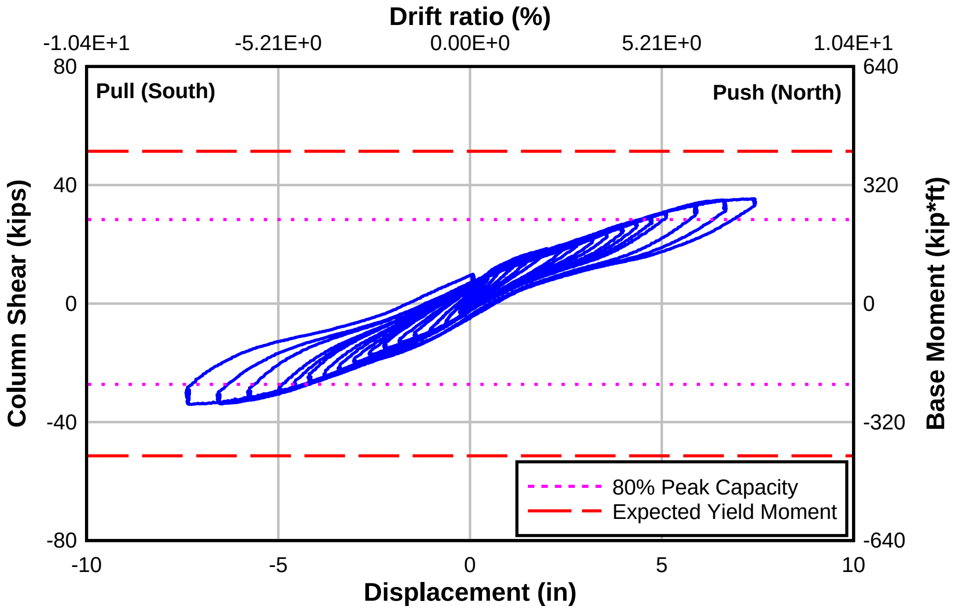

Figure 4.18 – Overall force-displacement response of Test 4, Specimen 3.

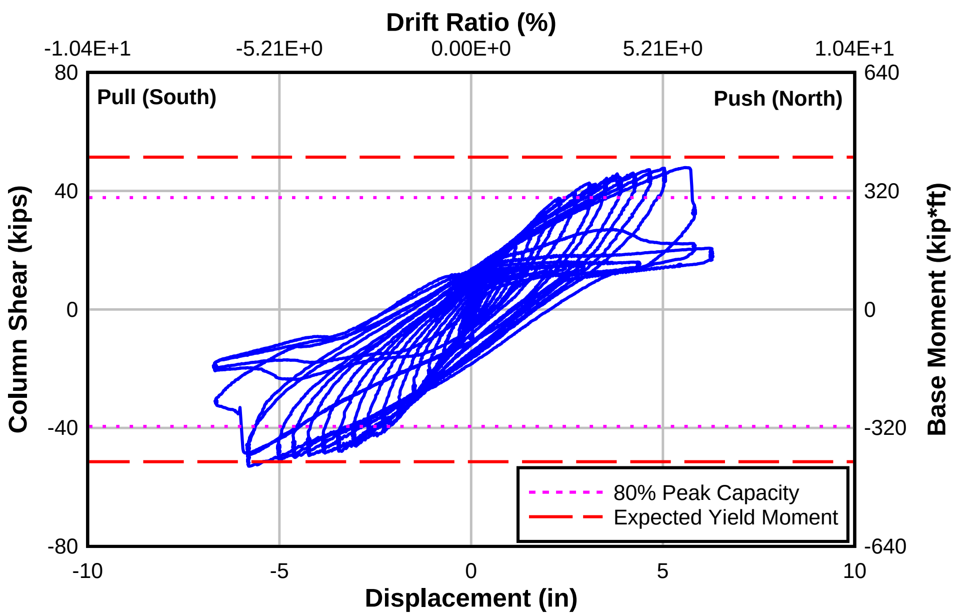

Figure 4.19 – Overall force-displacement response of Test 5, Specimen 3.

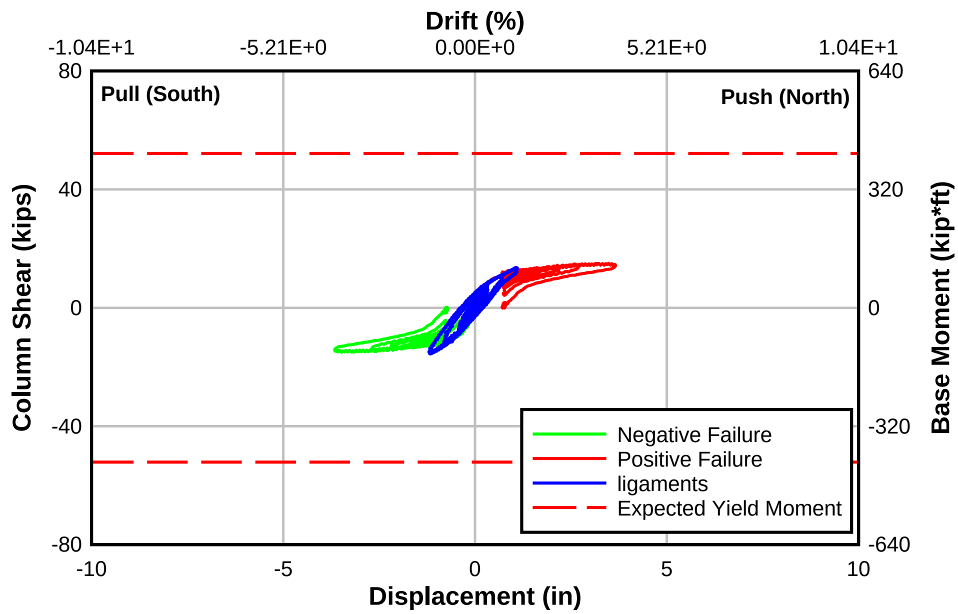

Figure 4.20 – Overall force-displacement response of Test 6, Specimen 3.

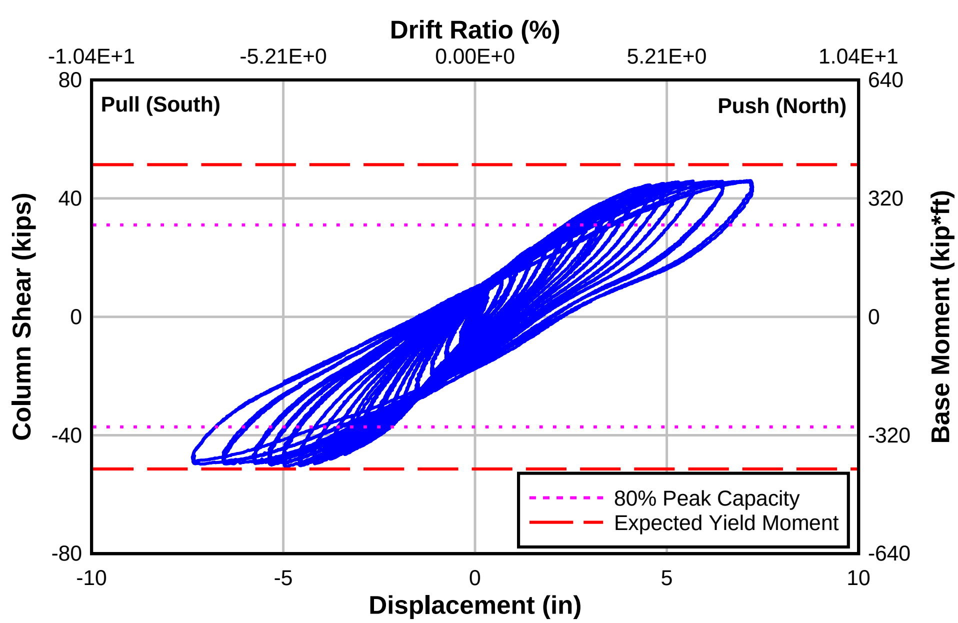

Figure 4.21 – Overall force-displacement response for Test 7, Specimen 3.

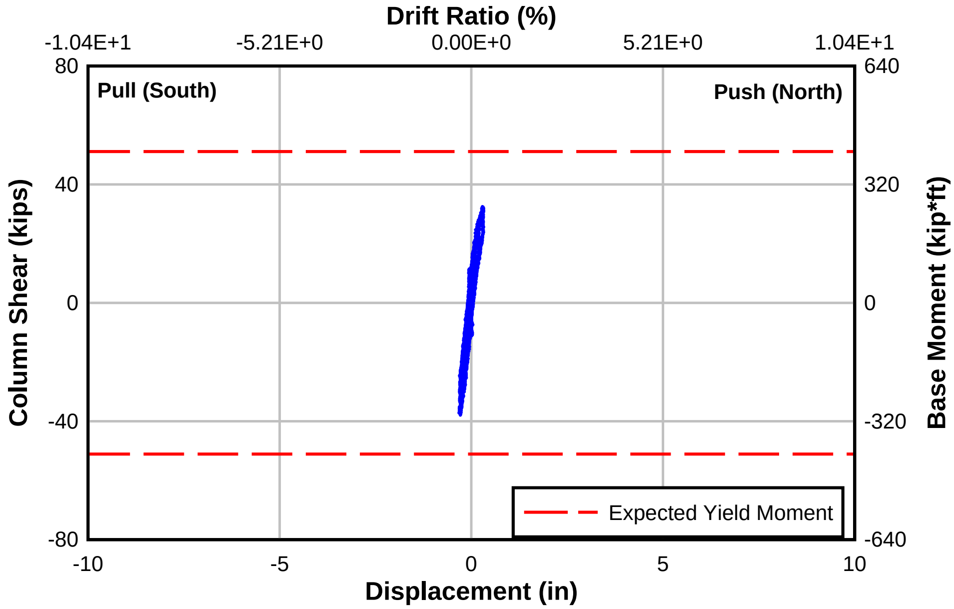

Figure 4.22 – Overall force-displacement response for Test 8, Specimen 2 (pre-failure).

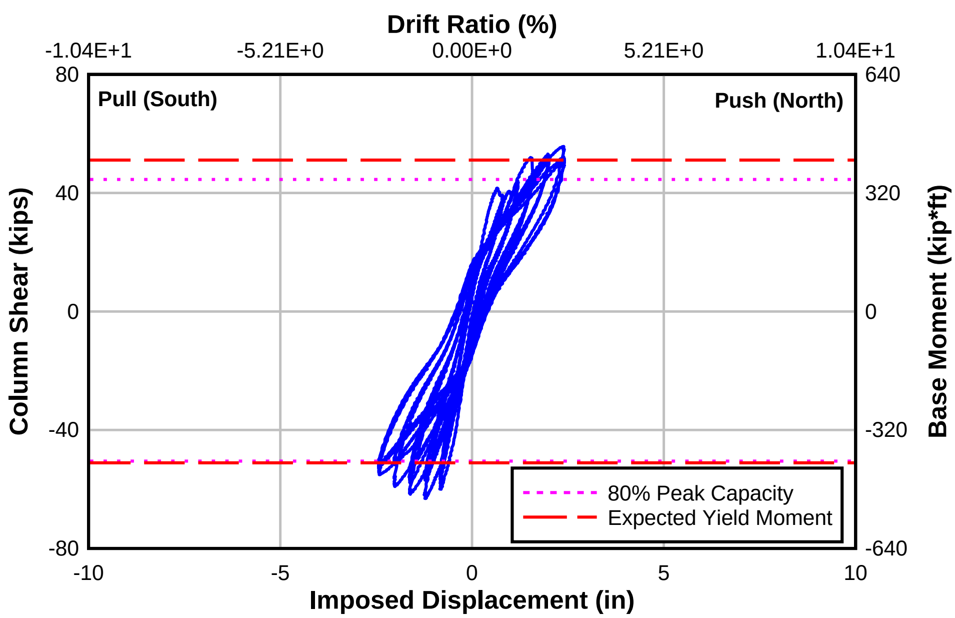

Figure 4.23 – Overall force-displacement response for Test 8, Specimen 2 (post-footing failure).

Table 4.1 - Summary of Key Vaules in Force Displacement.

Test Number - Specimen	Peak Capacity, kN (kip)		Drift Ratio (%) At Peak		Drift Ratio (%) At Failure	
	Push (+)	Pull (-)	Push (+)	Pull (-)	Push(+)	Pull (-)
T1-S1	199 (44.8)	209 (46.9)	9.9	10	2.2	2.4
T2-S2	121 (27.1)	112 (25.2)	4.5	5	0.79	0.8
T3-S3	188 (42.2)	197 (44.3)	6	6	2.2	2.3
T4-S3	158 (35.4)	151 (34)	7.7	7.6	5.2	5.3
T5-S3	212 (47.7)	235 (52.9)	5.9	6	-	-
T6-S3*	44.5 (10)	48.9 (11)	0.52	0.625	-	-
T7-S3	205 (46)	224 (50.3)	7.5	5.2	4.7	5.2
T8-S2	248 (55.7)	281 (63.1)	2.4	1.3	0.73	0.84

** T6-S3: Test was not conducted to failure. Values reported are recorded load and displacement when pre-compression is overcome.*

4.2.2 Components of Overall Force-Displacement

Because a flexible foundation was used to investigate soil-structure interaction (SSI), contributions to overall lateral displacement come from several different components. Therefore, to obtain the effective column drift relative to the top of the footing, other contributing deformation components must be removed from the measured overall column displacement. These components include rigid body translation and rigid body rotation as illustrated by Shrestha (2019) in Figure 4.24.

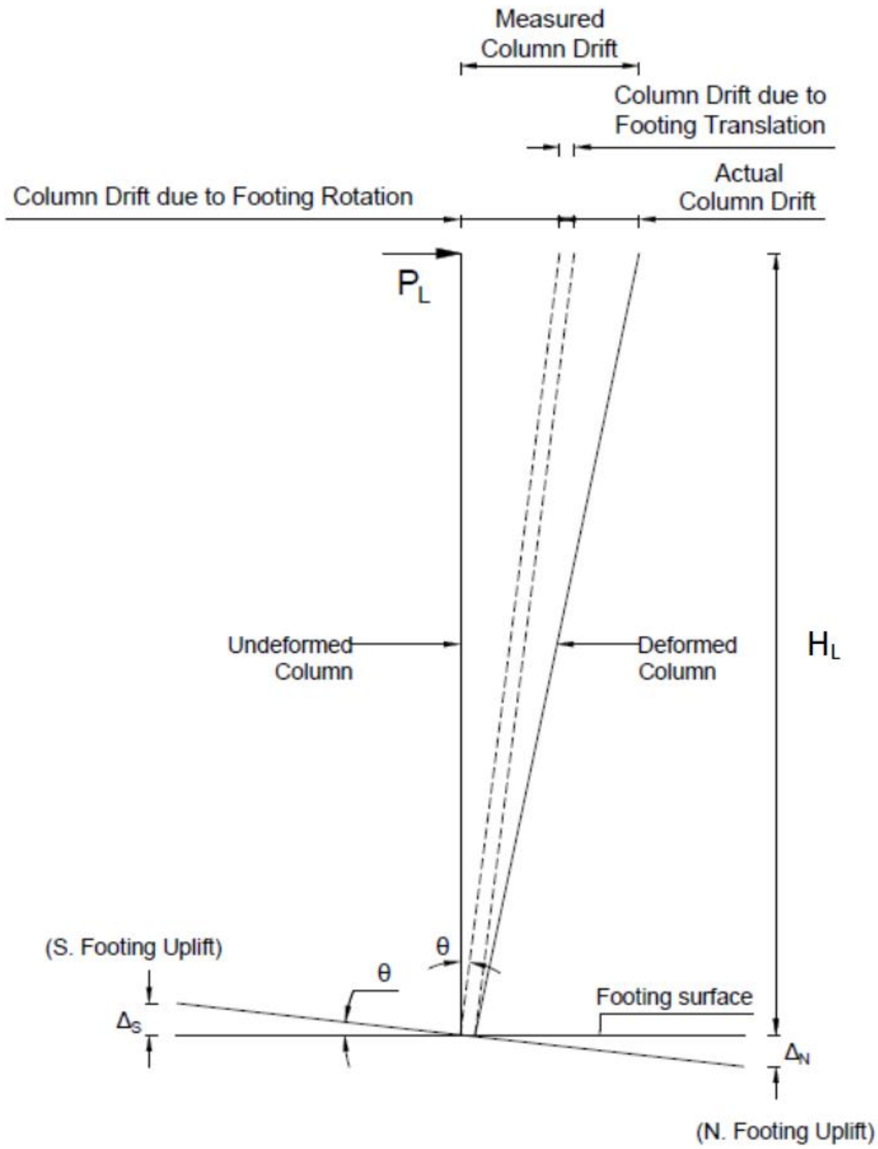

Figure 4.24 – Components of measured overall horizontal displacement in column at lateral loading point.

The rigid body translation, $\Delta_{slide,}$ in the direction of loading was measured using a string potentiometer on the West and East faces of the footing at the geometric center and was computed in equation E4.8 where SP is the string potentiometer reading on the face.

$$\Delta_{slide} = (SP_{West} + SP_{East})/2 \quad \text{E4.8}$$

The rigid body rotation was measured using three sensors on the top of the footing surface 76.2 mm (3 in.) from the North and South face with two sensors located at the corners and one in the center as seen in Appendix B, Figure B.3.1. Rigid body rotation was calculated in equations E4.9-E4.12:

$$\Delta_{rN} = (SP_{NW} + SP_{N} + SP_{NE})/3 \quad \text{E4.9}$$

$$\Delta_{rS} = (SP_{SW} + SP_{S} + SP_{SE})/3 \quad \text{E4.10}$$

$$\tan(\theta) = (\Delta_{rN} - \Delta_{rS})/54 \quad \text{E4.11}$$

$$\Delta_{rotation} = H_{L}\tan(\theta) \quad \text{E4.12}$$

Where Δ_{rN} and Δ_{rS} are the average measured displacements on the North and South side of the footing respectively, $\tan(\theta)$ is the difference in the measured displacements divided by the distance between sensors with units of inches, and H_L is the height of the column measured from the column footing interface to the point of loading. Effective column drift was determined by subtracting rigid body translation and rigid body rotation. These values were calculated in equation E4.13:

$$\Delta_{eff} = \Delta_{measured} - \Delta_{slide} - \Delta_{rotation} \qquad \text{E4.13}$$

Figure 4.25 illustrates the column the negligible contributions the column deformation makes to the overall measured displacements, and Figure 4.26 shows the contribution from the column during the vintage column failure. Component contributions to the measured displacements for all tests can be found in Appendix C.

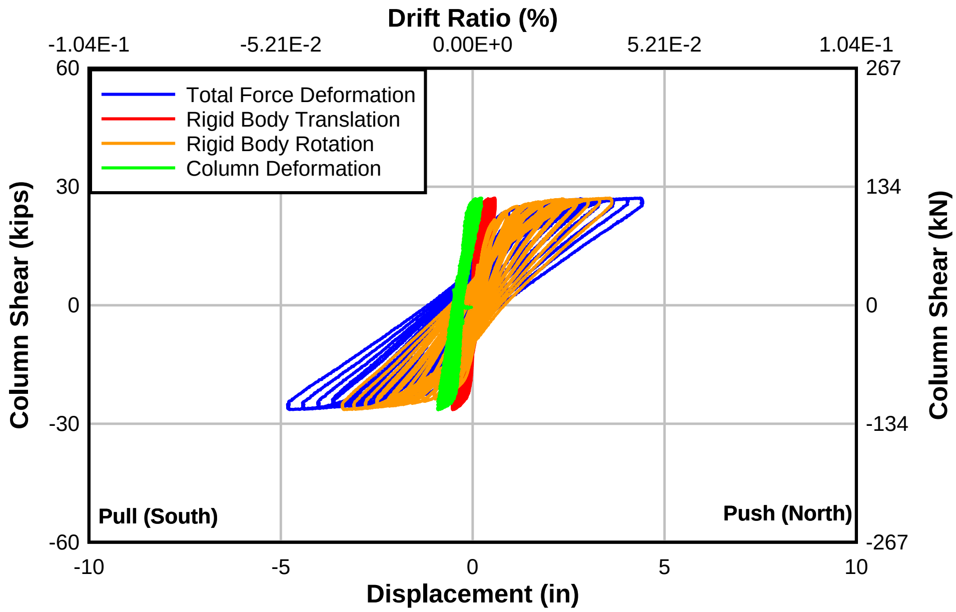

Figure 4.25 – Component contributions to measured displacement in T2-S2.

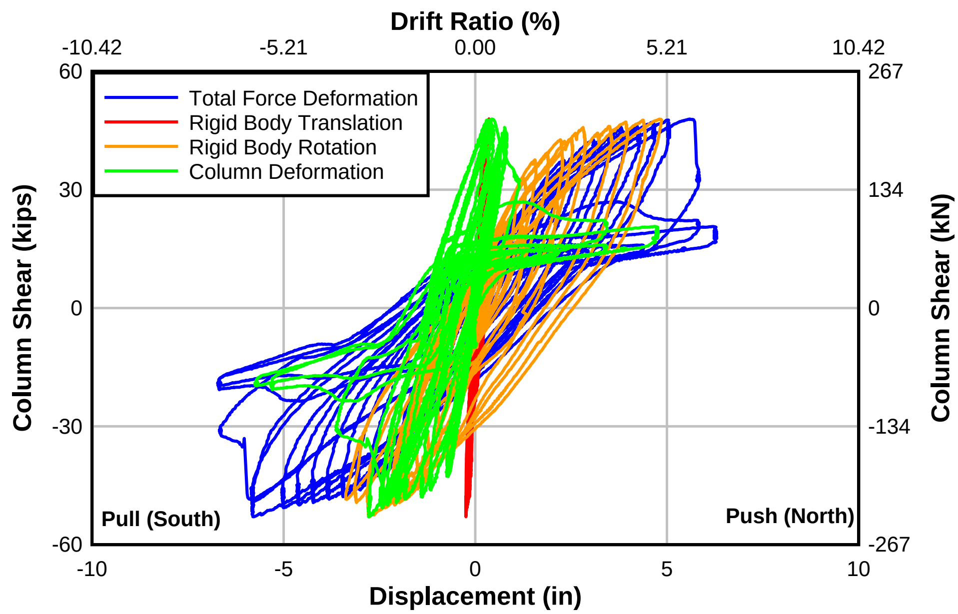

Figure 4.26 – Component contributions to measured displacement in T5-S3.

4.2.3 P-Delta Effects

Axial load applied at the top of the column creates a second-order moment due to the drift imposed by the lateral loading. While the horizontal component of the axial load is a restoring force that must be removed from the lateral loads to determine the internal moment in the column, the vertical component acting at a distance creates an additional overturning moment. This produces a softening response due to the negative stiffness associated with the vertical component that is linearly dependent on the lateral drift magnitude. To better understand the force-displacement response the degrading effects of P-Delta behavior were isolated using the geometric relationships established in 4.2.1. Equations E4.14 – E4.15 were used to remove P-Delta effects from the force-displacement response. Because P-Delta creates a softening response the difference in the moment must be added to the experimental response to obtain the response of the column without P-Delta.

$$M_{base\text{-}[remove\ P\text{-}D]} = P_L H_L - P_H H' \qquad \text{E4.14}$$

$$M_{w/o\ [P\text{-}D]} = M_{base} + (M_{base} - M_{base\ [remove\ P\text{-}D]}) \qquad \text{E4.15}$$

Where M_{base} is the moment at the base of the column calculated using equation E4.6. P-Delta commands a more significant effect on the column response at higher drift levels when the soil simulant is acting plastically. When removed, much of the post-peak degradation is attributed to the P-Delta effect as reported by Shrestha (2019),this can be seen in Figure 4.28.However, Shrestha (2019) used a fixed foundation. For a flexible foundation, a minor positive post-failure slope increases to a much larger positive post-failure slope due to the soil simulant eventually stiffening at large plastic deformations. This is evident in Figure 4.27, vintage column failure with a flexible foundation. P-Delta effects on the force-displacement response for all tests can be viewed in Appendix C.

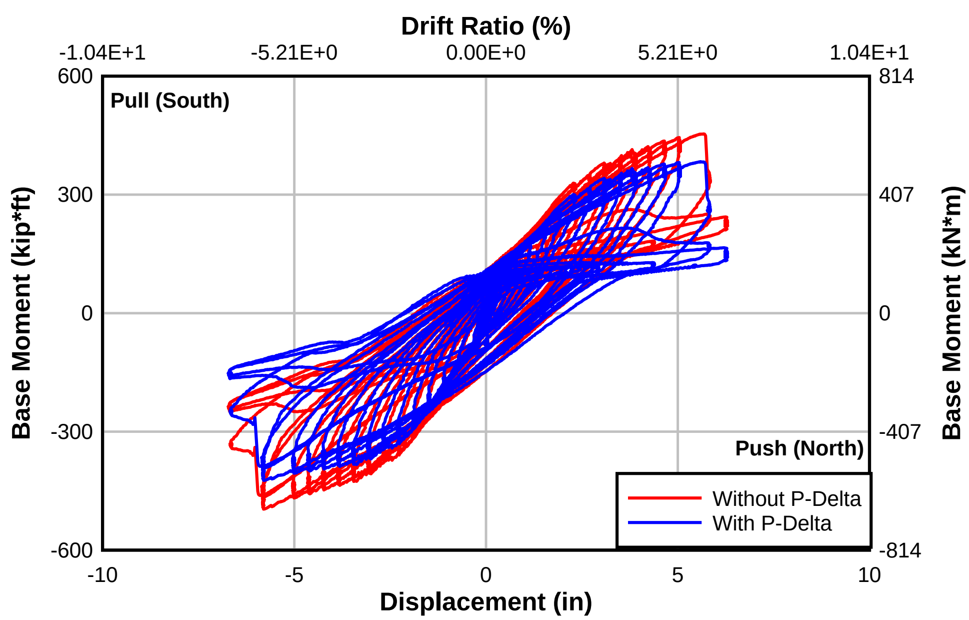

Figure 4.27 – P-Delta effect on T5-S3, vintage column failure.

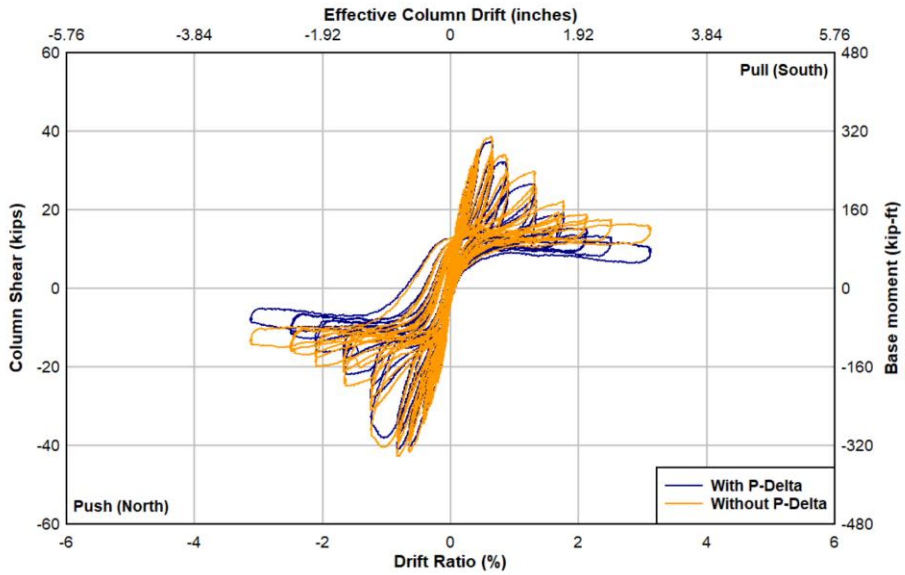

Figure 4.28 – P-Delta effects on vintage column failure with fixed base by Shrestha (2019).

4.4 Reinforcing Steel and TiAB Strains

Strain data from instrumented reinforcing steel and TiABs showed that yielding occur in only three tests; Test 1 of Specimen 1, Test 2 of Specimen 2, and Test 3 of Specimen 3. Yielding more often occurred in the pull cycle due to the higher stiffness of the horizontal reaction frame setup in this direction. This behavior did not appear to occur in the column bars on the pull cycle in Specimen 3 during Test 5 and is attributed to slipping of the spliced bars which occurred earlier on the South side than on the North side. During Test 5, the starter bars yielded before the column bar and column tie as seen in Figures 4.30 – 4.32. Figure 4.29 shows that the only bar that exhibited yielding in Test 1 ofSpecimen 1, was the center bar in the direction of loading at the bottom of the footing bar mesh. Lastly, Figure 4.33 and Figure 4.34 show that in Test 8 of Specimen 2 the NE starter bar yielded at the column footing interface and two (2) reinforcing steel bars in the footing mesh reached yield strain. Strain gauges in the TiABs were useful during characterization testing for the post-failure retrofit process as seen in Figure 4.8 in Section 4.1.6. All other strain data can be viewed in Appendix C.

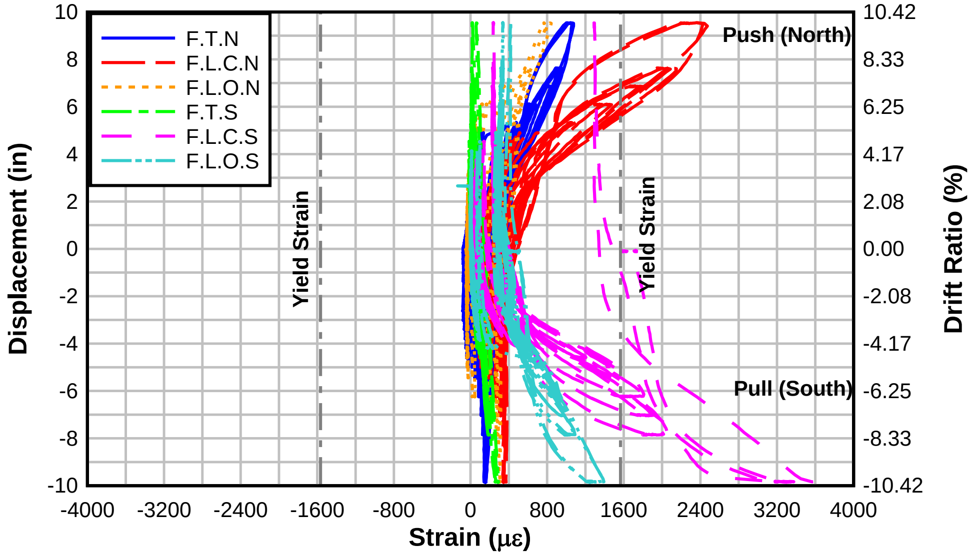

Figure 4.29 - Footing bar strains T1-S1.

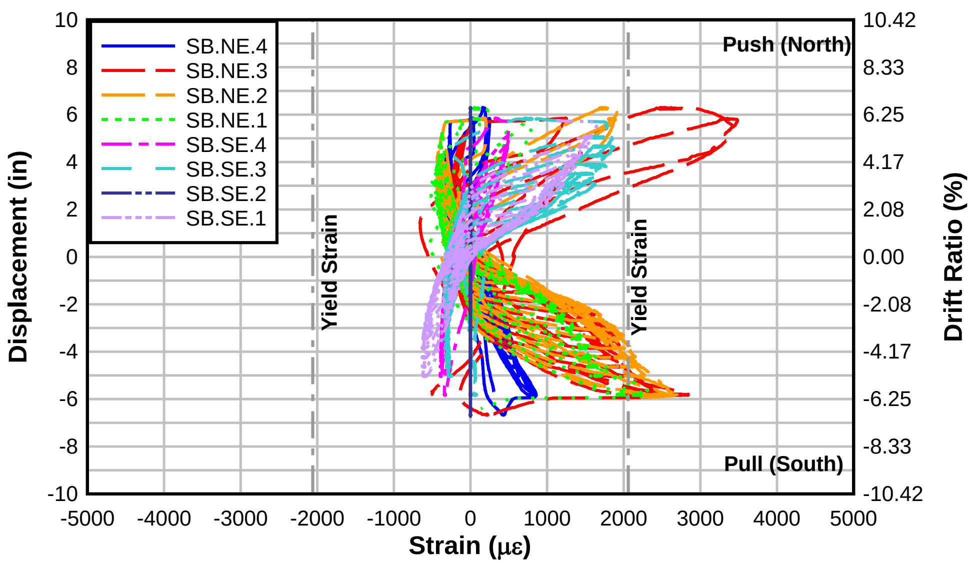

Figure 4.30 - Starter Bar Strains T5-S3.

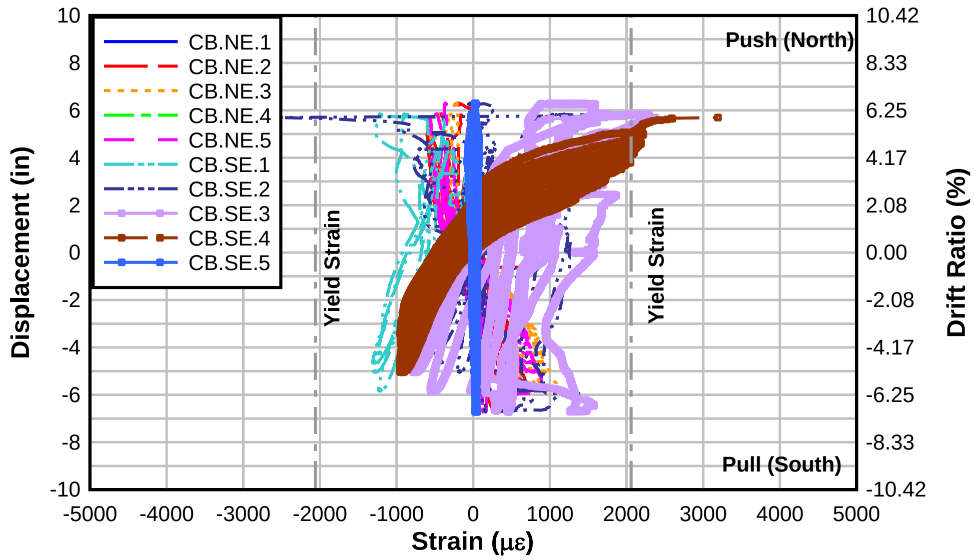

Figure 4.31 - Column bar Strains T5-S3.

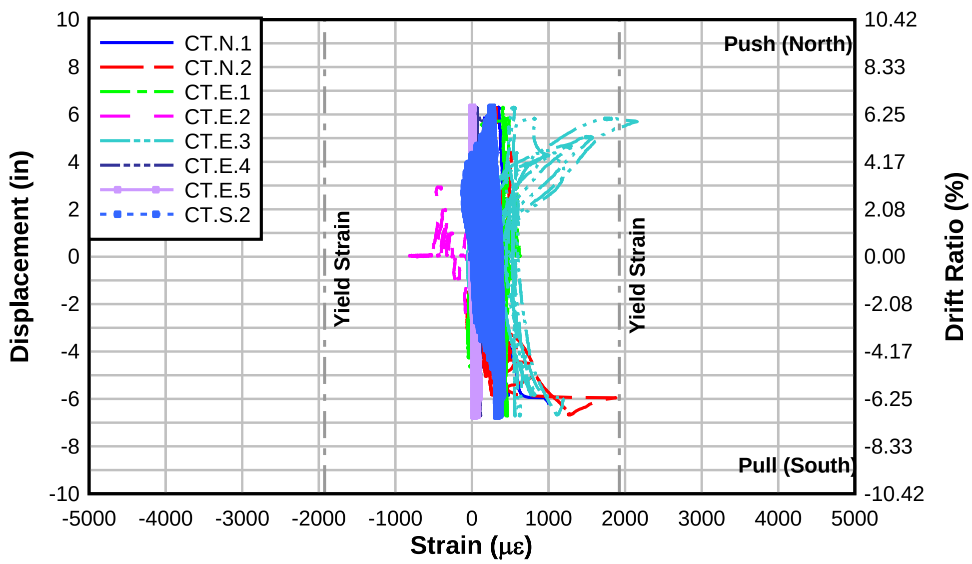

Figure 4.32 - Column Tie Strains T5-S3.

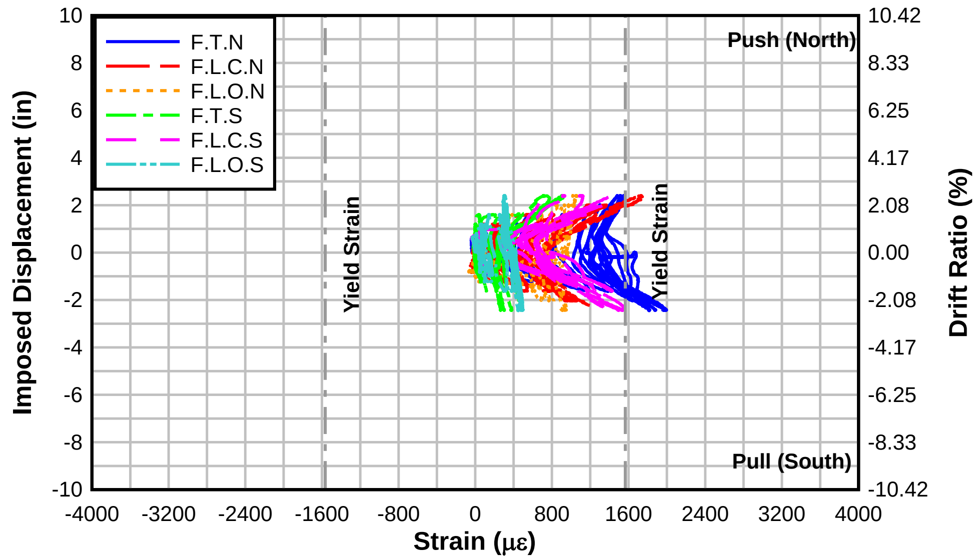

Figure 4.33 - Footing Bar Strains T8-S2 Postfailure.

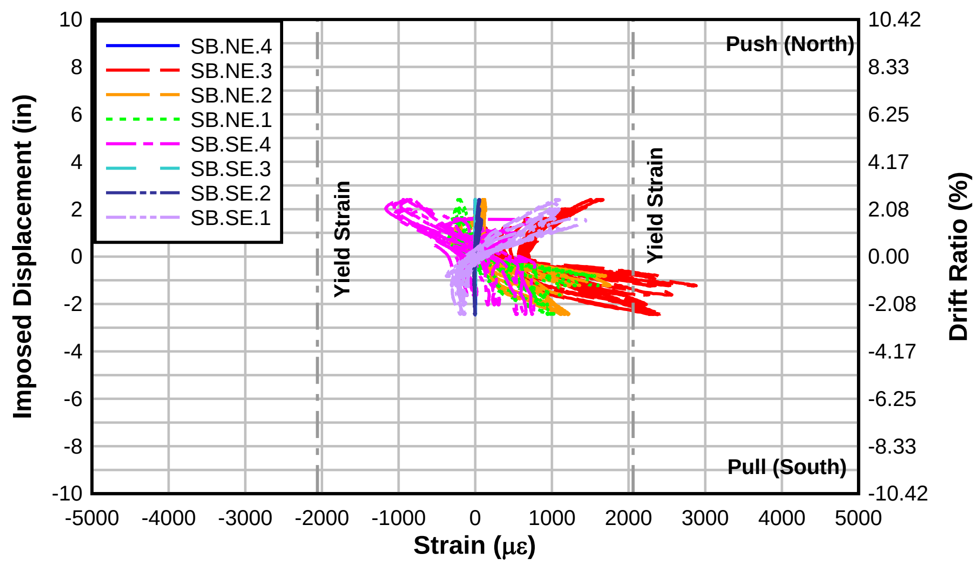

Figure 4.34 - Starter Bar Strains T8-S2 Postfailure.

4.5 Soil-Structure Interaction

The use of soil simulant allowed for the characterization of the substructure system including the occurrence of foundation rocking behavior. This facilitates a more realistic representation of an in-situ column-footing under laboratory controlled conditions. Response of the substructure under different soil characteristics including rocking, embedment, stiffness, settlement, and footing size can be captured with the soil simulant used in this study. The following section discusses the effects of soil-structure interaction (SSI) on the column-footing response.

4.5.1 Effect of Rocking on TiAB Retrofitted Bridge Columns

Effects of rocking foundation behavior were determined by comparing the results of Test 1 and the results of specimen R-S-R-LTi-90 tested by Shrestha (2019), and comparing the results of Test 5 with the results of specimen C-S-R tested by Shrestha (2019). Figure 4.35 displays the difference SSI made in the response of the vintage column. Test 5 was tested with a soil simulant subgrade and steel spring embedment soil, while C-S-R was tested with the footing fixed to the strong floor. There is a clear difference due to activation of rocking behavior of the column foundation. The rigid body motion seen in Test 5 exhibited a higher peak response of 235 kN (52.9 kips) at a drift of 6% before failure compared to the C-S-R with a peak shear of 182 kN (40.9 kips), at a drift of only 0.81% before failure. Furthermore, Test 5 was conducted after progressive damage in the column occurred during Tests 2 and 3 as described in Sections 4.1.3 and 4.1.4. It is also clear that the SSI produced a softer lateral load – deformation response which would influence the natural period of the structure and thus the response to ground accelerations. SSI also produced larger energy dissipation which would act to dampen dynamic response.

SSI can reduce the column demands and thereby ductility demands of columns. Figure 4.36 compares the results of Test 1 and the results of specimen R-S-R-LTi-90 tested by Shrestha (2019), both unretrofitted columns, but one on simulated soil and the other fixed to the laboratory floor Test 1 displayed a much lower column shear due to the soil acting as a fuse to limit the demands compared to specimen R-S-R-LTi-90. The simulated soil had a more stable response from the plastic material response of the soil simulant subgrade and passive pressure provided by a soil simulant embedment and the thresholds were sufficiently low as to prevent column failure. This demonstrates that SSI can be of significance when making retrofit decisions as component demands may be reduced compared to idealized fixity assumptions.

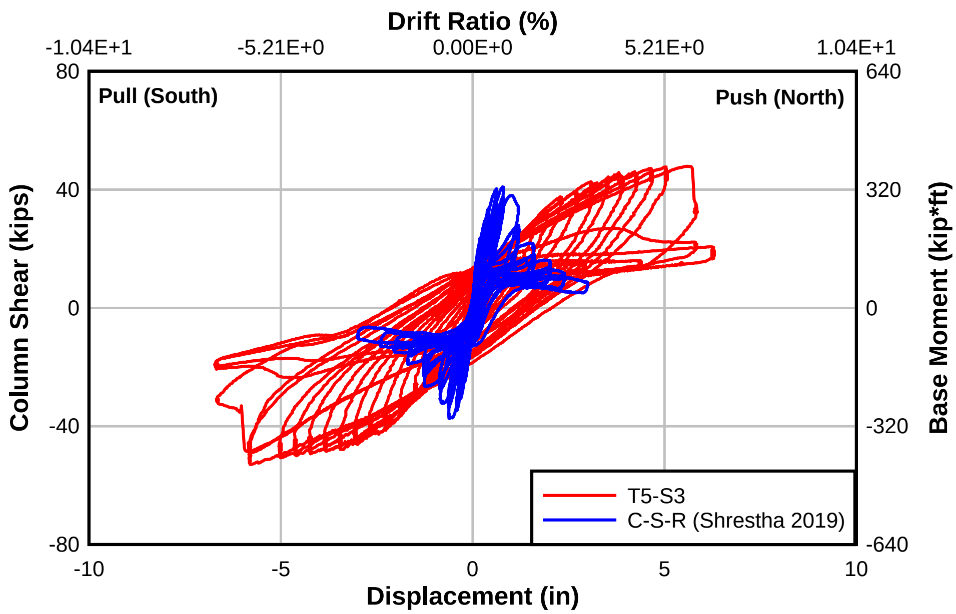

Figure 4.35 – Comparison of vintage columns with and without SSI.

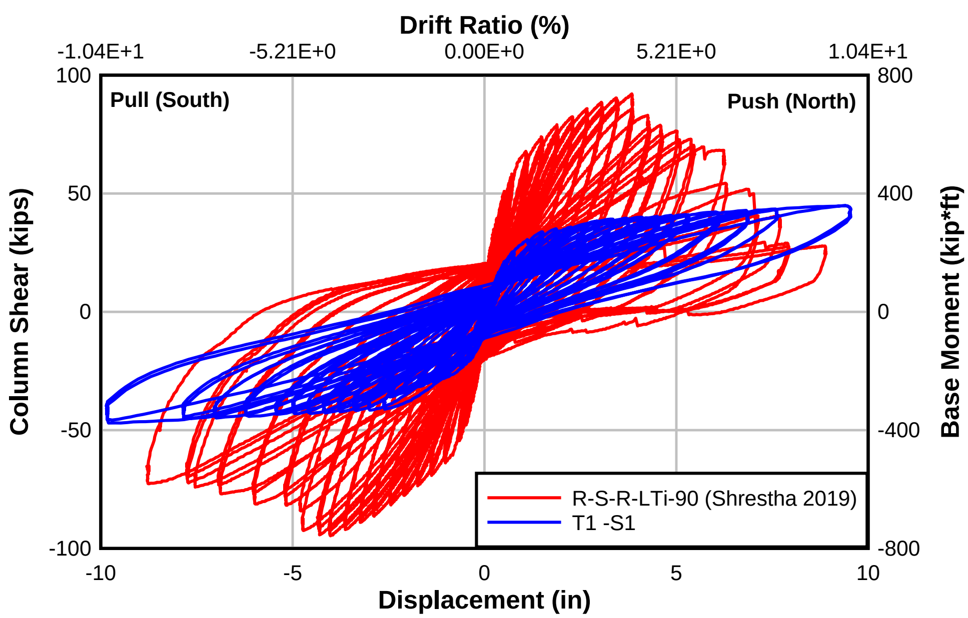

Figure 4.36 – Comparison of a complete TiAB retrofit with and without SSI.

4.5.2 Effect of Embedment Depth

Another factor in characterizing SSI response is the effect of embedment depth. Figure 4.37 compares the response from Test 1 of Specimen 1 and Test 2 of Specimen 2. In Test 1, a 0.61 m (2 ft.) embedment depth was provided using the soil simulant in series with the steel springs, and no embedment was provided in Test 2. Both specimens had the same as-built properties; therefore, the change in response is due to differences in embedment. Test 1 had a column shear of 179 kN (40.3 kips) at a drift of 4.7%, and Test 2 had a column shear of 118 kN (26.6 kips) at a drift of 4.6% on the push cycle. On the pull cycle, Test 1 had a column shear of 191 kN (43 kips) at a drift of 5.2%, and Test 2 had a column shear of 118 kN (26.6 kips) at a drift of 5% on the pull cycle. Without embedment the difference in stiffness between the push and pull cycles was removed; therefore, when comparing the difference in embedment the average was taken as the difference between the two sides. The average contribution to column shear from difference in embedment was 67 kN (15.1 kips). Furthermore, the post-yield slope is visibly larger in Test 1 compared to Test 2. Assuming a linear trend over the yield and post-yield slopes we see that the post-yield slope in Test 1 is approximately 3% of the yield slope, and 1.26% for Test 2. Therefore, most of the stiffness occurs due to embedment, and bearing pressures alone are enough to counter the negative slope effects from P-Delta due to the stiffening of the soil simulant at larger plastic deformations. Based on these results, the rocking behavior of the foundation is more likely to occur at reduced embedment.

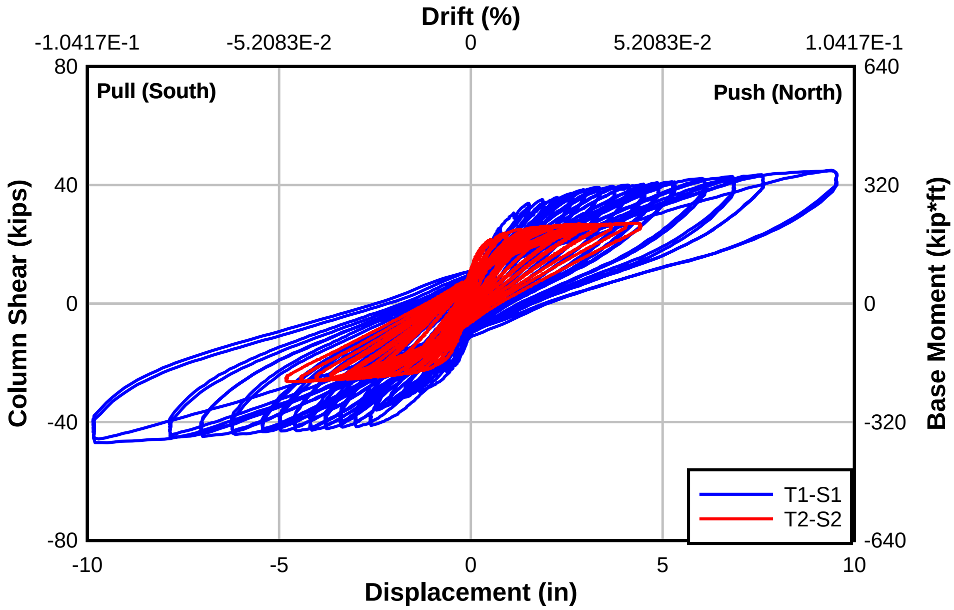

Figure 4.37 – Comparison of SSI response change with embedment.

4.5.3 Effect of Axial Loads

Test 3 was conducted with a 667 kN (150 kips) axial load. After completing the test, the axial load was lowered to 445 kN (100 kips) in an effort to decrease the yield moment of the column. Previous soil failure in Test 3 caused no participation from the embedment soil simulant. Furthermore, the soil simulant subgrade had already exhibited plastic deformations, which resulted in a softer response through the previous drift cycles. Participation from the embedment soil simulant starts to occur at a 6.1% drift on the push cycle, and 6% drift on the pull cycle in Test 4. On the push cycle, the column shear in Test 3 at 6.1% drift is 191 kN (43 kips), and the column shear in Test 4 is 147 kN (33.1 kips). On the pull cycle, the column shear in Test 3 at 6% drift is 196 kN (44 kips), and the column shear in Test 4 is 144 kN (32.3 kips) as seen in Figure 4.38. Even though the embedment soil simulant had failed during the previous test, the responses are comparable due to the recovery of the soil simulant. During both tests, at 6.1% and 6% drift, the face of the footing was in contact with the embedment soil simulant. A reduction in axial load reduced the column shear in the specimen at similar drift magnitudes.

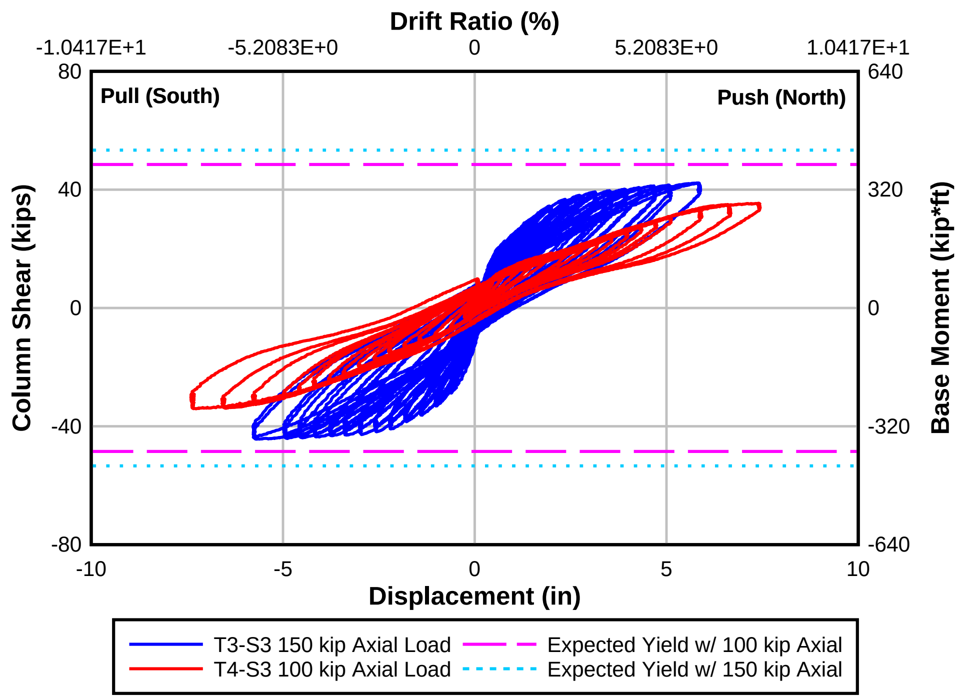

Figure 4.38 – Comparison of SSI with changes to axial load.

4.5.4 Effect of Soil Stiffness

Soil stiffness is a major contributing factor in characterizing SSI. The soil simulant subgrade was highly compressed and exhibited permanent deformation at larger excursions. These plastic deformations also result in increased the soil simulant stiffness as the loading continues. During lateral loading, the soil simulant is loaded non-uniformly due to the rocking behavior of the foundation, and as a result, there is an arch-like profile under the footing and as the column returns to the original position, a smaller area of soil simulant becomes loaded during subsequent cycles and in some cases subsequent tests on the same soil. Figure 4.39 illustrates the arch-like profile after Test 1. For Test 1, the soil simulant depth was recorded at 76.2 mm (3 in). increments along the length of the footing footprint. This record was taken after the specimen was removed. For other tests, punching and damage occurred to the soil simulant during subsequent tests and thus the soil profiles recorded were more variable but are reported in Appendix C. Based on test results there are four (4) important contributing factors to the evolution of the stiffness of the soil simulant;

elastic loading stiffness, strength upon nonlinear stress-strain response, large strain stiffening, and the strain rate.

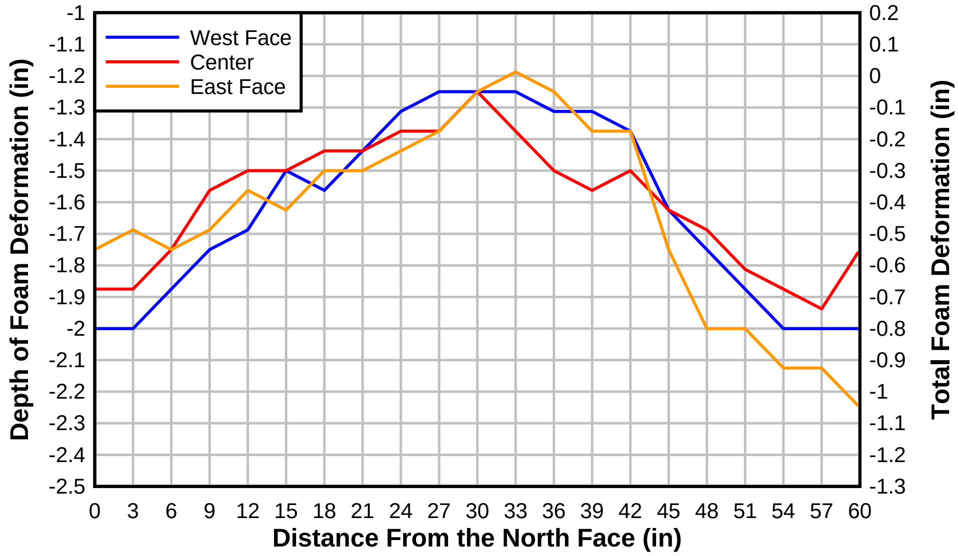

Figure 4.39 – Soil simulant profile after testing.

4.5.4.1 Evolution of Stiffness Degradation

The evolution of the overall stiffness degradation was developed for each test in terms of both the tangent stiffness and the secant stiffness. To obtain the tangent stiffness, the backbone curve of the overall force-displacement hysteresis was differentiated with respect to the displacement. The secant stiffness was determined from the slope of a line radiating from the origin to points on backbone curve. Both the tangent stiffnesses and secant stiffness variations were grouped for comparison based on whether new soil simulant was used in the test or the soil simulant that had already been damaged in a prior test. Figure 4.40 – Figure 4.43 compare the evolution of the stiffness degradation for each test. By observation, stiffness degraded for new soil simulant at a faster rate due to creation of at first localized plastic strains in the extreme edges of the footing that progressively take place over larger regions. Subsequent tests of previously damaged soil simulant produced smaller changes because large portions of the simulant were already plastified and thus having inelastic reloading stiffnesses.

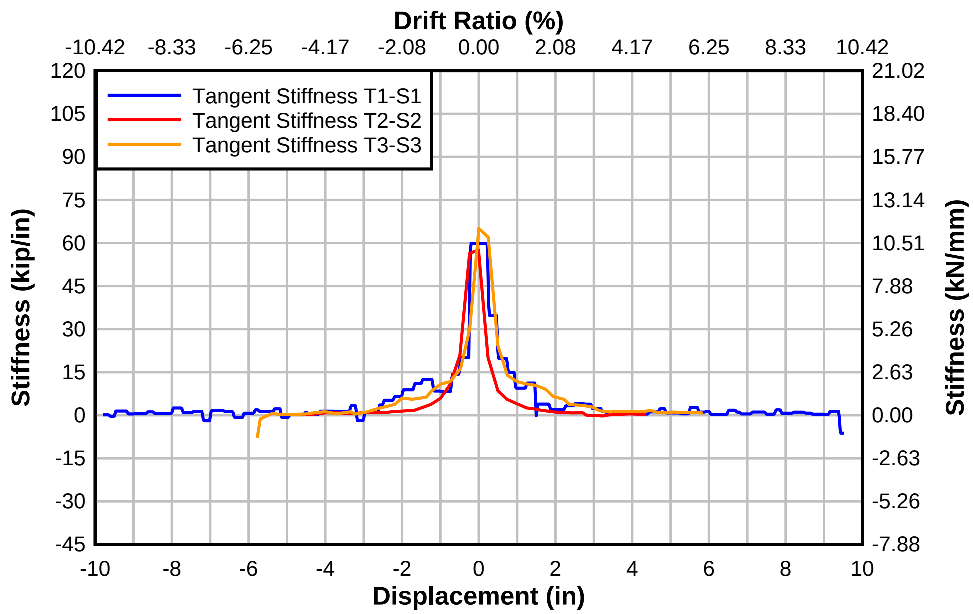

Figure 4.40 – Tangent stiffness degradation of specimens on new soil simulant.

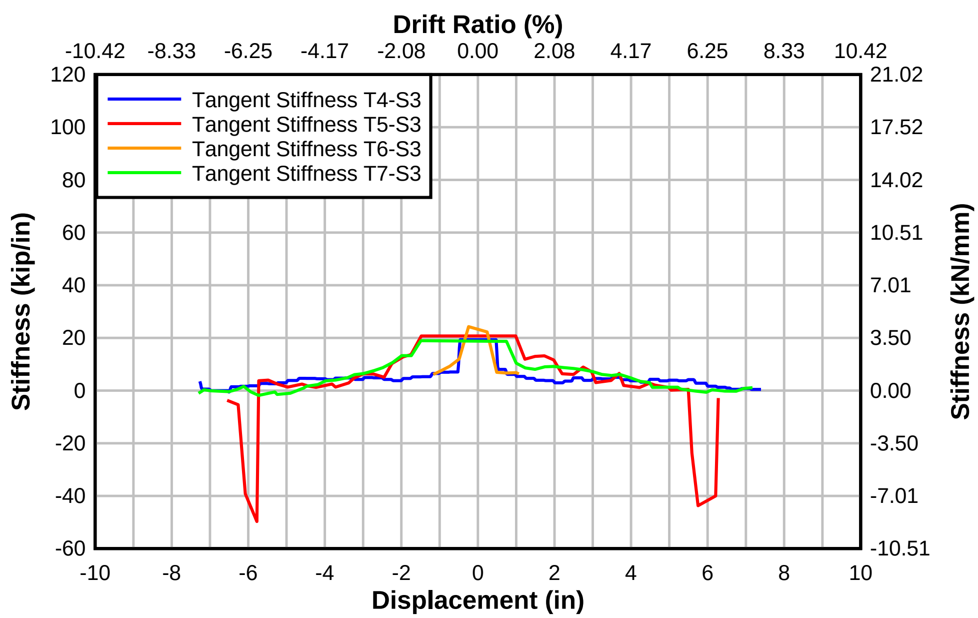

Figure 4.41 – Tangent stiffness of specimens on previously damaged soil simulant.

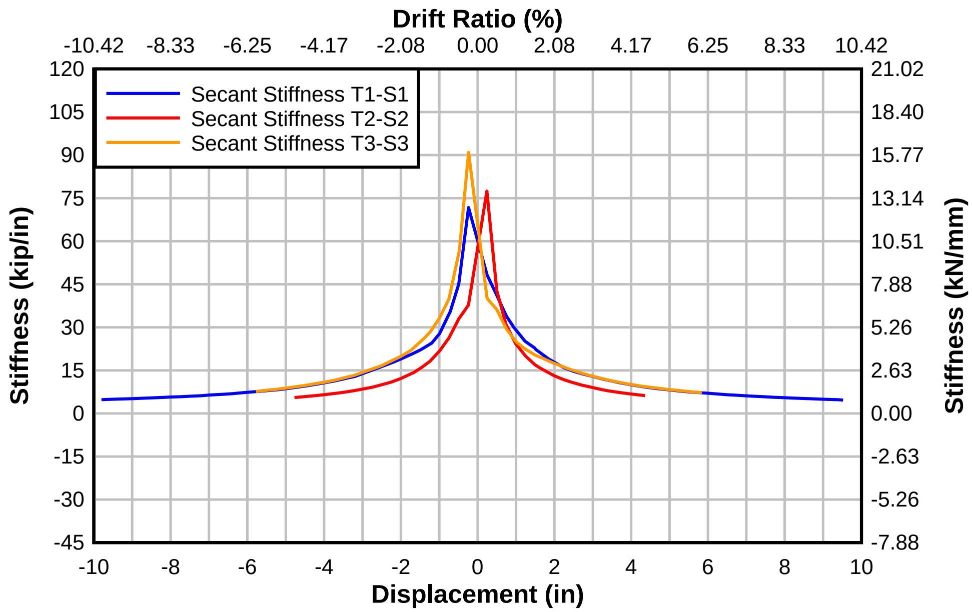

Figure 4.42 – Secant stiffness of specimens on new soil simulant.

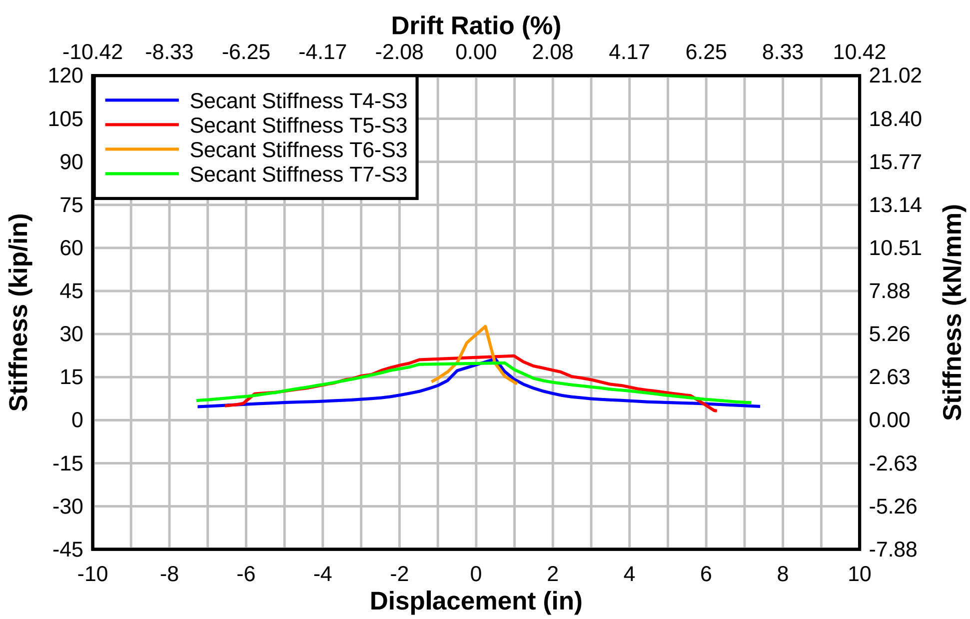

Figure 4.43 – Secant stiffness of specimens on previously damaged soil simulant.

4.5.4.2 Strain Rate

Because the chosen soil simulant is a polymer, it has viscoelastic material properties. Thus the stress can be sensitive to the strain rate (or rate of loading). Strain for the soil simulant under the footing was taken as an average of three sensors along the center of the footing on the East-West axis and divided by the original thickness of the subgrade. The stress was calculated by dividing the applied axial load in time by the original area of the subgrade in contact with the footing. After failure of the subgrade occurred the area in contact was unknown; therefore, all stress-strain relationships are averages of the engineering stress and engineering strain. As seen in Figure 4.44 and Figure 4.45, a slower strain rate results in a lower stiffness subgrade. While the first test was loaded at a strain rate of 252 με/sec and all subsequent tests on new soil simulant were loaded at a strain rate of 49.6 με/sec. Creep of the soil simulant can be observed in Fig. 4.45 whereby stain increases as the axial stress is held constant. A progressively softer stress-strain response was observed when loading previously damaged soil simulant subgrades due to the changing loaded area and reloading branch from plastically deformed soil simulant. Figure 4.46 shows the average engineering stress-strain relationship for previously failed soil simulant.

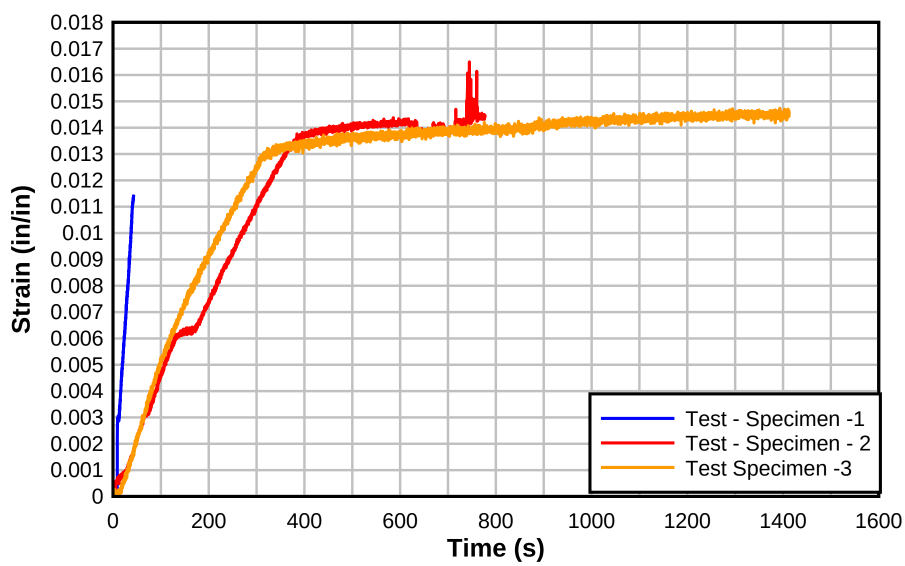

Figure 4.44 – Strain rate of axial loading on new soil simulant.

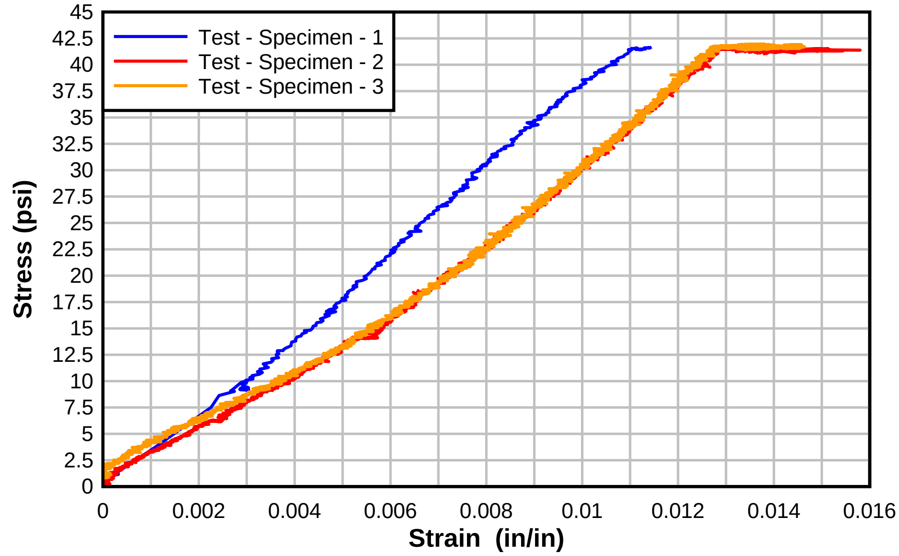

Figure 4.45 – Stress-strain relationship of axial loading on new soil simulant.

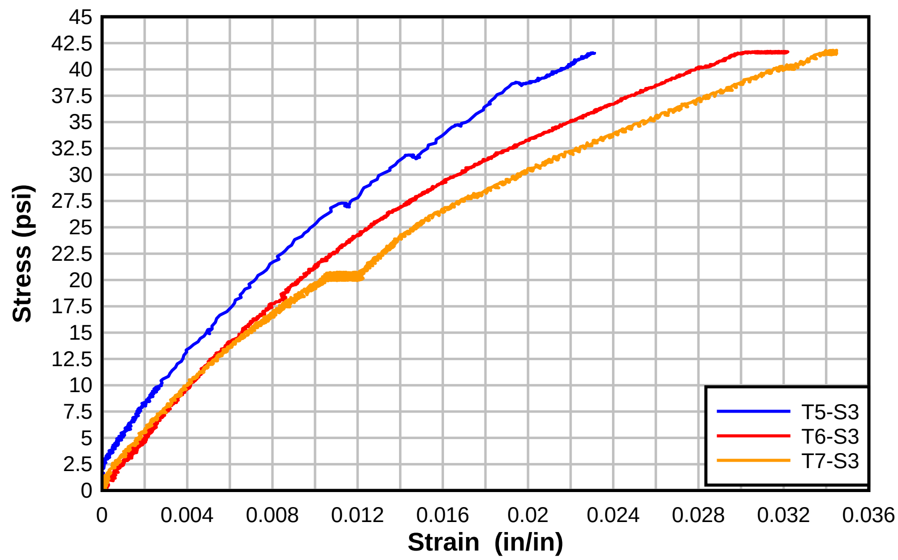

Figure 4.46 – Average engineering stress-strain relationship for subsequent loading of previously damaged soil simulant.

4.5.5 Footing Settlement due to Rocking

Settlement due to rocking for each test was taken as the average of the three sensors along the North and South face of the footing and plotted in relation to the drift ratio to compare the variation in settlement during testing, and on previously failed soil simulant. In Figure 4.47 settlement due to rocking, initial settlement distortions, and recovery of the soil simulant are shown. Settlement distortions were recorded for tests with soil simulant and can be found in Appendix C.

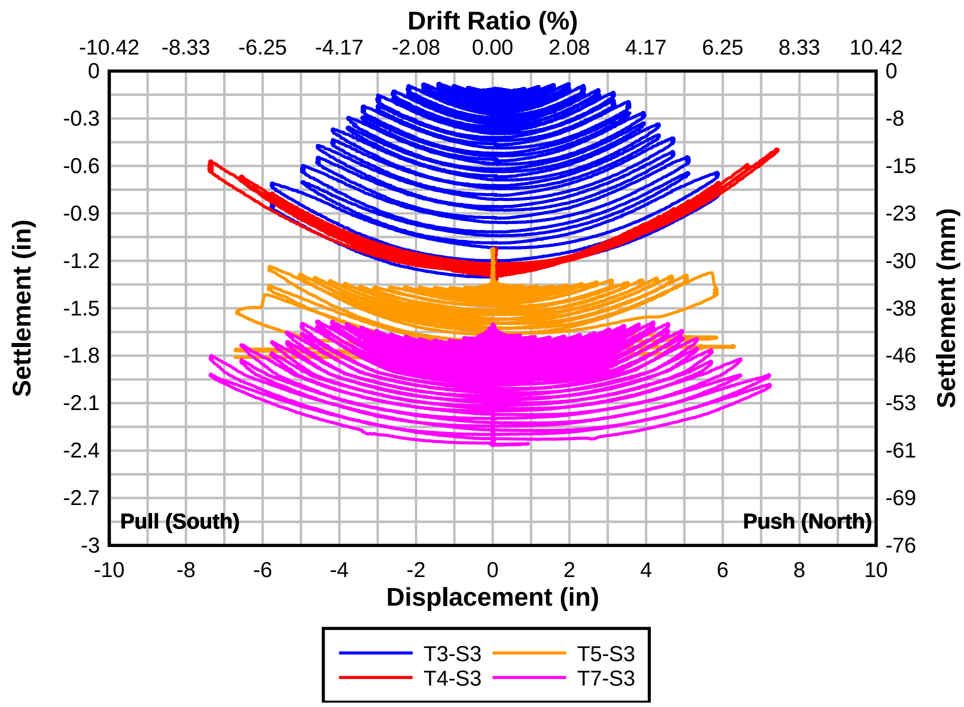

Figure 4.47 – Settlement with continued rocking on the soil simulant.

4.6 Soil Simulant Model

The experimentally observed SSI responses were used to develop an analytical model of the soil simulant assuming rigid body motion of the footing. The soil simulant was modeled as nonlinear contact springs along the base of the footing and nonlinear contact springs in series with the steel springs. The footing base and face were discretized into 102 mm (4 in.) strips as seen in Figure 4.48, with a length of 1524 mm (60 in.). The model was developed using the average effective elastic modulus of 21.96 MPa (3185 psi) from the axial loading on new soil simulant over the gross area of the footing. The soil simulant model was considered elasto-plastic, with the yield strain, 0.0355 in/in, and yield stress, 779 kPa (113 psi) based on the uniaxial tests completed by

Shrestha (2019). The base model was developed separately from the face model to facilitate flexibility in modeling, and compatibility in the rotation of the footing, and the point about which moments were summed was used to resolve the deformations for a particular rotation in both directions. The soil thickness used was 203 mm (8 in.). An axial load of 667 kN (150 kips) was applied, and initial stress, strain, and settlement were computed using equations E4.14 – E4.16, respectively. By convention, the down direction is negative for the base model and away from the springs in the face model.

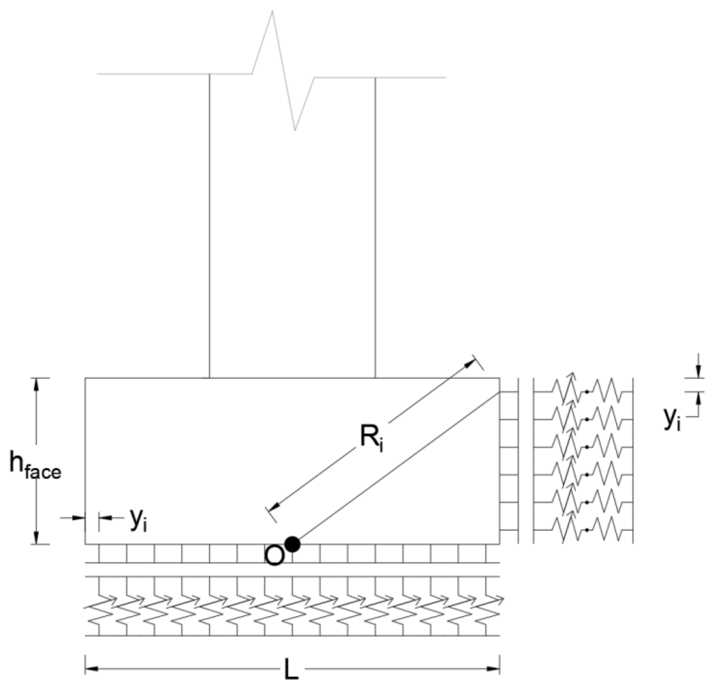

Figure 4.48 - Soil simulant model.

$$\sigma_{initial} = P/A_{footing} \qquad \text{E4.14}$$

$$\varepsilon_{initial} = \sigma_{initail}/E_{soil\ simulant} \qquad \text{E4.15}$$

$$\Delta_{intial\ settlement} = \varepsilon_{intial} * h \qquad \text{E4.16}$$

where P is the axial load, $A_{footing}$ is the area of the base of the footing, and h is the original thickness of the soil simulant.

4.6.1 Model for Contribution from Bottom of Footing

The contribution of the soil simulant at the bottom of the footing to force-displacement response was developed by first imposing a rotation to the footing about the origin labeled as O in Figure 4.48. Given this rotation, the average settlement is computed to achieve equilibrium and the displacement at the top of the column. Average settlement and the displacement at the top of the column were determined using equations E4.17-E4.19, respectively. In E4.17 to E4.19, $\theta_{rotation}$ is the rotation in radians, Δ_1 and Δ_2 are the vertical displacement at each edge of the footing, L is the length of the footing and the distance between the footing corners, and H_L is the distance from the bottom of the footing to the top of the column.

$$\theta_{rotation} = (\Delta_1 - \Delta_2)/L \quad \text{E4.17}$$

$$\Delta_{settlement} = (\Delta_1 + \Delta_2)/2 \quad \text{E4.18}$$

$$\Delta_{top} = \theta_{rotation} * H_L \quad \text{E4.19}$$

A vertical contribution was necessary to obtain equilibrium as the footing tips up on the toe due to the rotation. Total deformation at the i^{th} spring was found using equation E4.20, and strain in the i^{th} spring was found using equation E4.21.

$$\Delta_{Total,i} = \Delta_1 - (\theta_{rotation} * y_i) + \Delta_{vert} + \Delta_{settlement} \quad \text{E4.20}$$

$$\varepsilon_i = \Delta_{Total} / h \quad \text{E4.21}$$

where Δ_1 is the imposed displacement at the bottom of the footing, y_i is the distance from the toe, and Δ_{vert} is the vertical addition to obtain equilibrium. If the strain in the i^{th} spring is positive, the stress is set to zero because the spring is not in contact. If the strain in the i^{th} spring is more negative than the yield strain, then the stress is set to the yield stress, otherwise stress in the i^{th} spring is calculated using equation E4.22

$$\sigma_i = \varepsilon_i * E_{soil} \quad \text{E4.22}$$

The force in each spring is then calculated using equation E4.23.

$$p_i = \sigma_i * w_i * l_i \quad \text{E4.23}$$

where w_i is the width of the i^{th} spring, and l_i is the length of the i^{th} spring. The location of each spring was measured from the center of the footing, from the origin O, to the y^{th} depth. This was also the moment arm length used to calculate the moment contribution from each spring. Equations E4.24 and E4.25 were used to calculate the moment arm and moment contribution from each slice.

$$L_y = (L/2) - y_i \qquad \text{E4.24}$$

$$M_y = p_i * L_y \qquad \text{E4.25}$$

where L_y is the length of the moment arm from the center of the footing at point O, and M_y is the moment from the y^{th} slice. The total force, total moment, moment arm of the resultant reaction, and the force at the top of the column required to resist the footing induced moment were calculated using equations E4.26 – E4.29.

$$P_{footing} = \Sigma\, p_i \qquad \text{E4.26}$$

$$M = \Sigma M_y \qquad \text{E4.27}$$

$$L_M = M/P_{footing} \qquad \text{E4.28}$$

$$H = M/H_L \qquad \text{E4.29}$$

The initial assumption is that the point of rotation of the footing does not change from point O (Figure 4.48). However, because this point changes in reality a vertical addition is need to achieve equilibrium. The vertical addition was iterated to find equilibrium between the applied axial load, the reaction at the base of the footing, and the lateral load at the top of the column. According to the model, as the moment becomes constant, the soil simulant resultant force located 0.457 m (1.5 ft.) from point O (Figure 4.48). The force-displacement response backbone curve from the model was compared to the force-displacement backbone curve from Test 2 of Specimen 2 as seen in Figure 4.49. The response in the model was assumed to be symmetric. The pull side was closer to the experimental response than the push side because of the stiffer side of the test setup..

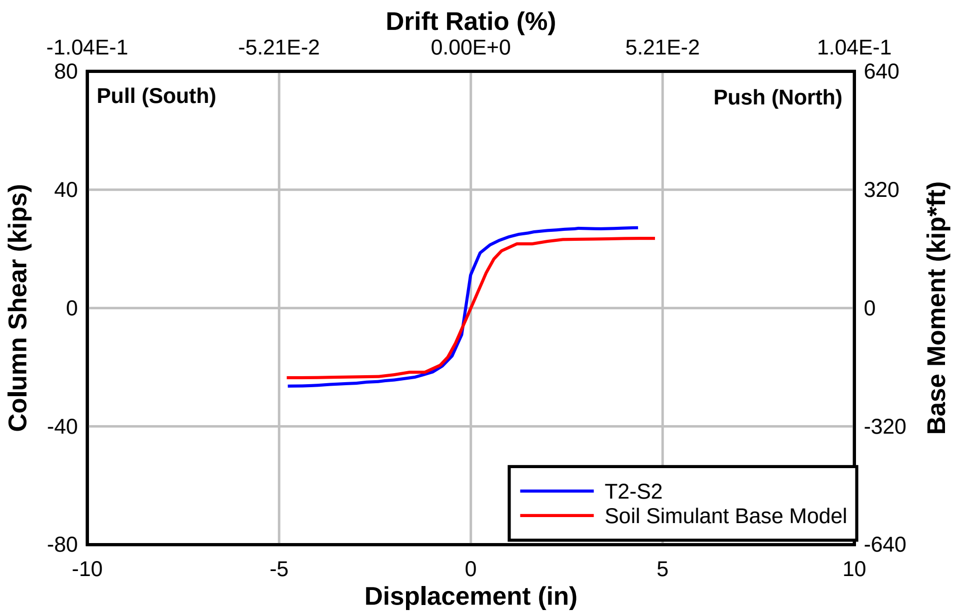

Figure 4.49 – Comparison of the soil simulant model with experimental response from Test 2 of Specimen 2.

4.6.2 Model for Contribution from Footing Face

The contribution from the soil simulant along the face of the footing was treated separately in the model using the same size nonlinear contact springs as the footing base along the 610 mm (24 in.) depth. The rotation from the footing base model was used to maintain compatibility when combining the footing base and face model contributions. The initial radius from the origin, O, to the center of each spring, where the intended reaction of each spring was assumed to be, was taken as equation E4.30, and an initial angle in radians was determined using equation E4.31.

$$R = ((L/2)^2 + (h_{face} - y_i)^2)^{1/2} \qquad \text{E4.30}$$

$$\theta = \arccos\,(L/R) \qquad \text{E4.31}$$

where L/2 is the length from the center of the footing, at point O, to the toe, h_{face} is the height of the footing on the face, and y_i is the depth of the i^{th} spring. An adjustment angle is then calculated as the difference between the original angle theta and the angle of imposed rotation, and a new horizontal deformation was calculated as seen in equations E4.32 and E4.33.

$$\theta_{adj.} = \theta - \theta_{rotation} \qquad \text{E4.32}$$

$$R_{adj.} = R * \cos(\theta_{adj.}) \qquad \text{E4.33}$$

$$\Delta_i = L' - L \qquad \text{E4.34}$$

The change in horizontal distance, Δ_i, is calculated as the difference between the new horizontal distance, L', and the original horizontal distance, L, as seen in equation E4.34. This difference is the displacement of the footing at y_i for any given rotation. Soil simulant strain can then be found using equation E4.35. Because the model uses contact springs and the footing rotates into the springs at the face at larger displacements the toe of the footing moves away from the springs; therefore, if the strain is negative the footing is not in contact with the springs. Stress in the soil simulant springs depends on the strain amplitude. If the strain is negative then the stress is set to zero, if the strain is greater than the yield strain then the stress is set to the yield stress as discussed in Section 4.6, otherwise it is calculated using equations E4.36.

$$\varepsilon_{soil} = \Delta_i / w_{soil} \qquad \text{E4.35}$$

$$\sigma_{soil} = \varepsilon_{soil} * E_{soil} \qquad \text{E4.36}$$

The force in each soil simulant spring could then be derived using equation E4.37. This was then be used to inform the displacement of the steel springs by equation E4.38, based on the stiffness of the steel springs discussed in Section 3.5.2.

$$p_i = \sigma_i * A_{soil} \qquad \text{E4.37}$$

$$\Delta_{steel} = p_i / K_{steel} \qquad \text{E4.38}$$

where A_{soil} is the area of the i^{th} spring series, and K_{steel} is the stiffness of the steel at the y^{th} depth. This process is iteratively solved from equations E4.34 – E4.38 for each spring along the height of the footing by updating the foam displacement based on the calculated steel displacement in the previous iteration. The moment contribution from the y^{th} depth was found using equation E4.39; moments are summed about the center of the footing at point O, as seen in equation E4.40, and the force resultant is determined using equation E4.41.

$$M_y = p_i*(h_{face}-y_i) \qquad \text{E4.39}$$

$$M_{face} = \Sigma M_y \qquad \text{E4.40}$$

$$H' = M_{face}/(H_L-h_{face}/2) \qquad \text{E4.41}$$

The forces acting on the face and the bottom of the footing were summed to combine their effects and produce a force-displacement backbone curve for the given displacements of the imposed lateral displacement protocol from Section 3.6. Figure 4.50 is a comparison of the model backbone curve to the backbone curve from Test 1-of Specimen 1 with new soil simulant.

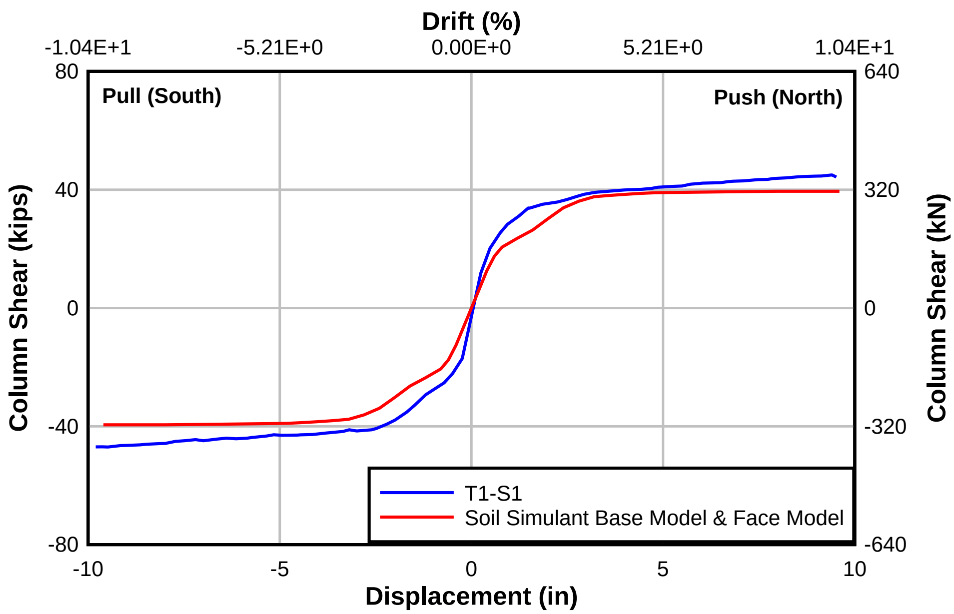

Figure 4.50 – Comparison of soil model, including face and base, with experimental results.

Because failure of the vintage column did not occur with the soil simulant, the soil simulant was removed and only the steel springs were used as an embedment soil for the footing face; furthermore, the soil simulant subgrade had already plastically deformed. Figure 4.51 illustrates the comparison of a backbone force-displacement response, with new soil simulant and steel embedment soil, with Test 5 of Specimen 3 backbone force-displacement response. Comparison plots were made for all tests assuming ideal springs and new soil simulant and can be found in Appendix C. It is important to note that in Test 5 progressive damage to the face of the footing reduced the reaction area of the springs, and the soil spring model does not have limits set for column failure or steel spring nonlinearity.

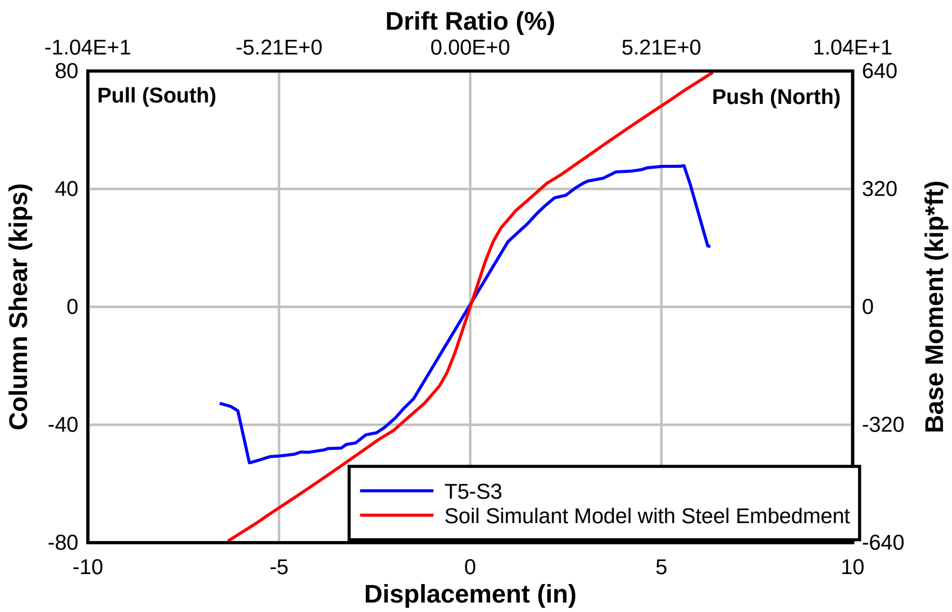

Figure 4.51 – Soil simulant model comparison using a previously damaged soil simulant under the footing and and steel springs at the face of the footing.

4.7 Post-Failure TiAB Retrofit

To better understand the performance of the TiAB retrofit two (2) tests were completed after the SSI investigation of the vintage column that produced failure of the unretrofitted column. Firstly, the column was left in place, latent spalled concrete was removed. Then the TiAB ligaments were installed and the specimen tested with small laterally imposed displacements. Then the retrofit was completed by installing the two TiAB spirals and casting the concrete shell. To mimic realistic conditions of column performance after failure and installation of the retrofit, the soil simulant that failed in previous tests 3-5 was kept under the specimen. The final conditions that resulted in the vintage column failure were repeated by placing only the steel spring soil embedment on the North and South footing faces. The intent of these tests was to investigate retrofit performance that might occur during aftershocks, or subsequent earthquakes.

As previously stated the column failed during Test 5 after failure of the lap-splice. Eventual loss of flexural tension capacity in the column occurred due to damage in the lap-splice region resulting in bond-slip of the column bars and starter bars. The response of the specimen in the failed condition at small excursions were captured for comparison with the incrementally retrofitted column.

The influence of the TiAB ligaments alone were shown previously in Figure 4.14 that shows that ligaments do not significantly increase the expected yield moment for a service axial load of 667 kN (150 kips). Their intent is not to provide strength, but an alternate flexural load path after failure of the reinforcing steel lap splice. This can also be seen in the overall force-displacement response for Test 6 (Figure 4.19) when comparing the capacity of the column after failure and the response of the column with only ligaments. Ligament installation occurred without the axial load applied. These results may be more directly compared to a case in which the damaged bridge is actively shored to remove axial load from the column during installation of the retrofit.

Lastly, the retrofit was completed as described in Section 3.3.3. Without retrofitting, or repair of the footing, the Specimen 3 was tested again in Test 7 and the results were compared with Test 1of Specimen 1 as seen in Figure 4.52. The completely retrofitted failed column was able to sustain a higher load than the pristine vintage column with a complete retrofit. This is most likely due to the steel spring soil simulant at the footing face for Test 7. The retrofitted failed column performed as well as a the retrofitted pristine column which can be attributed to casting of new concrete in the shell that also serves to restore the previously failed lap splice. The shell thus provided two benefits; it prevented pull-out and elastic buckling of the TiAB ligaments on the compression face of the column and it partially restored the bond strength between the lap-spliced bars.

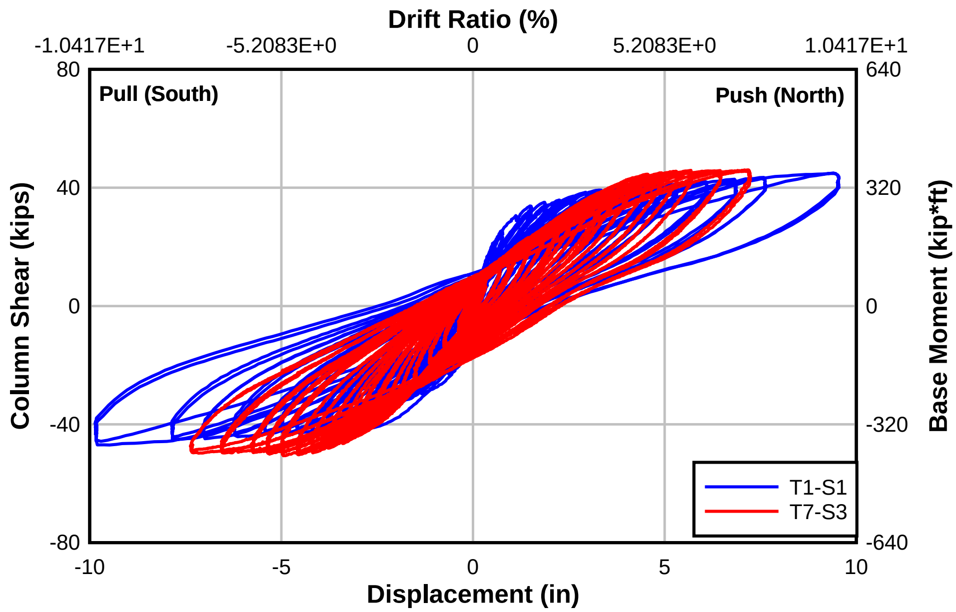

Figure 4.52 – Comparison of a failed column with a complete retrofit repair and pristine vintage column with a complete retrofit.

4.8 Vintage Footing Performance

After testing, the specimens were removed from the soil simulant and the base of each footing was inspected for damage. Observed damage was noted and recorded in specimens that exhibited cracking along the base. Shrestha (2019) observed a crack pattern in center of the footing in both directions. The footing of Specimen 1 after Test 1 exhibited a similar pattern. Figure 4.52 illustrates the crack patterns in each footing.

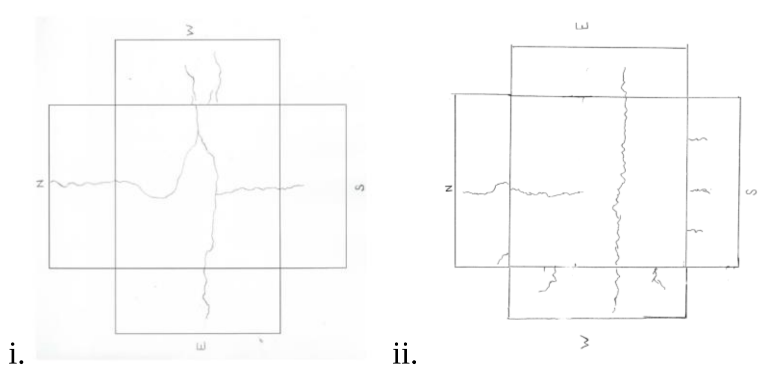

Figure 4.53 – Observed cracking patterns in the footing. i) Shrestha (2019) illustration of footing damage in specimen R-S-R-LTi-90-Spread, ii) illustration of footing damage in T1-S1.

In the direction of bending imposed on the column and footing in for the present study, cracking between the East and West faces across the bottom of the footing would be anticipated based on one-way bending. However, the cause of cracking between the North and South faces is less obvious, but can be anticipated when considering a truss model for the force transfer mechanism through the footing between the column soil. The cracking moment can be found using equations E4.42-4.44, with equation 4.43 from ACI 318-19 for the flexural tension strength of concrete (equation 19.2.3.1).

$$S = 1/6*b*h^2 \tag{E4.42}$$

$$f_r = 7.5*f'c^{0.5} \tag{E4.43}$$

$$M_c = S*f_r \tag{E4.44}$$

where S is the section modulus of the footing, b is the width of the footing, h is the height of the footing, $f'c$ is the compressive strength of the concrete, and M_c is the cracking moment. The cracking moment of the footing is nominally 244 kip*ft. As the soil force resultant location under the footing increases at higher rotations, the moment in the footing eventually becomes large enough to induce flexural cracking in the cracking due to one-way bending.

Capturing the cracking in the orthogonal direction of lateral loading requires development of a phenomenological model that represents the load path the axial load takes through the footing. To accomplish this task, a Strut-and-Tie Model (STM) was developed using Chapter 23 of ACI 318-19. The STM developed to represent the force flow through the footing is illustrated in Figures 4.53 to 4.55. At 2% lateral drift the soil simulant begins to yield; therefore, this displacement was chosen as the representative case for the STM. The nodal surfaces were first determined and then the nodes were turned 5˚ for mathematical and visual convenience. The length of the top node in the plan view was chosen as half of the width of the column.

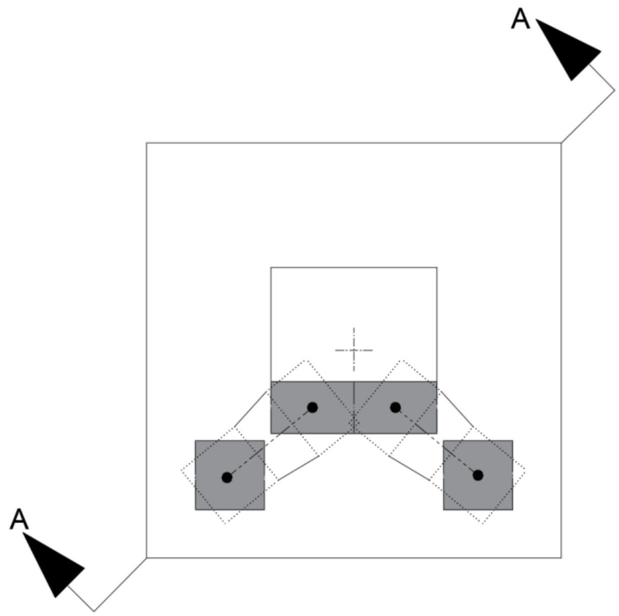

Figure 4.54 – Plan View of the STM.

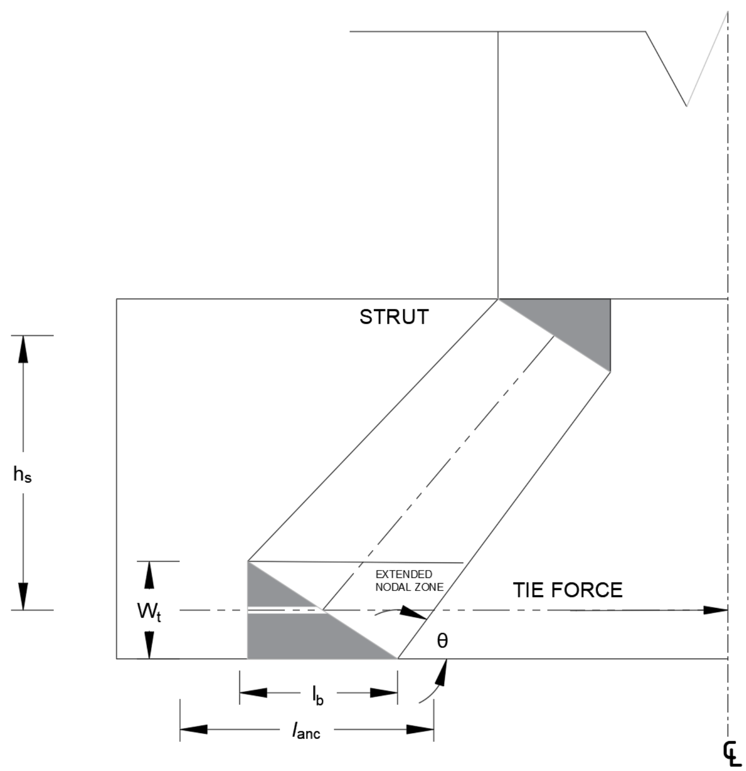

Figure 4.55 – Elevation of the STM at Section A-A with end nodes turned 45 degrees.

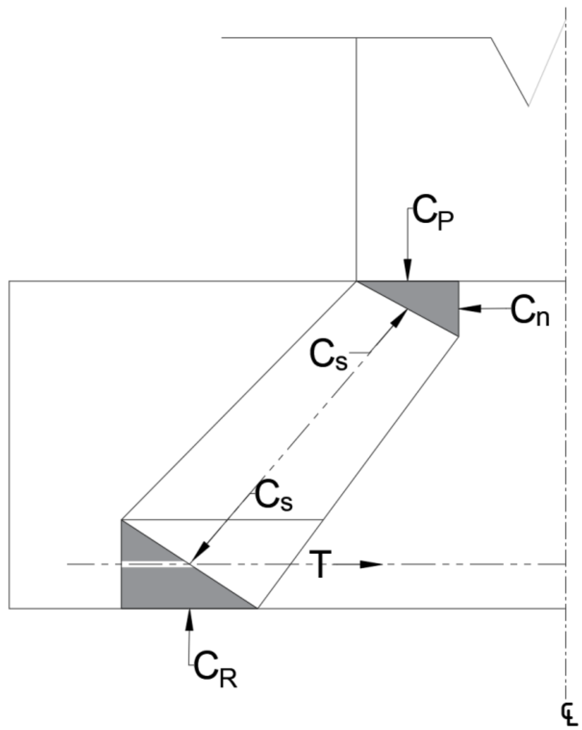

Figure 4.56 – Forces acting on nodes.

Considering axial load-moment interactions for the column and the actual material properties, the neutral axis location for 667 kN (150 kip) axial load in the column is190 mm (7.5 in.) from the compression face of the column as illustrated in Figure 4.56. This served as the length of the upper node. Because there is no distinguished bearing area under the footing as the specimen undergoes rocking behavior, the bearing area on the bottom of the footing was determined using the soil model described previously in Section 4.6.

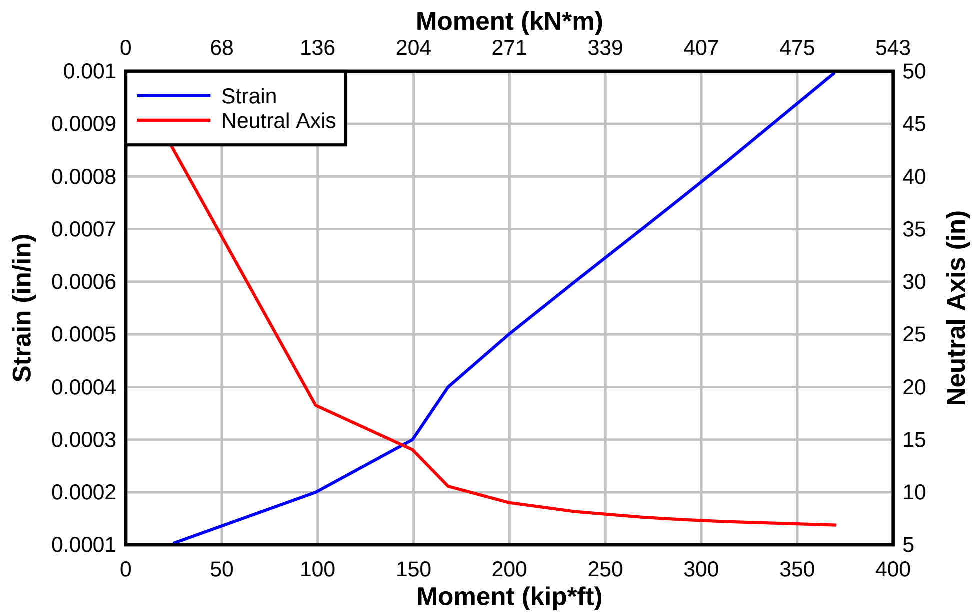

Figure 4.57 – Expected moment-column compression strain interaction as the neutral axis varies.

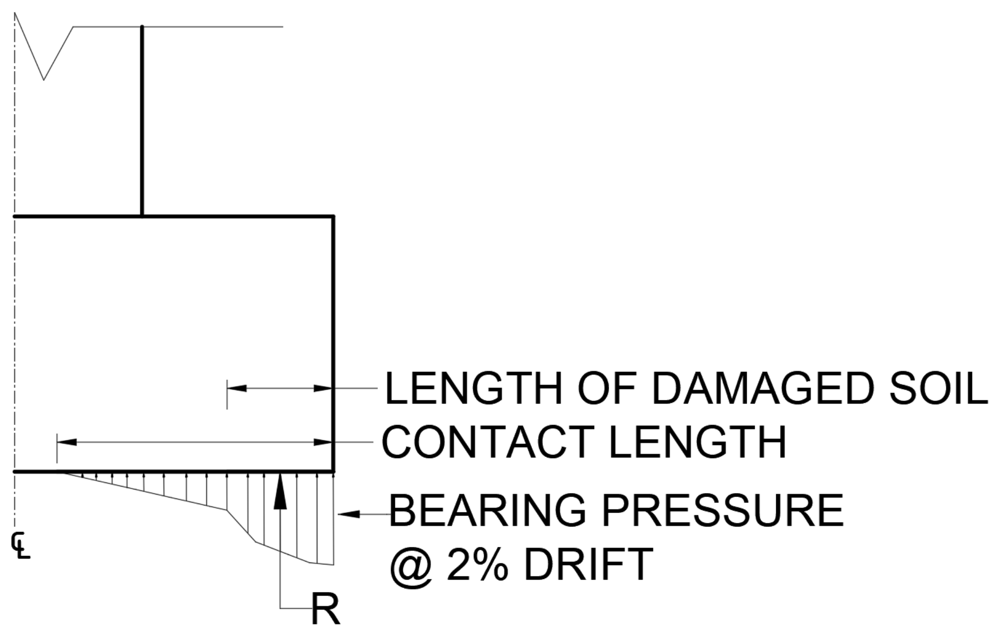

Figure 4.58 – Location of resultant and length of plastically deformed soil from soil simulant model at 2 % drift.

The bearing area for the bottom node in the footing was selected based on the length of soil simulant under the footing that achieved yield. Thus, a bottom node measuring 254 mm (10 in.) square was used, as seen in Figure 4.54. Furthermore, the bottom node was placed at the location of the soil force resultant. The dimension, W_t, of the bottom node was then chosen as 165 mm (6.5 in.) using ACI 318-19 R.23.8.1.a. The planes of the top and bottom nodal faces that intersect with the strut were assumed to be parallel and the remaining dimensions of the upper node were determined, making the W_t of the upper node as 124 mm (4 – 7/8 in.). The line of action of the strut was determined to be where the axial force, Cp, and the reaction force, C_R, intersect the diagonal face of each node. The tie, T, was drawn in-plane using the dimensions of the footing, with the center at 82.5 mm (3-1/4 in.), and has a line of action intersecting C_R and C_s.. An extended nodal zone was used to maximize available development length. The development length of the footing reinforcing steel was determined to be 305 mm (12 in.) in accordance with ACI 318- 19 section 25.4.2.1. The angle between the strut and tie was then determined, based on the geometry of the model, to be 54˚. The width of the strut W_s at the face of each node as determined using equation given in ACI 318-19 Fig. R23.2.6.b seen below as equation E4.45.

$$W_s = W_t * \cos\theta + l_b \sin\theta \qquad \text{E4.45}$$

The smaller area of the face of each node in which the forces converged was then calculated using equation E4.46 as described in ACI 318-19 R23.4. The effective compressive strength of the compressive elements was also determined using ACI 318-19 23.4.3, written as equation E4.47. β_c and β_s were found to be 1.0 and 0.7 respectively, from ACI318-19 Table 23.4.3.

$$A_{cs} = W_s * 12\text{in.} \qquad \text{E.4.46}$$

$$f_{ce} = 0.85\beta_c\beta_s f'_c \qquad \text{E4.47}$$

Tie strength is derived from the reinforcing bars that are oriented in both directions at the bottom of the footing. The strength of the tie oriented in the 45˚ orientation used for the model was broken down based on the vector components. In the direction of loading, N-S direction, all of the steel participates based on the footing surface in bearing. This was observed in the experimental data where even bars under the column exhibited yield. In addition, four (4) bars were assumed to be acting E-W direction based on the length of footing in bearing in this direction. The strength of the strut was calculated as 1103 N (247.8 kips), and the tie strength was calculated to be 192 N (43.2

kips). The strengths were determined in accordance with ACI 318-19 23.4.1 and 23.7.2 using equations E4.48 and E4.49.

$$F_{ns} = f_{ce} * A_{cs} \quad \text{E4.48}$$

$$F_{nt} = A_{ts} * f_y \quad \text{E4.49}$$

where A_{ts} is taken as the participating area of steel reinforcement, and f_y is the yield strength of the steel reinforcement. The strength of the node was then determined to be 690 N (155 kips), in accordance with ACI318-19 23.9, using equations E4.50 and E4.51. β_n was computed as 0.8 from ACI318-19 Table 23.9.2, and A_{nz} was taken as the area of the smallest face on the upper node as a conservative estimate.

$$F_{nn} = f_{ce} * A_{nz} \quad \text{E4.50}$$

$$f_{ce} = 0.85\beta_c \beta_n f'_c \quad \text{E4.51}$$

The component strengths were then compared to the forces acting in each element. The applied axial force of 667 kN (150 kips) was divided into each of the two (2) column nodes. This means there was 334 kN (75 kips) acting vertically into the top node, equal and opposite to the reaction force in the bottom of the footing. Based on the geometry of the STM, the force acting in the strut was 412 kN (92.7 kips) and the force in the tie was 243 kN (54.5 kips). Based on the results of the analysis it was determined that the limiting components in the STM are the upper node and the tension tie. The STM can then be implemented for larger footing rotations to determine controlling strength.

V. CONCLUSIONS

Many bridges remain in service in the United States and worldwide that constructed without consideration of modern seismic design standards and practices. These bridges are expected to exhibit poor performance under seismic loading. The source of poor performance is often due to inadequate RC substructures, especially the supporting columns which have seismically deficient details. The most common deficiencies include insufficient lap-splice length, lap-splices located within the plastic hinge region, and insufficient confinement of the concrete core due to a lack of transverse reinforcement. These deficiencies contribute to non-ductile behavior during earthquakes that can lead to collapse and significant impairment of the transportation system. The most financially and environmentally sustainable approach for improving the seismic robustness of seismically deficient substructures is to seismically retrofit them. There are many techniques available to retrofit deficient RC columns; however, each technique has inherent drawbacks. This led to the more recent development of a novel retrofit approach that makes use of TiABs. Due to durable and high-strength material properties, ease of installation, and resulting high seismic performance TiABs are a viable option for seismic retrofitting deficient RC bridge columns.

While the flexural capacity and ductility of deficient RC columns retrofitted with TiAB have been established, sufficient data on the impact of soil-structure interaction on the seismic retrofit design decisions are not available. In general, there is limited data on soil-structure interactions including nonlinear soil response for full-scale RC substructures.

This research reports on eight experimental tests of three full-scale square RC column-footing specimens constructed with vintage reinforcing details. The specimen proportions, materials, and details were based on an ODOT bridge inventory review of critical transportation corridors consisting of I-5, US-97, and OR-58. All footings were 1.52 m (5 ft.) square spread footings that measure 0.61 m (2 ft.) in-depth and all columns were 0.61 m square and were 2.44 m (8 ft.) tall. All specimens were subjected to column axial load and then tested under fully reversed-cyclic lateral displacements. The experimental results were described in terms of overall force-displacement response, components of overall force-displacement, P-Delta effects, strain distribution, and the effects of SSI.

Based on the experimental findings, an analytical model was developed to capture the effects of the soil simulant used under and at the vertical faces of the footing. Nonlinear contact springs were developed with the elastic stiffness based on the effective bulk properties of the measured experimental response during application of the axial load and the nonlinear stress-strain results from previous uniaxial testing. The model was used to inform on the observed behavior in the soil simulant and help further develop a design model for the footing using STM.

7.1 Conclusions

The following conclusions are based on the experimental results and analytical findings:

1. Installation of a second spiral only requires a single person and is not more difficult to place than a single spiral.
2. Axial soil simulant stiffness was greatly dependent on strain rate. During lateral loading, the soil simulant is subjected to varying strain rates over the surface of contact with the footing.
3. The vintage columns retrofitted before failure did not exhibit notable damage when lateral displacement was applied to very large drift levels for the given conditions studied here. Instead, rocking of the foundation occurred with large plastic deformations in the soil simulant that limited forces in the column and footing.
4. Embedment provided approximately 1/3 of the lateral capacity during a rocking footing condition. The contributions from deeper embedment and stiffer/stronger soils would be expected to further increase this effect. If the soil strength is sufficient, it can lead to higher column demands which could lead to failure of unretrofitted columns.
5. Bearing capacity was sufficiently large to counter P-Delta effects during rocking but should not be relied on in the design of bridge substructure.
6. Reduced axial load on a column specimen increased the tensile demand in the flexural steel of the column resulting in more flexural damage along the lap-splice length. Even with the

increased demands, the soil simulant enabled foundation rocking which limited the overall demand and the column did not fail even at very large drift.

7. Flexural cracking over the lap-splice length was observed at large drifts during rocking, but the lap splices did not fail when the soil simulant was used at the faces of the footing.
8. When stiffer soil simulant was placed at the faces of the footing (steel soil springs), sufficient resistance was produced by the foundation to increase the demand in the column and eventually failure of the unretrofitted vintage column. The specimen eventually exhibited non-ductile behavior due to failure of the lap splices.
9. TiAB ligaments provide an alternative flexural tension load path replace the reinforcing steel after the lap splice fails.
10. If the TiAB ligaments are used without the concrete shell, they can buckle elastically when put into flexural tension.
11. TiABs begin to act more strongly in tension after the column axial load precompression is overcome. A retrofitted failed column performed as well as a pristine retrofitted column when placed on simulated soil that allowed foundation rocking to occur. .
12. Lack of reinforcement in the top of the footing produced a non-ductile response of the footing during cyclic testing. Significant retrofitting of the footing may be required if a retrofit approach seeks to prevent foundation rocking.
13. The soil simulant used in this study exhibited viscoelastic material properties and provided properties that allowed reasonable laboratory simulation of column-footing-soil response including settlement, plastic soil deformations due to rocking, stiffening of the soil, and rocking footing behavior.
14. Soil recovery was observed to be larger than the initially imposed settlement caused by the axial load. Upon releasing the axial load after plastically deforming the soil simulant, the footing is engaged with a smaller area.
15. A model was developed that could capture the footing pressures acting on the bottom and face of the footing that reasonably predicted the experimentally observed overall response.
16. A 3D strut-and-tie model can capture the performance of the poorly reinforced footing and explains the observed cracking in the footing.

17. The findings of this study demonstrate that interactions between the column-footing-soil should be properly accounted for to ensure the desired design outcome when considering and implementing seismic retrofit strategies on bridge substructures.

7.2 Future Research

Further work on the modes of failure and performance of the system should be undertaken. Further advancement of the research could include the following:

1. Confirm the ductility gained from the addition of a second spiral over the plastic hinge length.
2. Evaluate the flexural capacity and ductility of the column after failure.
3. Perform uniaxial tests on the soil simulant to evaluate the effect of strain rate, and better characterize the viscoelastic properties of the soil simulant.
4. Conduct full-scale in-situ testing of vintage column-footing specimens in both soft and stiff soil conditions
5. Evaluation of the dynamic response of the soil under column footings by conducting snap-back testing through seasonal changes
6. Perform full-scale tests on columns with TiAB retrofits in-situ
7. Consider full-scale studies on the dynamic response of TiAB retrofitted columns during a shake table experiment.

REFERENCES

AASHTO. (2017). *AASHTO LRFD Bridge Design Specifications* (8th ed.). American Association of State Highway and Transportation Officials

ACI Committee 318. (2014). *Building code requirements for structural concrete (ACI 318-14): an ACI standard : commentary on building code requirements for structural concrete (ACI 318R-14), an ACI report*. Farmington Hills, MI: American Concrete Institute.

ACI Committee 440. (2017). *ACI 440.2R-17: Guide for the Design and Construction of Externally Bonded FRP Systems for Strengthening Concrete Structures*. *ACI 440.2R-17*. Detroit, MI.

Allmond, J. D. (2014). Shallow Rocking Foundations in Liquefiable and Saturated Soil Conditions. PhD Dissertation, University of California, Davis.

Allmond, J., Kutter, B. L., Bray, J. and Hayden, C., (2015). New database for foundation and ground performance in liquefaction experiments. *Earthquake Spectra*, *31(4),* pp.2485-2509.

Anastasopoulos, I., Gazetas, G., Loli, M., Apostolou, M., Gerolymos, N. (2010). "Soil Failure Can Be Used for Seismic Protection of Structures." *Bulletin of Earthquake Engineering, 8,* 309-326

Anastasopoulos, I., Gelagoti, F., Kourkoulis, R., and Gazetas, G. (2011) "Simplified Constitutive Model for Simulation of Cyclic Response of Shallow Foundations: Validation against Laboratory Tests" *Journal of Geotechnical and Geoenvironmental Engineering ASCE 137(12),* 1154–1168.

Anastasopoulos, I., Kourkoulis, R., Gelagoti, F. and Papadopoulos, E. (2012). Rocking Response of SDOF Systems on Shallow Improved Sand: An Experimental Study. *Soil Dynamics and Earthquake Engineering, 40,* pp.15-33.

Andrawes, B., Shin, M. and Wierschem, N., (2010). Active Confinement of Reinforced Concrete Bridge Columns using Shape Memory Alloys. *Journal of Bridge Engineering, 15(1),* pp.81-89.

Apostolou, M., Gazetas, G., and Garini, E. (2007). Seismic Response of Slender Rigid Structures with Foundation Uplifting," *Soil Dynamics and Earthquake Engineering 27(7),* 642–654.

Barker, L. (2014). Flexural Anchorage Performance and Strengthening on Negative Moment Regions Using Near-Surface Mounted Retrofitting in Reinforced Concrete Bridge Girders (Master's thesis). Oregon State University, Corvallis, OR.

Beck, J. and Skinner, R. I. (1974.) The Seismic Response of a Reinforced Concrete Bridge Pier Designed to Step. *Earthquake Engineering and Structural Dynamics 2(4),* 637–655.

Breña, S., and Schlick, B. (2007). Hysteretic Behavior of Bridge Columns with FRP-Jacketed Lap Splices Designed for Moderate Ductility Enhancement. *Journal of Composites for Construction*, 11(December), 565–574

Bournas, D. A., T. C. Triantafillou, K. Zygouris, and F. Stavropoulos. (2009). "Textile-Reinforced Mortar versus FRP Jacketing in Seismic Retrofitting of RC Columns with Continuous or Lap-Spliced Deformed Bars." *Journal of Composites for Construction* 13, no. 5: 360–71.

Cairns, J., & Arthur, P. D. (1979). Strength of Lapped Splices in Reinforced Concrete Columns. *ACI Journal Proceedings*, *76*(2). https://doi.org/10.14359/6947

Campbell, K. W. (1977). The Use of Seismotectonics in the Bayesian Estimation of Seismic Risk, Report UCLA-ENG-7744, School of Engineering and Applied Science, University of California, Los Angeles, CA

Chai, Y. H., Priestley, M. J. N., and Seible, F. (1994). Analytical Model for Steel-Jacketed RC Circular Bridge Columns. *ASCE Journal of Structural Engineering, 120(8),* 2358–2376

Chai, Y. H., Priestley, M. J. N., and Seible, F. (2008). Seismic Retrofit of Rectangular Bridge Columns by Steel Jacketing. In Third Bridge Engineering Conference: Papers Presented at the Third Bridge Engineering Conference, March 10-13, 1991, Denver, Colorado (pp. 95–103)

Chaudhary, M.T.A., Abé, M. and Fujino, Y. (2001). Performance Evaluation of Base-isolated Yama-agé Bridge with High Damping Rubber Bearings using Recorded Seismic Data. *Engineering Structures, 23(8),* pp.902-910.

Chen, Y.H., Liao, W.H., Lee, C.L. and Wang, Y. P. (2006). Seismic Isolation of Viaduct Piers by Means of a Rocking Mechanism. *Earthquake Engineering and Structural Dynamics, 35(6),* pp.713-736.

Cheng, C. T. and Mander, J. B. (1997). Seismic Design of Bridge Columns based on Control and Repairability of Damage.

Ciampoli, M. and Pinto, P. E., (1995). Effects of Soil-Structure Interaction on Inelastic Seismic Response of Bridge Piers. *Journal of structural engineering, 121(5),* pp.806-814.

Daudey, X., & Filiatrault, A. (2000). Seismic Evaluation and Retrofit with Steel Jackets of Reinforced Concrete Bridge Piers Detailed with Lap-Splices. *Canadian Journal of Civil Engineering*, *27*(1), 1–16.

Deng, L., Kutter, B. L., and Kunnath, S. K. (2012). Centrifuge Modeling of Bridge Systems Designed for Rocking Foundations. *Journal of Geotechnical and Geo-environmental Engineering, ASCE*, *138(3)*: 335–344.

ElGawady, M., Endeshaw, M., McLean, D., & Sack, R. (2010). Retrofitting of Rectangular Columns with Deficient Lap Splices. *Journal of Composites for Construction*, *14*(1), 22–35. https://doi.org/10.1061/(asce)cc.1943-5614.0000047

Elghazouli, A. Y. (2009). *Seismic Design of Buildings to Eurocode 8,* Spon Press

Faccioli, E., Vanini, M. and Paolucci, R. (1999). TRISEE: 3D Site Effects and Soil-Foundation Interaction in Earthquake and Vibration Risk Evaluation. European commission. DirectorateGeneral 12. Science, Research and Development.

Fraino, M., Ventura, C. E., Liam Finn, W.D. and Taiebat, M. (2012). September. Seismic SoilStructure Interaction Effects in Instrumented Bridges. In Proceedings of the 15th World Conference on Earthquake Engineering (pp. 1-10). Portuguese Association for Earthquake Engineering.

Gajan, S., Kutter, B. L., Phalen, J. D., Hutchinson, T. C., Martin, G. R. (2005). "Centrifuge Modeling of Load-Deformation Behavior of Rocking Shallow Foundations." *Soil Dynamics and Earthquake Engineering, 25,* 773–783.

Gajan, S. and Kutter, B. (2008). Capacity, Settlement, and Energy Dissipation of Shallow Footings Subjected to Rocking," *Journal of Geotechnical and Geoenvironmental Engineering ASCE 135(3),*
407–420.

Galal, K., A. Arafa, and A. Ghobarah. (2005). "Retrofit of RC Square Short Columns." *Engineering Structures* 27, no. 5 (April): 801–13.

Gamble, W. L., Hawkins, N. M., and Kaspar, I. I. (1996). Seismic Retrofitting Experience and Experiments in Illinois. Proc. 5th National Workshop on Bridge Research in Progress, National Center for Earthquake Engineering Research (NCEER), State Univ. of New York at Buffalo, Buffalo, N.Y., 245–250.

Gazetas, G. (2019). Benefits of Unconventional Seismic Foundation Design. BGS 59th Rankine Lecturer, https://www.youtube.com/watch?reload=9&v=pOXzqjTo34o&feature=youtu.be.

Gazetas, G., Apostolou, M. and Anastasopoulos, J. (2003). Seismic Uplifting of Foundations on Soft Soils, with Examples from Adapazari (Izmit 1999 Earthquake). Proc. of BGA International Conference on Foundations: Innovations, observations, design and practice, Dundee. 37-49.

Gazetas, G., and Mylonakis, G. (2001). "Soil–Structure Interaction Effects on Elastic and Inelastic Structures." In Fourth International Conference on Recent Advances in Geotechnical Earthquake Engineering and Soil Dynamics. Symposium in Honor of Professor WD Liam Finn, 1–13. Paper No. SOAP 2, San Diego, California, University of Missouri-Rolla.

Gazetas, George, and Kenneth H. Stokoe. 1991. "Free Vibration of Embedded Foundations: Theory versus Experiment." *Journal of Geotechnical Engineering* 117 (9): 1382–1401. https://doi.org/10.1061/(ASCE)0733-9410(1991)117:9(1382).

Girard, C., & Bastien, J. (2002). Finite-Element Bond-Slip Model for Concrete Columns under Cyclic Loads. *ASCE Journal of Structural Engineering*, *128*(12), 1502–1510. https://doi.org/10.1061/(ASCE)0733-9445(2002)128:12(1502)

Goksu, C., Yilmaz, H., Chowdhury, S. R., Orakcal, K., & Ilki, A. (2014). The Effect of Lap Splice Length on the Cyclic Lateral load Behavior of RC Members with Low-Strength Concrete and Plain Bars. *Advances in Structural Engineering*, *17*(5), 639–658. https://doi.org/10.1260/1369-4332.17.5.639

Gupta, B. N. 1972. "Effect of Foundation Embedment on the Dynamic Behaviour of the Foundation-Soil System." *Géotechnique* 22 (1): 129–37. https://doi.org/10.1680/geot.1972.22.1.129.

Hakhamaneshi, M. (2014). Rocking Foundations for Building Systems-Effect of Footing Shape, Soil Environment, Embedment and Normalized Moment-to-Shear Ratio. PhD Dissertation, University of California, Davis, CA, USA.

Harajli, M. H. (2008). Seismic Behavior of RC Columns with Bond-Critical Regions: Criteria for Bond Strengthening Using External FRP Jackets. *Journal of Composites for Construction, 12(1)*, 69–79.

Harajli, M. H. (2009). Bond Stress-Slip Model for Steel Bars in Unconfined or Steel, FRC, or FRP Confined Concrete under Cyclic Loading. *ASCE Journal of Structural Engineering*, *135*(5), 509–518.

Haroun, Medhat A., and Hussein M. Elsanadedy. (2005). "Fiber-Reinforced Plastic Jackets for Ductility Enhancement of Reinforced Concrete Bridge Columns with Poor Lap-Splice Detailing." *Journal of Bridge Engineering 10,* no. 6 (November): 749–57.

Harries, K. A. ., Ricles, J. R. ., Pessiki, S., & Sause, R. (2006). Seismic Retrofit of Lap Splices in Non-ductile Columns Using CFRP Jackets. *ACI Structural Journal*, *103*(6), 874–884. https://doi.org/10.14359/18242

Higgins, C. C., Knudtsen, J., Amneus, D., & Barker, L. (2017). Shear and Flexural Strengthening of Reinforced Concrete Beams with Titanium Alloy Bars. *Proceedings of the 2nd World Congress on Civil, Structural, and Environmental Engineering (CSEE'17)*, 1–8. https://doi.org/10.11159/icsenm17.141

Housner, G. W. (1956). Limit Design of Structures to Resist Earthquakes. Proc. of World Conference on Earthquake Engineering, Earthquake Engineering, Research Institute, University of California, Berkeley.

Housner, G. W. (1963) The Behavior of Inverted Pendulum Structures during Earthquakes. *Bulletin of the Seismological Society of America 53(2)*, 404–417.

Huckelbridge, A. A. and Ferencz, R. M. (1981). Overturning Effects on Stiffened Building Frames," *Earthquake Engineering and Structural Dynamics 9(1)*, 69–83.

Hung, H., Liu, K., Ho, T., and Chang, K. (2011). An Experimental Study on the Rocking Response of Bridge Piers with Spread Footing Foundations," *Earthquake Engineering and Structural Dynamics*, 40(7), 749–769.

Inukai, Tomoyuki, Tamio Imazawa, Kaoni Kusakabe, and M. Yamaoto. "Dynamic behavior of embedded structure on hard rock site." *Proceedings*, pp. 1695-1700. 1992.

Kawashima, K. and Nagai, T. (2006). Effectiveness of rocking seismic isolation on bridges. In 4th International Conference on Earthquake Engineering, National Center for Research on Earthquake Engineering of Taiwan (pp. 12-13).

Kent, D. C., & Park, R. (1971). Flexural Members with Confined Concrete. *ASCE Journal of Structural Division, 97(7)*, 1969–1990.

Krish, Z.F., Kowalsky, M.J., Nau, J.M. and Seracino, R., (2018). Repair of Reinforced Concrete Bridge Columns via Plastic Hinge Relocation, Volume 1: Repair Using Conventional Materials (No. Report No. 4000 (142)).

Knudtsen, J. (2016). Shear Strengthening Reinforced Concrete Bridge Girders Using Near Surface Mounted Titanium Alloy Bars (Master's thesis). Oregon State University, Corvallis, OR

Kutter, B. L., Hutchinson, T. C, Aschheim, M., Kunnath, S., Liu, W., and Hakhamaneshi, M. (2011). Design of Soil and Structure Compatible Yielding to Improve System Performance. 2011 NSF Engineering Research and Innovation Conference, Atlanta, GA, Jan 4-7.

Kutter, B.L., Moore, M., Hakhamaneshi, M. and Champion, C. (2016). Rationale for Shallow Foundation Yocking Provisions in ASCE 41-13. *Earthquake Spectra, 32(2)*, pp.1097-1119.

Lin, Albert N., and Paul C. Jennings. 1984. "Effect of Embedment on Foundation - Soil IMPEDANCES." *Journal of Engineering Mechanics* 110 (7): 1060–75. https://doi.org/10.1061/(ASCE)0733-9399(1984)110:7(1060).

Lukose, K., Gergely, P., & White, R. N. (1982). Behavior of Reinforced Concrete Lapped Splices for Inelastic Cyclic Loading. *Journal of American Concrete Institute*, *79*(5), 355–365.

Lynn, A. C., Moehle, J. P., Mahin, S. A., and Holmes, W. T. (1996). Seismic Evaluation of Existing Reinforced Concrete Building Columns. *Earthquake Spectra, 12(4),* 715–739.

Lysmer, J., & Kuhlemeyer, R. L. (1969). Finite Dynamic Model for Infinite Media. *Journal of the Engineering Mechanics Division*, *95*(4), 859–877. https://doi.org/10.1061/JMCEA3.0001144

Mander, J. B., Priestley, M. J. N., & Park, R. (1988). Observed Stress-Strain Behavior of Confined Concrete. *ASCE Journal of Structural Engineering*, *114*(8), 1827–1849.

Mander, J. B., Priestley, M. J. N., & Park, R. (1988). Theoretical Stress-Strain Model for Confined Concrete. *ASCE Journal of Structural Engineering*, *114*(8), 1804–1826.

McLean, D. I. and Marsh, M. L. (1999). "Seismic Retrofitting of Bridge Foundations". *Structural Journal*, 96(2), pp.174-182.

Mergos, P. E. and Kawashima, K. (2005). Rocking Isolation of a Typical Bridge Pier on Spread Foundation. Journal of Earthquake Engineering, 9(sup2), pp.395-414.

Melek, M., & Wallace, J. W. (2004). Performance of Columns with Short Lap Splices. In *13th World Conference on Earthquake Engineering Vancouver, B.C., Canada August 1-6, 2004 Paper No. 1034* (pp. 1–15). https://doi.org/10.1002/eqe.4290180114

Mirmiran, A., Shahway, M., Samaan, M., Echary, H. El, Mastrapa, J. C., & Pico, O. (1998). Effect of Column Parameters on FRP-Confined Concrete. *Journal of Composites for Construction*, *2*(November), 175–185.

Mylonakis, G. and Gazetas, G. (2000). Seismic Soil-Structure Interaction: Beneficial or Detrimental?. *Journal of Earthquake Engineering, 4(3)*, pp.277-301.

National Earthquake Hazards Reduction Program (NEHRP) (2004). Recommended Seismic Design Criteria for New Steel Moment-frame Buildings, FEMA-273, Federal Emergency Management Agency, Washington, DC, USA.

Negro, P., Paolucci, R., Pedretti, S., and Faccioli, E. (2000). Large-Scale Soil–Structure Interaction Experiments on Sand under Cyclic Load. Proc. of the 12th World Conference on Earthquake Engineering, Auckland, New Zealand.

Novak, Milos. 1970. "Prediction of Footing Vibrations." *Journal of the Soil Mechanics and Foundations Division* 96 (3): 837–61. https://doi.org/10.1061/JSFEAQ.0001422.

Novak, Milos. 1974. "Effect of Soil on Structural Response to Wind and Earthquake." *Earthquake Engineering & Structural Dynamics* 3 (1): 79–96. https://doi.org/10.1002/eqe.4290030107.

Novak, Milos, and Youpele O. Beredugo. 1972. "Vertical Vibration of Embedded Footings." *Journal of the Soil Mechanics and Foundations Division* 98 (12): 1291–1310. https://doi.org/10.1061/JSFEAQ.0001815.

Ozcan, O., Binici, B., & Ozcebe, G. (2008). Improving Seismic Performance of Deficient Reinforced Concrete Columns Using Carbon Fiber-Reinforced Polymers. *Engineering Structures*, *30(6),* 1632–1646. https://doi.org/10.1016/j.engstruct.2007.10.013

Ozcebe, G., & Saatcioglu, M. (1987). Confinement of Concrete Columns for Seismic Loading. *ACI Structural Journal*. https://doi.org/10.14359/1660

Paulay, T. (1982). Lapped Splices in Earthquake-Resisting Columns. *Journal of American Concrete Institute, 79(6),* 458–469.

Pecker, A. (2003). "Aseismic foundation design process, lessons learned from two major projects: the Vasco de Gama and the Rion Antirion bridges," in ACI Int. Conf. Seismic Bridge Design and Retrofit (La Jolla: University of California at San Diego).

Priestley, M. J. N., Verma, R., and Xiao, Y. (1995). Seismic Shear Strength of Reinforced Concrete Columns. *ASCE Journal of Structural Engineering*, 120(8), 2310–2329

Priestley, M. J. N., Seible, F., and Calvi, G. M. (1996). Seismic Design and Retrofit of Bridges, John Wiley and Sons, New York, NY.

Razvi, S. W. N., & Shaikh, M. G. (2018). Effect of Confinement on Behavior of Short Concrete Column.*Procedia Manufacturing*, *20(01),* 563–570. https://doi.org/10.1016/j.promfg.2018.02.084

Rosebrook K. R. (2001). Moment Loading on Shallow Foundations: Centrifuge Test Data Archives. M.Sc. Thesis. University of California at Davis, School of Engineering.

Saatcioglu, M., & Ozcebe, G. (1989). Response of Reinforced Concrete Columns to Simulated Seismic Loading. *ACI Structural Journal*, *86(1),* 3–12.

Saatcioglu, M. and Yalcin, C., (2003). External Prestressing Concrete Columns for Improved Seismic Shear Resistance. *Journal of Structural Engineering*, *129(8),* pp.1057-1070.

Saiidi, M.Saiid, David Sanders, and Suresh Acharya. (2001). "Seismic Retrofit of Spread Footings Supporting Bridge Columns with Short Dowels." *Construction and Building Materials 15, no. 4* (June): 177–85.

Sakellaraki, D.I.M.I.T.R.A. and Kawashima, K. (2006). Effectiveness of Seismic Rocking Isolation of Bridges based on Shake Table Test. Proc. First European Conf. on Earthquake Engineering and Seismology.

Santamarina, J. Carlos. 2001. "Soil Behavior at the Microscale: Particle Forces." *In Soil Behavior and Soft Ground Construction*, 25–56. Cambridge, Massachusetts, United States: American Society of Civil Engineers. https://doi.org/10.1061/40659(2003)2.

Santamarina, J. C., & Cho, G. C. (2004). "Soil behaviour: The role of particle shape". Proc. Skempton Conference, London.

Sharma, K. (2019). Field Investigation and Performance-Based Seismic Design of Rocking Shallow Foundations in Cohesive Soil. PhD Dissertation, University of Alberta, Edmonton, Alberta, CA.

Sheikh, S. A., & Uzumeri, S. M. (1982). Analytical Model for Concrete Confinement in Tied Columns. *ASCE Journal of Structural Division*, *108(12)*, 2703–2722.

Shrestha, S. (2019). Seismic Retrofit of Square Reinforced Concrete Bridge Columns using Titanium Alloy Bars. PhD Dissertation, Oregon State University, Corvallis, OR.

Storie, L., Pender, M., Clifton, G., and Wotherspoon, L. (2014). Soil Foundation-Structure Interaction for Buildings on Shallow Foundations in the Christchurch Earthquake. Proc. of 10th NCEE, Anchorage, Alaska.

Takahashi, Y., Muto, I., Hitoshi, S., Tadokoro, Y., & Tagomori, N. (1994). Application of Titanium to Construction and Civil Engineering. https://doi.org/UDC669.295.7:624/627

Valluvan, R., Kreger, M. E., & Jirsa, J. O. (1993). Strengthening of Column Splices for Seismic Retrofit on Non-ductile Reinforced Concrete Frames. *ACI Structural Journal*, *90(4)*, 432–433.

Wang, D., Wang, Z., Yu, T., & Li, H. (2018). Seismic Performance of CFRP-Retrofitted LargeScale Rectangular RC Columns Under Lateral Loading in Different Directions. *Composite Structures*, *192*(3), 475–488. https://doi.org/10.1016/j.compstruct.2018.03.029

Watson, S., Zahn, F. A., & Park, R. (1994). Confining Reinforcement for Concrete Columns. *ASCE Journal of Structural Engineering*, *120(6)*, 1798–1824.

Xiao, Y., and Ma, R. (1997). Seismic Retrofit of RC Circular Columns Using Prefabricated Composite Jacketing. *ASCE Journal of Structural Engineering*, *123(10)*, 1357–1364.

Xiao, Y., Priestley, M.N. and Seible, F. (1996). Seismic Assessment and Retrofit of Bridge Column Footings. *Structural Journal*, *93(1)*, pp.79-94.

Zahn, F. A., Park, R., & Priestley, M. J. N. (1989). Strength and Ductility of Square Reinforced Concrete Column Sections Subjected to Biaxial Bending. *ACI Structural Journal*.

Zong-Cai, D., Daud, J.R. and Hui, L. (2014). Seismic Behavior of Short Concrete Columns with Prestressing Steel Wires. *Advances in Materials Science and Engineering*

APPENDICIES

APPENDIX A – MATERIAL PROPERTIES

A.1 Concrete

The concrete mix design for the columns, footings, and shell were all the same. The design contained 4.75 mm (3/8 in.) aggregate, slag, no air entrainment, and a 28-day design compressive strength of 28 MPa (4 ksi). Table A.1.1 contains the 28 compressive tests of

102 x 203 mm (4 x 8 in.) cylinders in accordance with ASTM C39M/ C39M-05 and ASTM C617-98. After the shell was cast for specimen 3 it was tested a week after casting and before the 28 day period, and the results can be found in Table A.1.2 and Table A.1.3 with the day of test results for the other specimens.

Table A.1.1 - 28 Day Concrete Compressive Strength.

Specimen ID	Specimen Component	Compressive Strength, MPa (psi)	Standard Deviation	Coefficient of Variation
S.1	Footing	27.07 (3926)	238	6
S.1	Column	27.06 (3924)	181	4.6
S.1	Shell	35.07 (5086)	160	3.1
S.2	Footing	27.07 (3926)	238	6
S.2	Column	27.06 (3924)	181	4.6
S.2	Shell	35.07 (5086)	160	3.1
S.3	Footing	38.90 (5647)	161	2.9
S.3	Column	30.86 (4476)	141	3.1

Day of test compressive were conducted according to ASTM C39M/ C39M-05 and ASTM C617-98 and the results can be found in Table A.1.2. Tests were not conducted for specimen Tests 2, 5, and 6. While failure occurred in specimen Test 5 limited test cylinders prevented day of test compressive and tensile tests from being completed. No damage to the concrete was observed during test 2 and 6; therefore, no compressive or tensile were conducted on the day of specimen testing. Furthermore, specimen Tests 3, and 4 were conducted on the same day. Due to limited cylinder availability tensile tests were conserved for column failure and were only conducted for Test 8, and because only the footing exhibited damage it was the only component tested. Tensile tests were conducted on 152 x 305 mm (6 x 12 in.) cylinders in accordance with ASTM C496/ C496M-04 and results can be found in Table A.1.3.

Table A.1.2 - Day of Test Concrete Compressive Strength.

Specimen ID	Test ID	Test Date	S.C.	Compressive Strength, MPa (psi)	Standard Deviation	Coefficient of Variation
S.1	1	11/17/2021	Footing	39.70 (5757)	77.9	1.4
S.1	1	11/17/2021	Column	46.24 (6707)	216	3.2
S.1	1	11/17/2021	Shell	39.0 (5655)	132	2.3
S.3	3,4	12/17/2021	Footing	47.39 (6873)	179	2.6
S.3	3,4	12/17/2021	Column	36.59 (5307)	277	5.2
S.3	7	4/20/2022	Shell	24.35 (3532)	109	3.1
S.2	8	6/1/2022	Footing	39.84 (5778)	124	2.1

Table A.1.3 - Day of Test Concrete Tensile Strength.

Specimen ID	Test ID	Test Date	S.C.	Compressive Strength, MPa (psi)	Standard Deviation	Coefficient of Variation
S.2	8	6/1/2022	Footing	2.68 (389)	66.1	17

A.2 Reinforcing Steel

A local rebar fabricator fabricated all of the reinforcing steel. Shrestha (2019) tested the #10M (#3) Grade 40 column ties using a 490 kN (110 kip) universal testing machine with a 51 mm (2.1 in.) gauge length extensometer to measure strain. For the column ties the yield point in the stress-strain profile was taken as the 0.2% offset, and the results from Shrestha (2019) can be found in Table A.2.1.

Table A.2.1 - Tensile Test Results of #10M (#3) Steel Bars (Shrestha 2019).

Yield Strength, MPa (ksi)	**Yield Strain (με)**	**Tensile Strength, MPa**	**Ultimate Elongation (%)**
386 (56)	1,923	583 (86)	27.78

Tensile tests were conducted on the remaining steel reinforcement by cutting 457 mm (18 in.) coupons from spare bars and delivered to a nearby testing facility to validate the mill certifications of the manufacturer. The testing facility used the 0.2% offset method for the yield strength and tested bars in accordance with ASTM A370-20. The results of the tests can be viewed in Table A.2.2. All remaining bars were Grade 60.

Table A.2.2 - Tensile Test Results of Reinforcing Steel.

Bar Size	**Bar Type**	**Tensile Strength, MPa (ksi)**	**Yield Strength, MPa (ksi)**	**Elongation in 4D (%)**	**Reduction of Area (%)**	**Original Gauge Diameter, mm**
#13M, #4	Tie	738 (107)	552 (80)	26	66	6.4 (0.252)
#13M, #4	Footing	614 (89)	372 (54)	28	56	6.4 (0.252)
#32M, #10	Column/ Starter	758 (110)	490 (71)	21	49	12.8 (0.503)

A.3 Titanium Alloy Bars

Because the Titanium Alloy Bar (TiAB) spirals remained elastic during the tests conducted by Shrestha (2019), They were able to be reused for the three specimens. Shrestha (2019) used a sample from the stock of unused TiAB was tested to validate the mill certified properties. The results of the test indicated that the mill certified properties were accurate; therefore, the mill certified properties were used as the actual properties for the #10M (#3) TiAB ligaments and the #16M (#5) TiAB spirals. The tensile properties of the TiAB spirals used be Shrestha (2019) can be found in Table A.3.1. The manufacturer tested the mechanical properties of the TiAB ligaments used in accordance with ASTM E8/EN and the results can be found in Table A.3.2.

Table A.3.1 - Tensile Test Results of TiABs.

TiAB Bar Type	Tensile Strength, MPa (ksi)	Yield Strength, MPa (ksi)	Elongation 4D (%)	Reduction of Area (%)
Ligament	1126 (163.3)	1037 (150.4)	21	55
Spiral	1010 (146.5)	920 (133.4)	19	50

A.4 Soil Simulant

Soil was simulated for Tests 1-7 with FOAMULAR® 1000 Extruded Polystyrene (XPS) Rigid Foam Insulation. All of the tests used 4 – 50.8 mm (2 in.) thick layers of foam for the subgrade. For Tests 1, 3, and 4 with foam embedment 3 – 50.8 mm (2 in.) thick layers were used on the North and South face on the footings. The manufacturer reports minimums of 689 kPa (100 psi) compressive strength and 965 kPa (140) psi flexural strength on their website: commercial.owenscorning.com.

Shrestha (2019) completed cyclic compressions tests on 3 cylindrical test samples measuring 96.5 mm (3.8 in.) in diameter and 152 mm (6 in.) in depth. Figures A.4.1, A.4.2., and A.4.3 display the tests results and Table A.4.1 displays a summary of critical information from the tests.

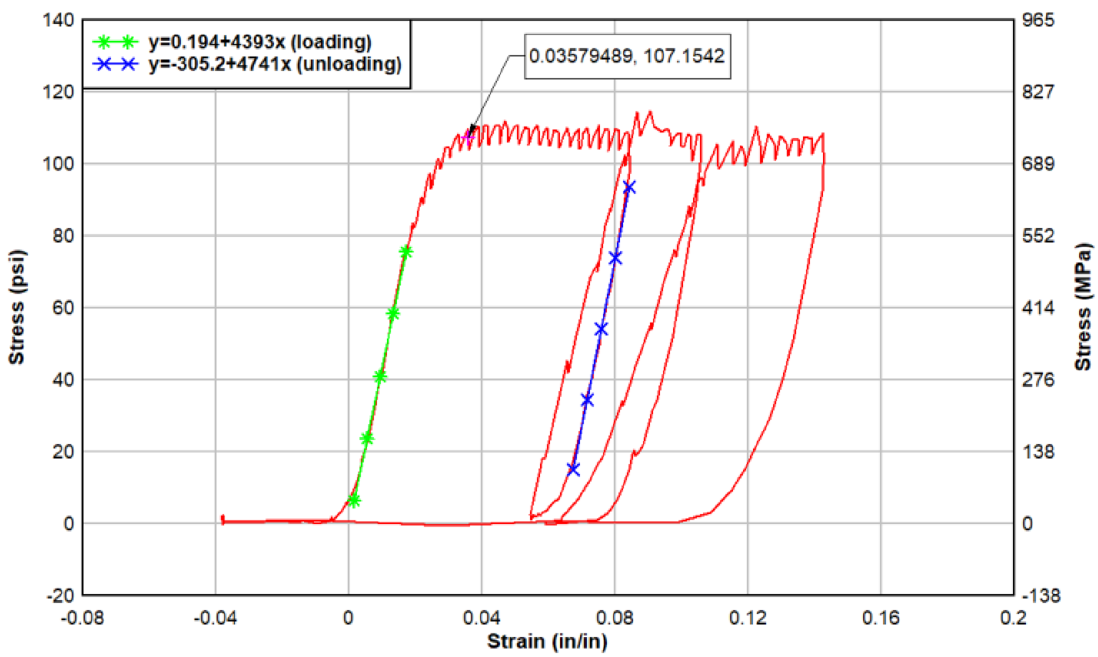

Figure A.4.1 – Shrestha (2019) Compression Test Result, Foam Cylinder 1.

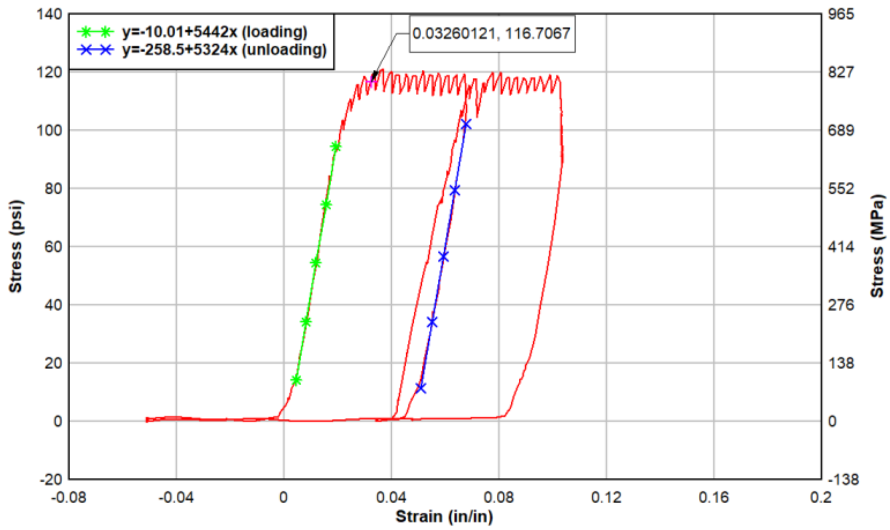

Figure A.4.2 – Shrestha (2019) Compression Test Result, Foam Cylinder 2.

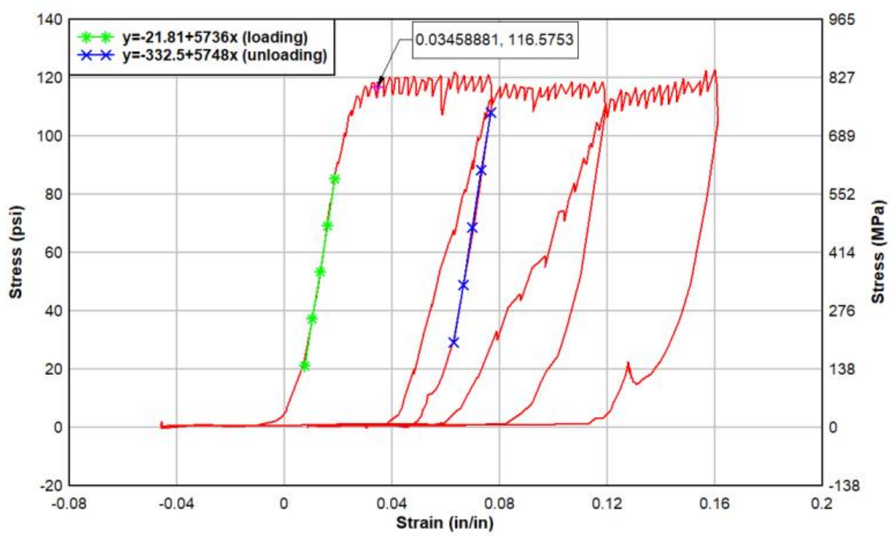

Figure A.4.3 – Shrestha (2019) Compression Test Result, Foam Cylinder 3.

Table A.4.1 - Shrestha (2019) Summary of Foam Compression Test Results.

Foam Cylinder	Surface Area, mm^2 ($in.^2$)	Yield Strength, Mpa (ksi)	Peak Stress, kPa (psi)	Strain (%)
1	7135 (11.06)	30.3 (4.39)	738 (107)	3.58
2	7090 (10.99)	37.5 (5.44)	807 (117)	3.26
3	7155 (11.09)	39.6 (5.74)	793 (115)	3.14

PROPERTY	TEST METHOD[3]	400	600	1000
Thermal Resistance, R-Value (180 days) minimum, $hr{\cdot}ft^2{\cdot}°F/Btu$ (RSI, $°C{\cdot}m^2/W$) @ 75°F (24°C) mean temperature	ASTM C518	5.0 (0.88)	5.0 (0.88)	5.0 (0.88)
@ 40°F (4.4°C) mean temperature		5.4 (0.95)	5.4 (0.95)	5.4 (0.95)
@ 25°F (-3.9°C) mean temperature		5.6 (0.99)	5.6 (0.99)	5.6 (0.99)
Long-Term Thermal Resistance, LTTR-Value,[4] minimum $hr{\cdot}ft^2{\cdot}°F/Btu$ (RSI, $°C{\cdot}m^2/W$) @ 75°F (24°C) mean temperature	CAN/ ULC S770-03	5.0 (0.88)	5.0 (0.88)	5.0 (0.88)
Compressive Strength,[5] minimum psi (kPa)	ASTM D1621	40 (276)	60 (414)	100 (689)
Flexural Strength,[6] minimum psi (kPa)	ASTM C203	90 (621)	120 (828)	150(1035)
Water Absorption,[7] maximum % by volume	ASTM C272	0.3	0.3	0.3
Water Vapor Permeance,[8] maximum perm ($ng/Pa{\cdot}s{\cdot}m^2$)	ASTM E96	1.1 (63)	1.1 (63)	1.1 (63)
Dimensional Stability, maximum % linear change	ASTM D2126	2.0	2.0	2.0
Flame Spread[9, 10]	ASTM E84	10	10	10
Smoke Developed[9, 10]	ASTM E84	175	175	175
Oxygen Index,[9] minimum % by volume	ASTM D2863	24	24	24
Service Temperature, maximum °F (°C)	–	165 (74)	165 (74)	165 (74)
Linear Coefficient of Thermal Expansion, in/in/°F (m/m/°C)	ASTM E228	3.5×10^{-5} (6.3×10^{-5})		

2 Properties shown are representative values for 1-inch-thick material, unless otherwise specified.
3 Modified as required to meet ASTM C578.
4 R means the resistance to heat flow; the higher the value, the greater the insulation power. This insulation must be installed properly to get the marked R-value. Follow the manufacturer's instructions carefully. If a manufacturer's fact sheet is not provided with the material shipment, request this and review it carefully. R-values vary depending on many factors, including the mean temperature at which the test is conducted and the age of the sample at the time of testing. Because rigid foam plastic insulation products are not all aged in accordance with the same standards, it is useful to publish comparison R-value data. The R-value for FOAMULAR® & FOAMULAR® NGX™ XPS insulation is provided from testing at mean temperatures of: -4°C (25°F), 4.4°C (40°F), and 24°C (75°F) and aging techniques of 180-day real-time aged (as mandated by ASTM C578) and accelerated aging "Long-Term Thermal Resistance" (LTTR) per CAN/ULC S770-03. The R-value at 180-day real-time age and 75°F mean temperature is commonly used to compare products and is the value printed on the product.
5 Values at yield or 5% deflection.
6 Properties shown are representative values for 2-inch-thick material, unless otherwise specified. Value at yield or 5%, whichever occurs first.
7 Data ranges from 0.00 to value shown due to the level of precision of the test method.
8 Water vapor permeance decreases as thickness increases.
9 These laboratory tests are not intended to describe the hazards presented by this material under actual fire conditions.
10 Data from Underwriters Laboratories Inc.® classified. See Classification Certificate U-197.

Figure A.4.4 –FOAMULAR® 1000 material properties as reported by manufacturer, Owens Corning (owenscorning.com/en-us/insulation/products/foamular-400 accessed on 7/19/2022).

A.5 Bonding Epoxy

The epoxy used to bond the #10M (#3) TiAB spirals and the #16M (#5) TiAB ligaments was Hilti HIT-RE 500 V3. The following information from the manufacturer's website: hilti.com provides the material specifications used:

- Bond strength per ASTM C882-13A: 10.8 MPa (1.56 ksi) for a 2 day cure time, and 11.7 MPa (1.69 ksi) for a 14 day cure time.
- Tensile strength per 7 day ASTM D638-14: 49.3 MPa (7.15 ksi)
- Nominal bit diameter: 12.7 mm (1/2 in.) for #10M (#3) bar, 19 mm (3/4 in.) for #16M (#5) bar
- Effective minimum embedment: 60 mm (2-3/8 in.) for #10M (#3) bar, and 76 mm (3 in.) for #16M (#5) bar

APPENDIX B – SENSOR NAMING CONVENTIONS AND PLACEMENT

B.1 - Strain Gauge Naming Convention

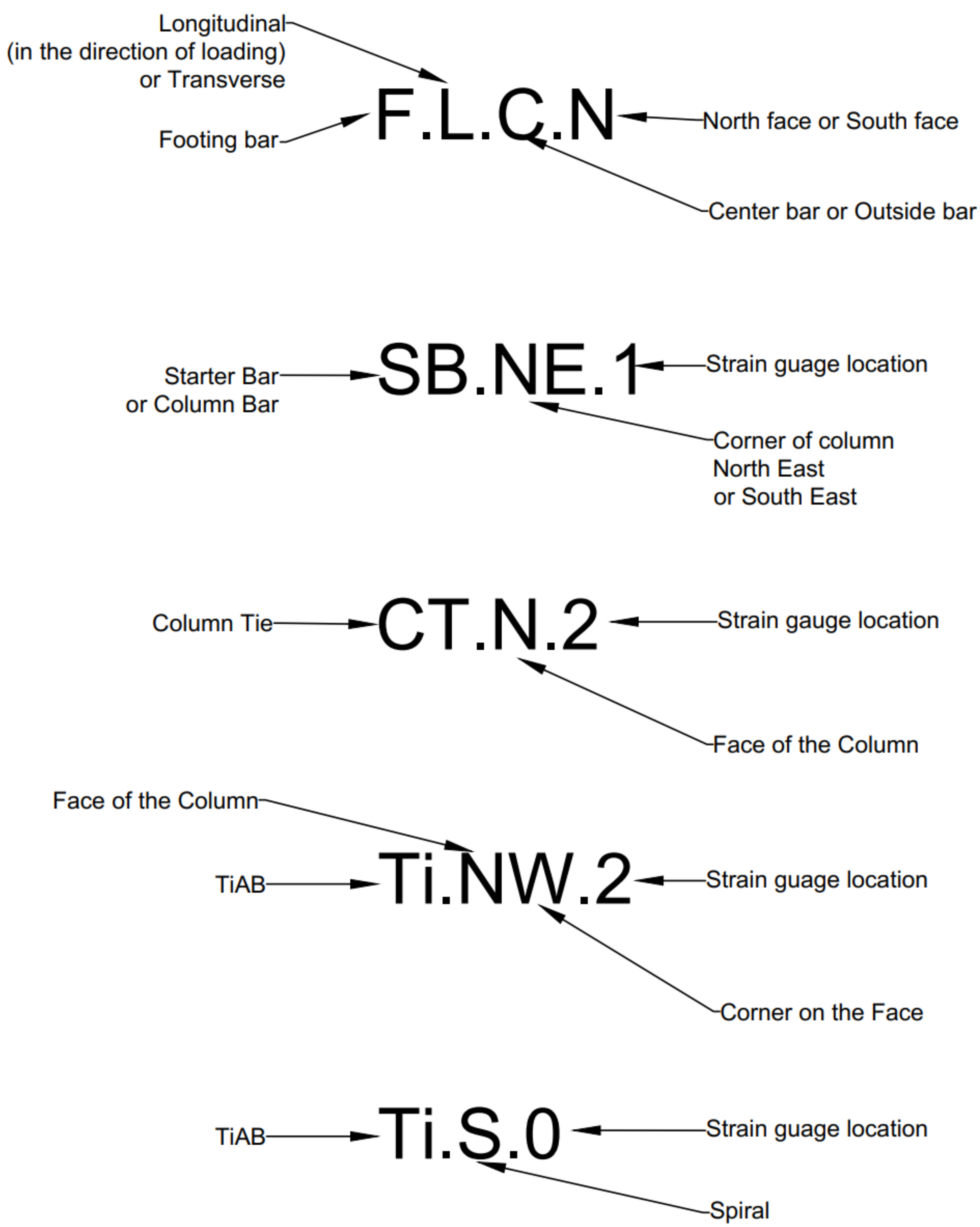

B.2 - Strain Gauge Sensor Locations

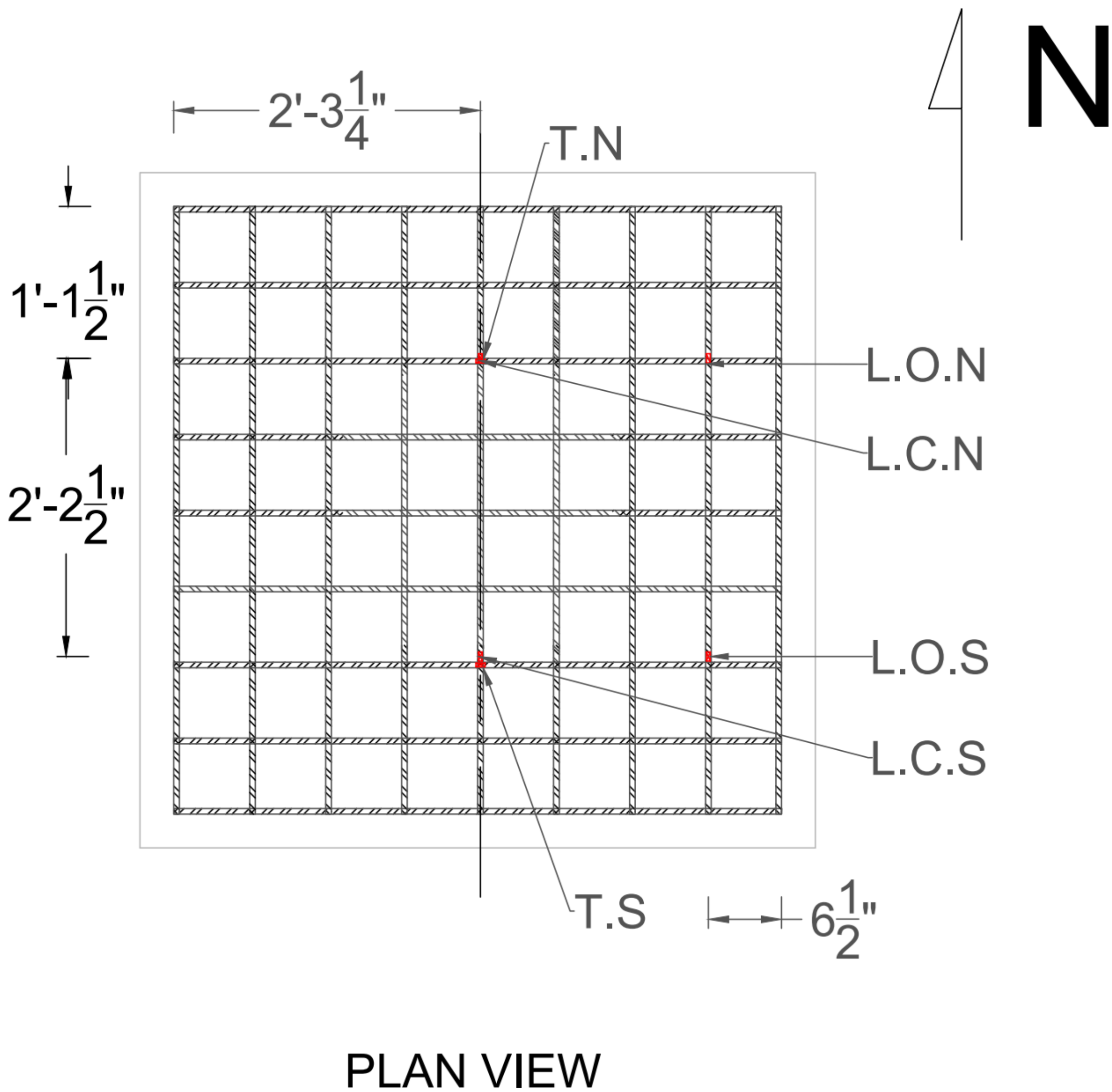

Figure B.2.1 – Location of footing strain gauges.

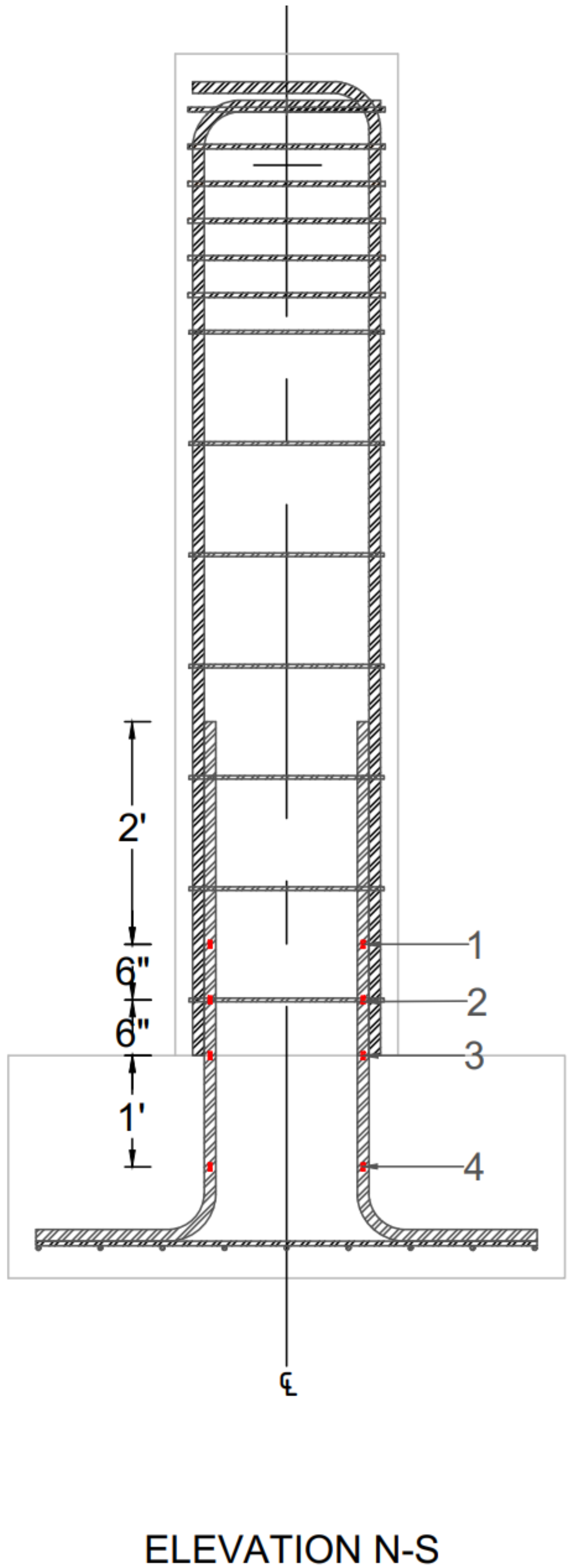

Figure B.2.2 – Starter bar strain gauge locations.

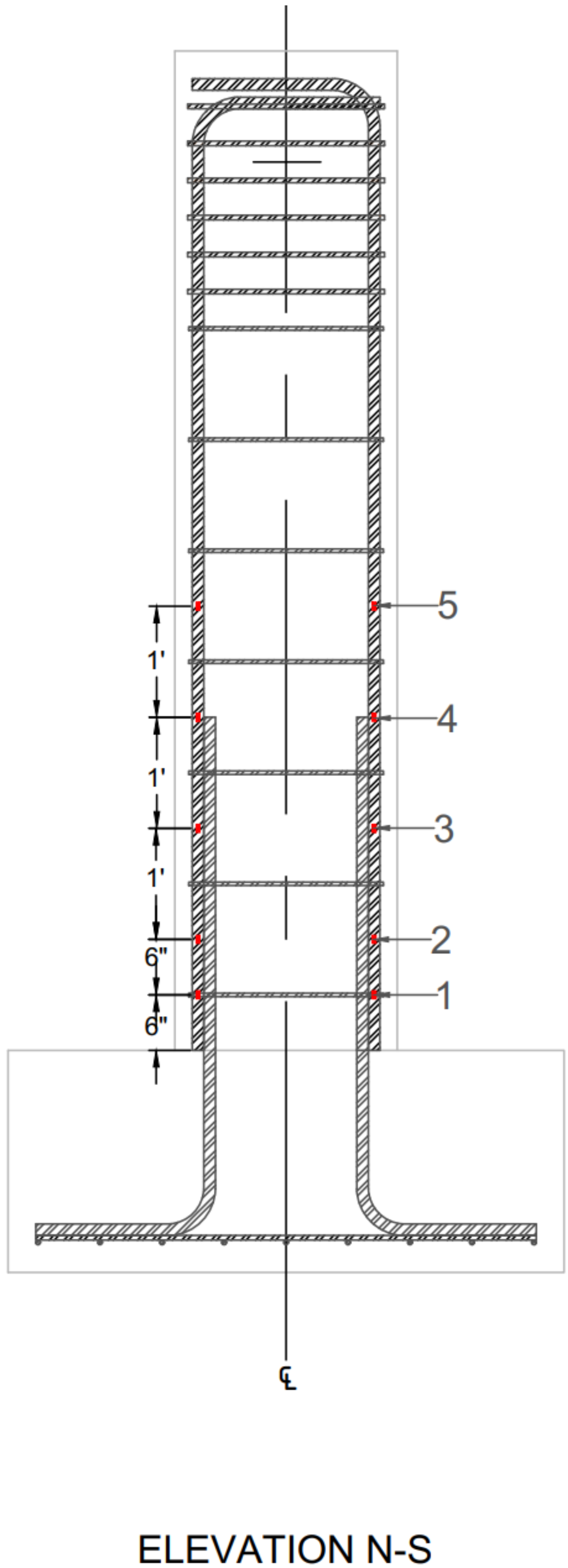

Figure B.2.3 – Column bar strain gauge locations.

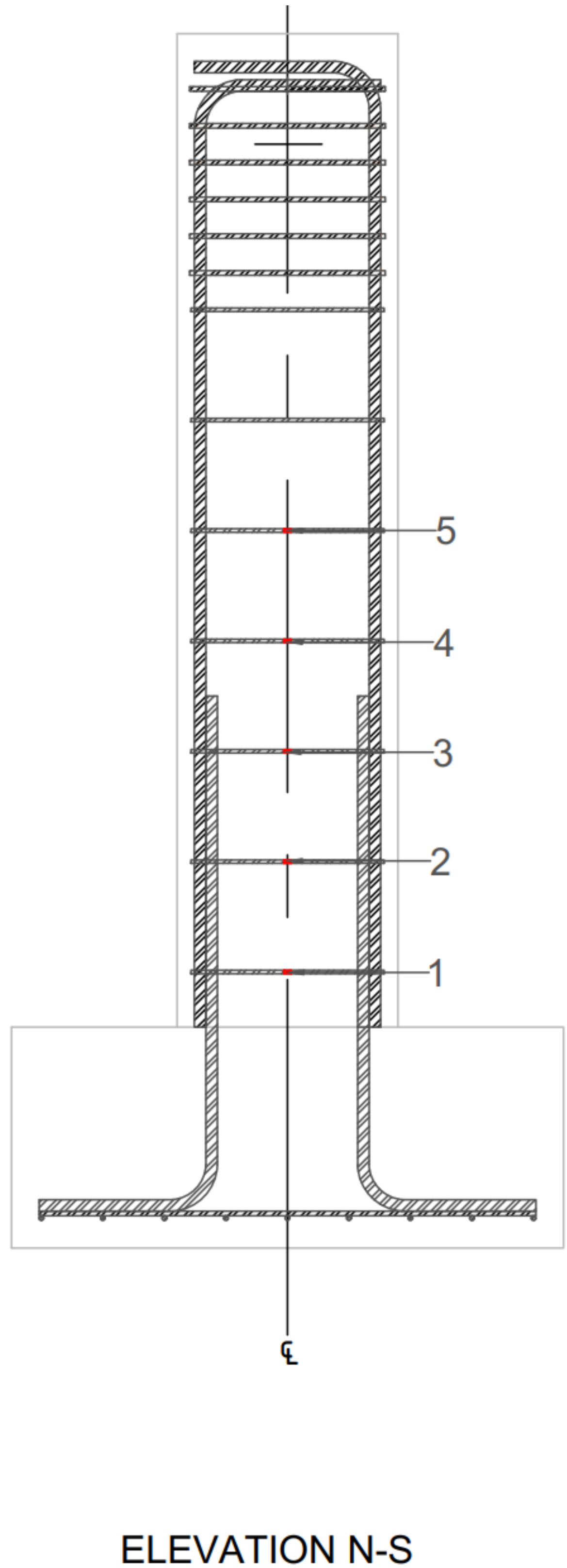

Figure B.2.4 – Column tie strain gauge locations on the East face.

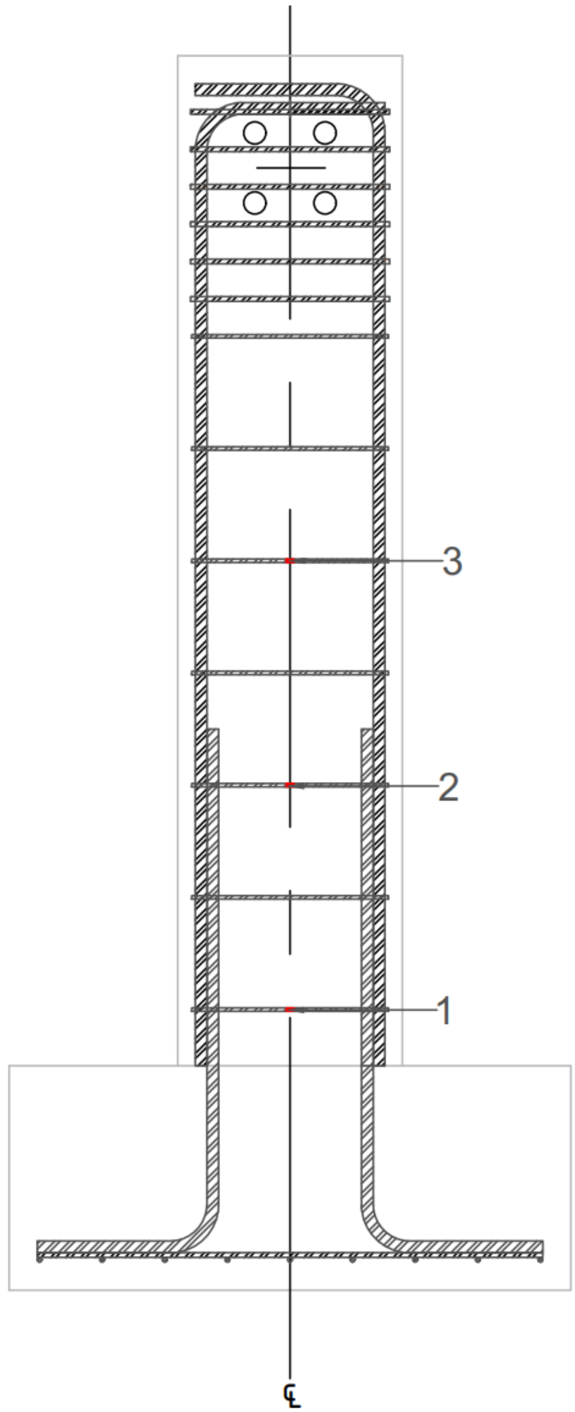

ELEVATION E-W

Figure B.2.5 – Column tie strain gauge locations on the North face.

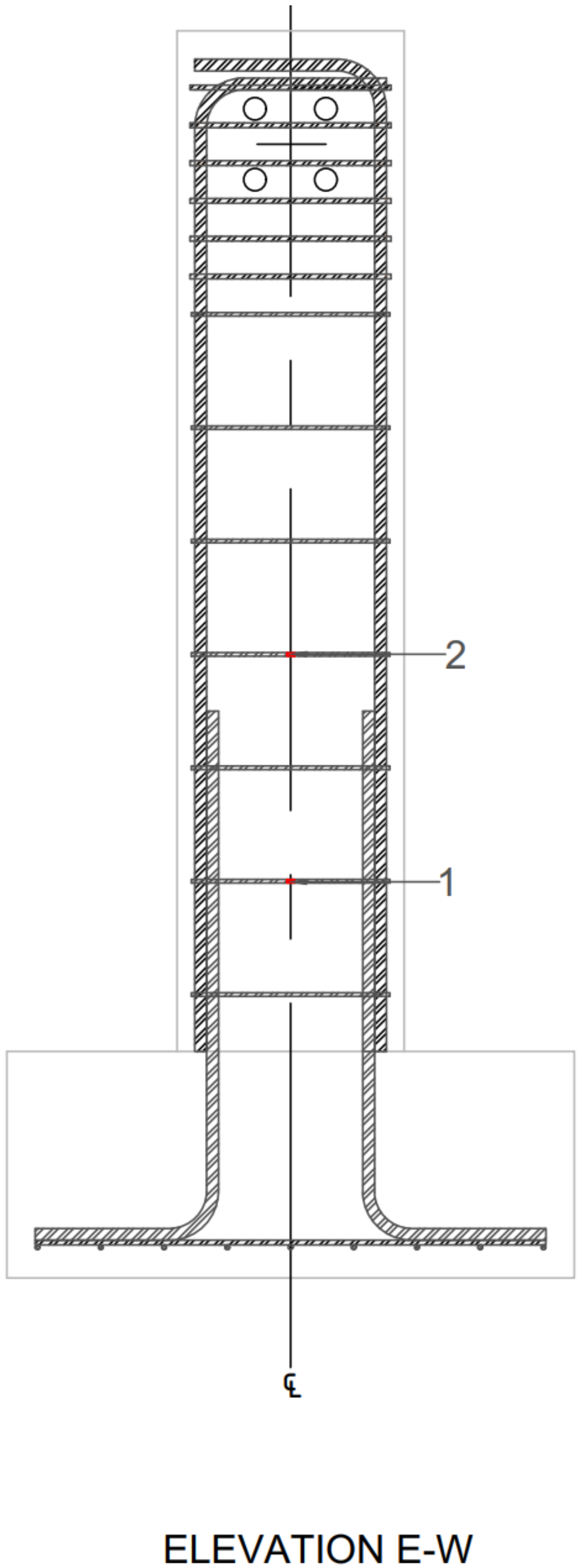

Figure B.2.6 – Column tie strain locations on the South face.

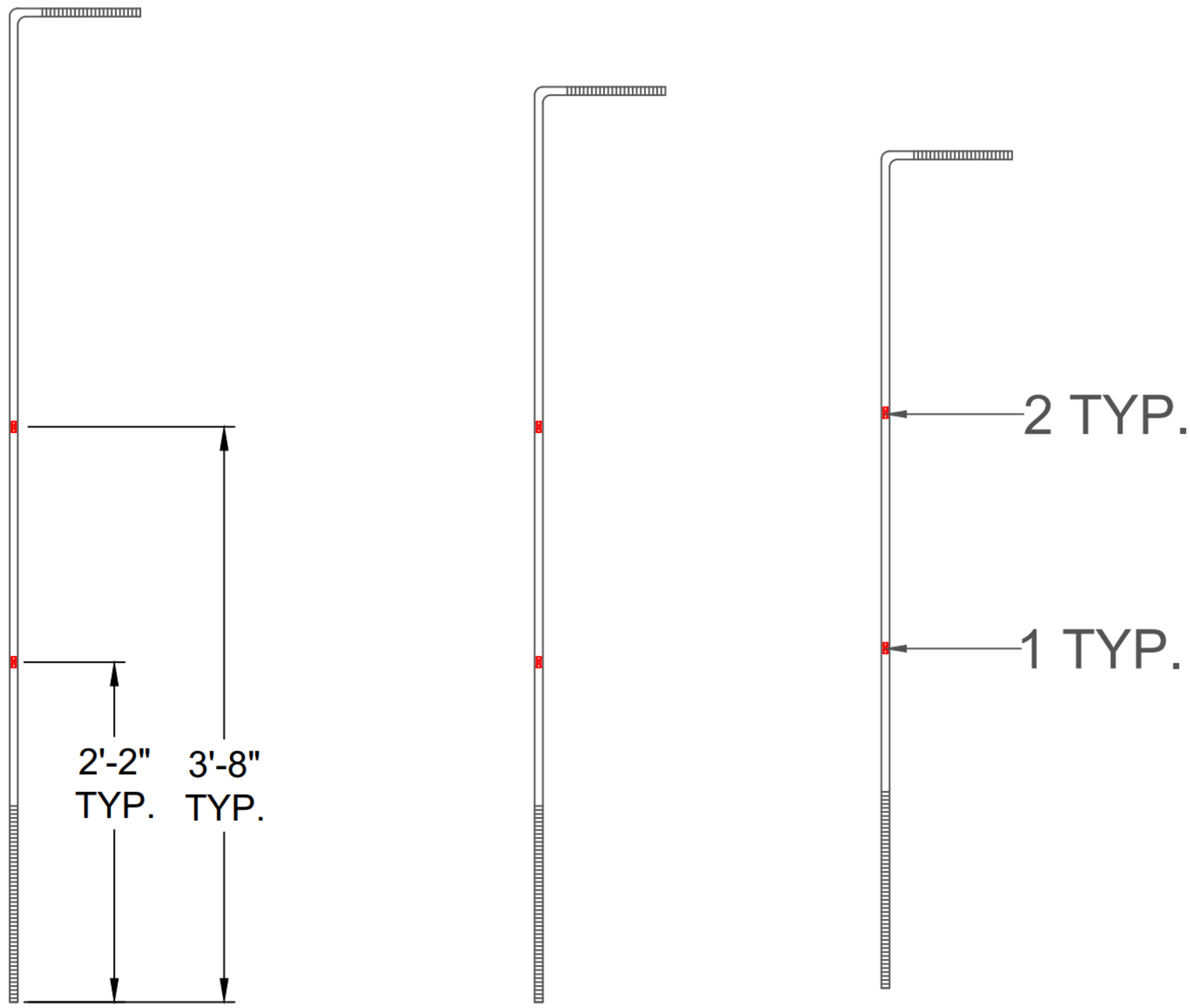

B.2.7 – TiAB ligament strain gauge locations.

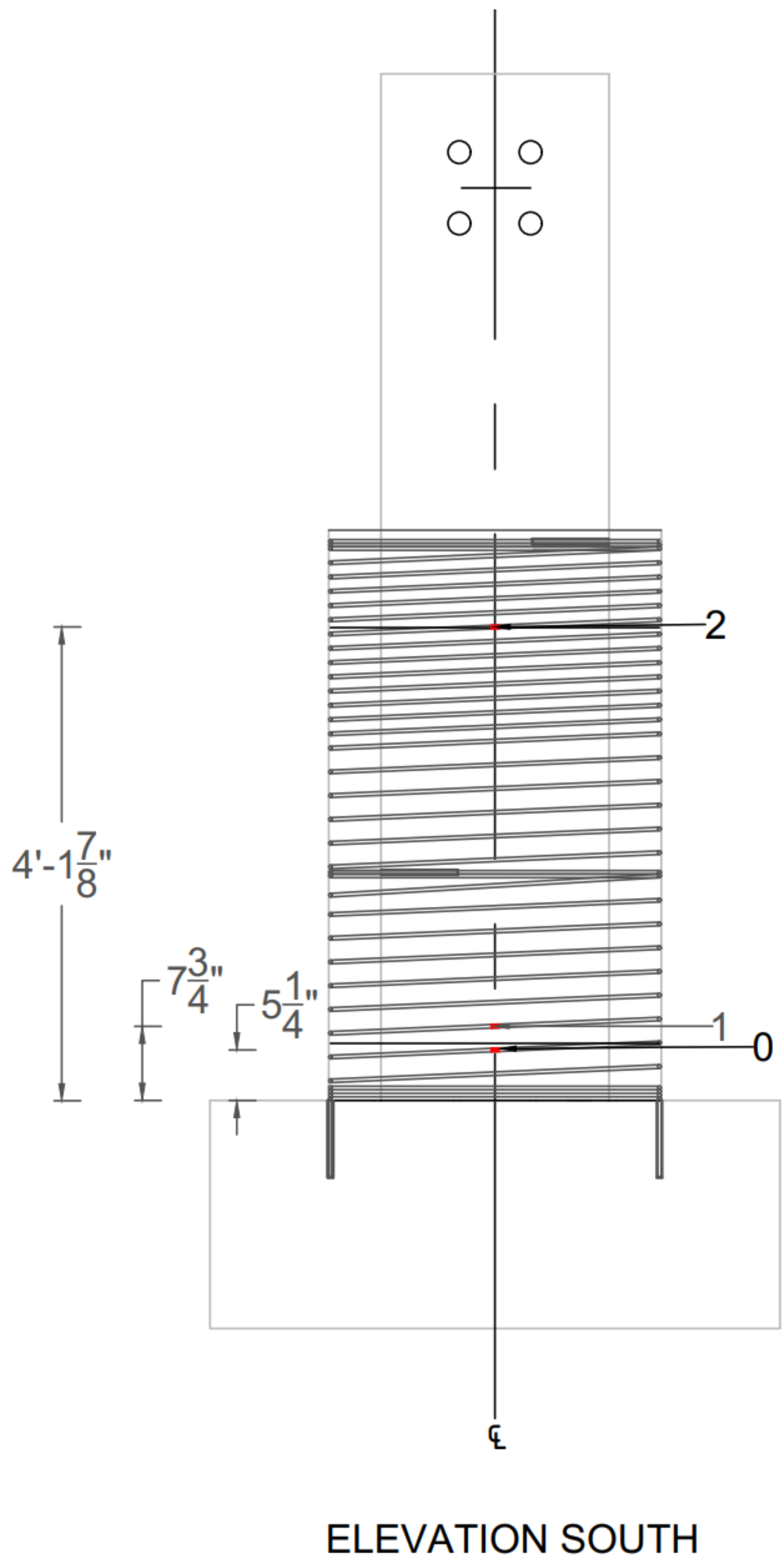

Figure B.2.8 – TiAB spiral strain gauge locations.

B.3 – String Potentiometer Sensor Locations

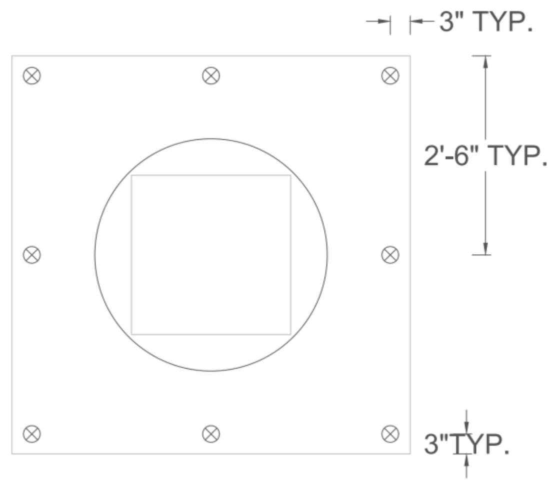

Figure B.3.1 – String potentiometer locations on the top of the footing.

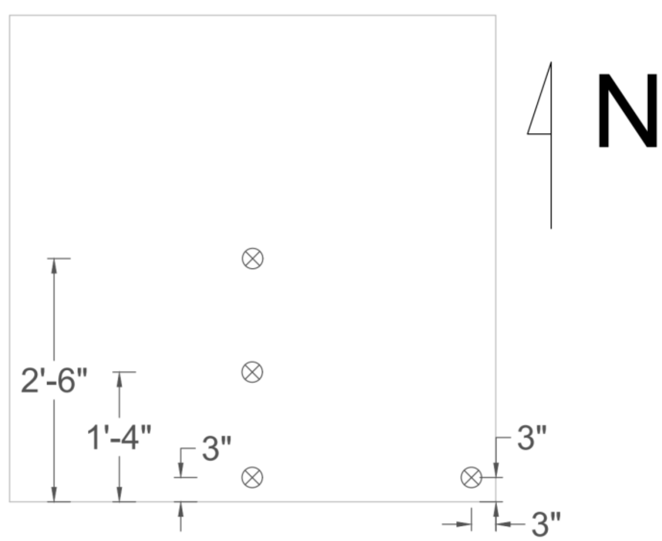

Figure B.3.2 – String potentiometers on the bottom of the footing.

Figure B.3.3 – String Potentiometer locations on the East and West of the footing.

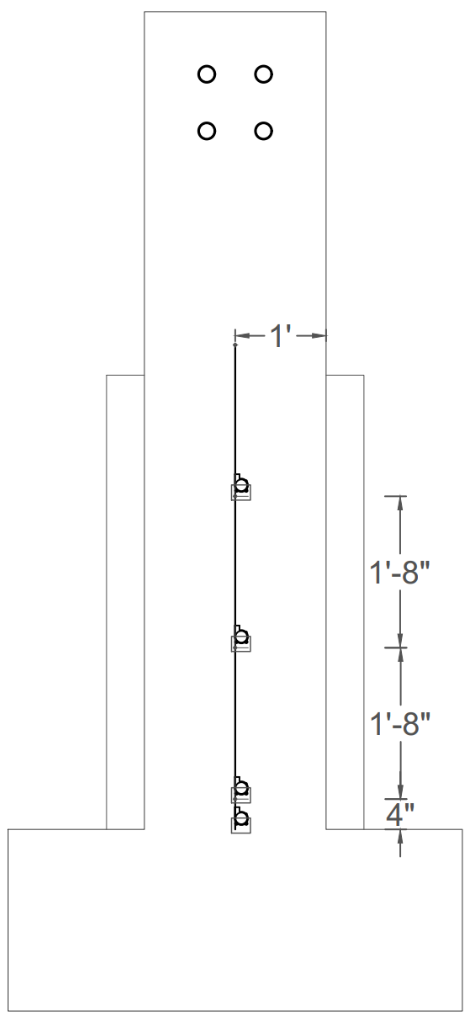

Figure B.3.4 – String potentiometer locations on the North and South face of the column.

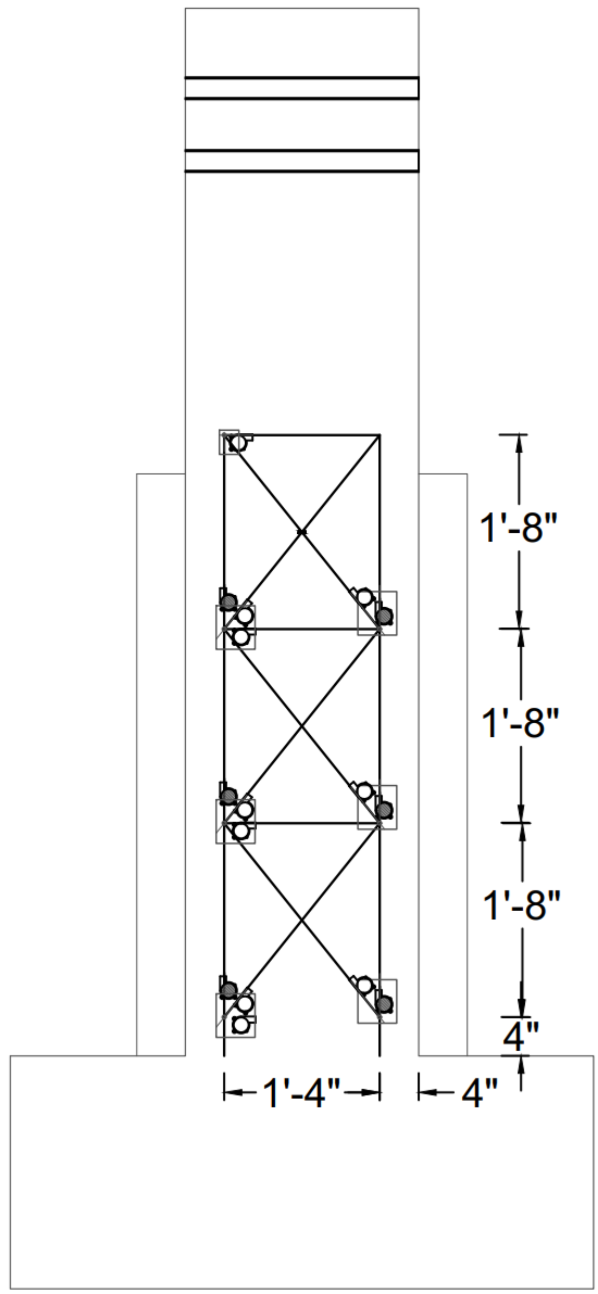

Figure B.3.5 – String Potentiometer locations on the West face.

APPENDIX C – EXPERIMENTAL DATA FOR ALL TESTS

C.1 Test 1 - Specimen 1: Complete Retrofit with Foam Embedment & Subgrade

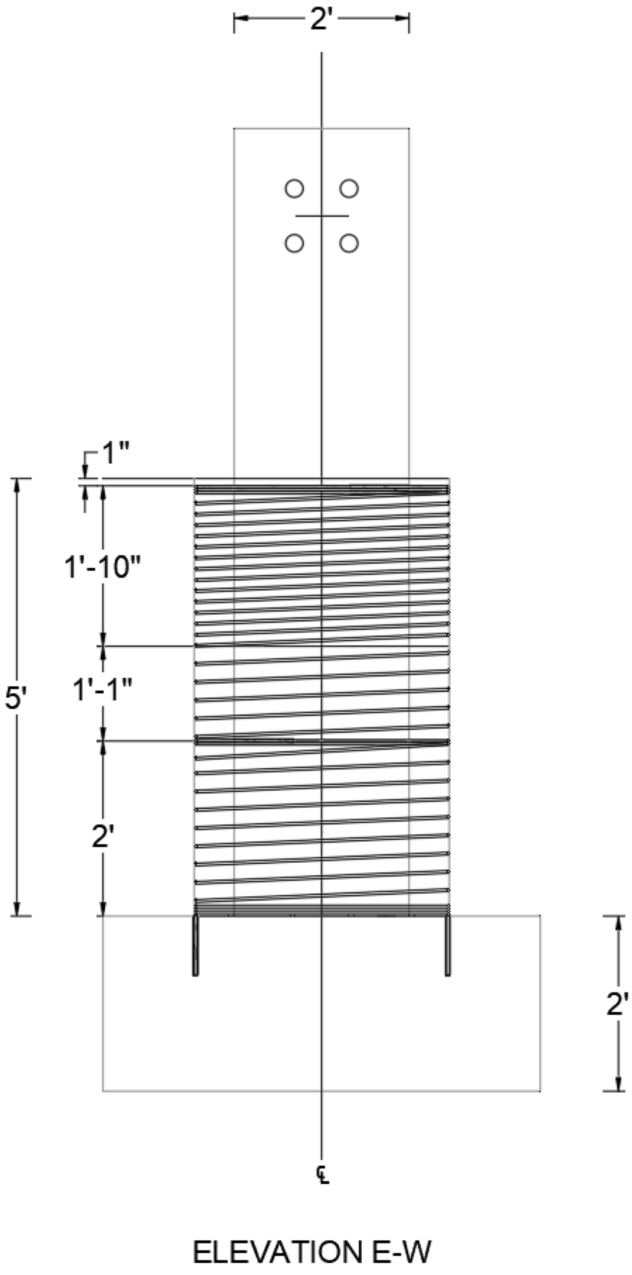

Figure C.1.1 – Elevation View of Specimen 1 used in Test 1.

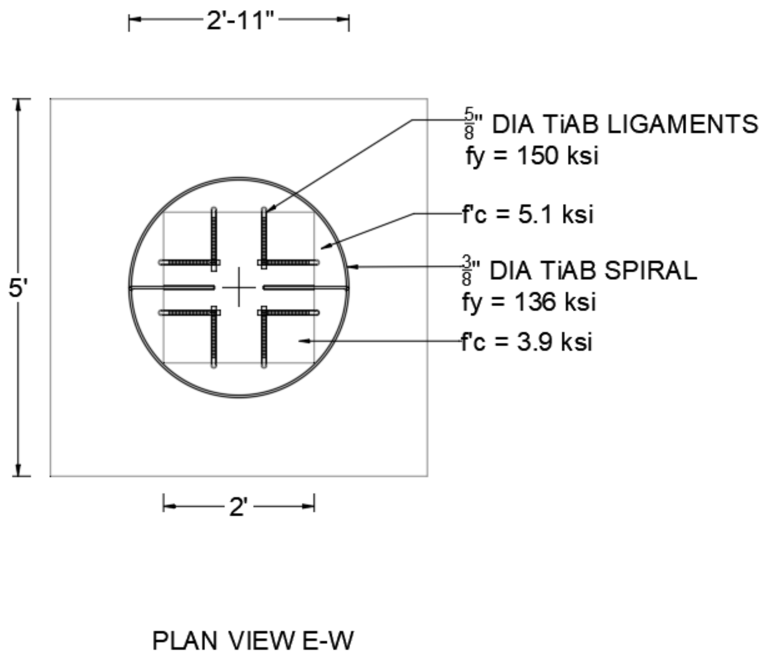

Figure C.1.2 – Plan View of Specimen 1 used in Test 1.

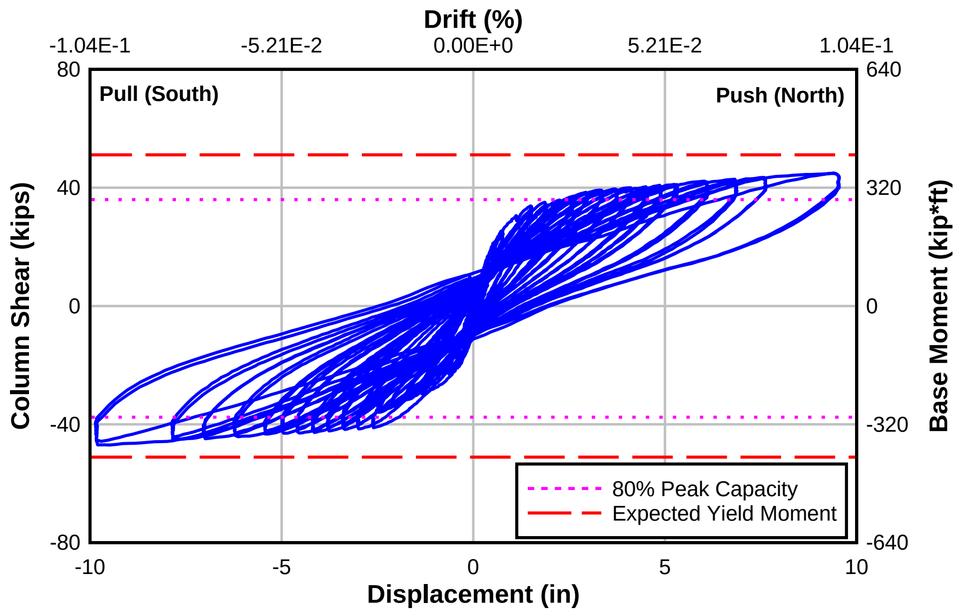

Figure C.1.3 – Overall Force Displacement Response – Test 1.

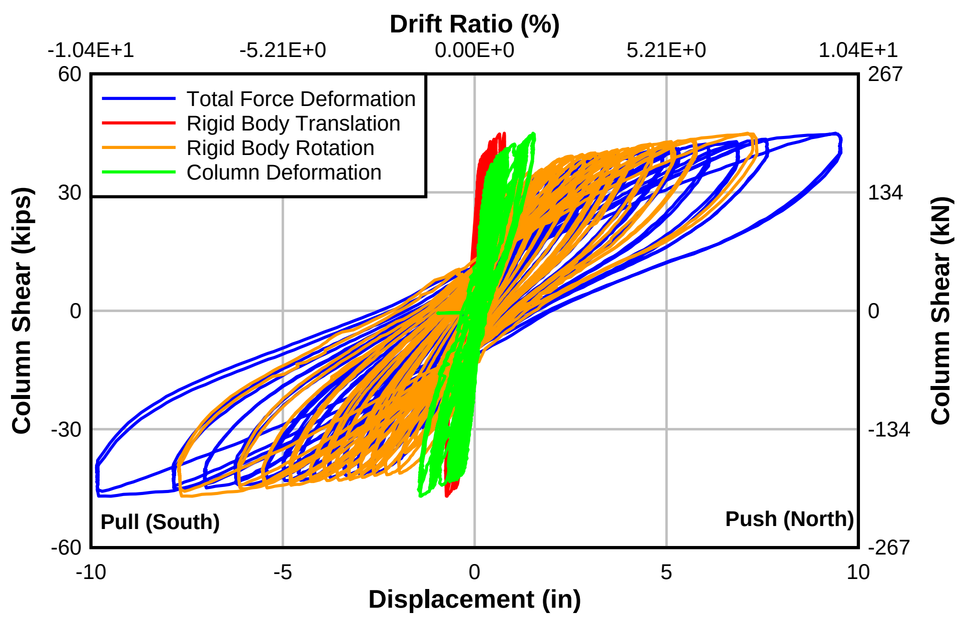

Figure C.1.4 – Component Contributions to Force Displacement – Test 1.

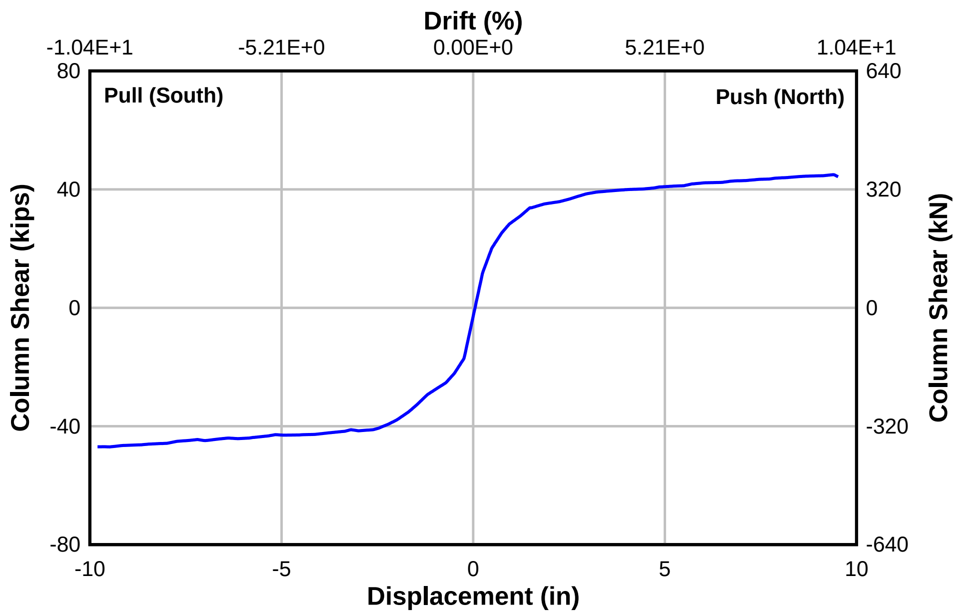

Figure C.1.5 – Overall Force Displacement Backbone Curve – Test 1.

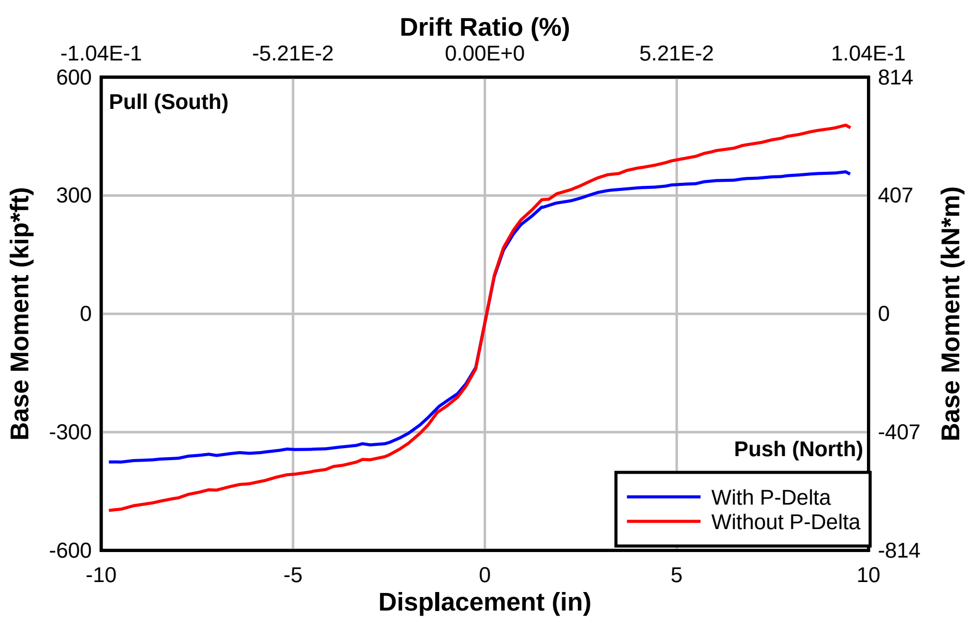

Figure C.1.6 – P-Delta Effects Backbone Curve – Test 1.

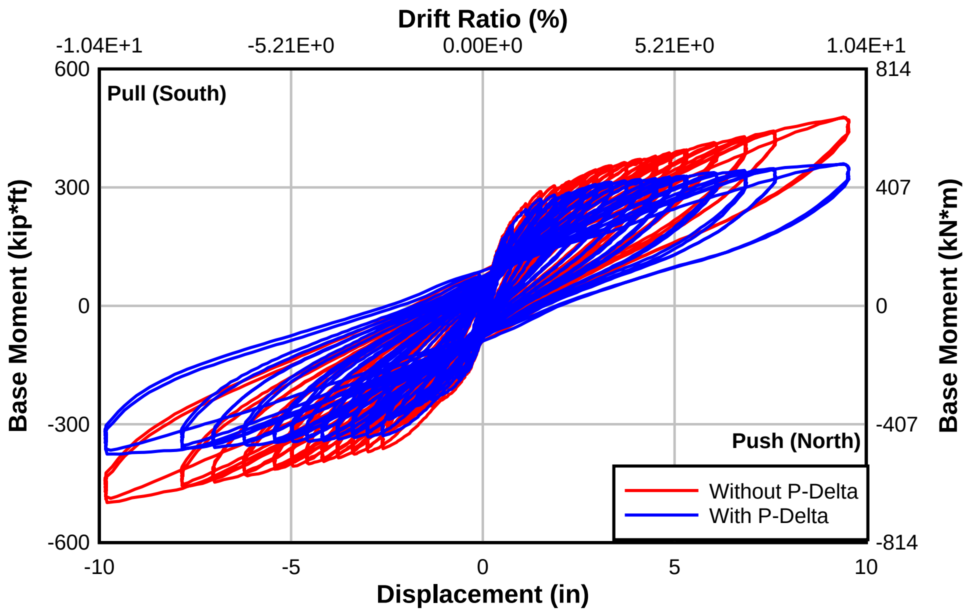

Figure C.1.7 – P-Delta Effects – Test 1.

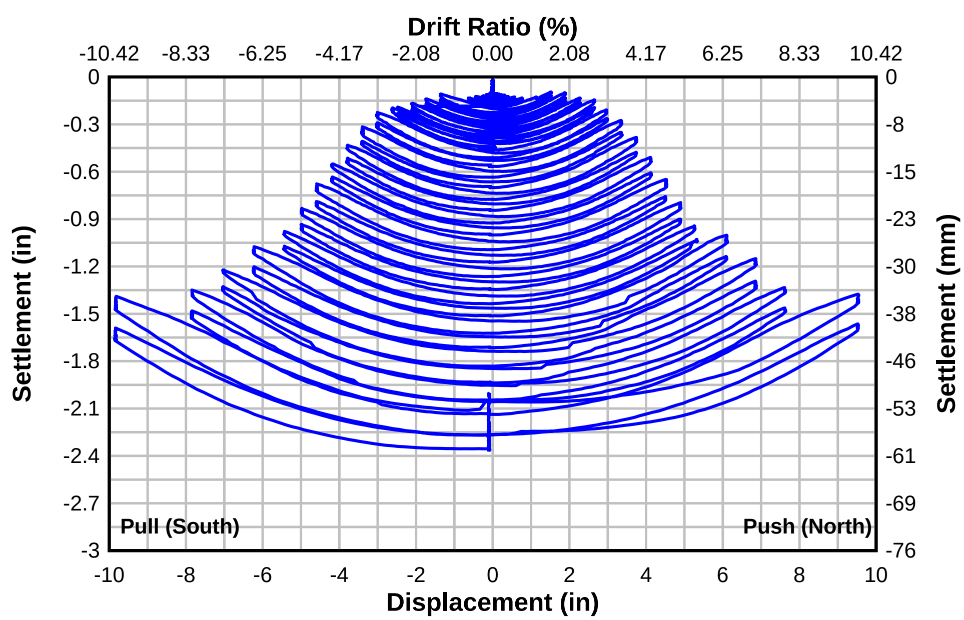

Figure C.1.8 – Settlement – Test 1.

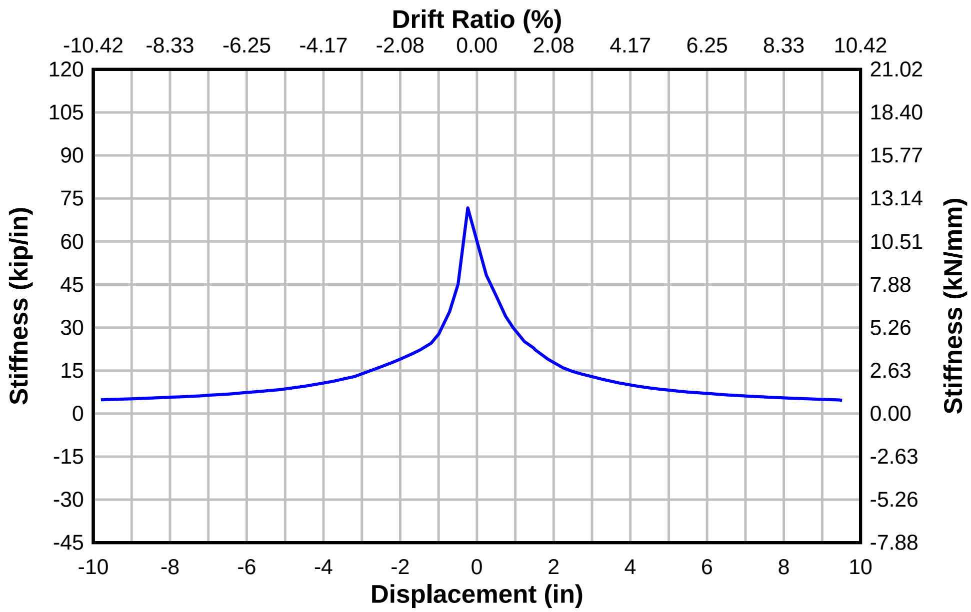

Figure C.1.9 – Evolution Secant Stiffness – Test 1.

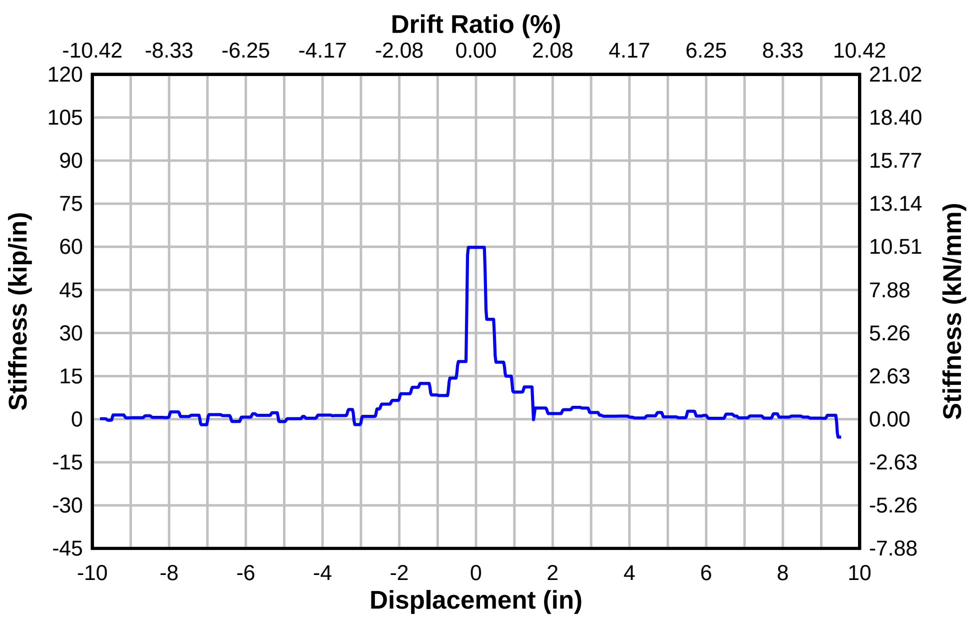

Figure C.1.10 – Evolution of Tangent Stiffness – Test 1.

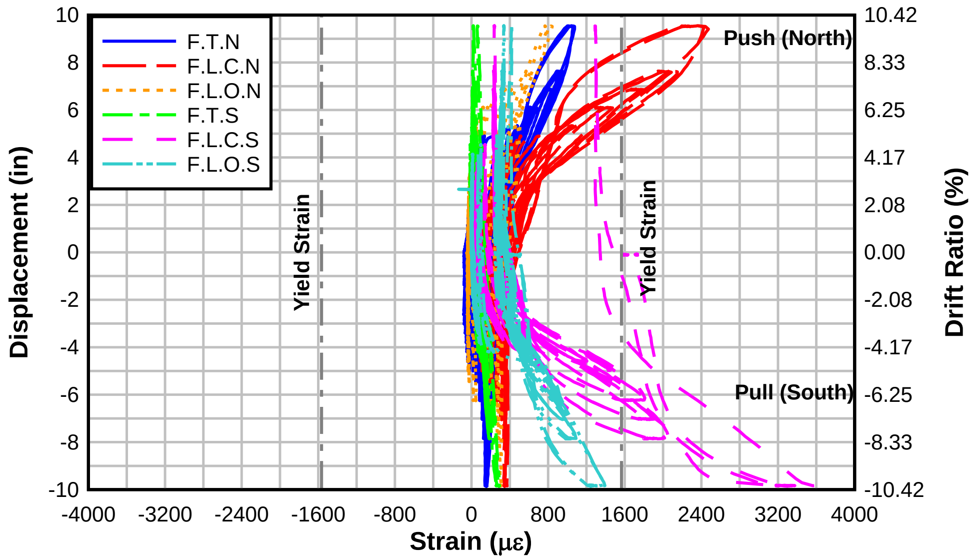

Figure C.1.11 – Footing Bar Strains – Test 1.

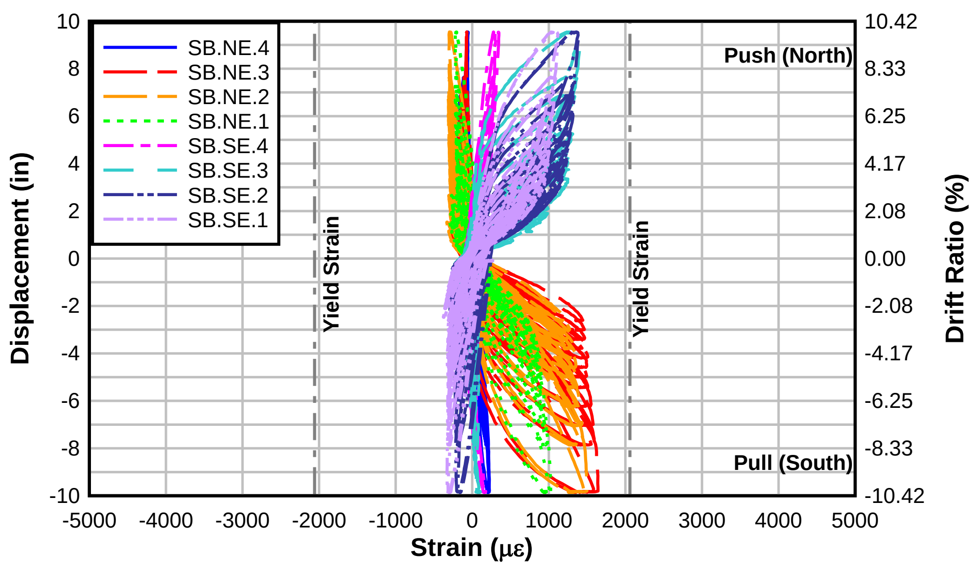

Figure C.1.12 – Starter Bar Strains – Test 1.

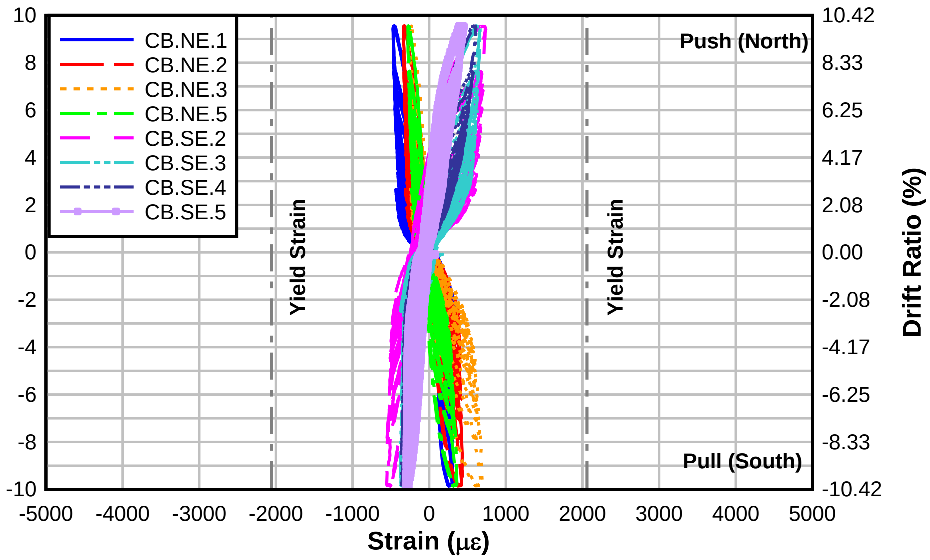

Figure C.1.13 – Column Bar Strains – Test 1.

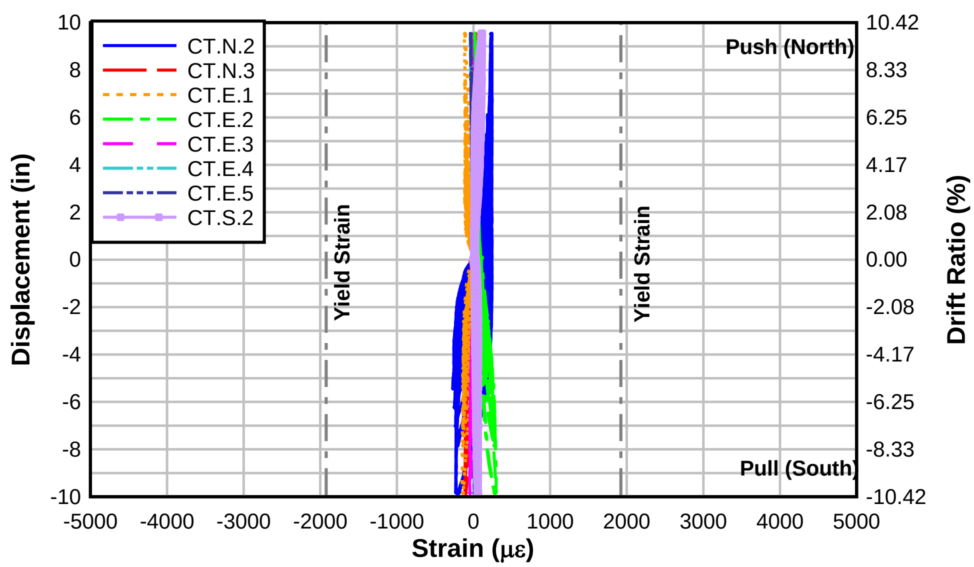

Figure C.1.14 – Column Tie Strains – Test 1.

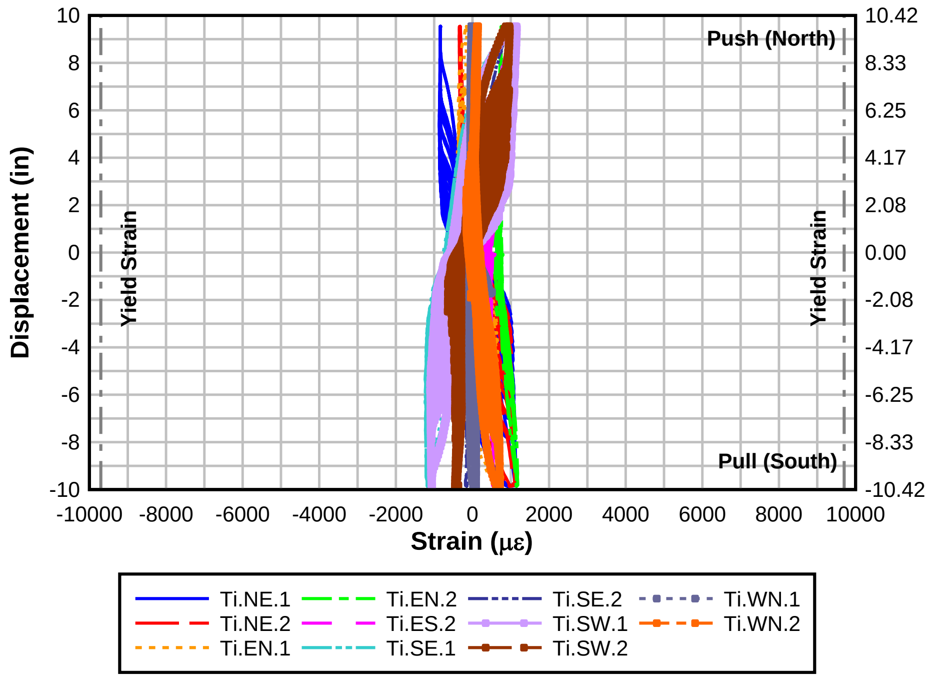

Figure C.1.15 – TiAB Ligament Strains – Test 1.

Figure C.1.16 – TiAB Spiral Strains – Test 1.

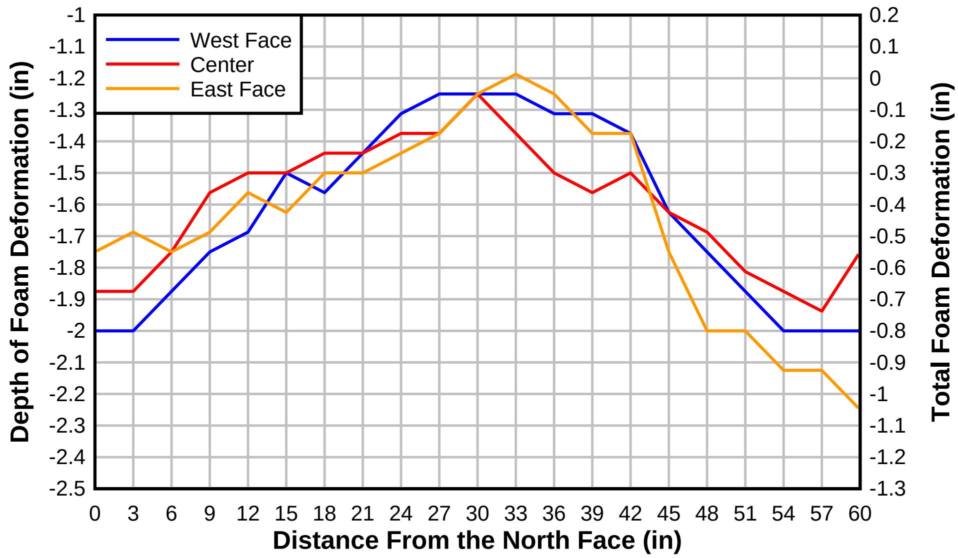

Figure C.1.17 – Soil Simulant Profile After Testing – Test 1.

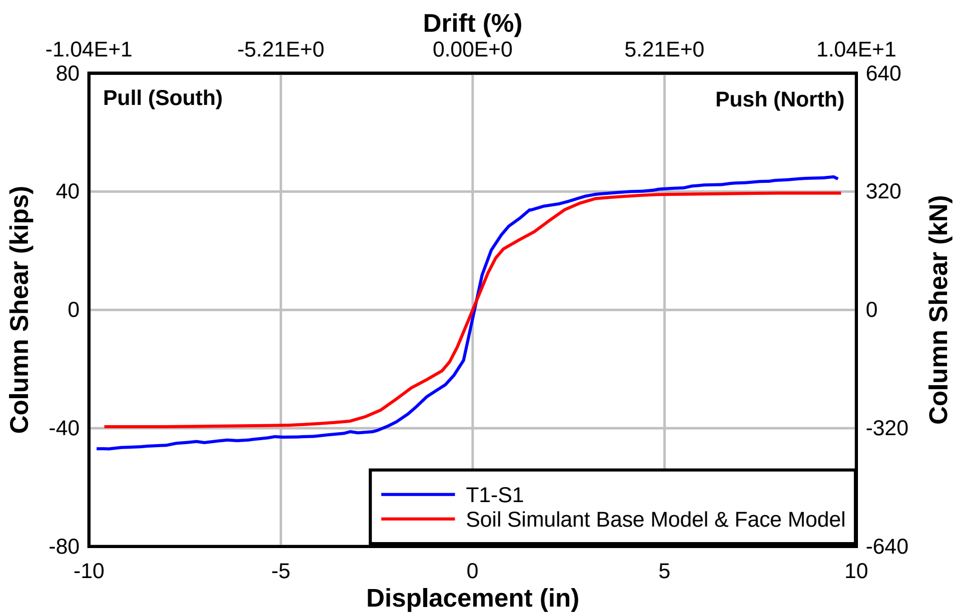

Figure C.1.18 – Soil Simulant Model Comparison – Test 1.

C.2 Test 2 - Specimen 2: Complete Retrofit with No Embedment & Foam Subgrade

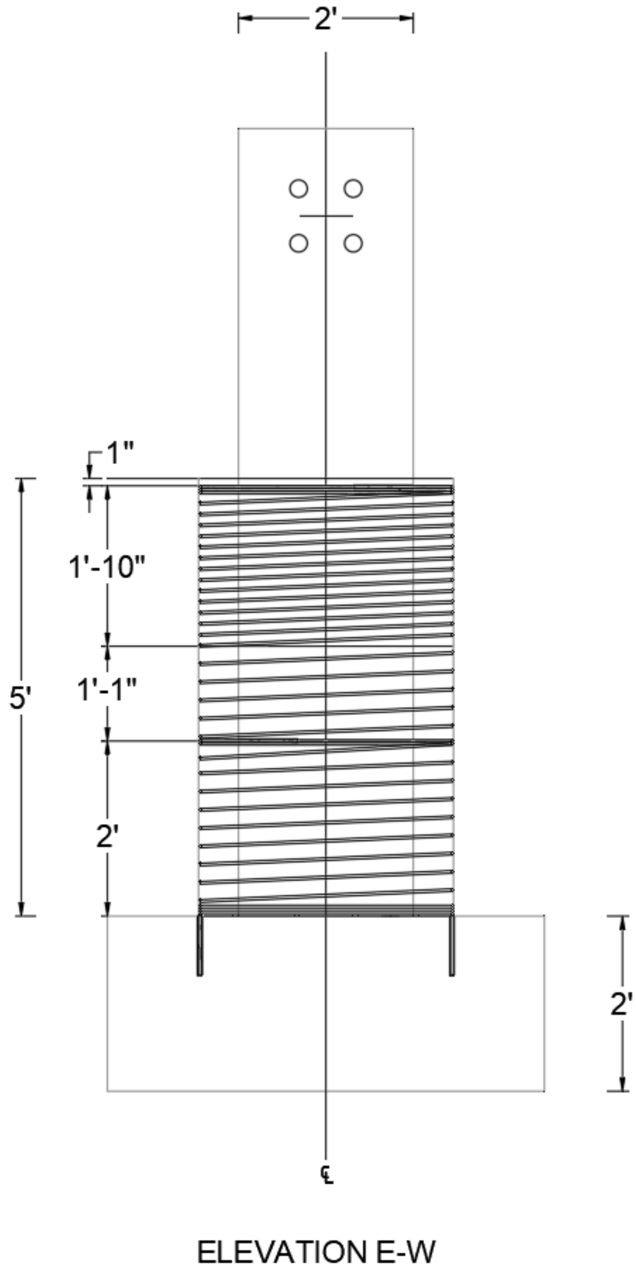

Figure C.2.1 - Elevation View of Specimen 2 used in Test 2.

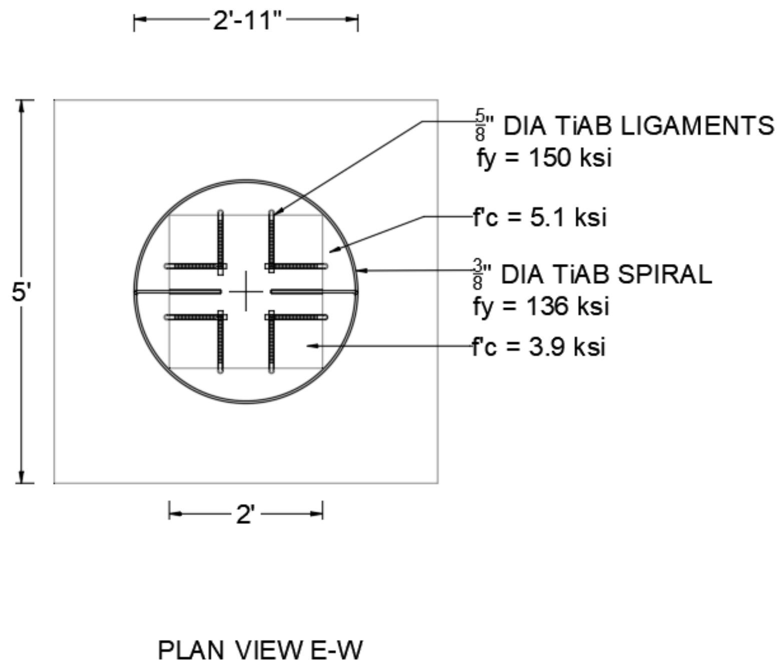

Figure C.2.2 – Plan View of Specimen 2 used in Test 2.

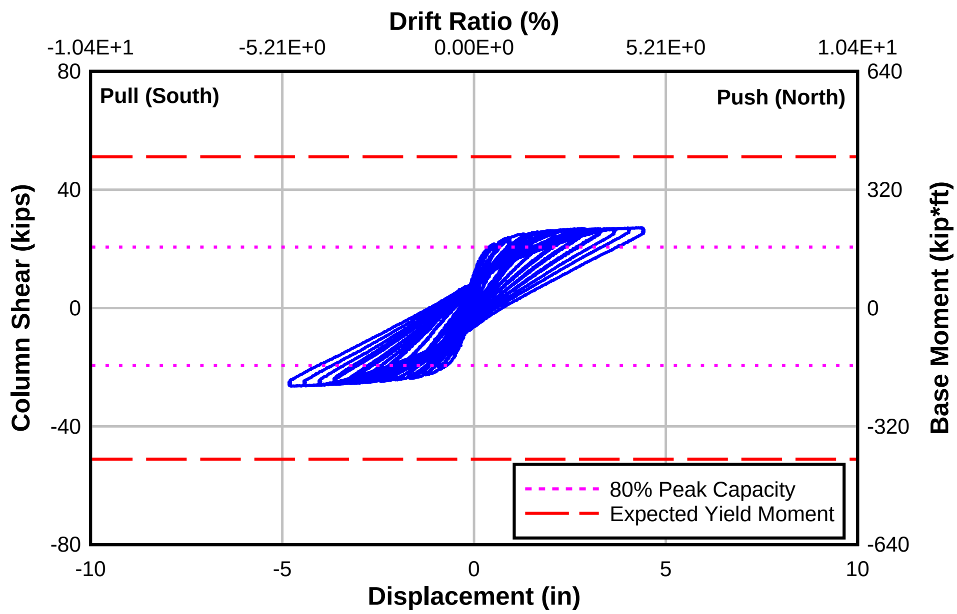

Figure C.2.3 – Overall Force Displacement Response – Test 2.

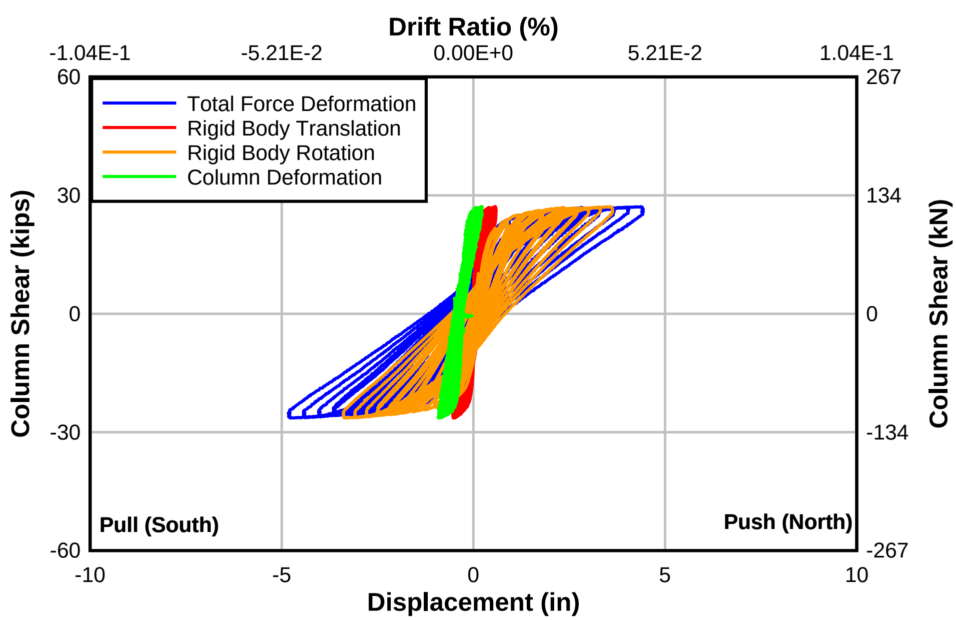

Figure C.2.4 – Component Contributions to Force Displacement – Test 2.

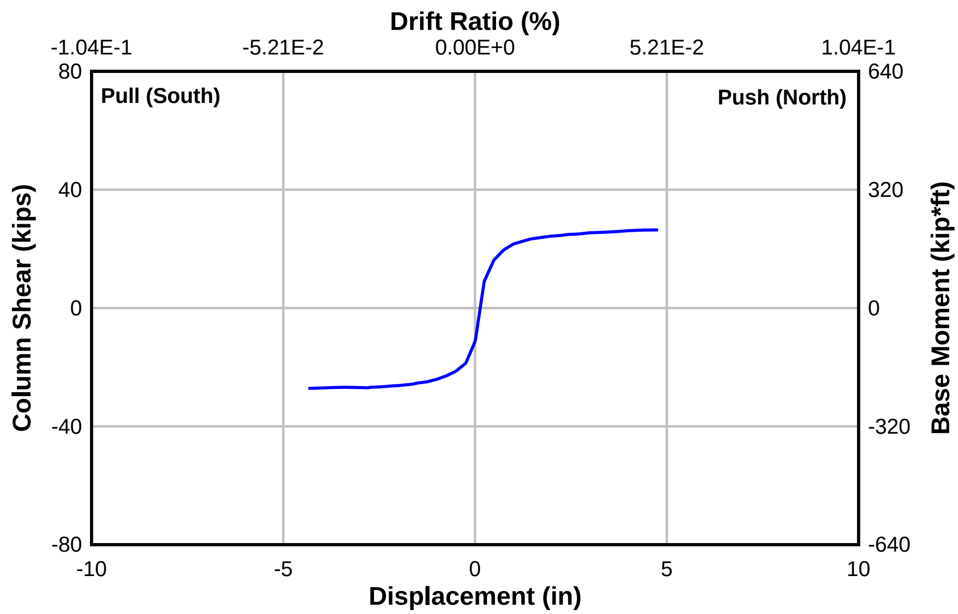

Figure C.2.5 – Overall Force Displacement Backbone Curve – Test 2.

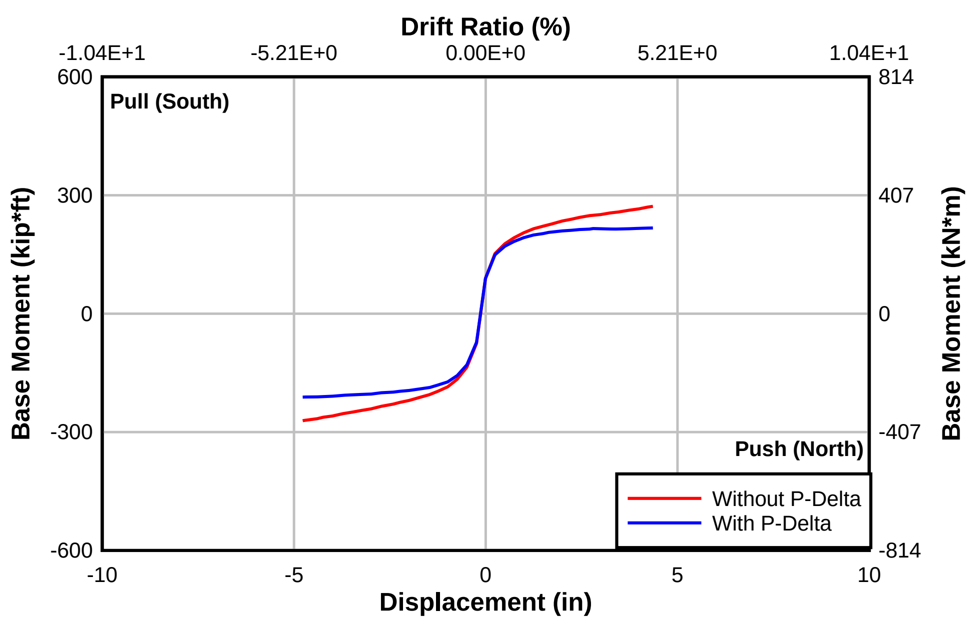

Figure C.2.6 – P-Delta Effects Backbone Curve – Test 2.

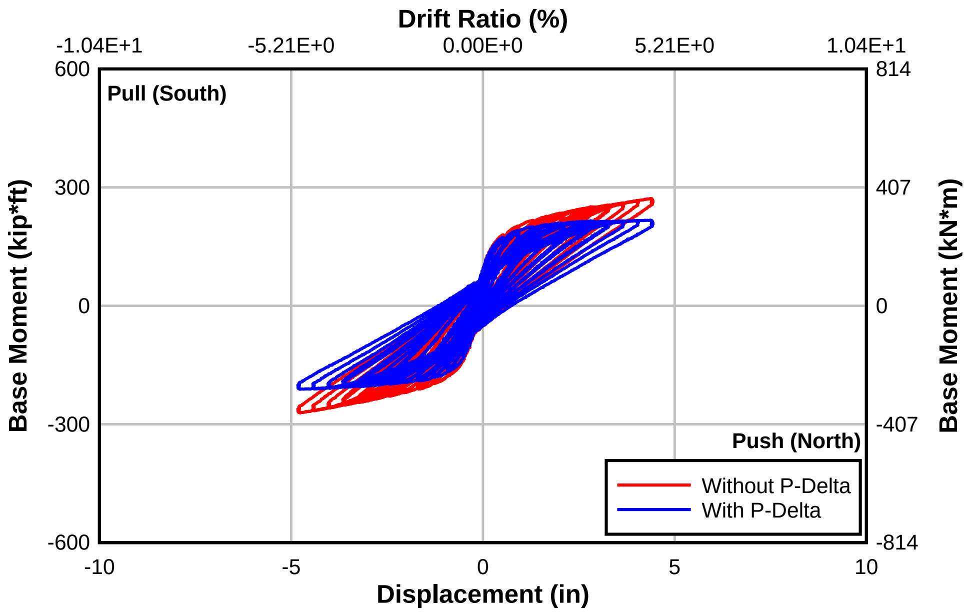

Figure C.2.7 – P-Delta Effects – Test 2.

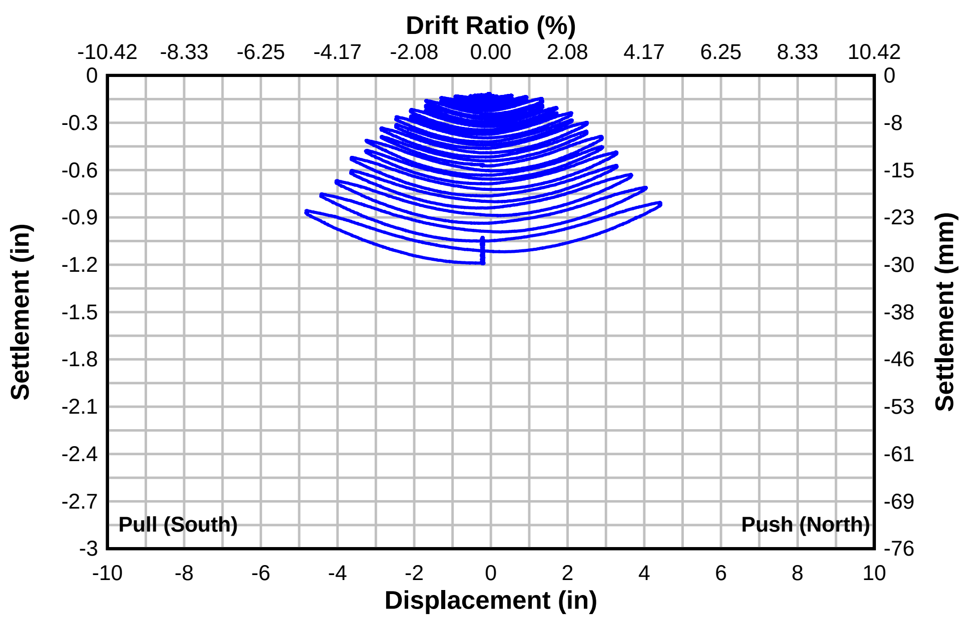

Figure C.2.8 – Settlement – Test 2.

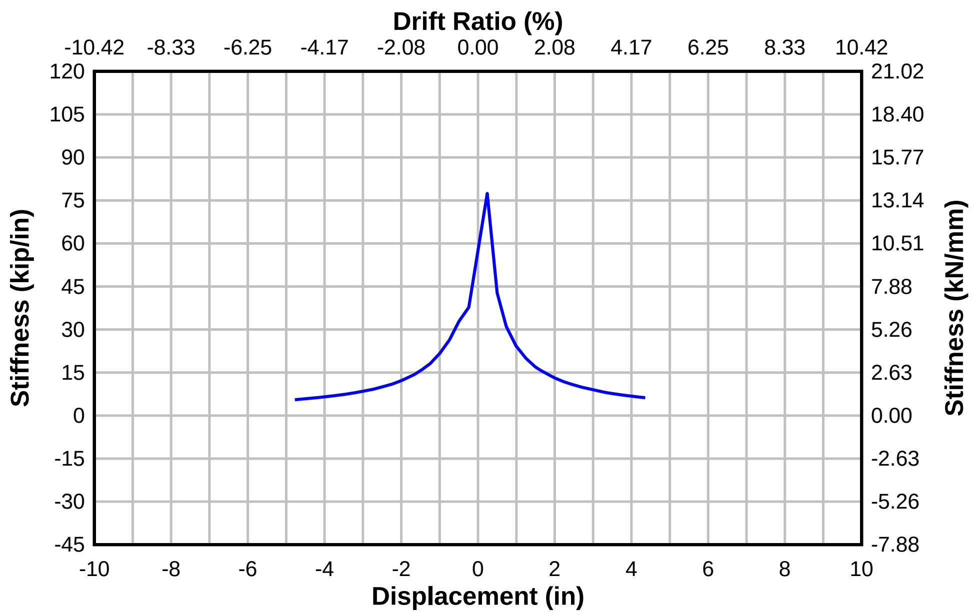

Figure C.2.9 – Evolution of Secant Stiffness – Test 2.

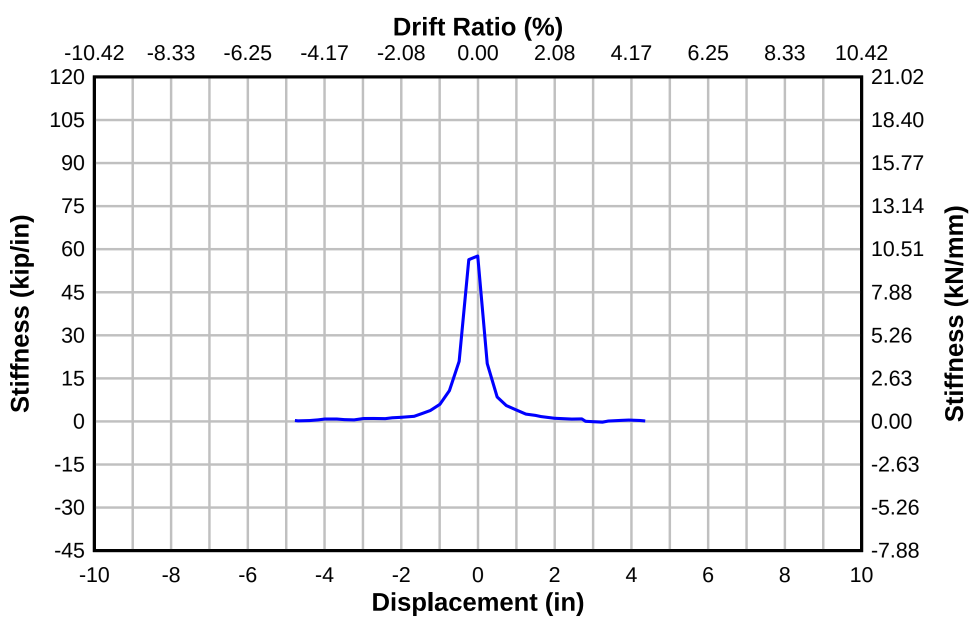

Figure C.2.10 – Evolution of Tangent Stiffness – Test 2.

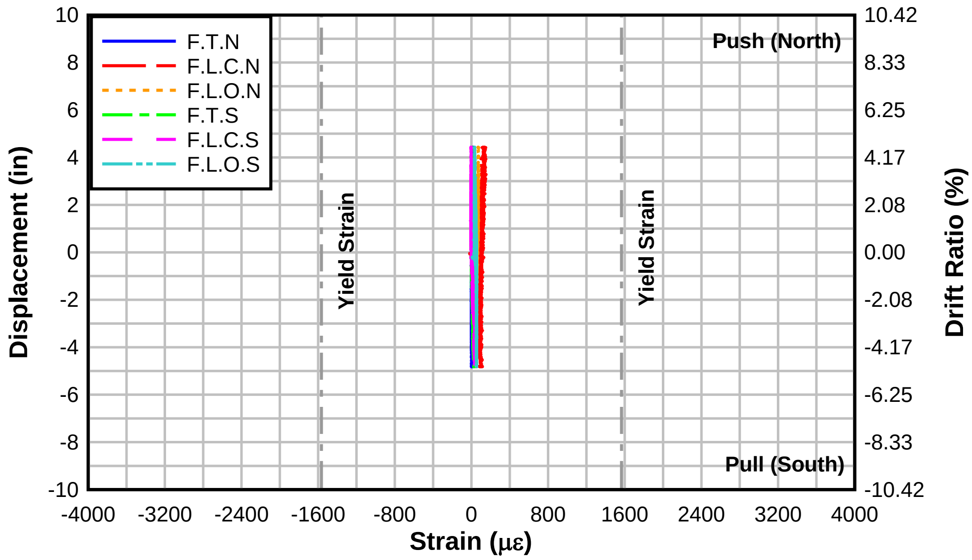

Figure C.2.11 – Footing Bar Strains -Test 2.

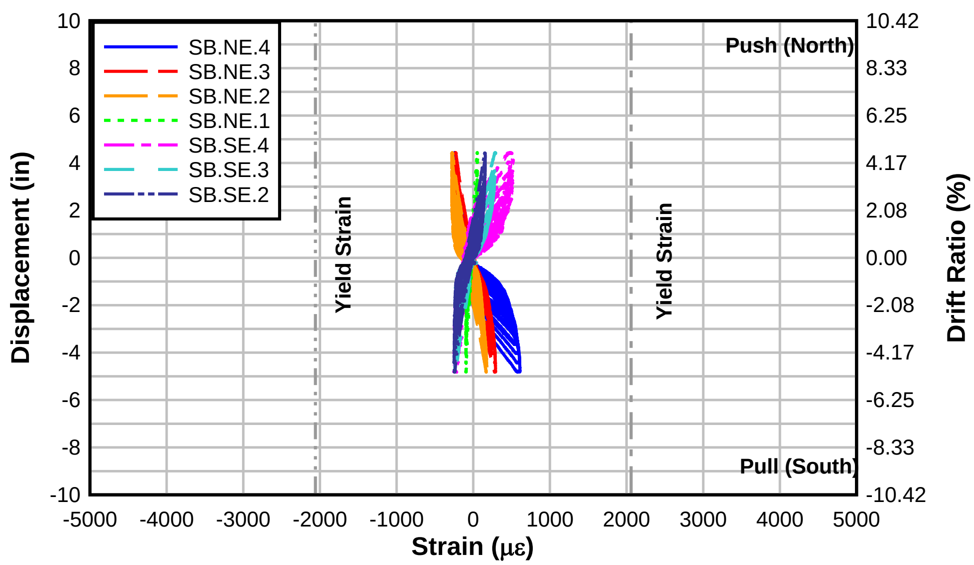

Figure C.2.12 – Starter Bar Strains – Test 2.

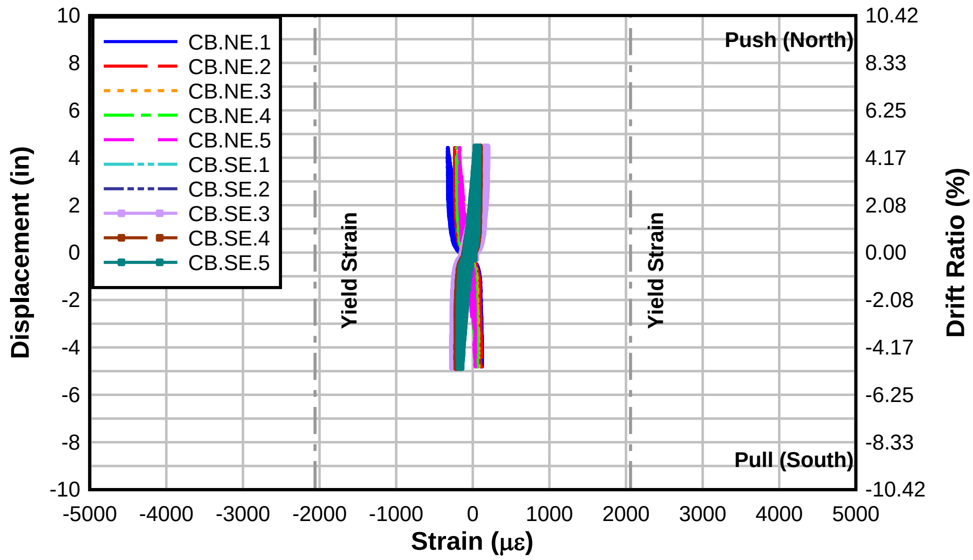

Figure C.2.13 – Column Bar Strains – Test 2.

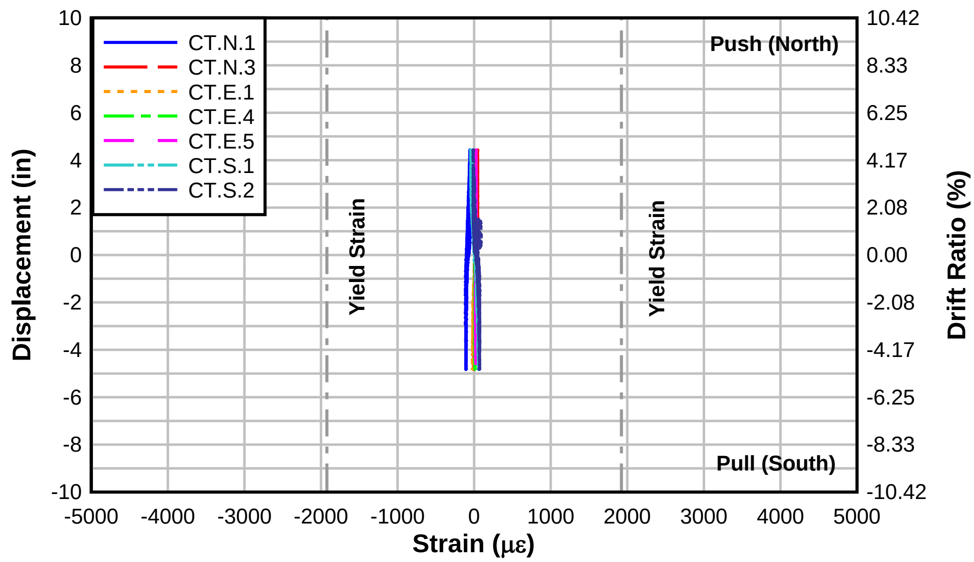

Figure C.2.14 – Column Tie Strain – Test 2.

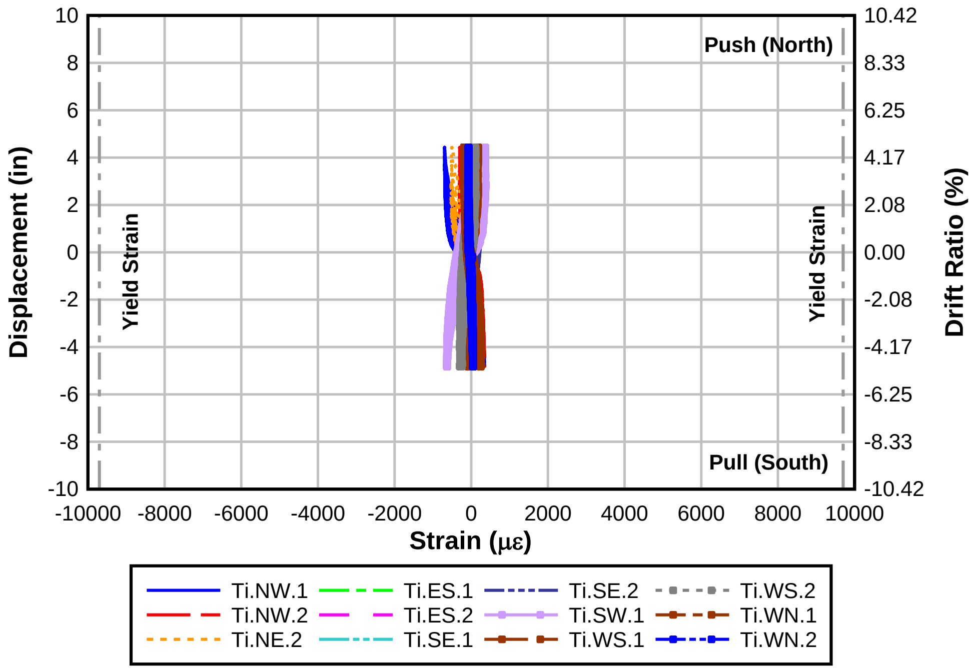

Figure C.2.15 – TiAB Ligament Strain – Test 2.

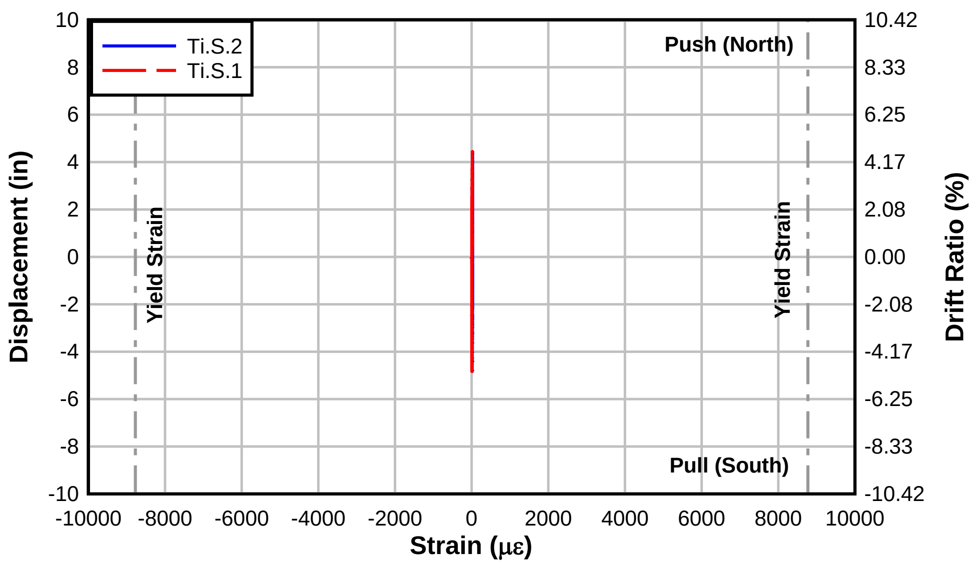

Figure C.2.16 – TiAB Spiral Strain – Test 2.

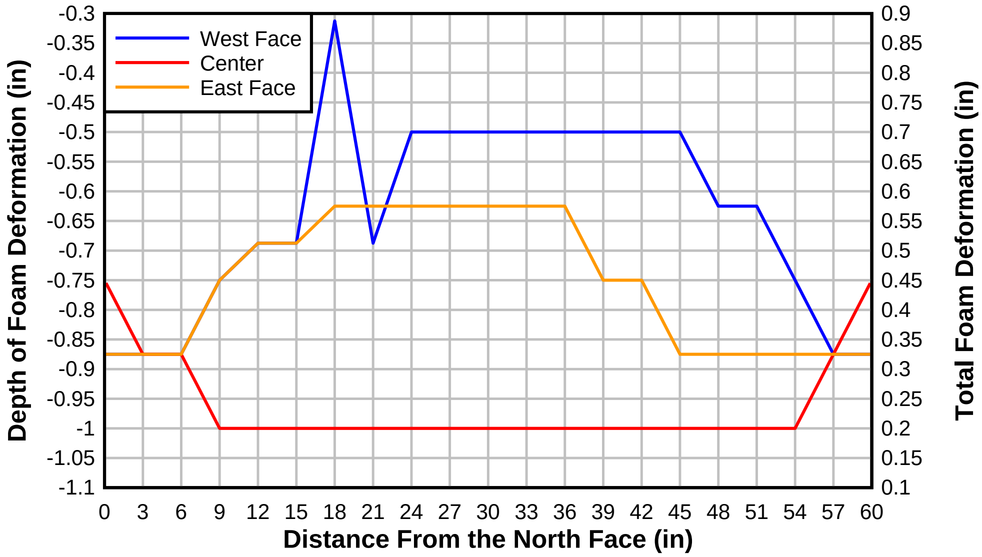

Figure C.2.17 – Soil Simulant Profile After Testing – Test 2.

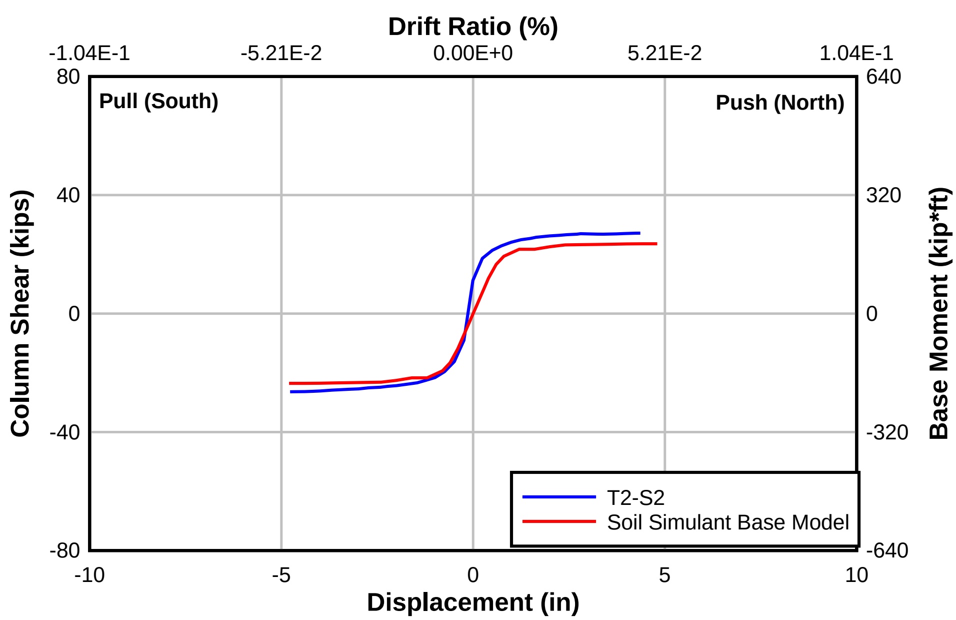

Figure C.2.18 – Soil Simulant Model Comparison -Test 2.

C.3 Test 3 – Specimen 3: Vintage with Foam Embedment, Subgrade, & 150 kip Axial Load

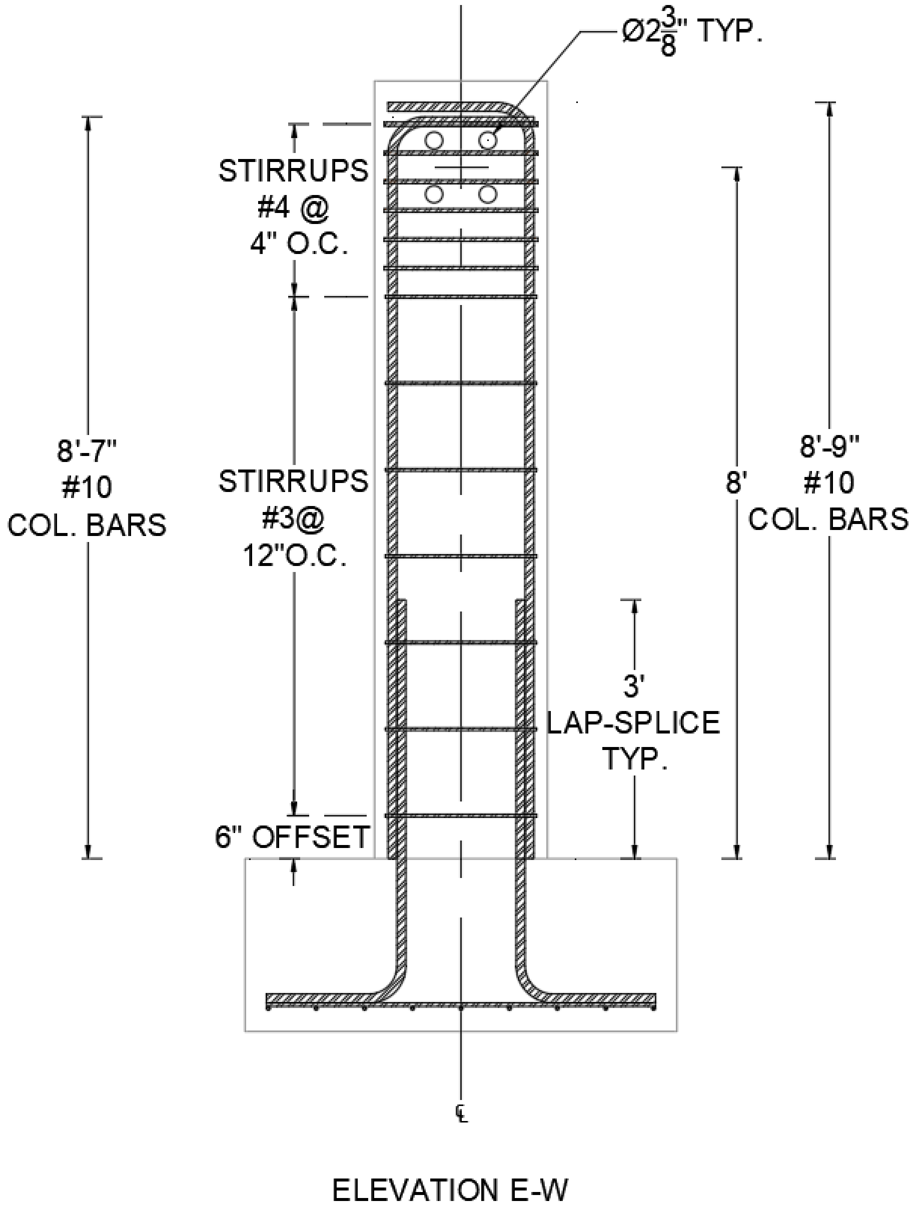

Figure C.3.1 - Elevation View of Specimen 3 used in Test 3.

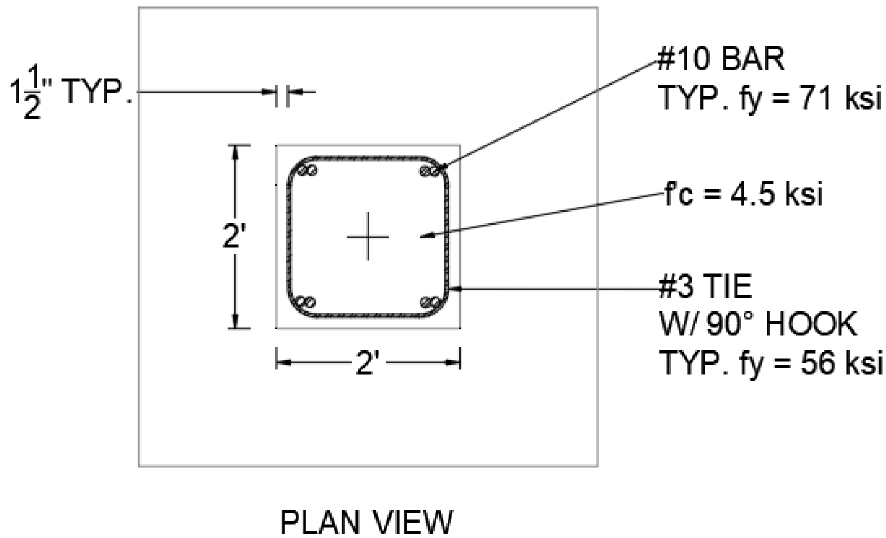

Figure C.3.2 - Plan View of Specimen 3 used in Test 3.

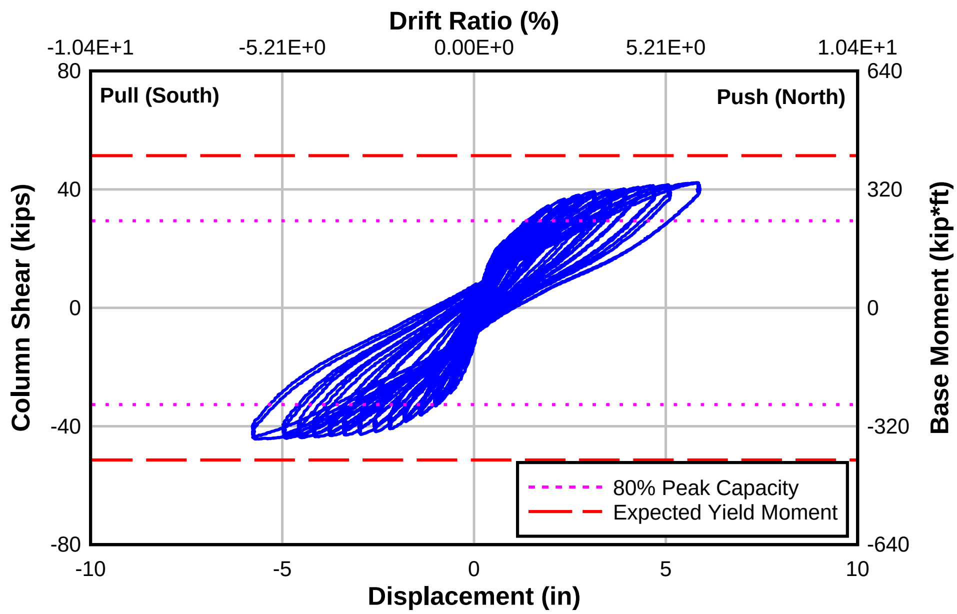

Figure C.3.3 – Overall Force Displacement Response – Test 3.

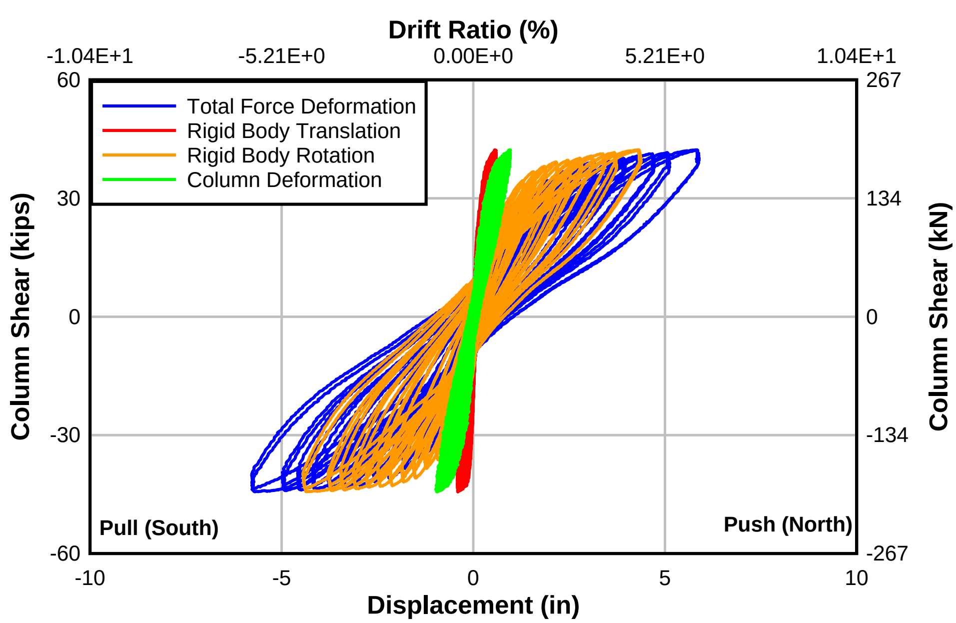

Figure C.3.4 – Component Contributions to Force Displacement – Test 3.

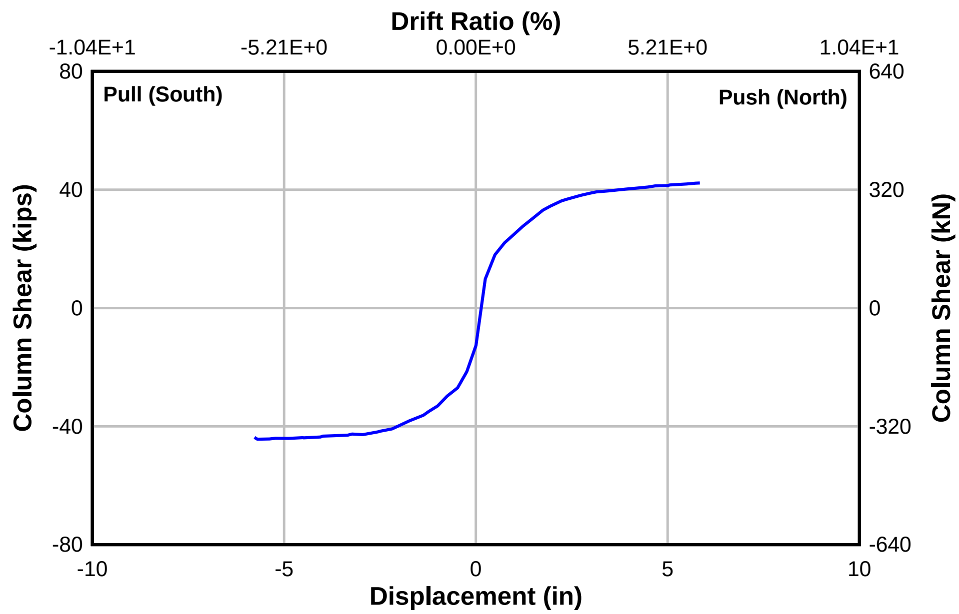

Figure C.3.5 – Overall Force Displacement Backbone Curve – Test 3.

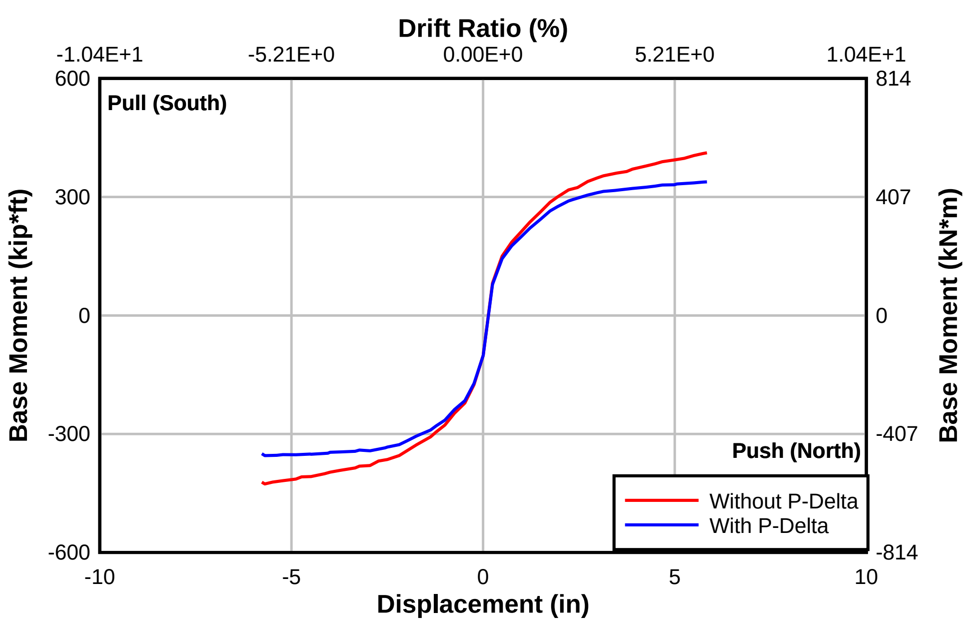

Figure C.3.6 – P-Delta Effects Backbone Curve – Test 3.

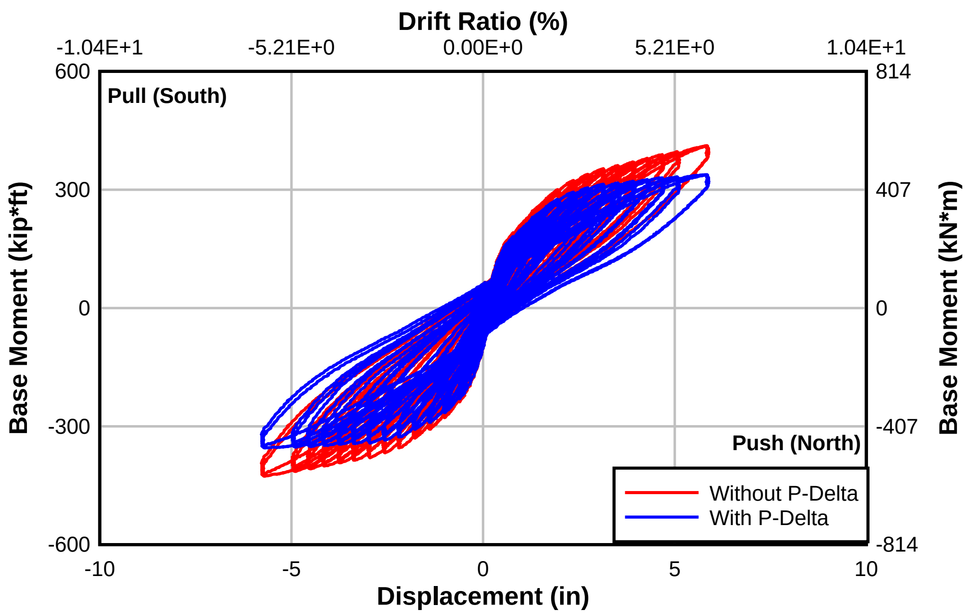

Figure C.3.7 – P-Delta Effects – Test 3.

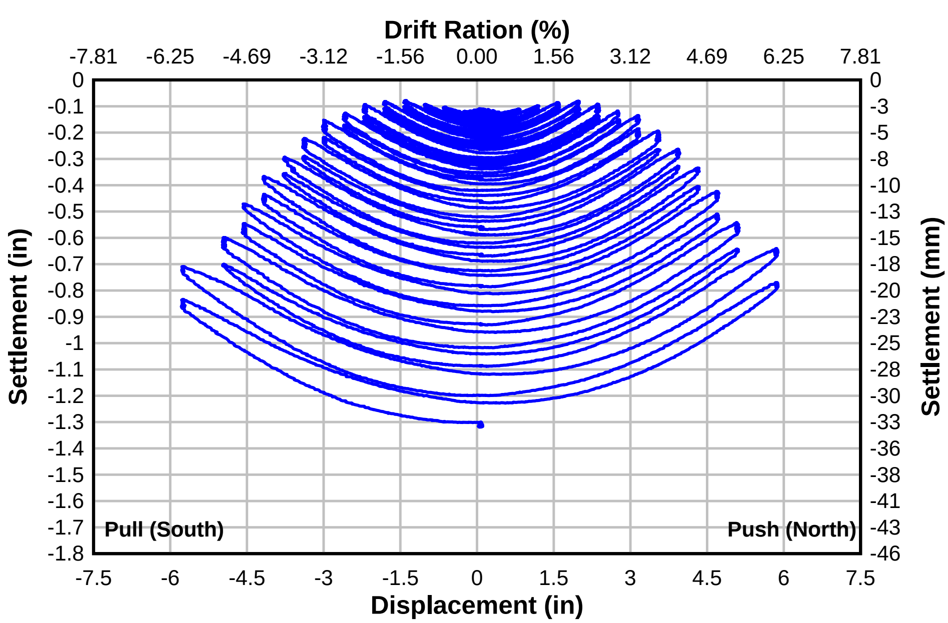

Figure C.3.8 – Settlement – Test 3.

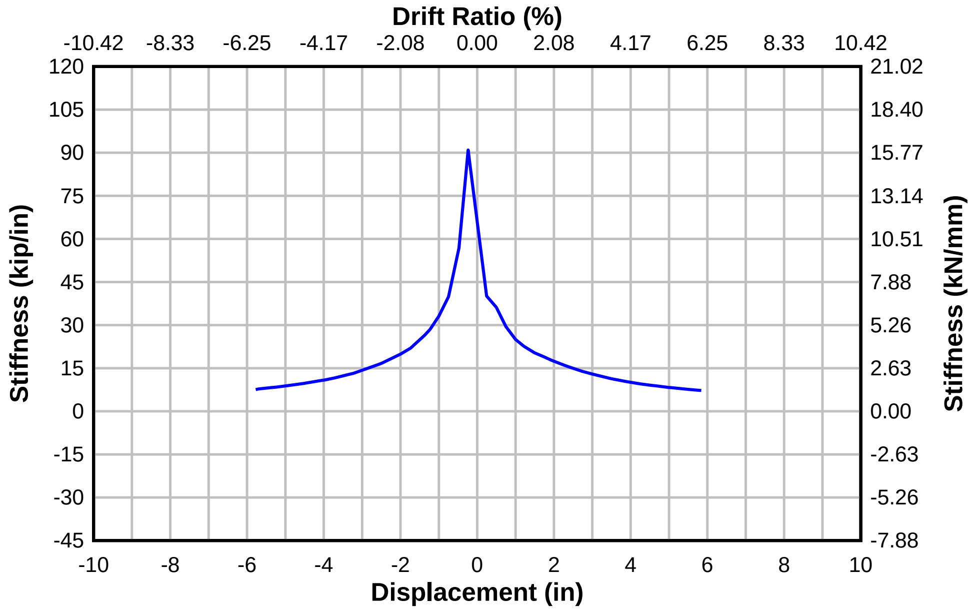

Figure C.3.9 – Evolution of Secant Stiffness – Test 3.

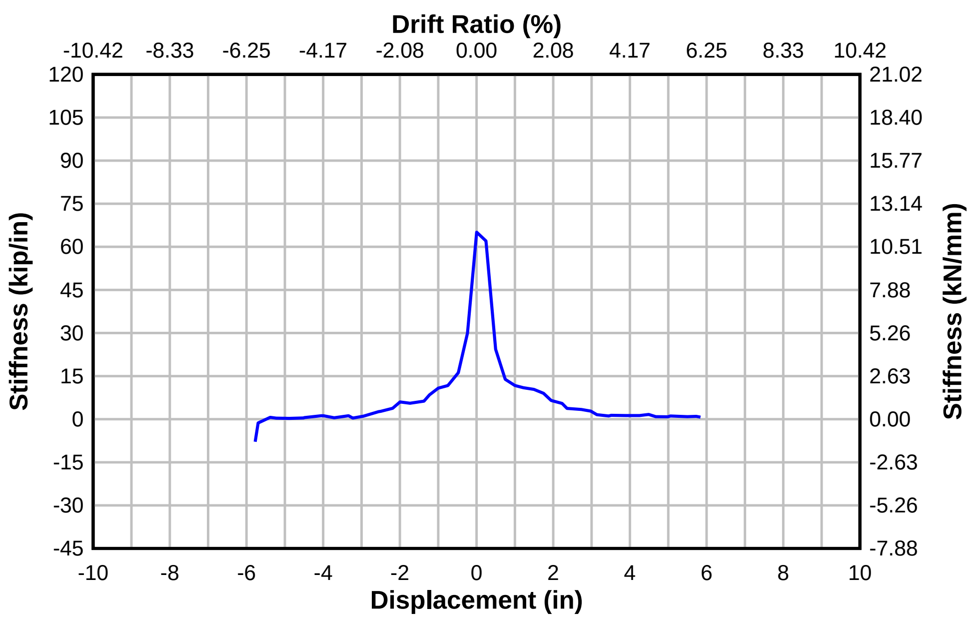

Figure C.3.10 – Evolution of Tangent Stiffness – Test 3.

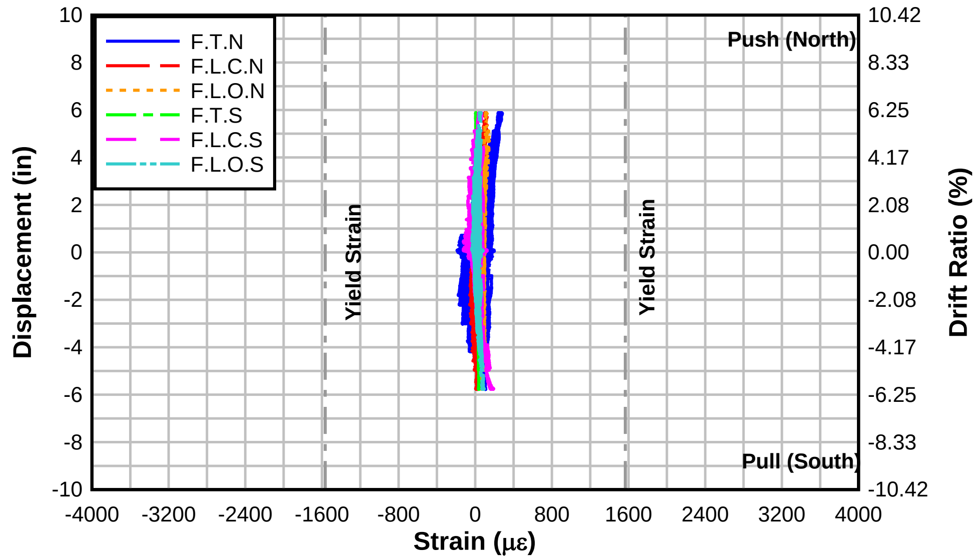

Figure C.3.11 – Footing Bar Strains – Test 3.

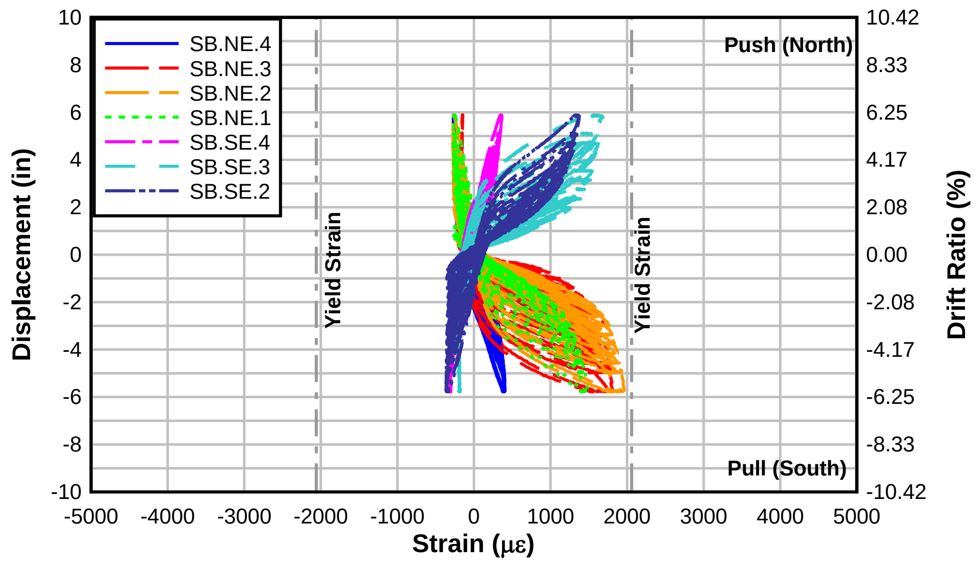

Figure C.3.12 – Starter Bar Strains – Test 3.

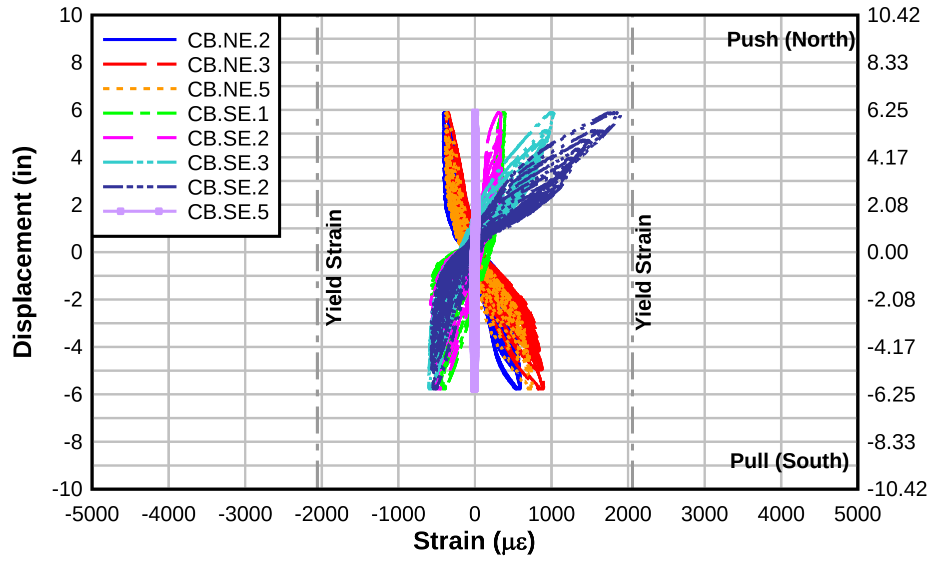

Figure C.3.13 – Column Bar Strains – Test 3.

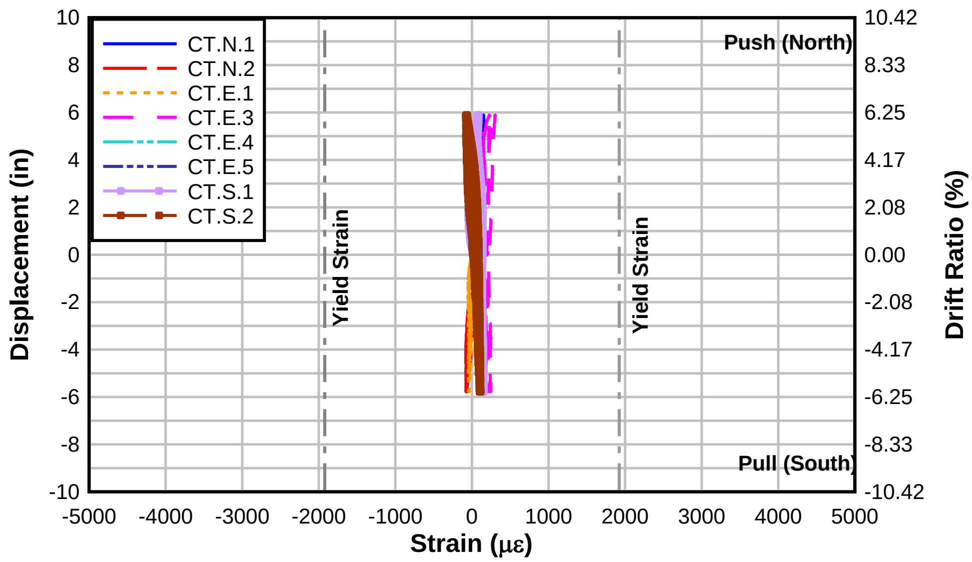

Figure C.3.14 – Column Tie Strains – Test 3.

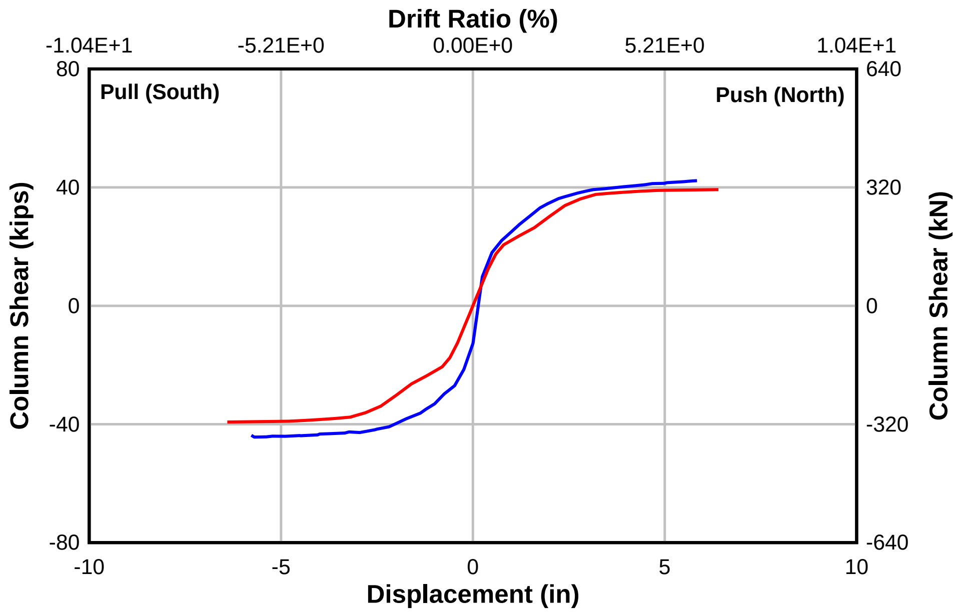

Figure C.3.15 – Soil Simulant Model Comparison – Test 3.

C.4 Test 4 – Specimen 3: Vintage with Foam Embedment, Subgrade, & 100 kip Axial Load

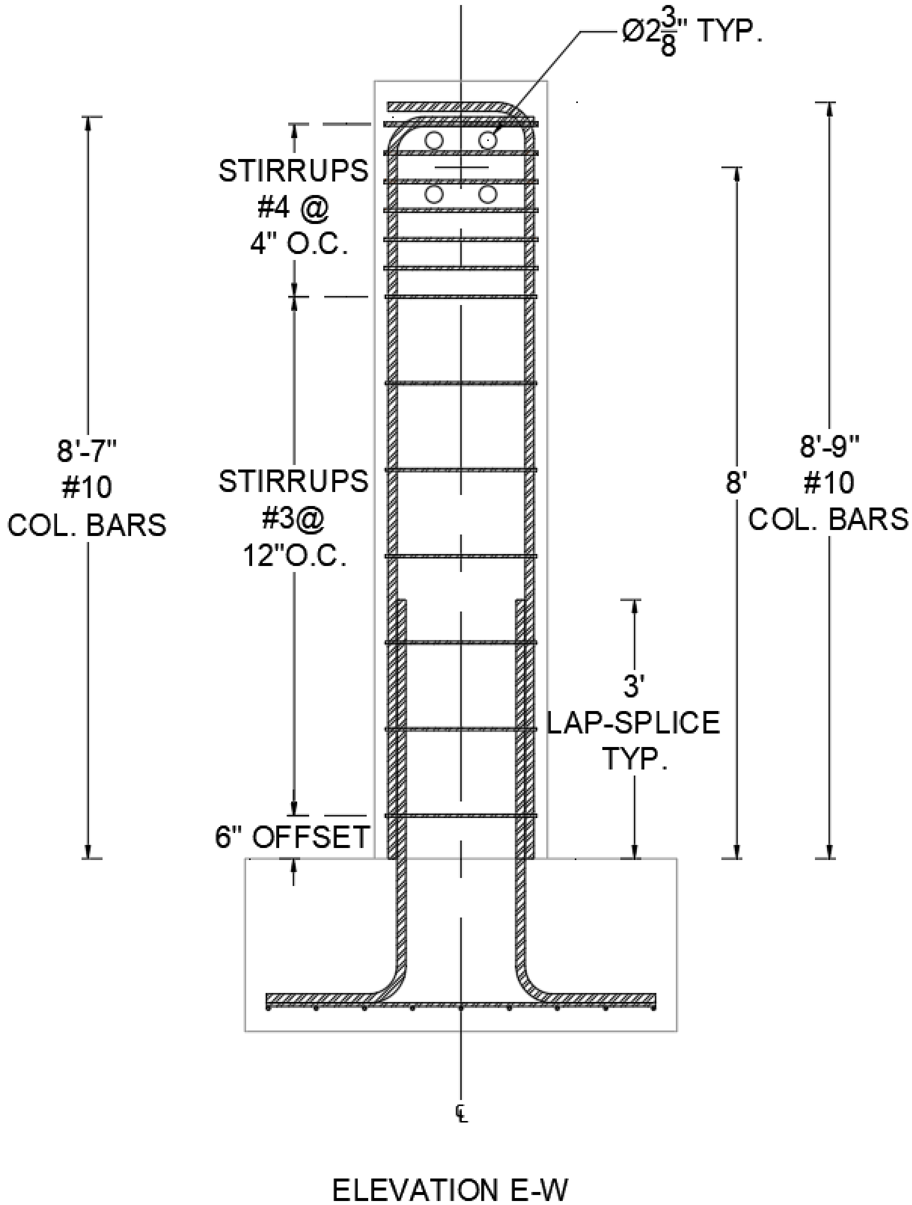

Figure C.4.1 - Elevation View of Specimen 3 used in Test 4.

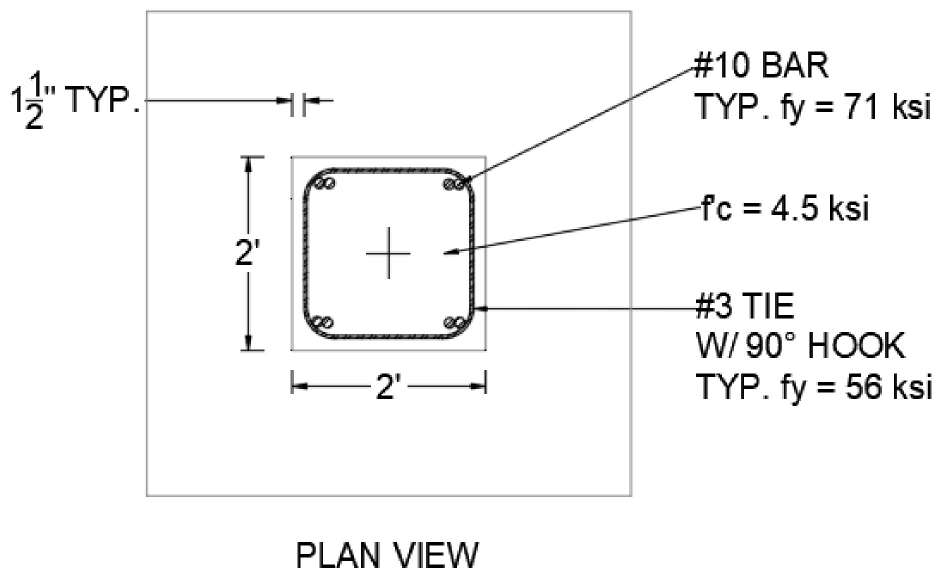

Figure C.4.2 - Plan View of Specimen 3 used in Test 4.

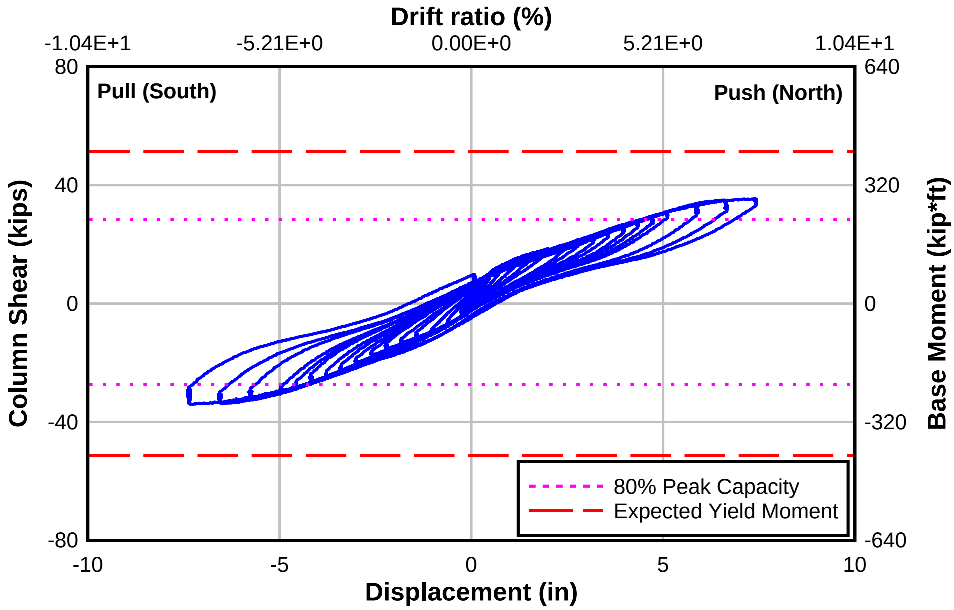

Figure C.4.3 – Overall Force Displacement Response -Test 4.

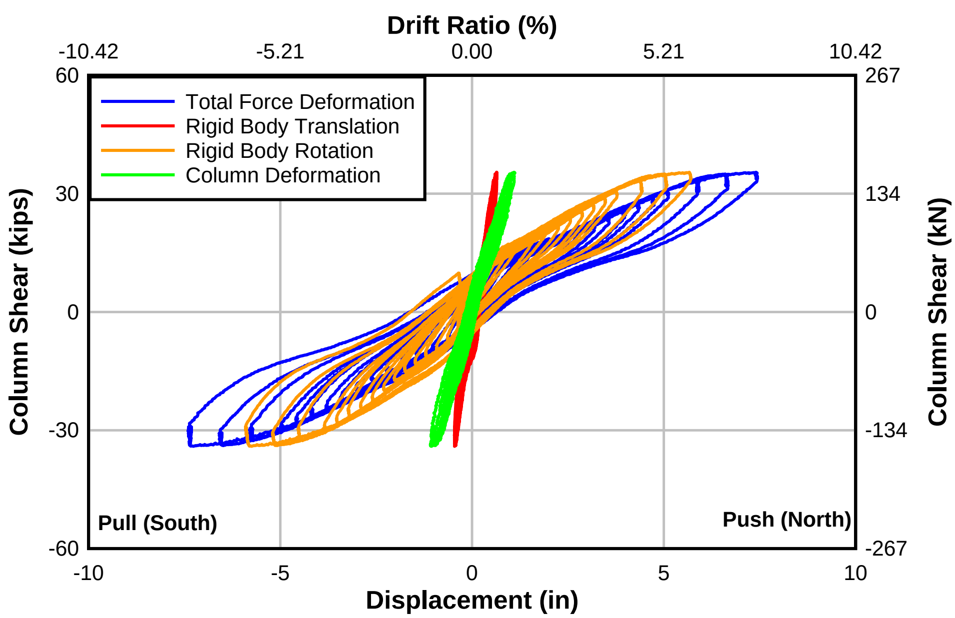

Figure C.4.4 – Component Contributions to Force Displacement – Test 4.

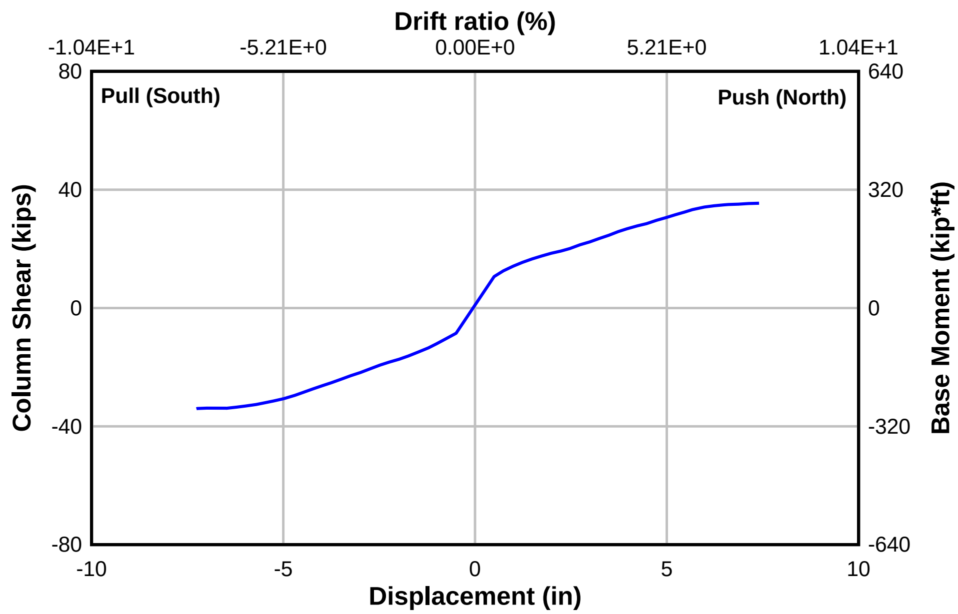

Figure C.4.5 – Overall Force Displacement Backbone Curve – Test 4.

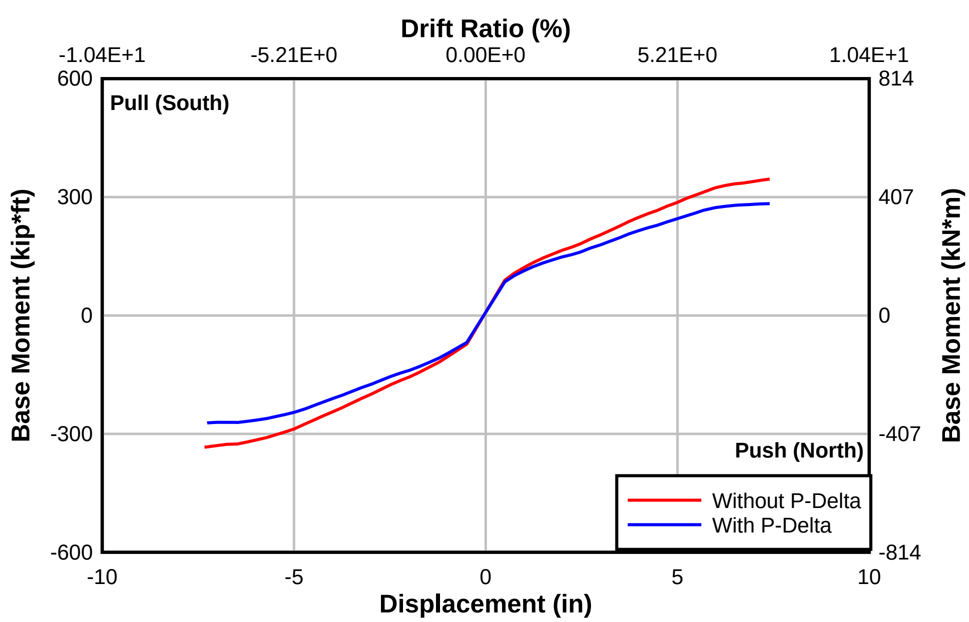

Figure C.4.6 – P-Delta Effects Backbone Curve – Test 4.

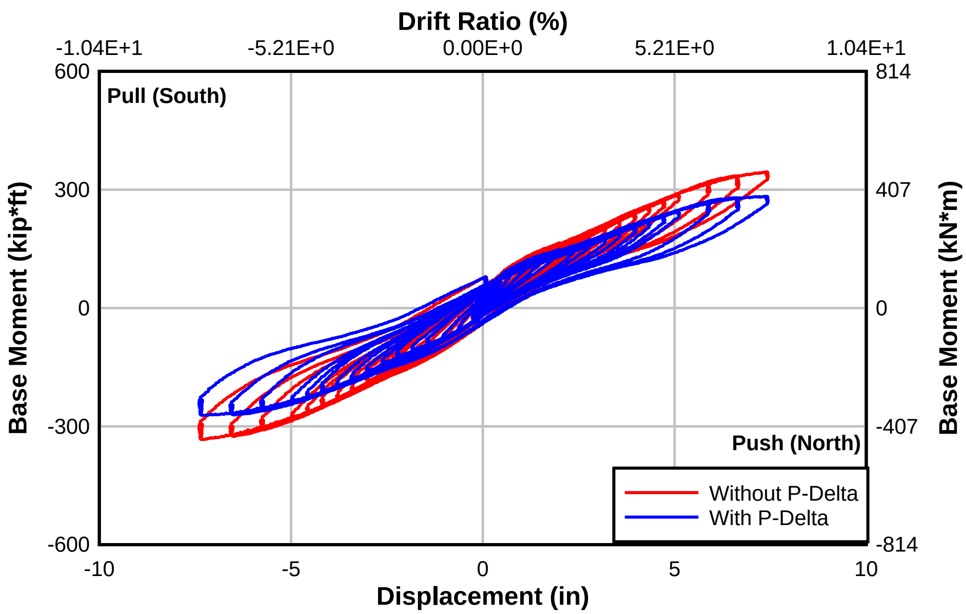

Figure C.4.7 – P-Delta Effects – Test 4.

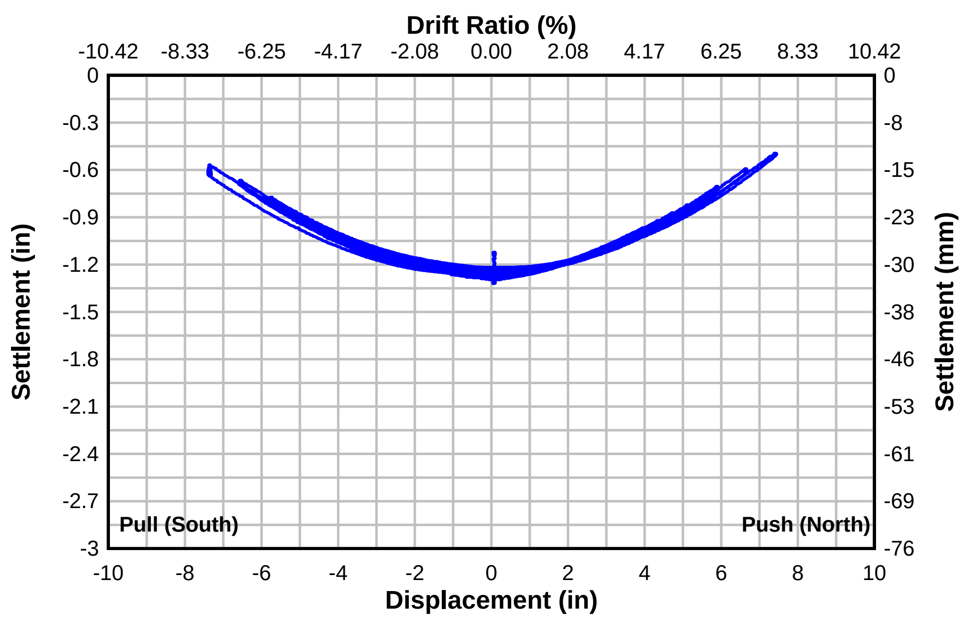

Figure C.4.8 – Settlement – Test 4.

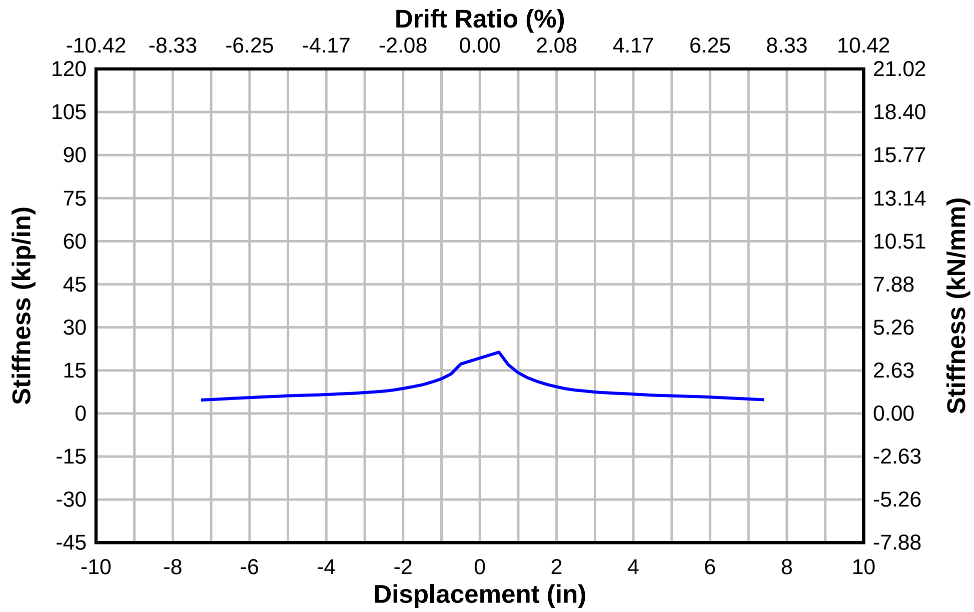

Figure C.4.9 – Evolution of Secant Stiffness – Test 4.

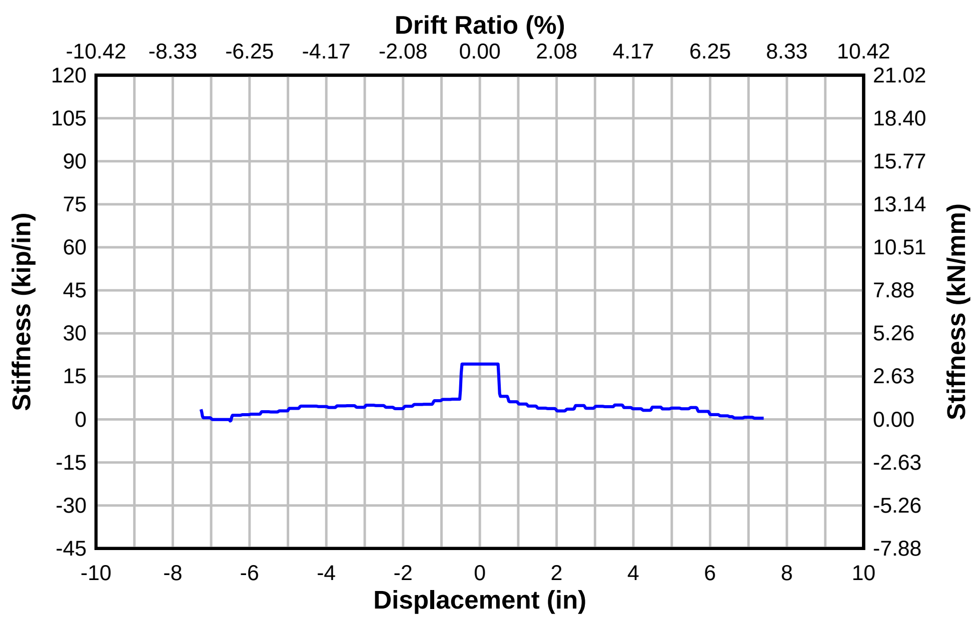

Figure C.4.10 – Evolution of Tangent Stiffness – Test 4.

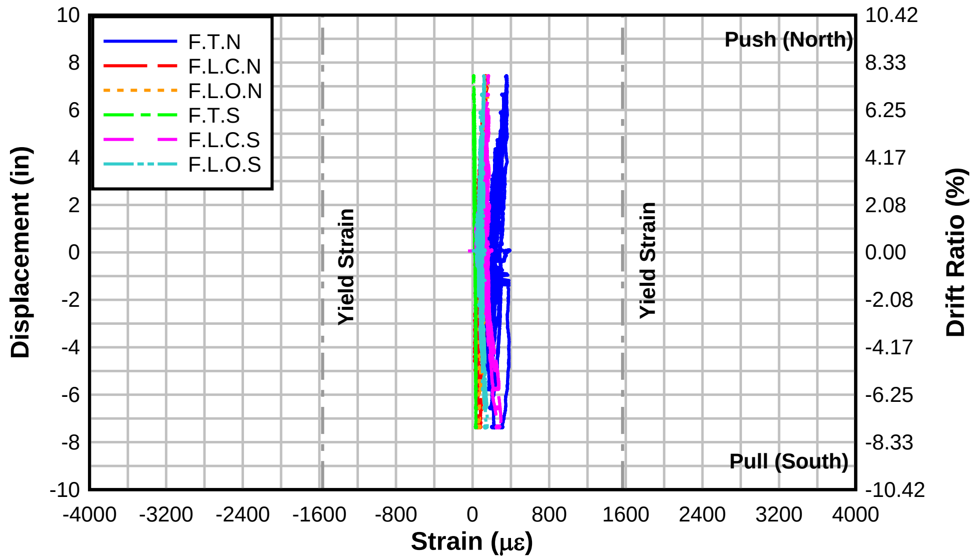

Figure C.4.11 – Footing Bar Strains – Test 4.

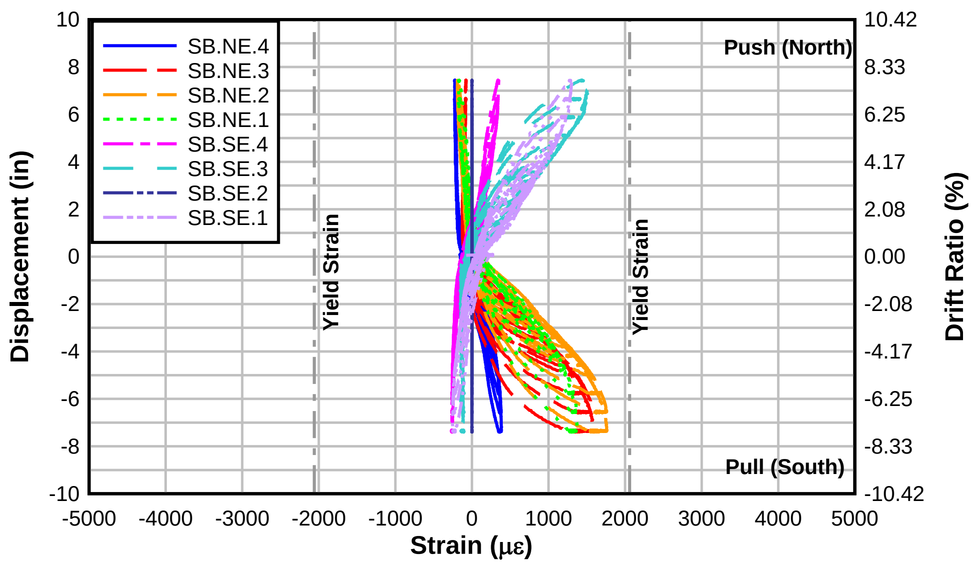

Figure C.4.12 – Starter Bar Strains – Test 4.

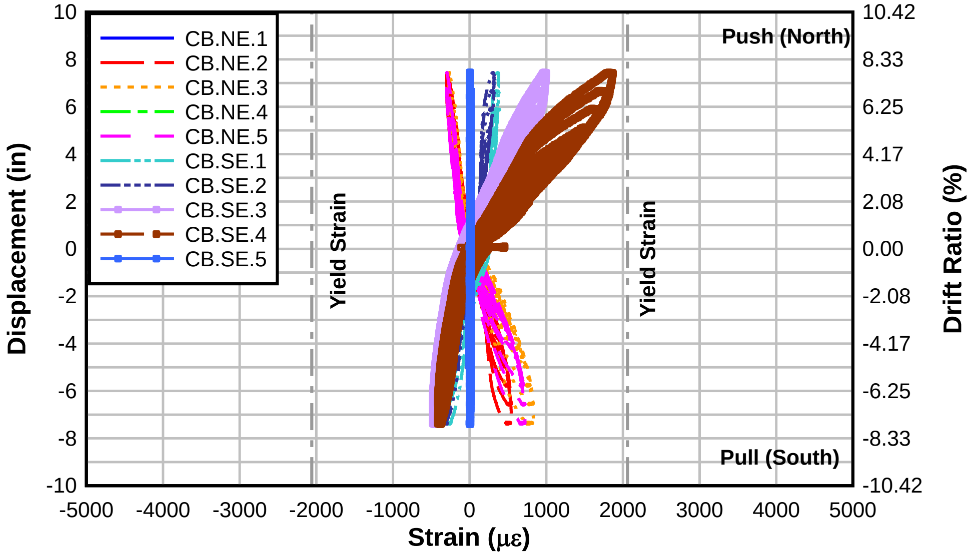

Figure C.4.13 – Column Bar Strains – Test 4.

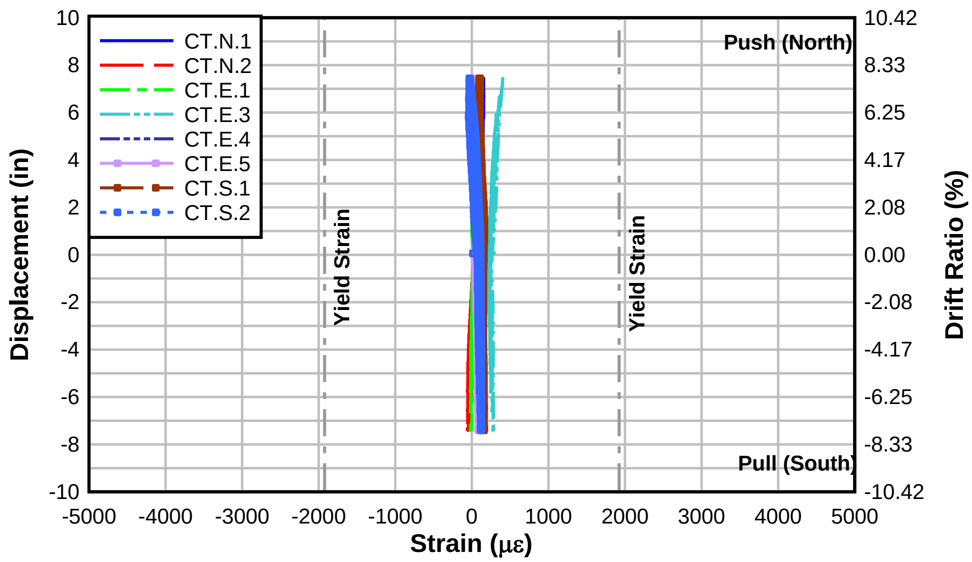

Figure C.4.14 – Column Tie Strains – Test 4.

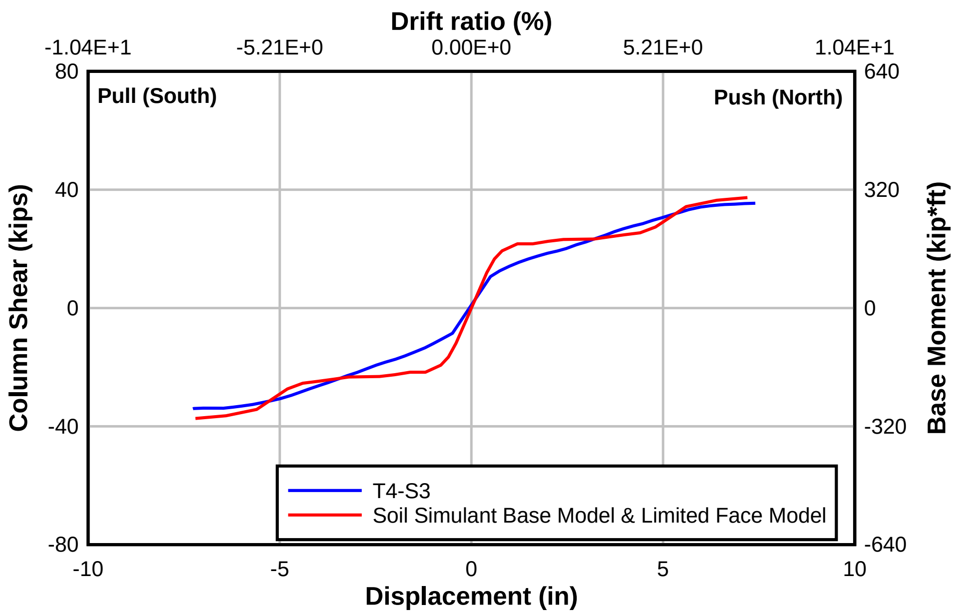

Figure C.4.14 – Soil Simulant Model – Test 4.

C.5 Test 5 – Specimen 3 -Vintage Failure with Foam Subgrade & Steel Embedment

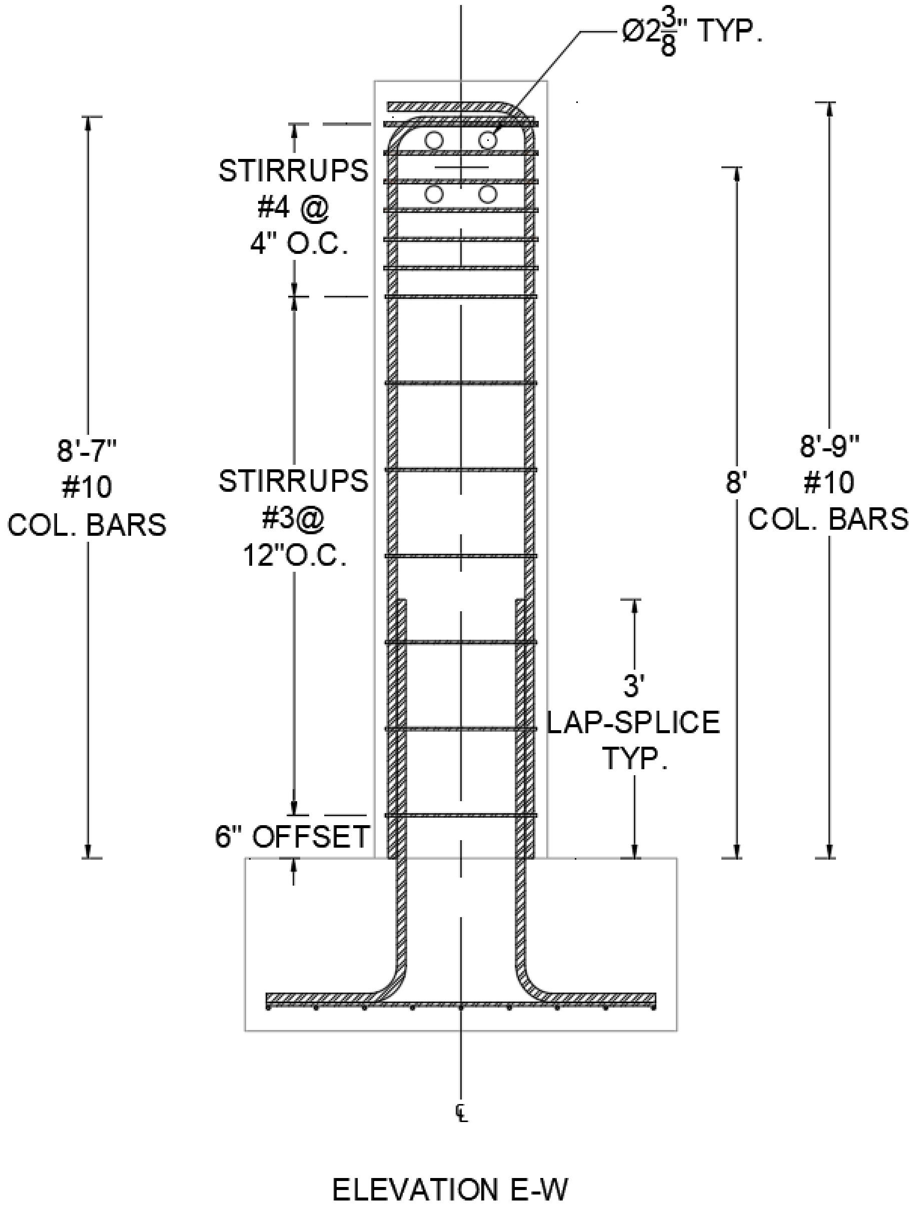

Figure C.5.1 - Elevation View of Specimen 3 used in Test 5.

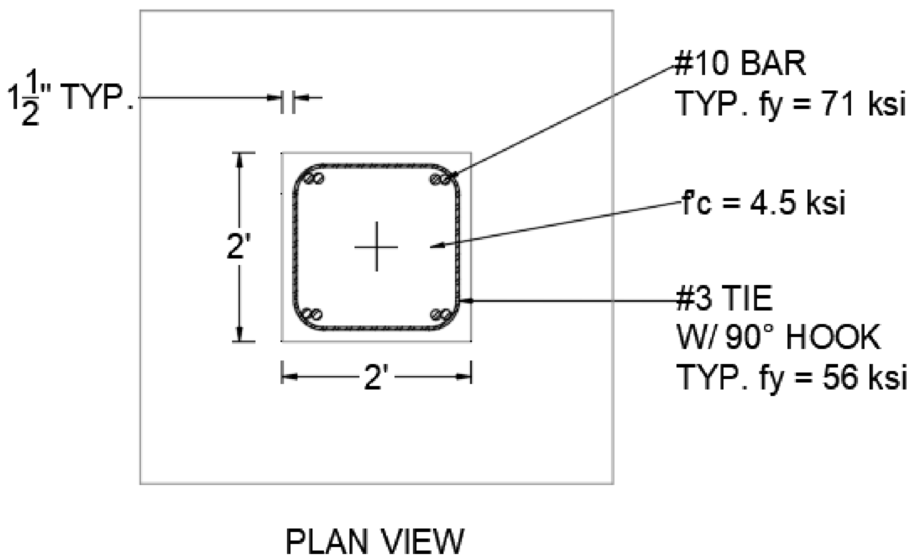

Figure C.5.2 - Plan View of Specimen 3 used in Test 5.

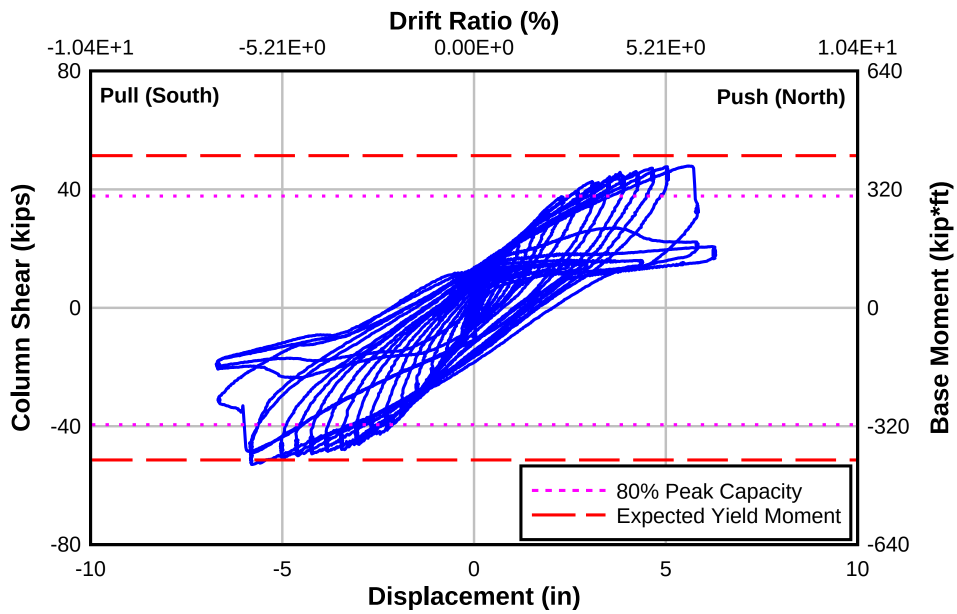

Figure C.5.3 – Overall Force Displacement Response – Test 5.

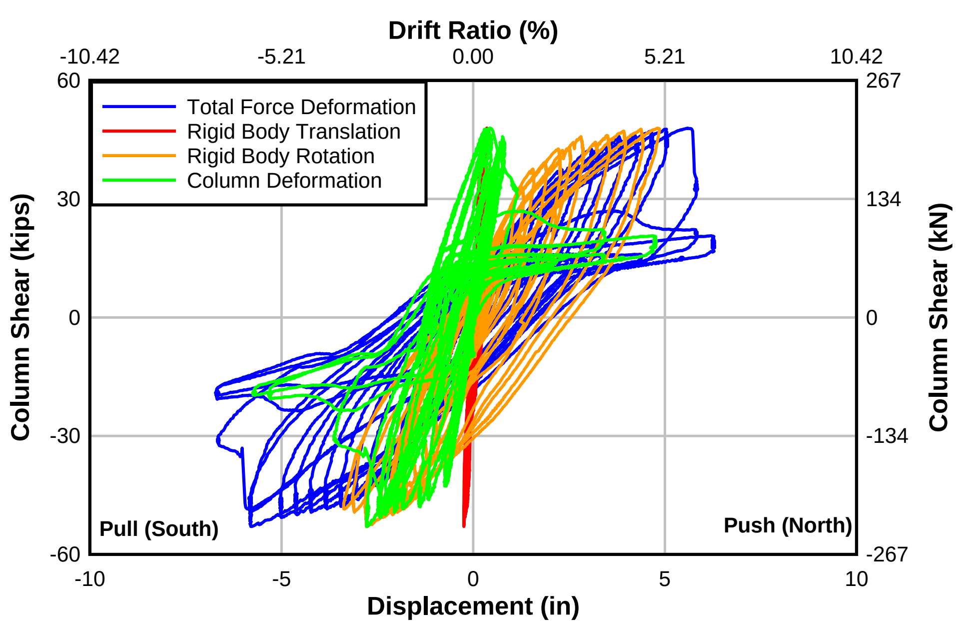

Figure C.5.4 – Component Contributions to Force Displacement – Test 5.

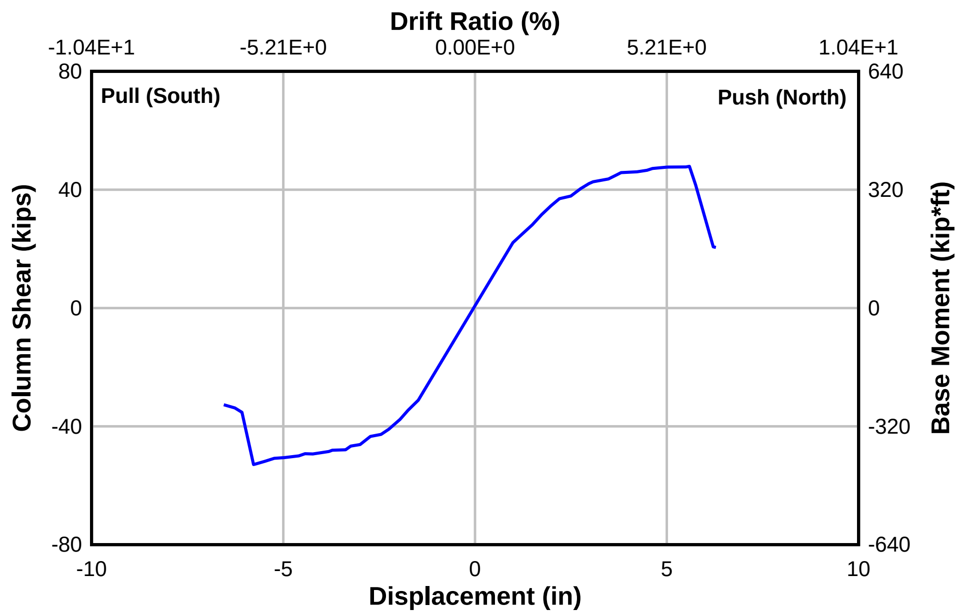

Figure C.5.5 – Overall Force Displacement Backbone Curve – Test 5.

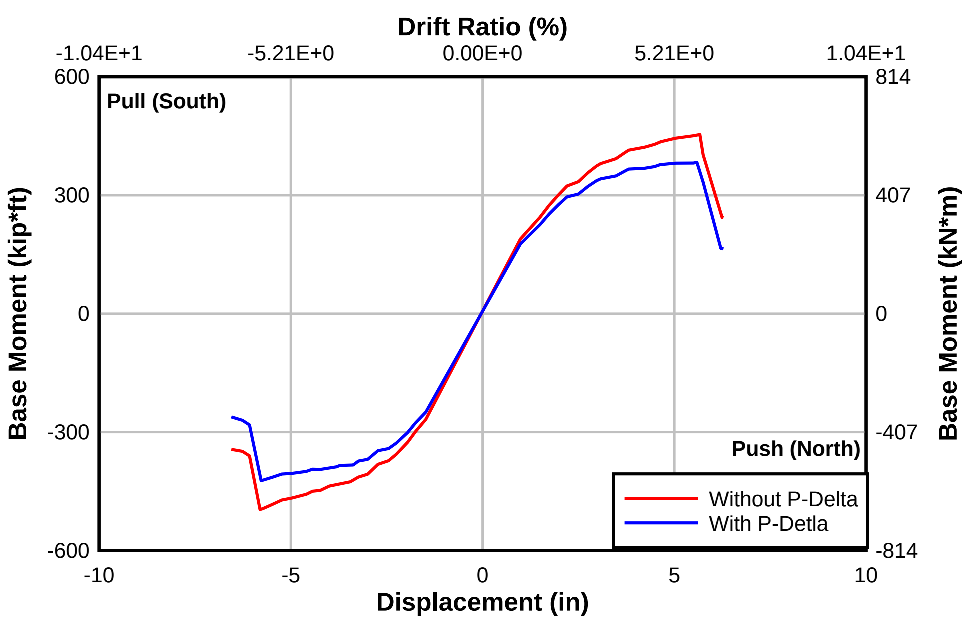

Figure C.5.6 – P-Delta Effects Backbone Curve – Test 5.

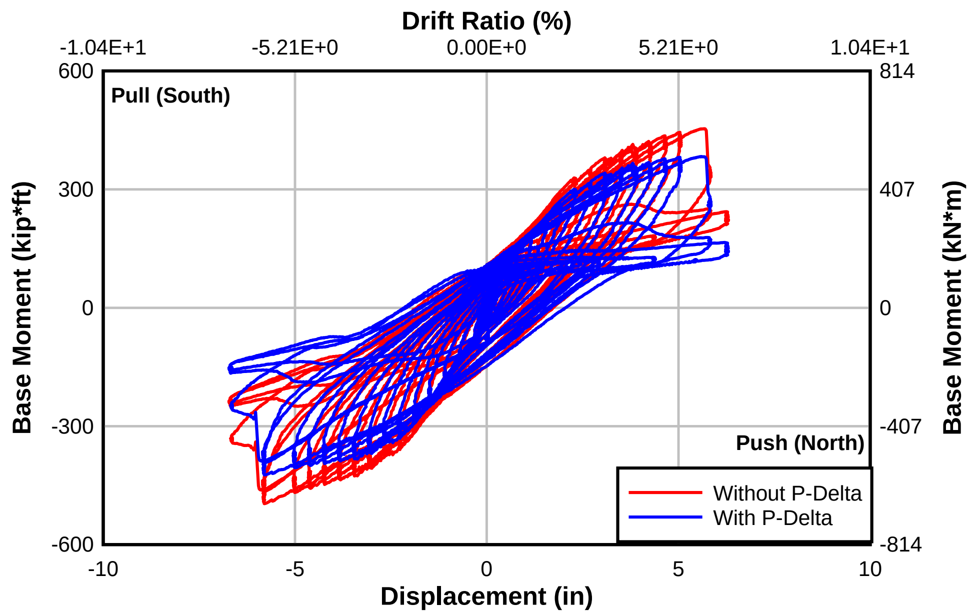

Figure C.5.7 – P-Delta Effects – Test 5.

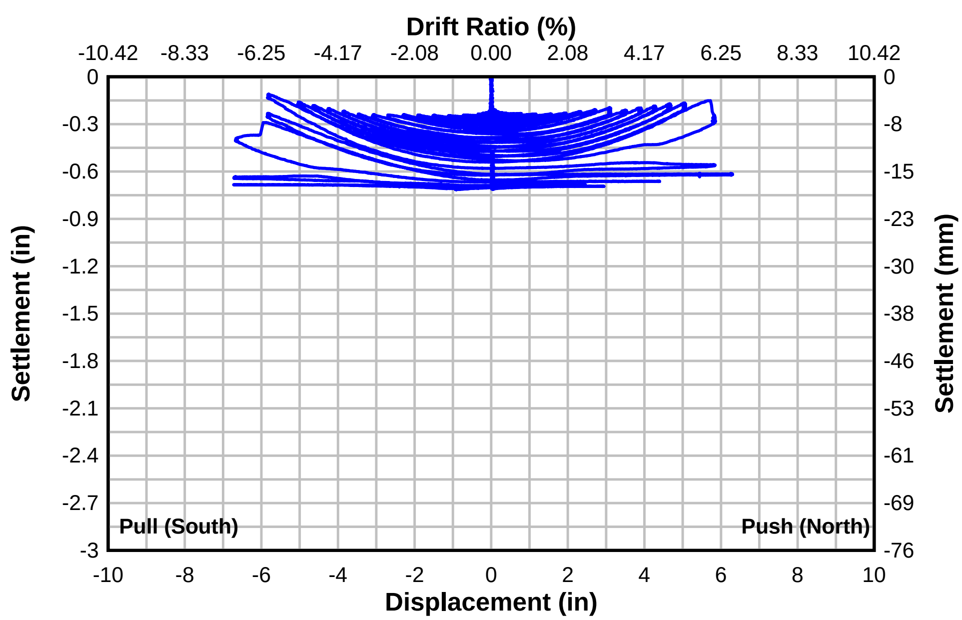

Figure C.5.8 – Settlement – Test 5.

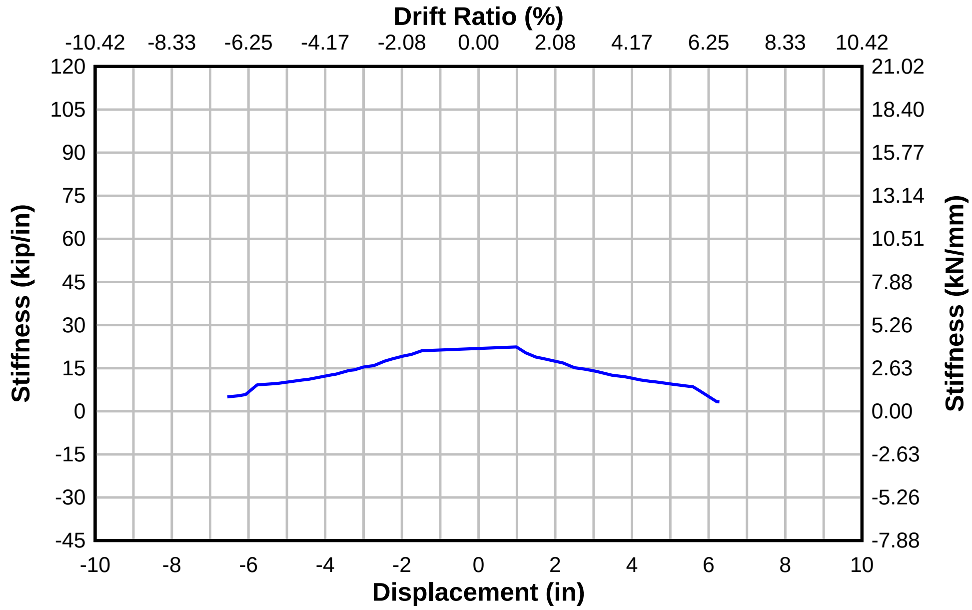

Figure C.5.9 – Evolution of Secant Stiffness – Test 5.

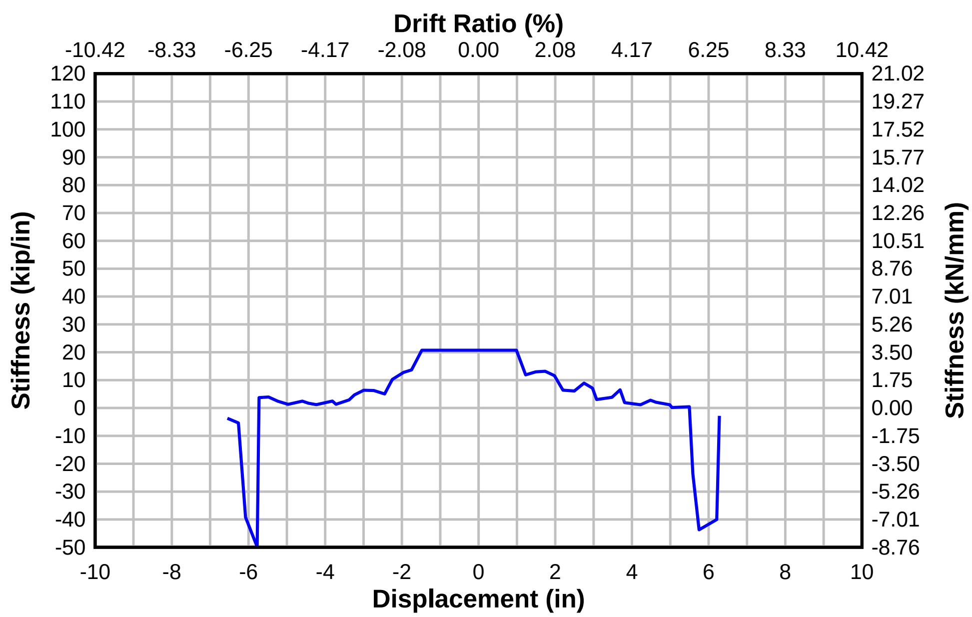

Figure C.5.10 – Evolution of Tangent Stiffness – Test 5.

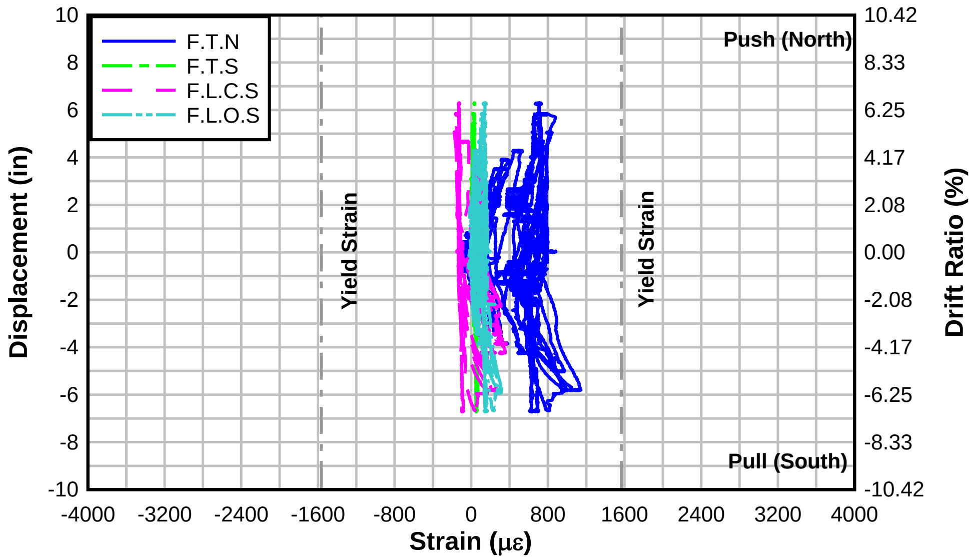

Figure C.5.11 – Footing Bar Strains – Test 5.

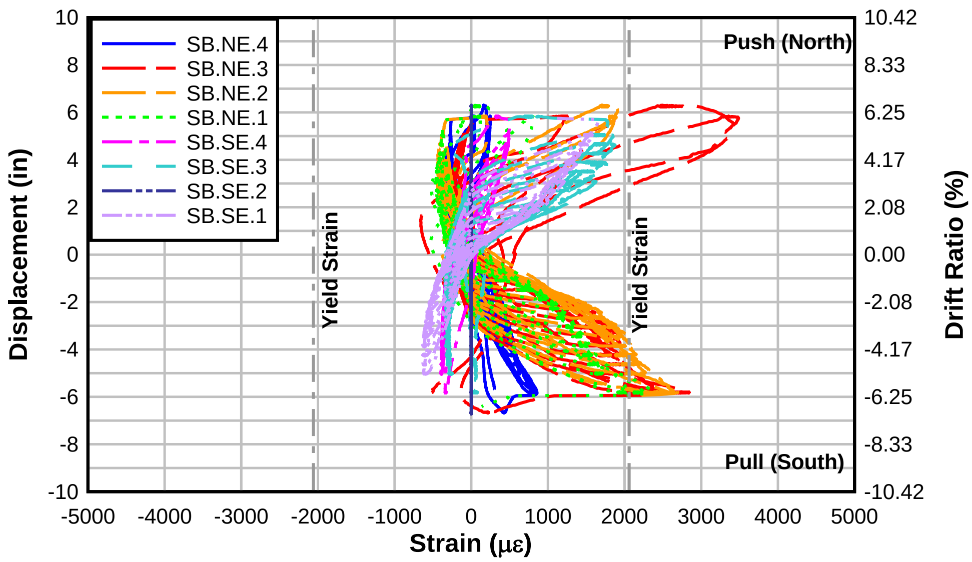

Figure C.5.12 – Starter Bar Strains – Test 5.

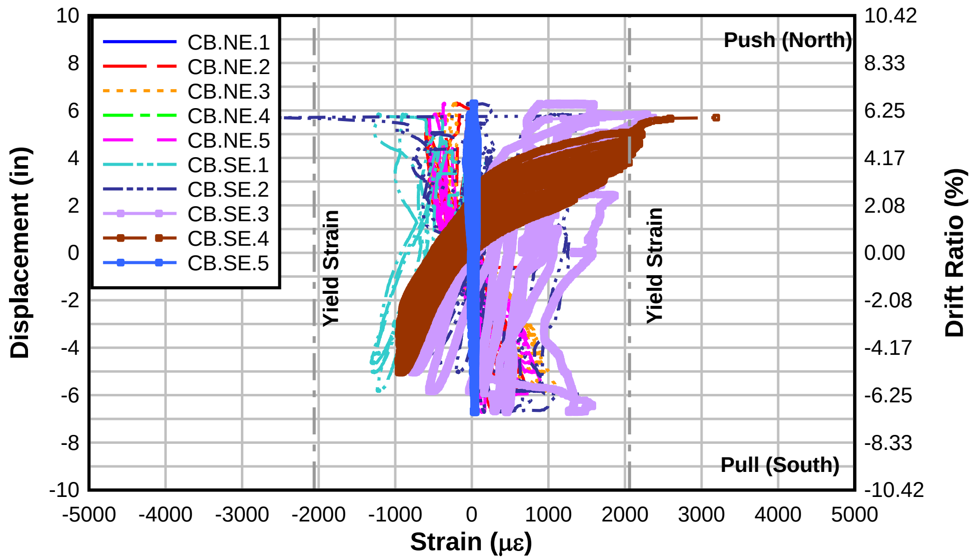

Figure C.5.13 – Column Bar Strains – Test 5.

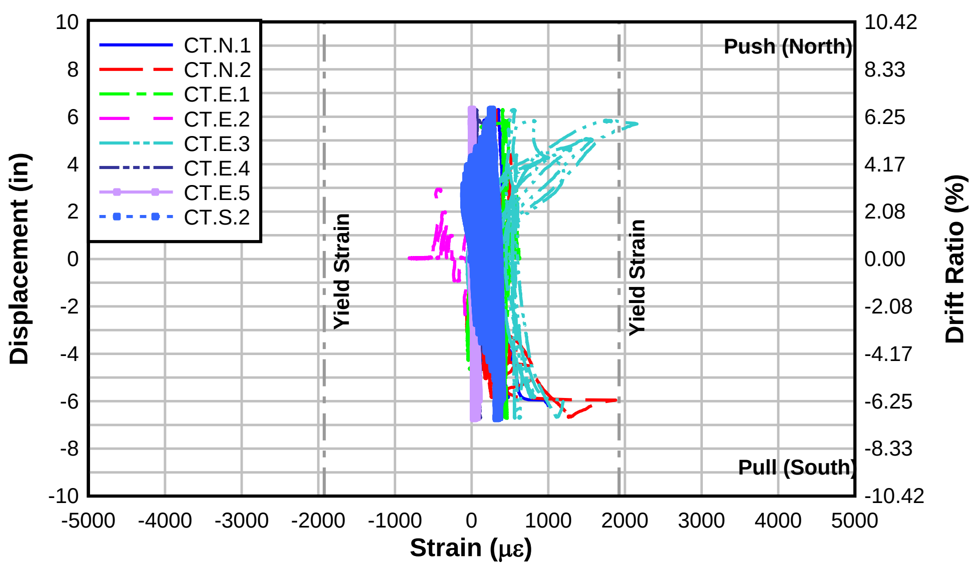

Figure C.5.14 – Column Tie Strains – Test 5.

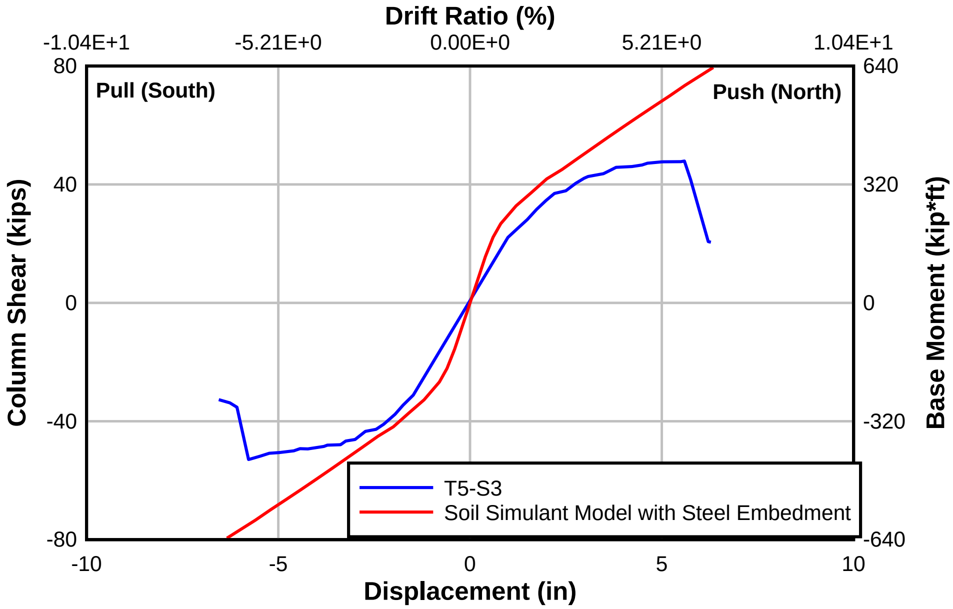

Figure C.5.15 – Soil Simulant Model – Test 5.

C.6 Test 6 – Specimen 3: Vintage TiAB Ligament Retrofit with Foam Subgrade & Steel Embedment

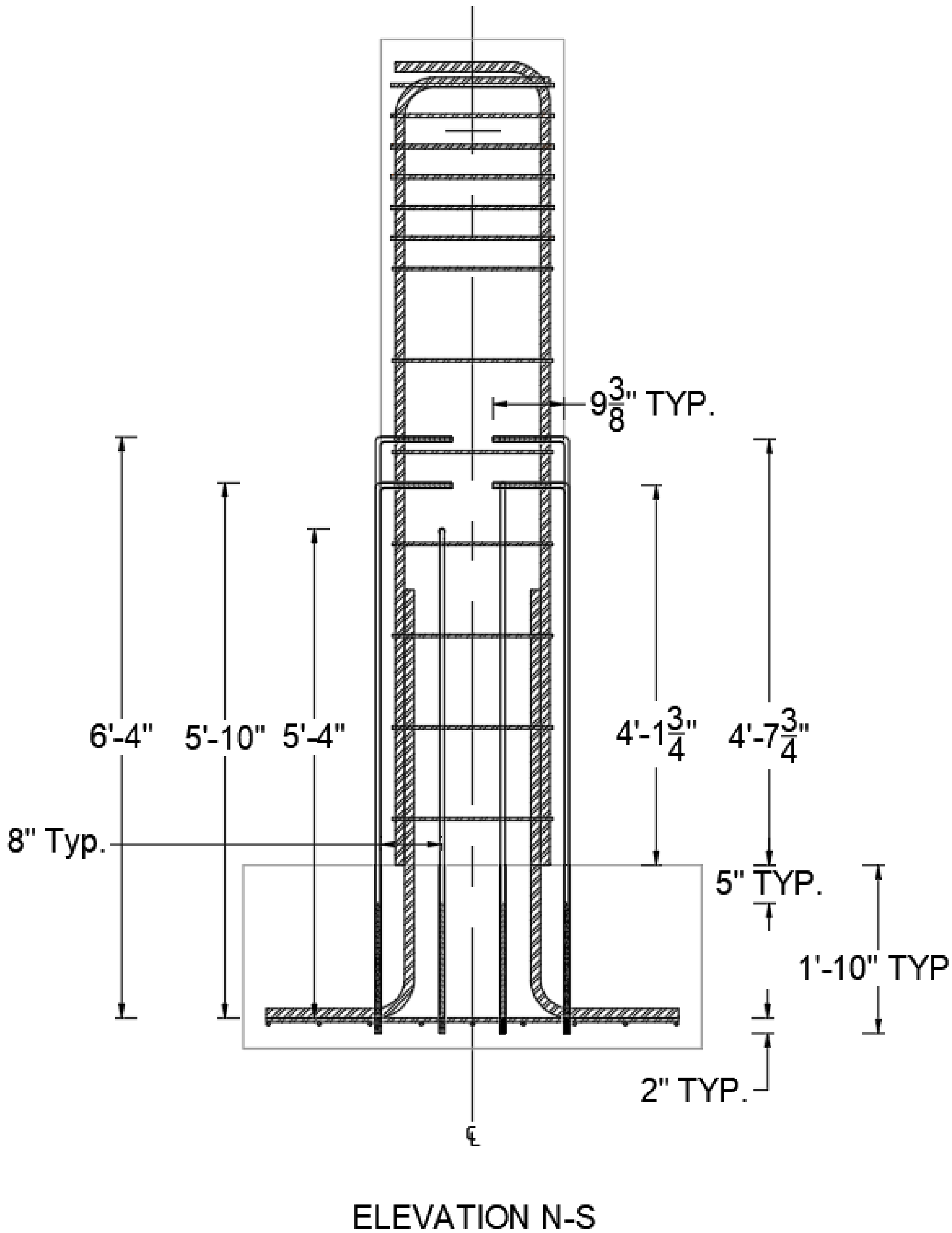

Figure C.6.1 - Elevation View of Specimen 3 used in Test 6.

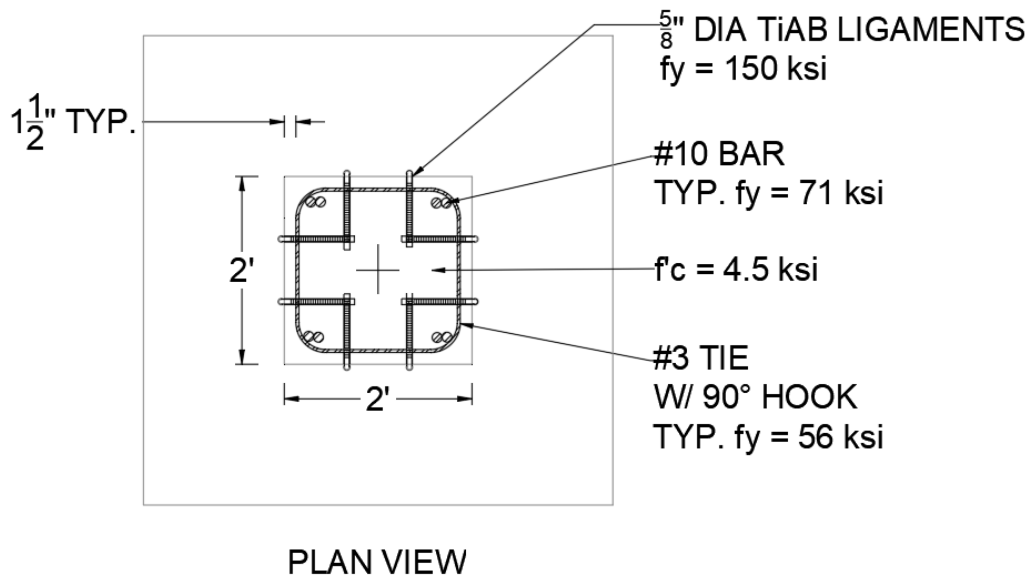

Figure C.6.2 - Plan View of Specimen 3 used in Test 6.

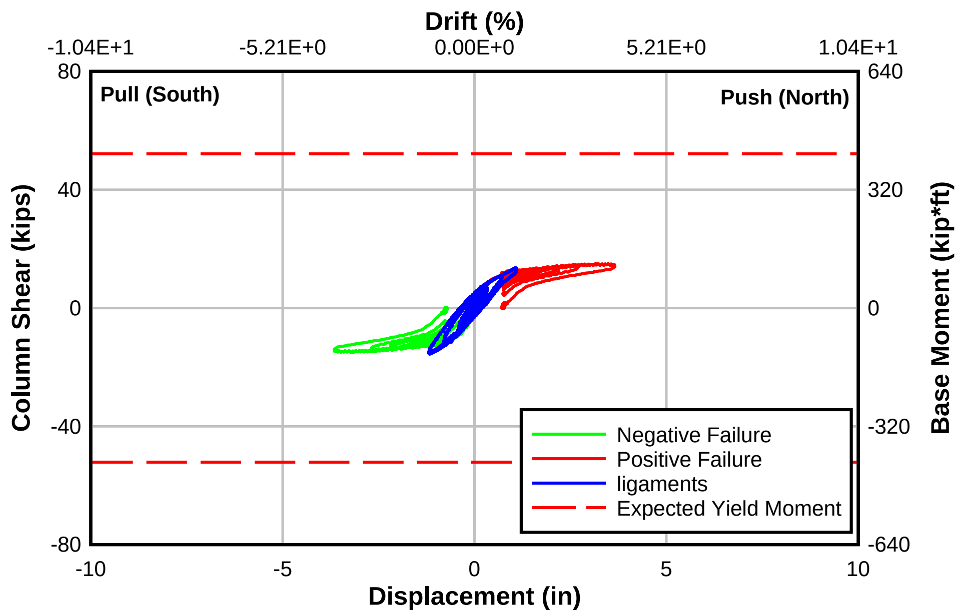

Figure C.6.3 – Overall Force Displacement Response – Test 6.

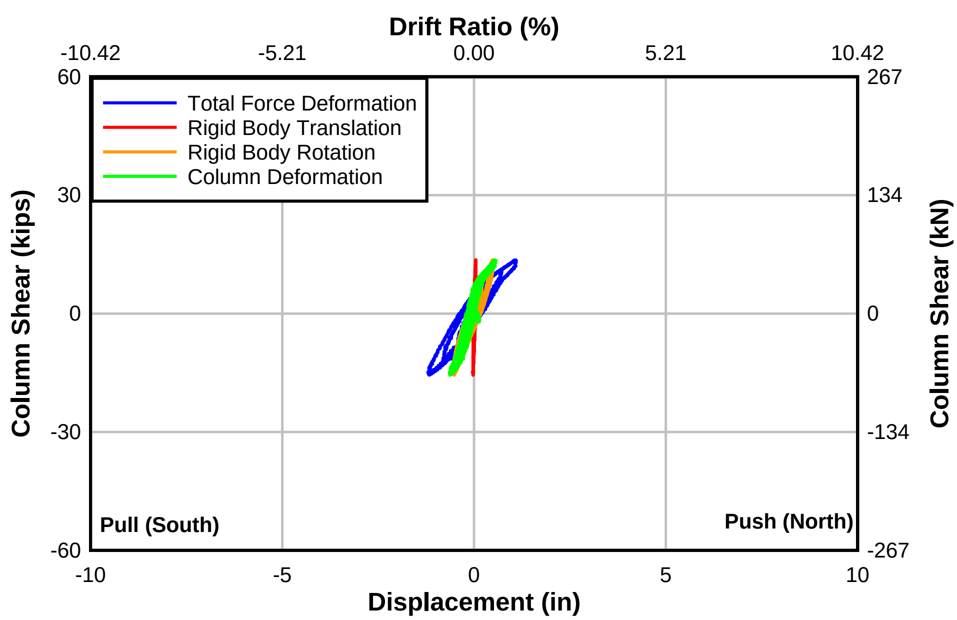

Figure C.6.4 – Component Contributions to Force Displacement – Test 6.

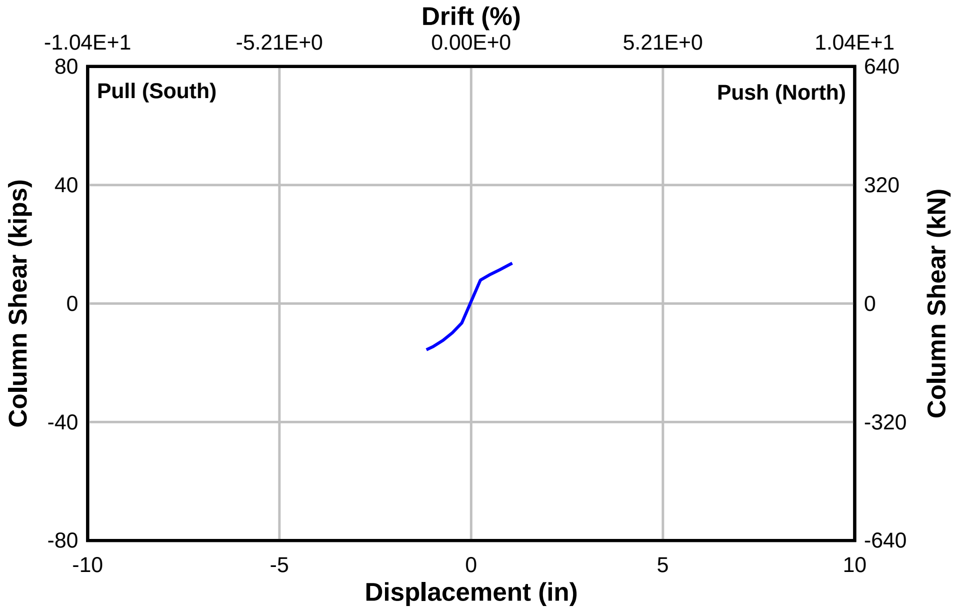

Figure C.6.5 – Overall Force Displacement Backbone Curve – Test 6.

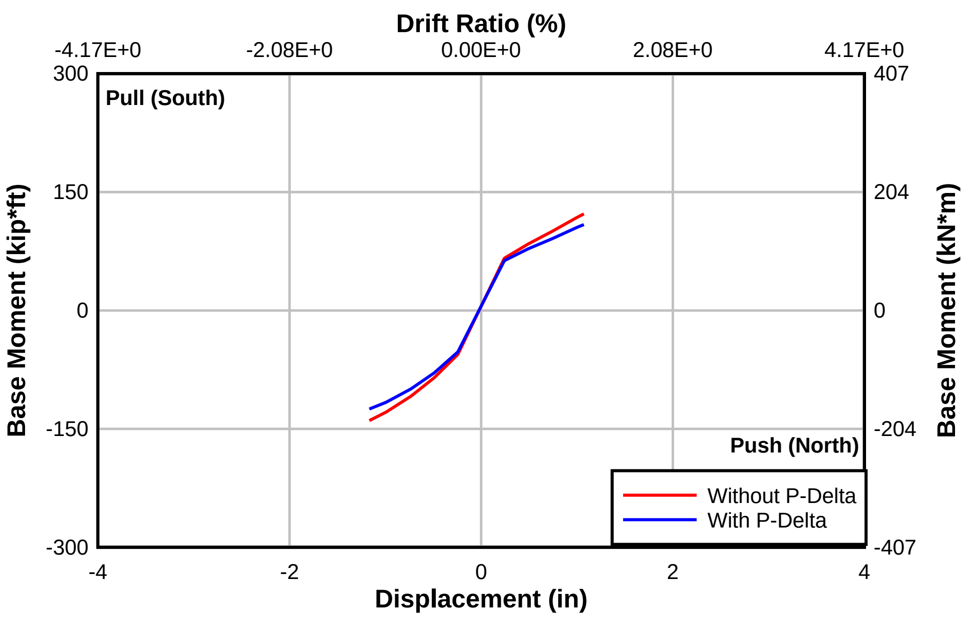

Figure C.6.6 – P-Delta Effects Backbone Curve – Test 6.

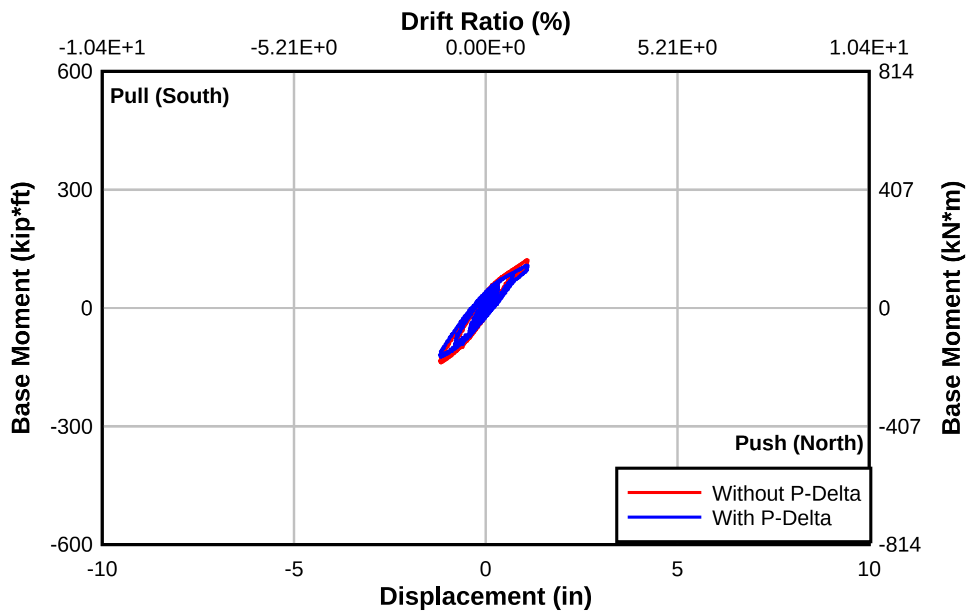

Figure C.6.7 – P-Delta Effects – Test 6.

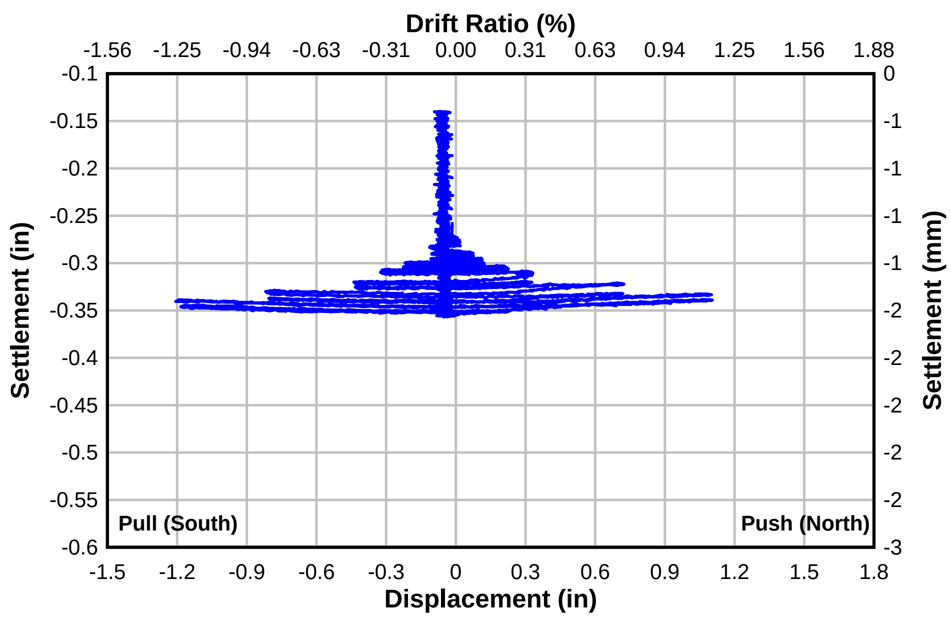

Figure C.6.8 – Settlement – Test 6.

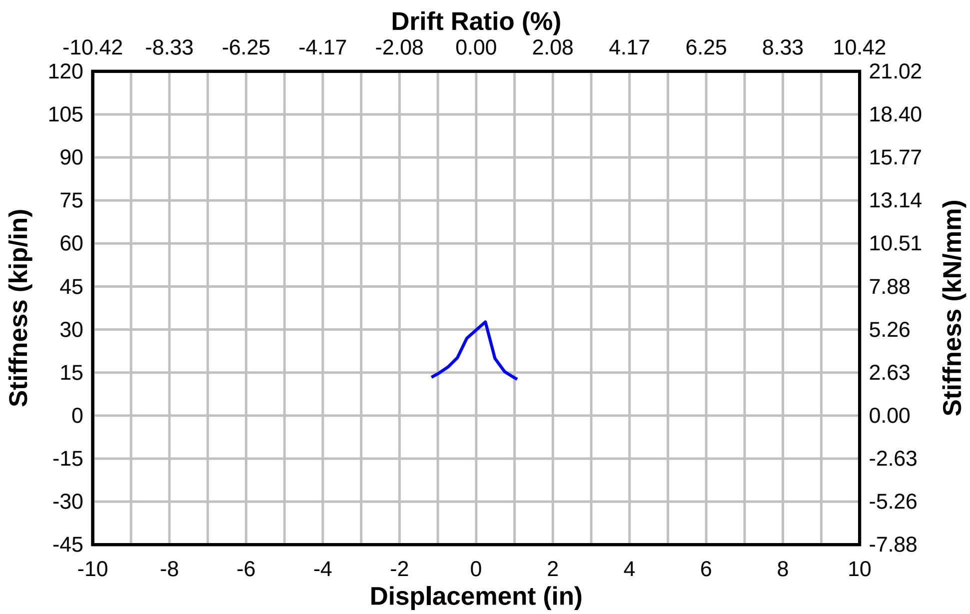

Figure C.6.9 – Evolution of Secant Stiffness – Test 6.

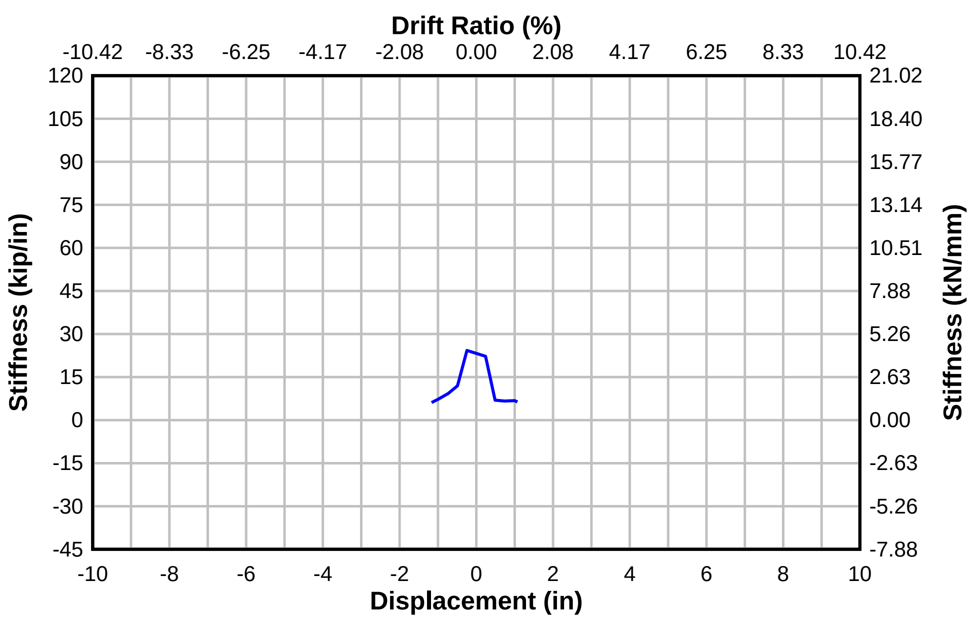

Figure C.6.10 – Evolution of Tangent Stiffness – Test 6.

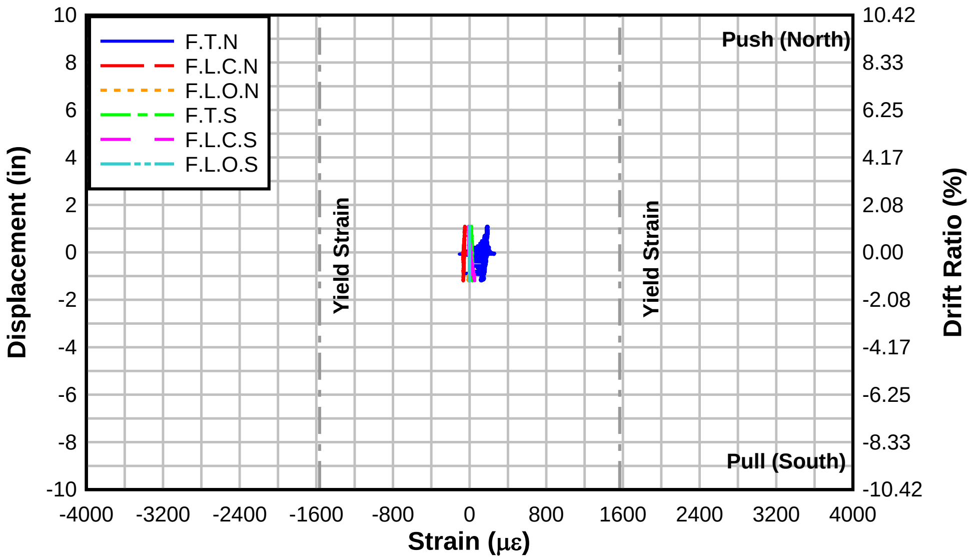

Figure C.6.11 – Footing Bar Strains – Test 6.

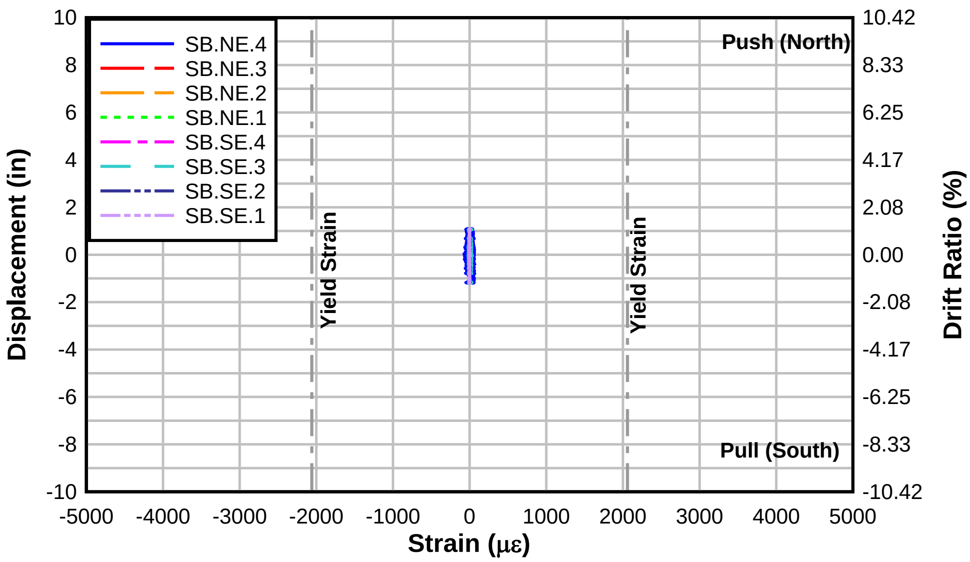

Figure C.6.12 – Starter Bar Strains – Test 6.

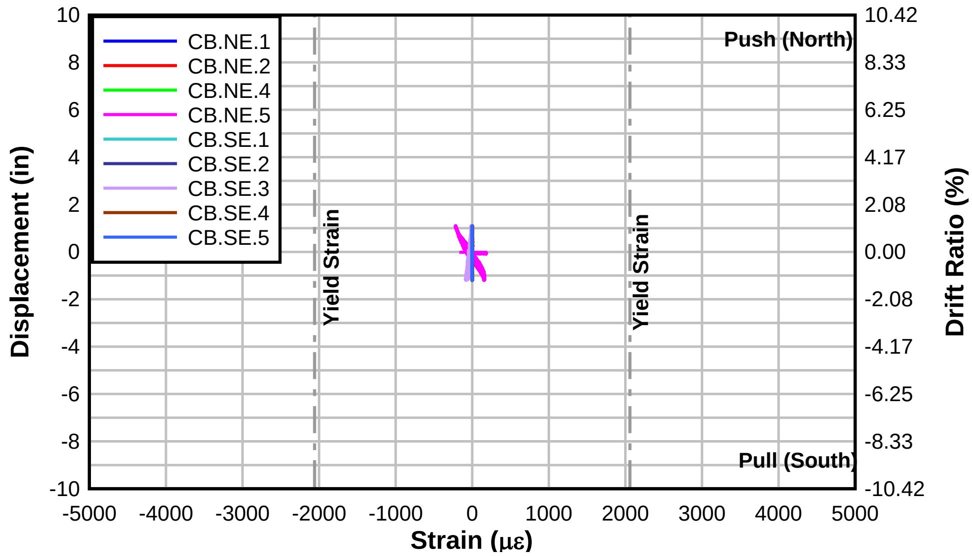

Figure C.6.13 – Column Bar Strains – Test 6.

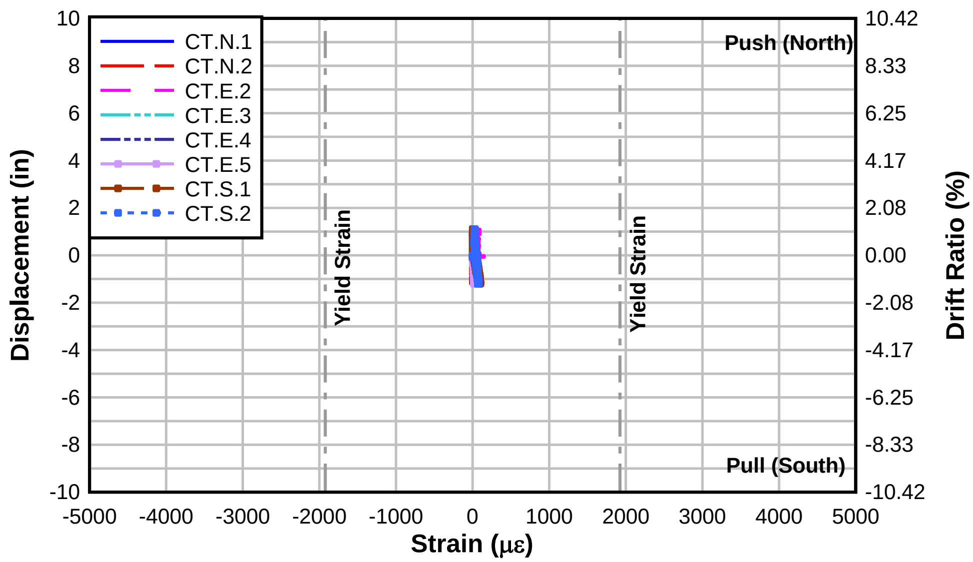

Figure C.6.14 – Column Tie Strains – Test 6.

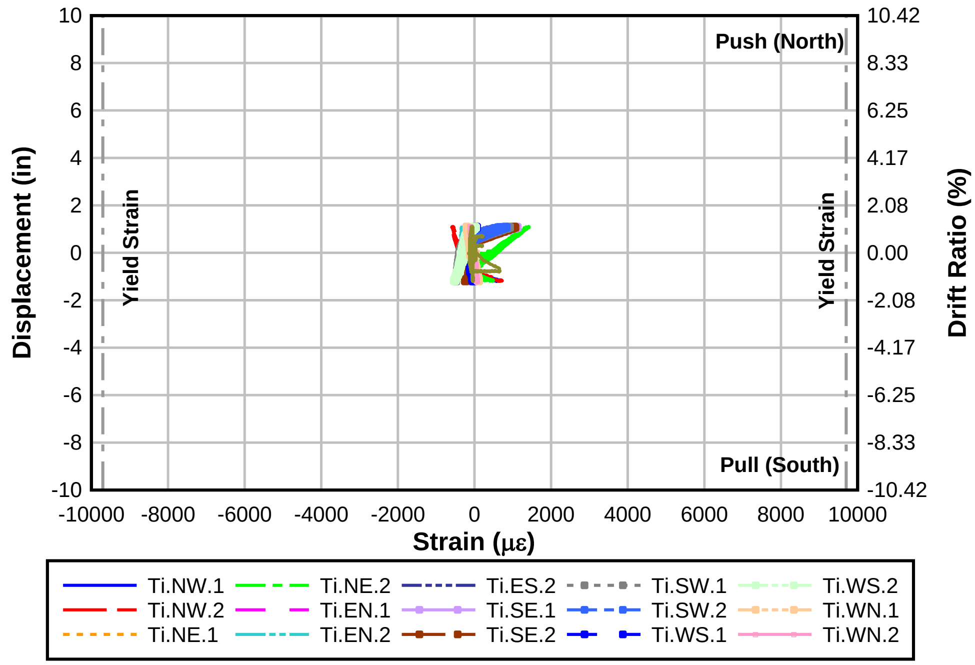

Figure C.6.15 – TiAB Ligament Strains – Test 6.

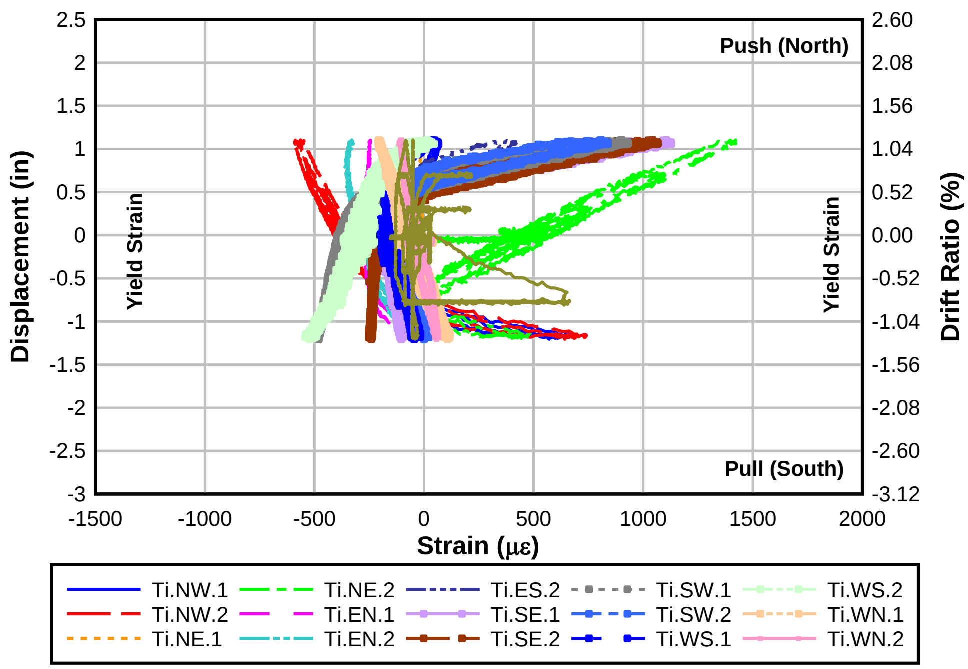

Figure C.6.16 – TiAB Ligament Strains Close Up – Test 6.

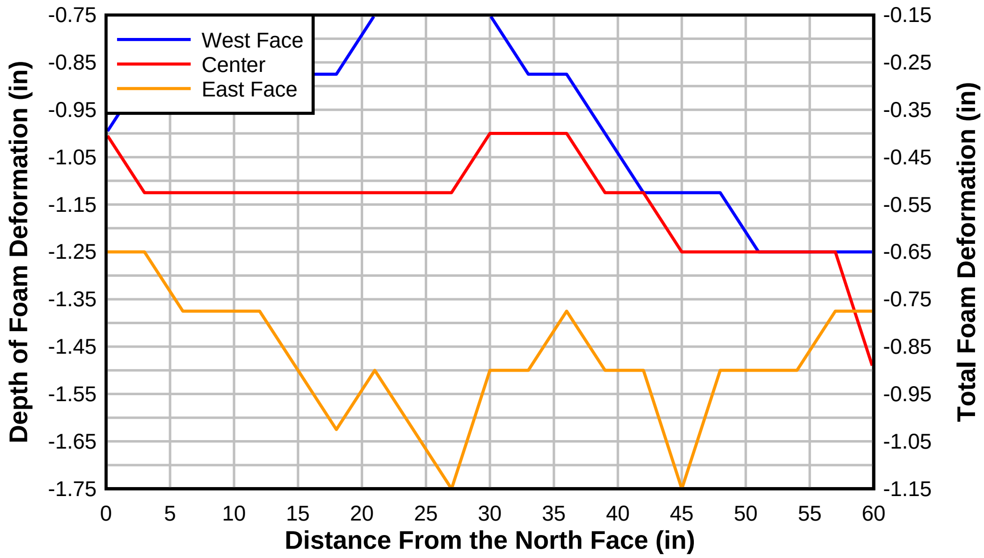

Figure C.6.17 – Soil Simulant Profile After Test 6.

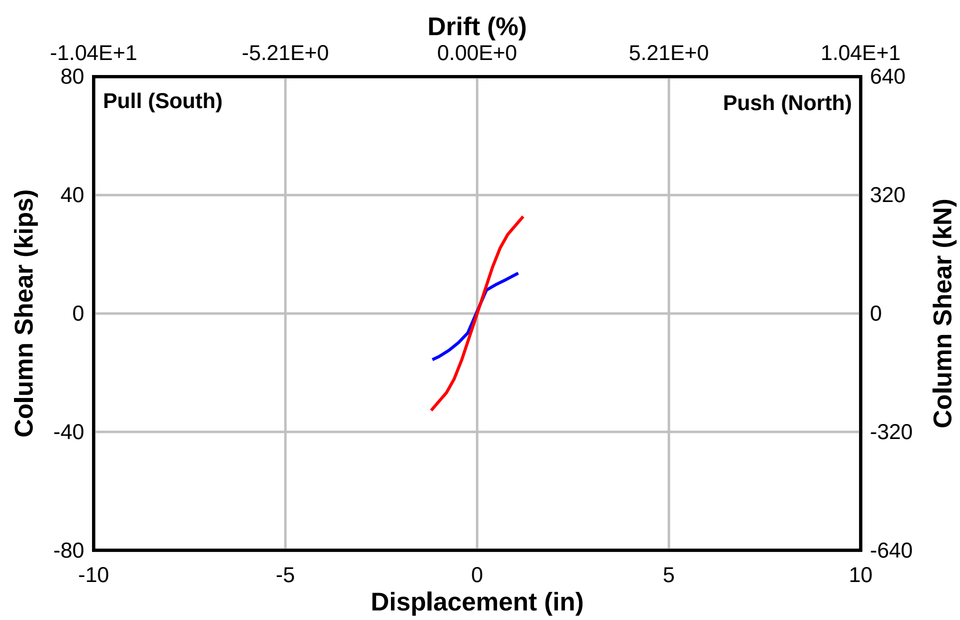

Figure C.6.18 – Soil Simulant Model Comparison – Test 6.

C.7 Test 7 – Specimen 3 – Vintage Complete Retrofit with Foam Subgrade & Steel Embedment

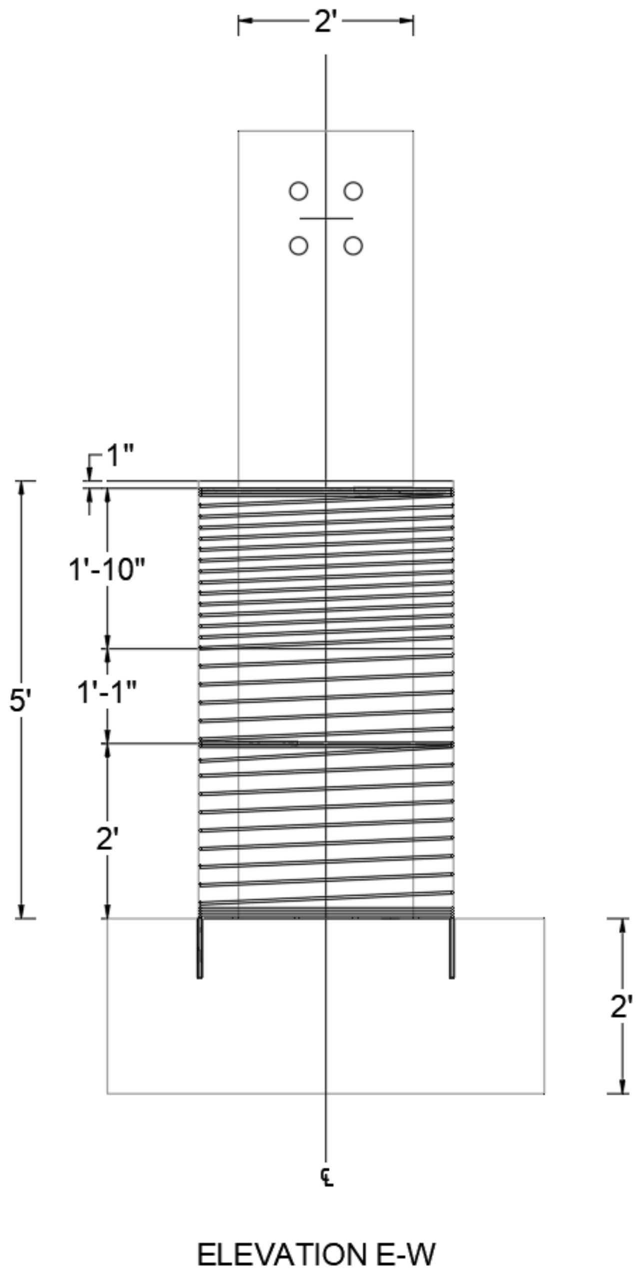

Figure C.7.1 – Elevation View of Specimen 3 used in Test 7.

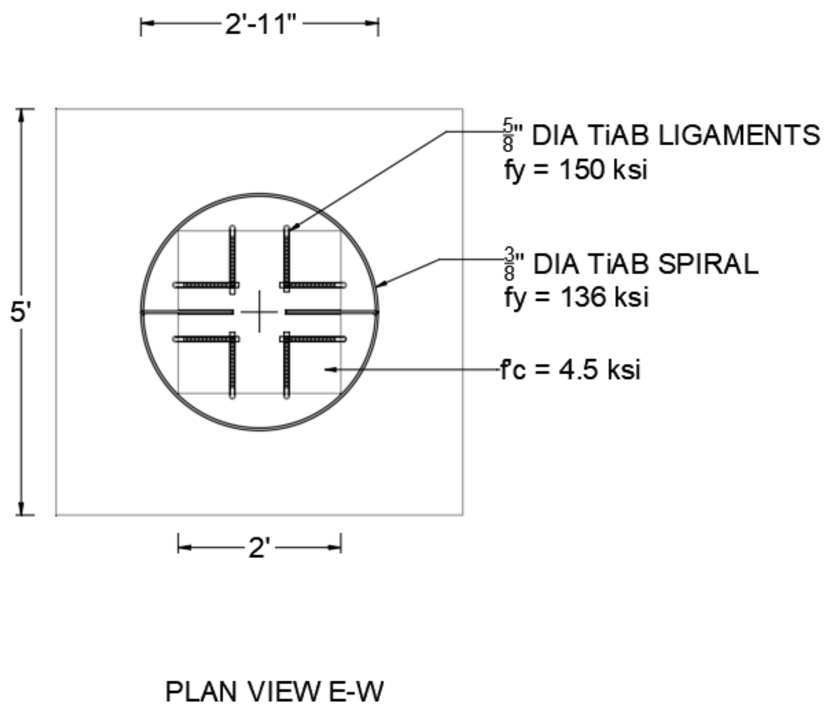

Figure C.7.2 – Plan View of Specimen 3 used in Test 7.

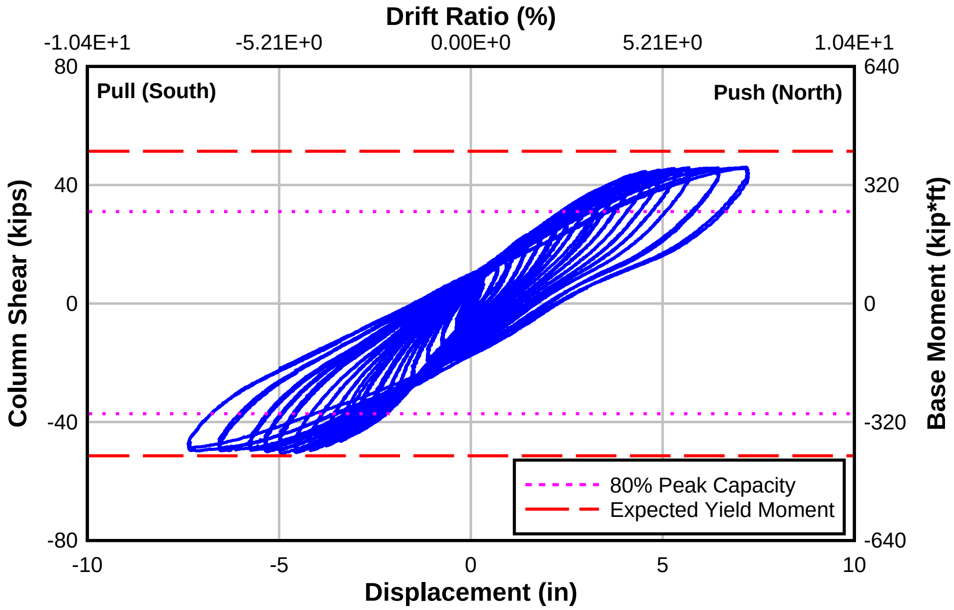

Figure C.7.3 – Overall Force Displacement Response – Test 7.

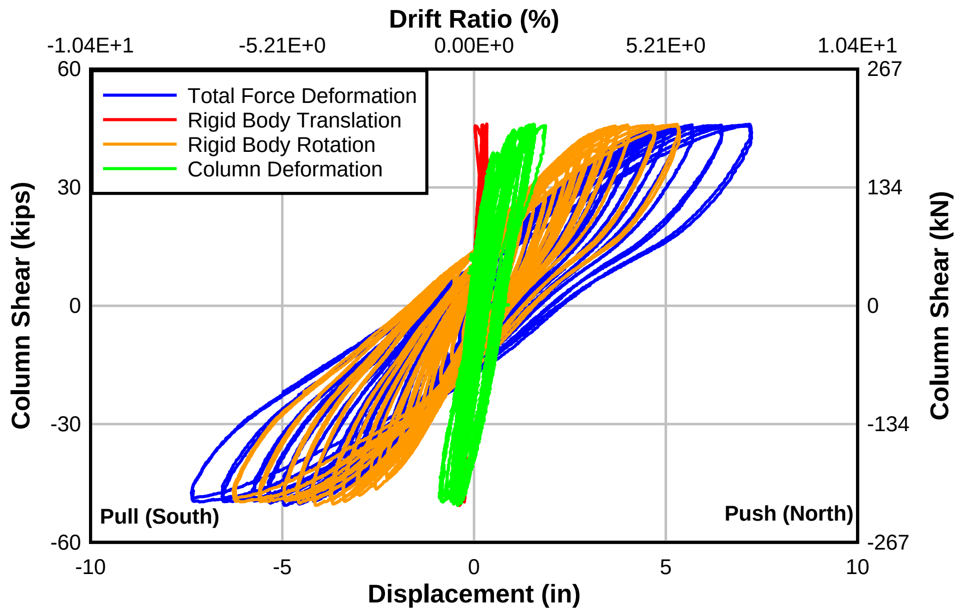

Figure C.7.4 – Component Contributions to Force Displacement -Test 7.

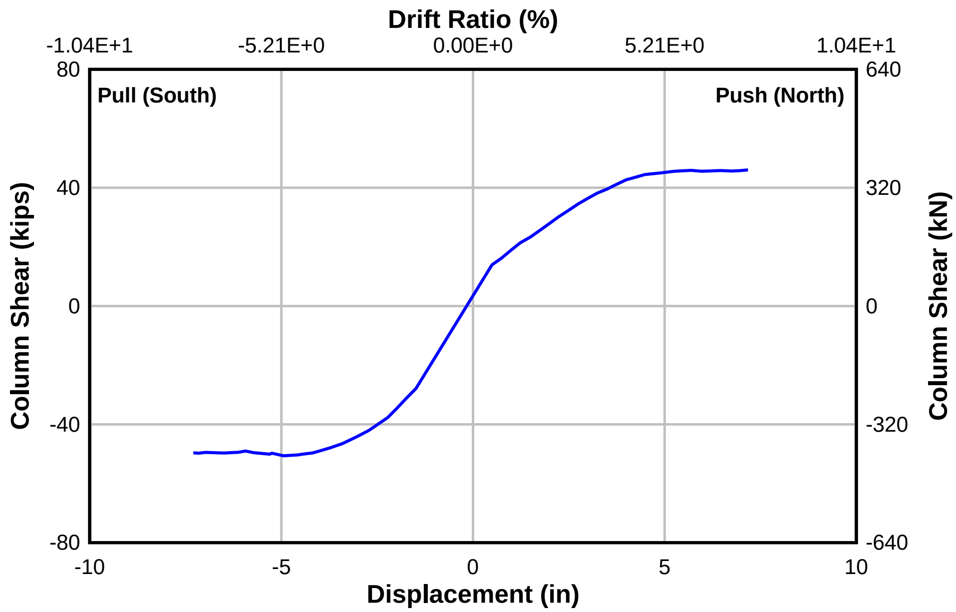

Figure C.7.5 – Overall Force Displacement Backbone Curve – Test 7.

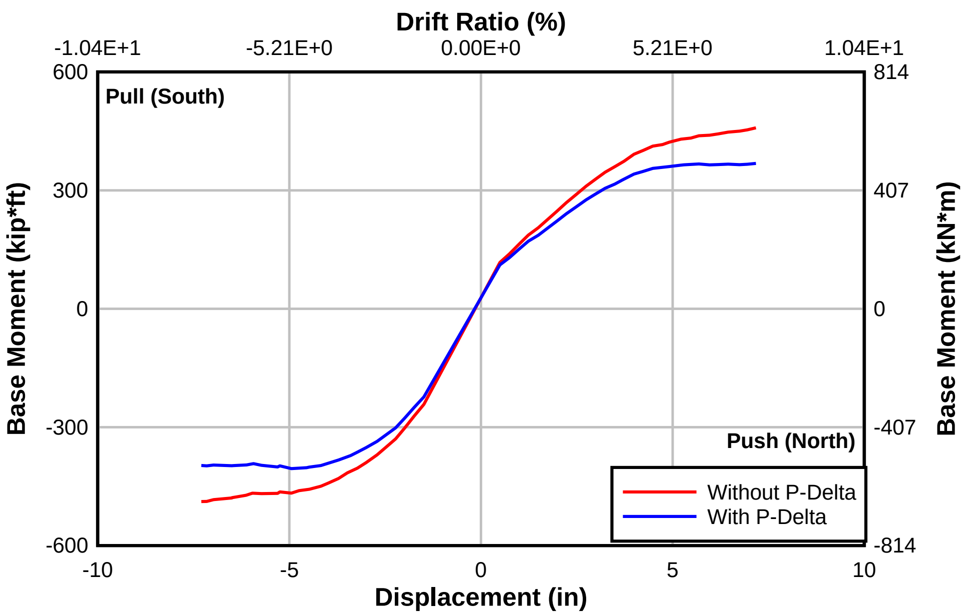

Figure C.7.6 – P-Delta Effects Backbone Curve – Test 7.

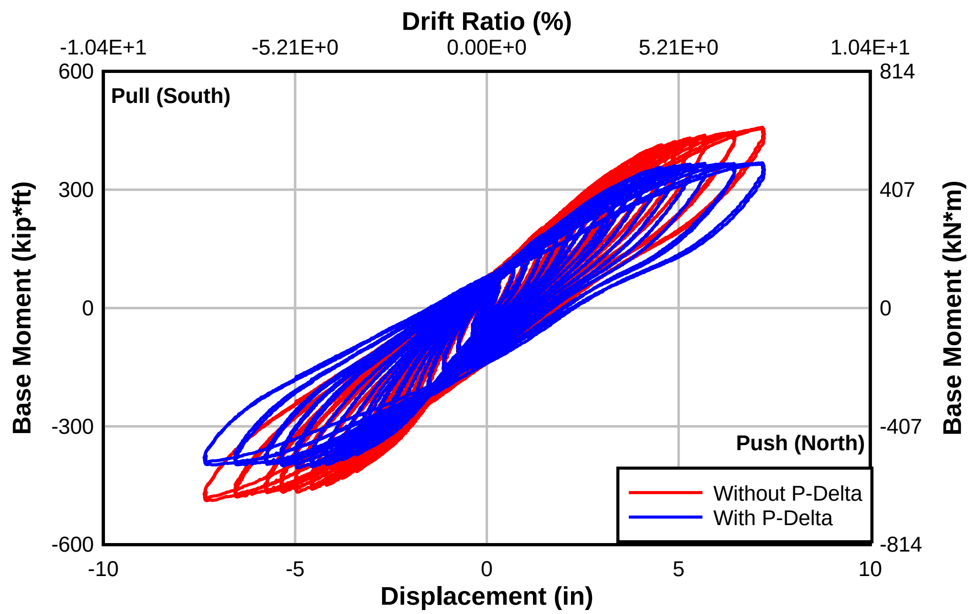

Figure C.7.7 – P-Delta Effects – Test 7.

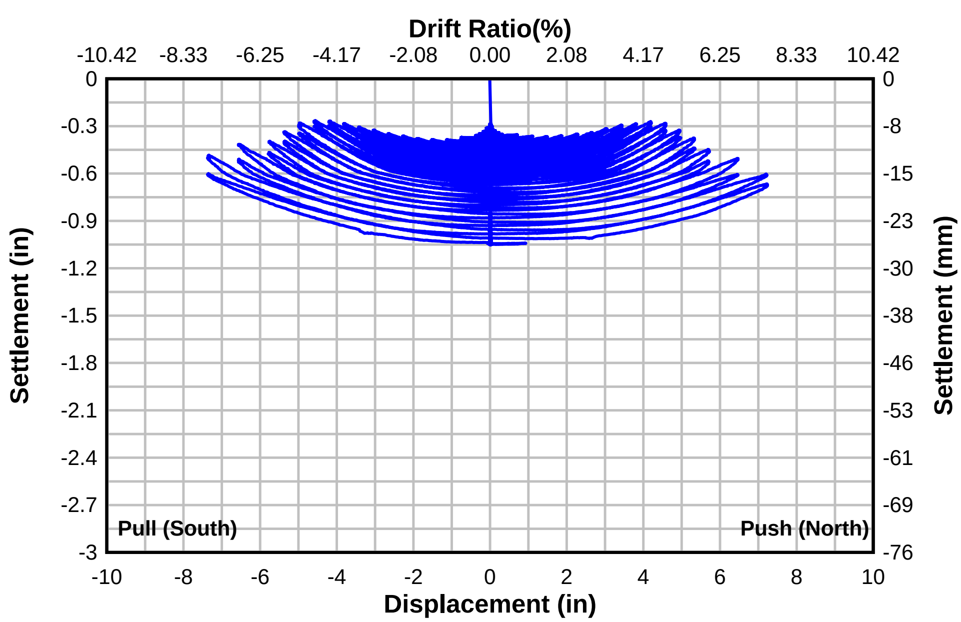

Figure C.7.8 – Settlement – Test 7.

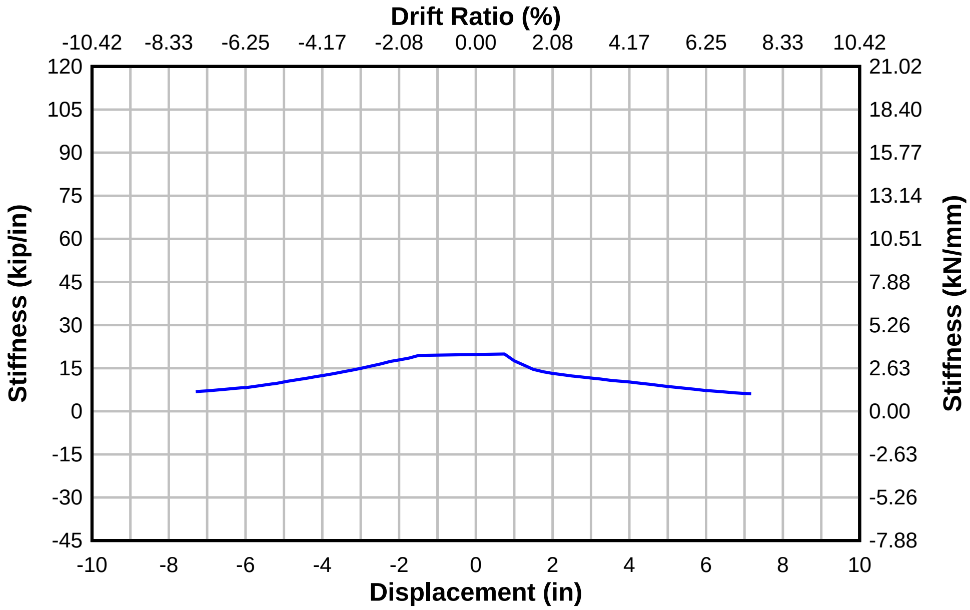

Figure C.7.9 – Evolution of Secant Stiffness – Test 7.

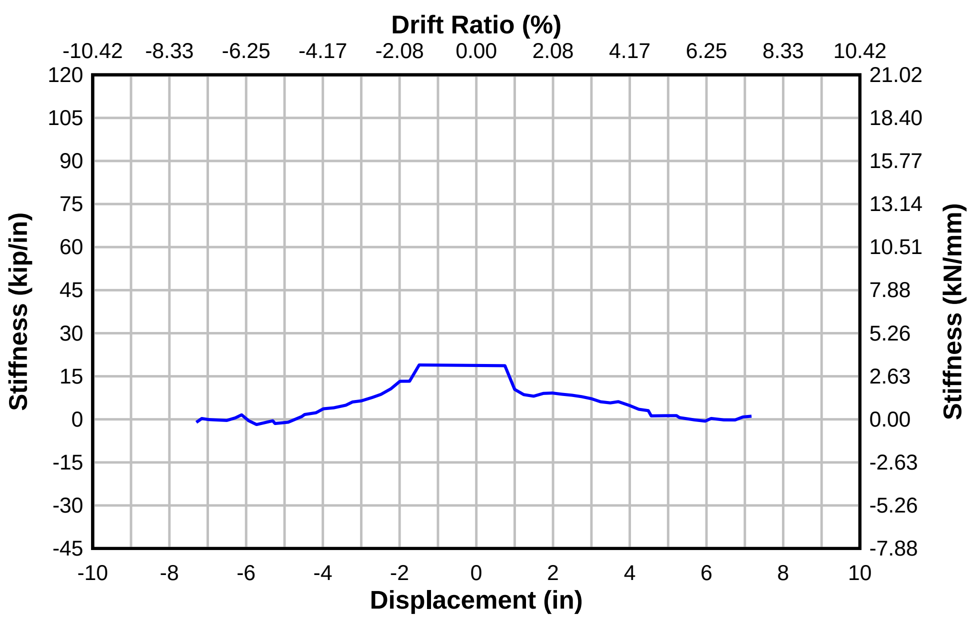

Figure C.7.10 – Evolution of Tangent Stiffness – Test 7.

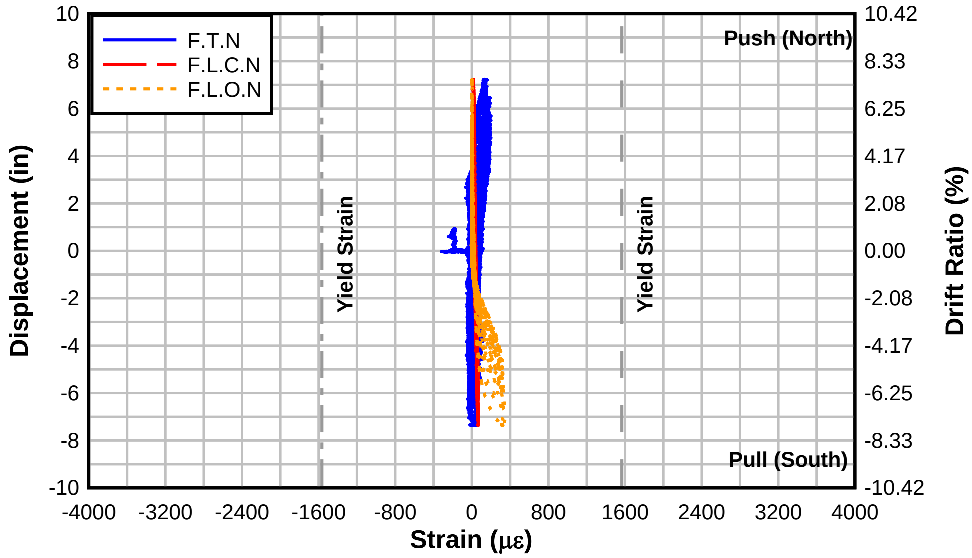

Figure C.7.11 – Footing Bar Strains – Test 7.

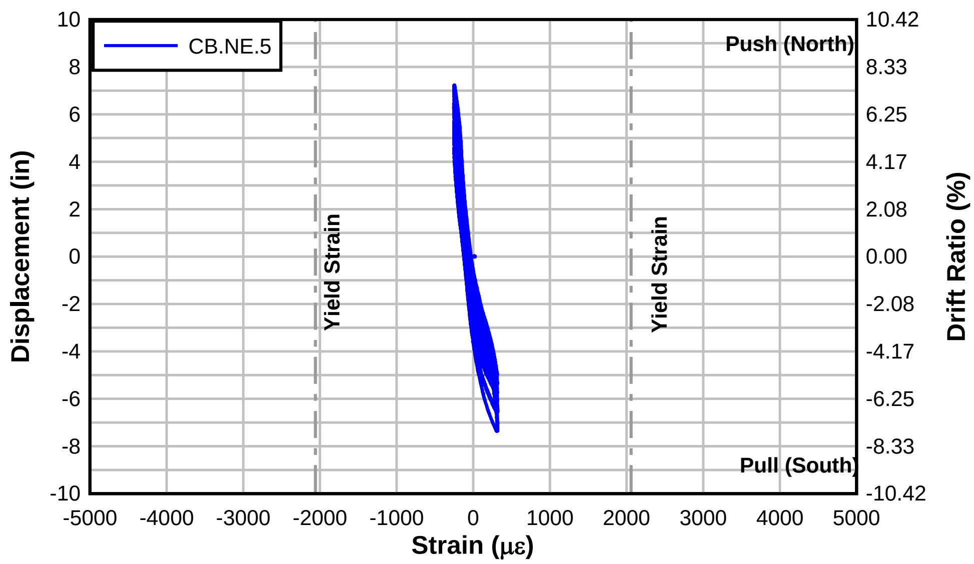

Figure C.7.12 – Column Bar Strains – Test 7.

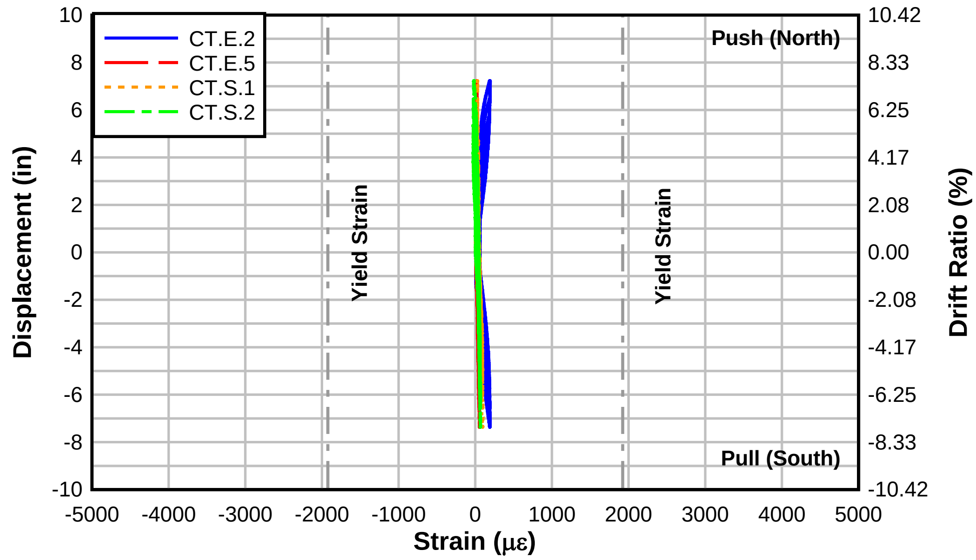

Figure C.7.13 – Column Tie Strains – Test 7.

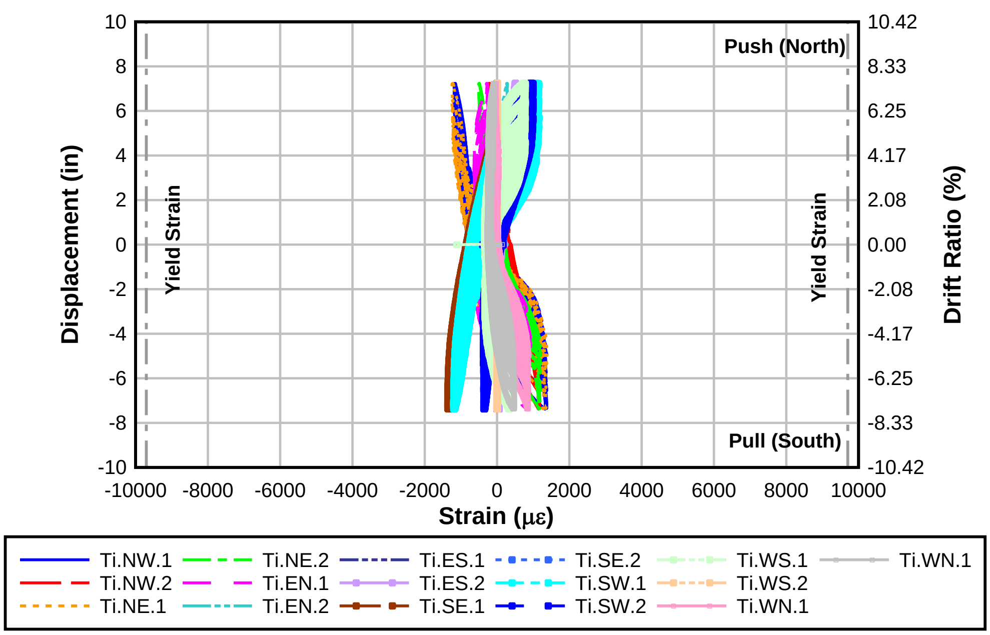

Figure C.7.14 – TiAB Ligament Strains – Test 7.

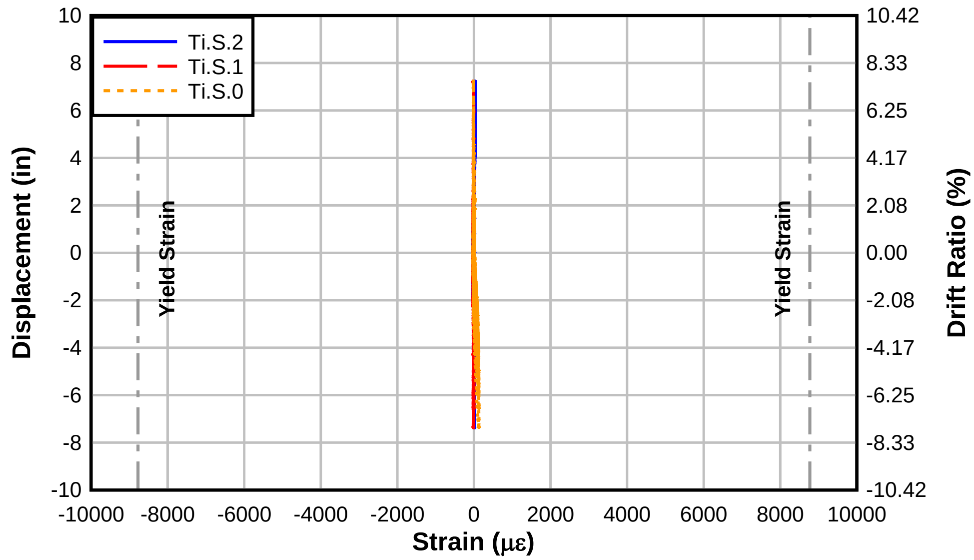

Figure C.7.15 – TiAB Spiral Strains – Test 7.

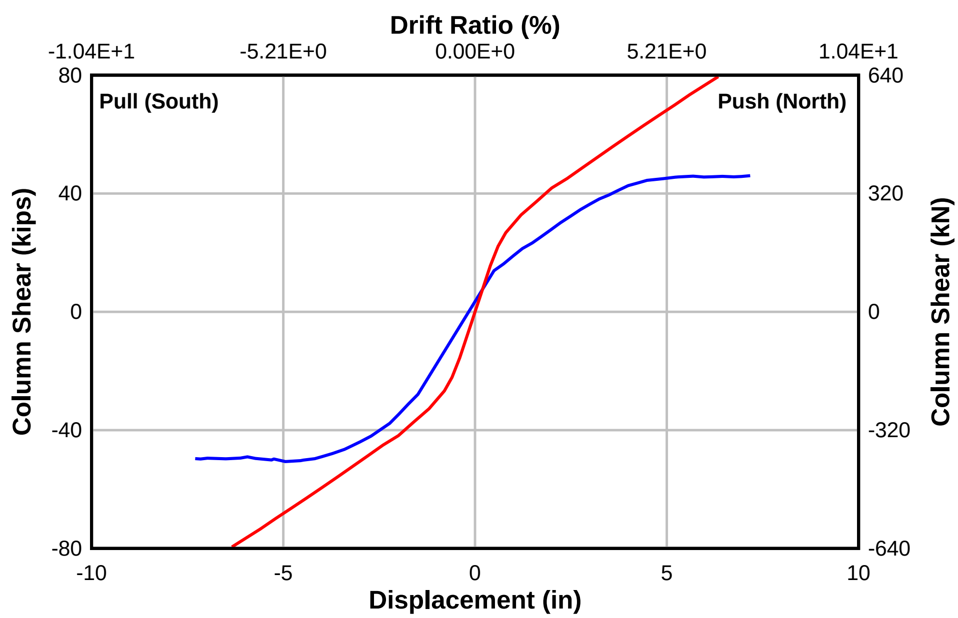

Figure C.7.16 – Soil Simulant Model Comparison – Test 7.

C.8 Test 8 – Specimen 2: Complete Retrofit with Tied Down Footing

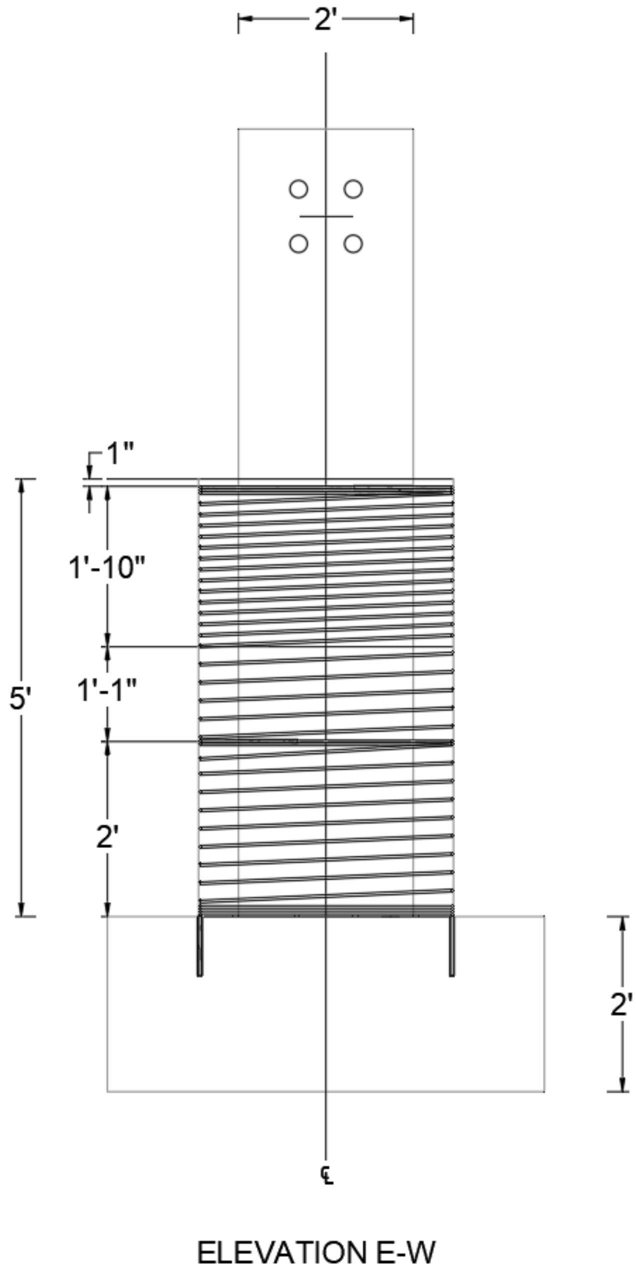

Figure C.8.1 – Elevation View of Specimen 2 used in Test 8.

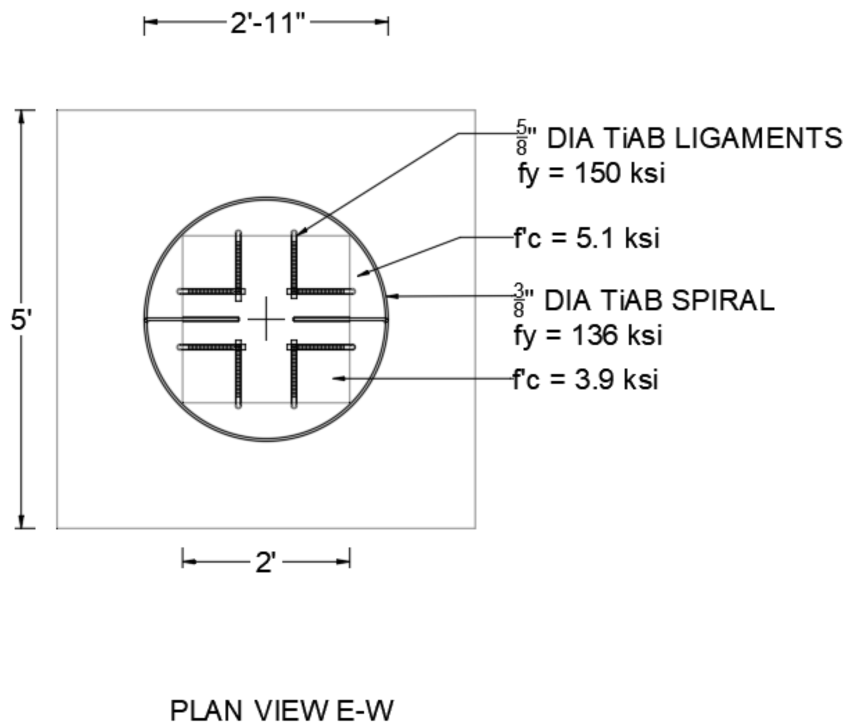

Figure C.8.2 – Plan View of Specimen 2 used in Test 8.

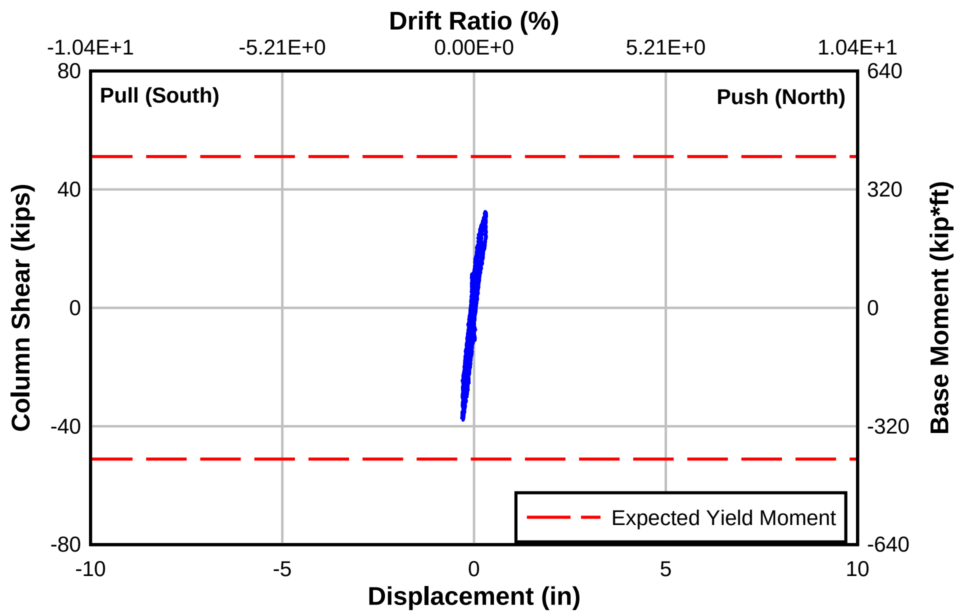

Figure C.8.3 – Overall Force Displacement Response Pre-failure – Test 8.

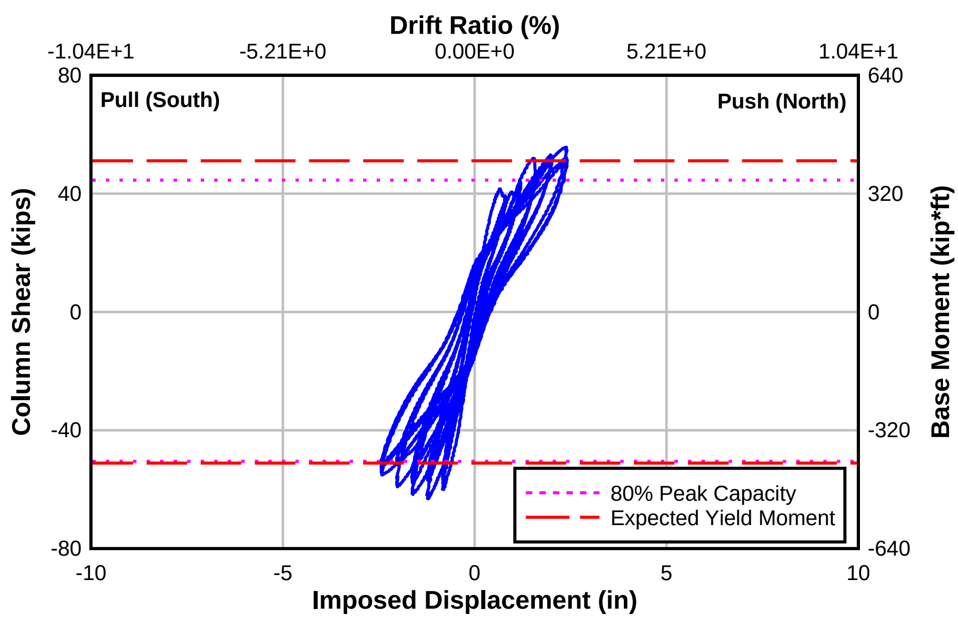

Figure C.8.4 – Overall Force Displacement Response Post-failure – Test 8.

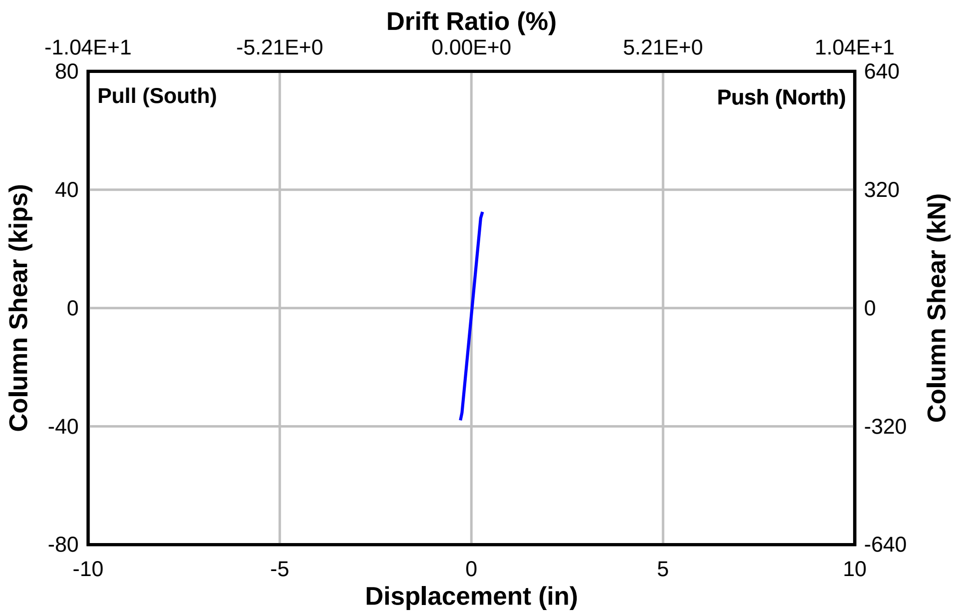

Figure C.8.5 – Overall Force Displacement Backbone Curve Pre-failure – Test 8.

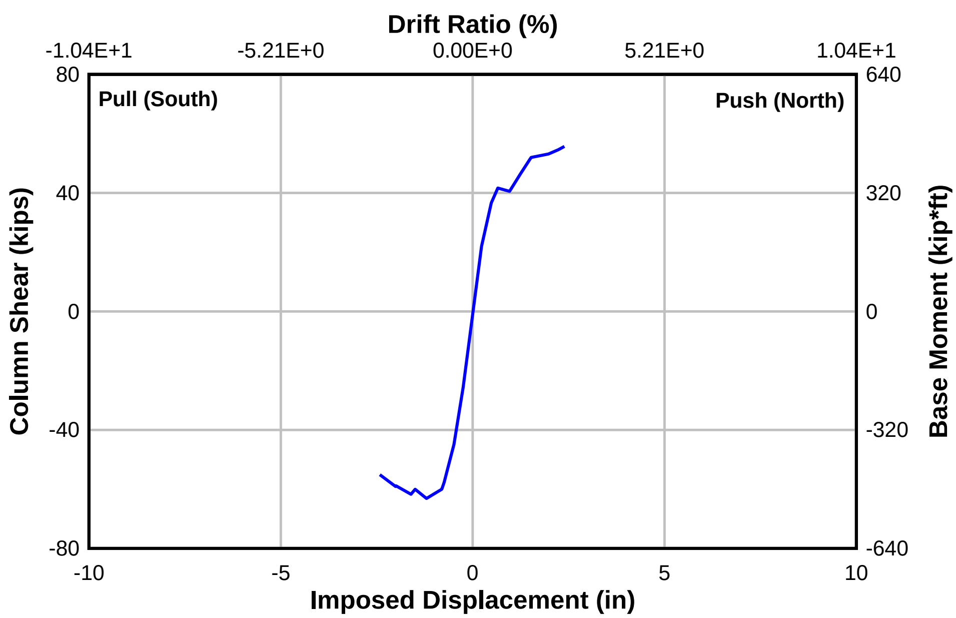

Figure C.8.6 – Overall Force Displacement Backbone Curve Post-failure – Test 8.

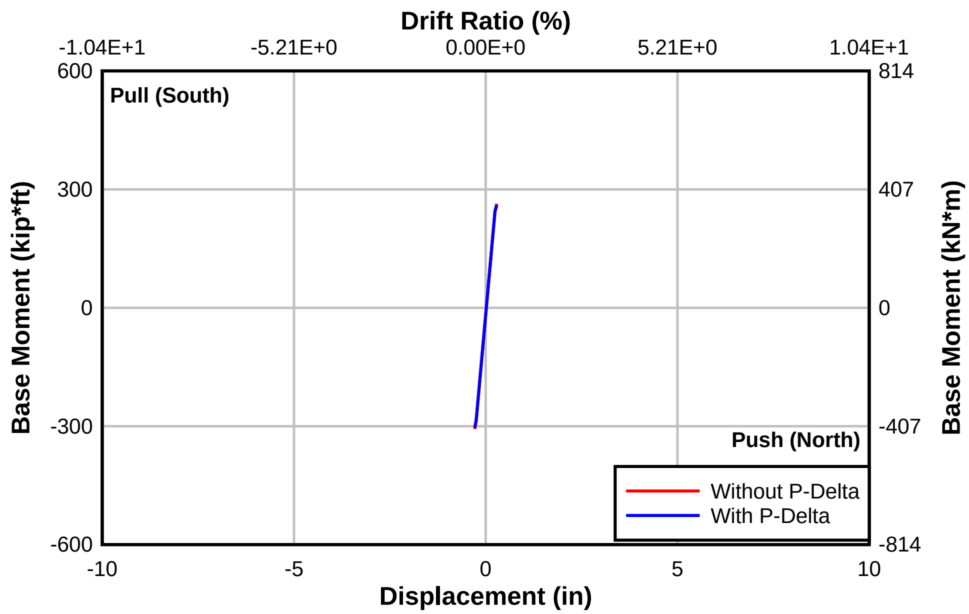

Figure C.8.7 – P-Delta Effects Backbone Curve Pre-failure – Test 8.

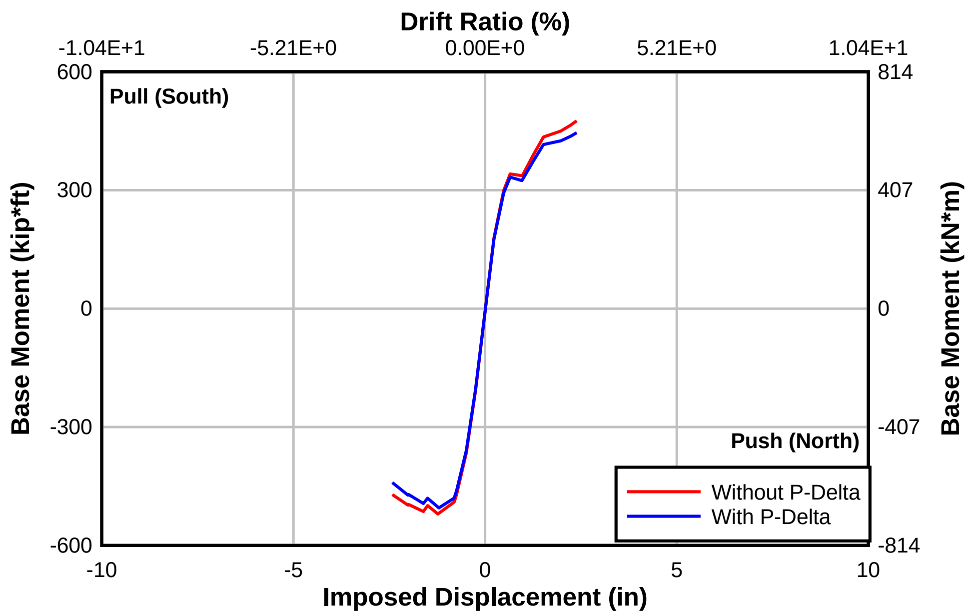

Figure C.8.8 – P-Delta Effects Backbone Curve Post-failure – Test 8.

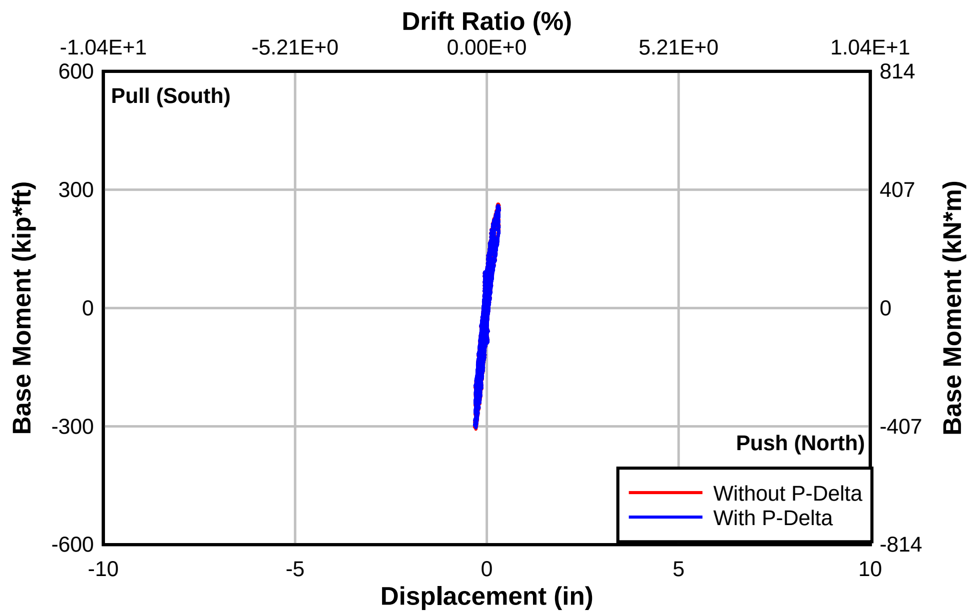

Figure C.8.9 – P-Delta Effects Pre-failure – Test 8.

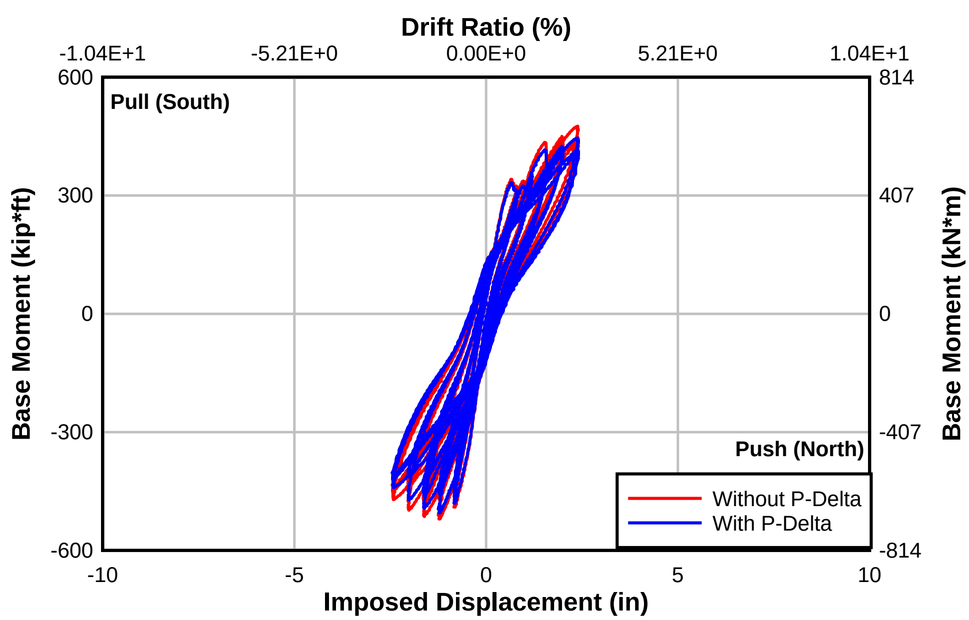

Figure C.8.10 – P-Delta Effects Post-failure – Test 8.

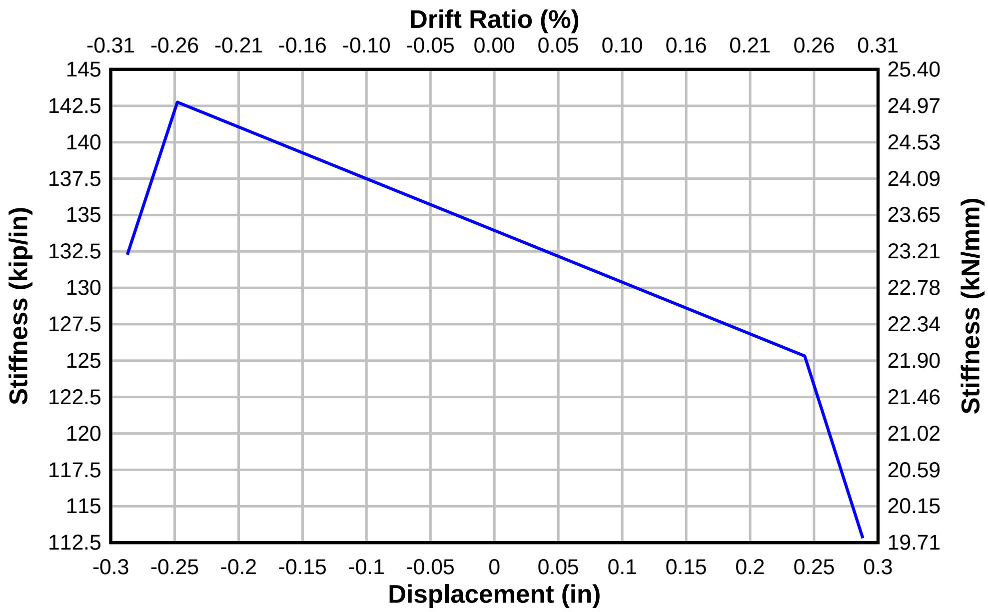

Figure C.8.11 – Evolution of Secant Stiffness Pre-failure – Test 8.

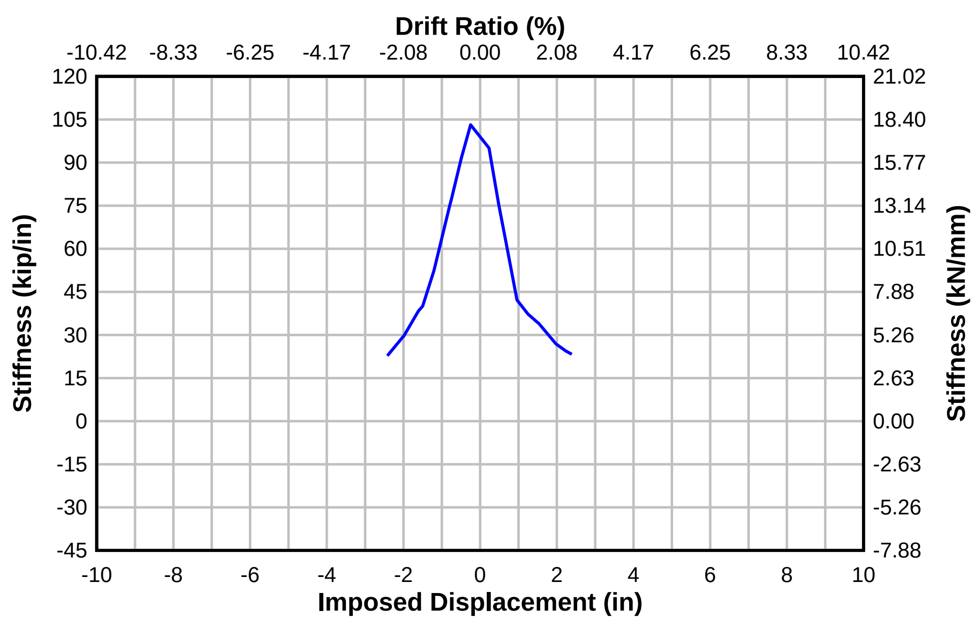

Figure C.8.12 – Evolution of Secant Stiffness Post-Failure – Test 8.

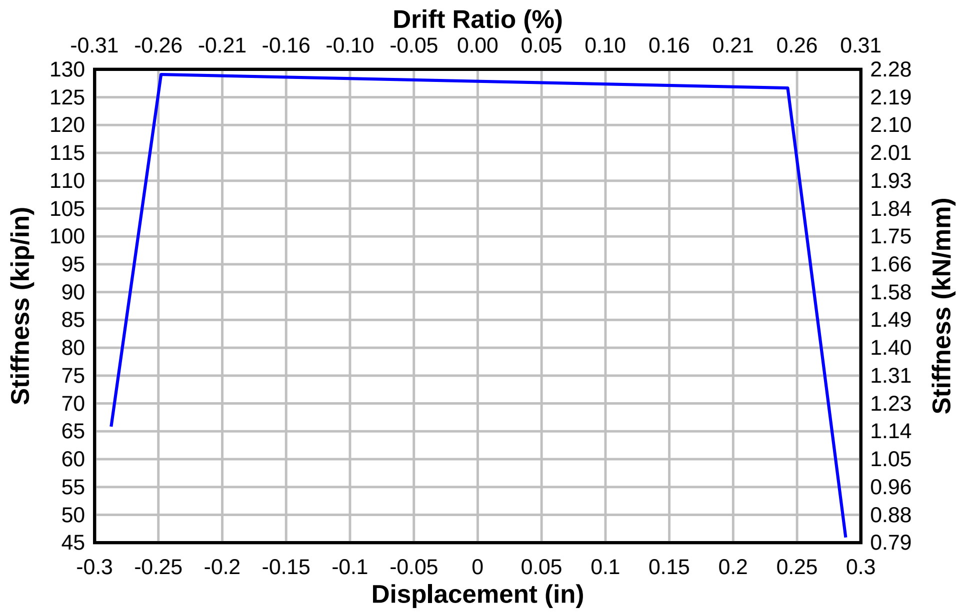

Figure C.8.13 – Evolution of Tangent Stiffness Pre-failure – Test 8.

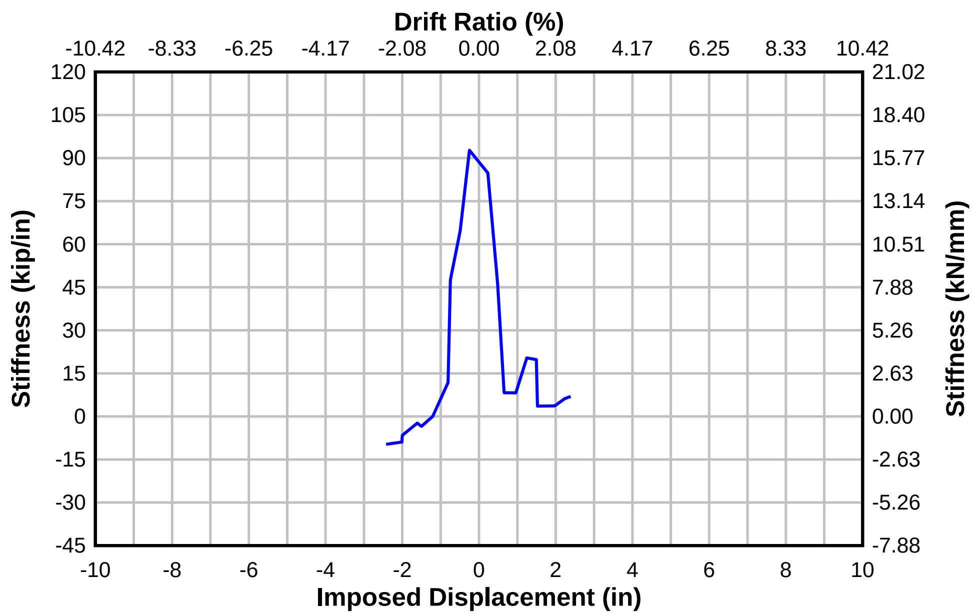

Figure C.8.14 – Evolution of Tangent Stiffness Post-Failure – Test 8.

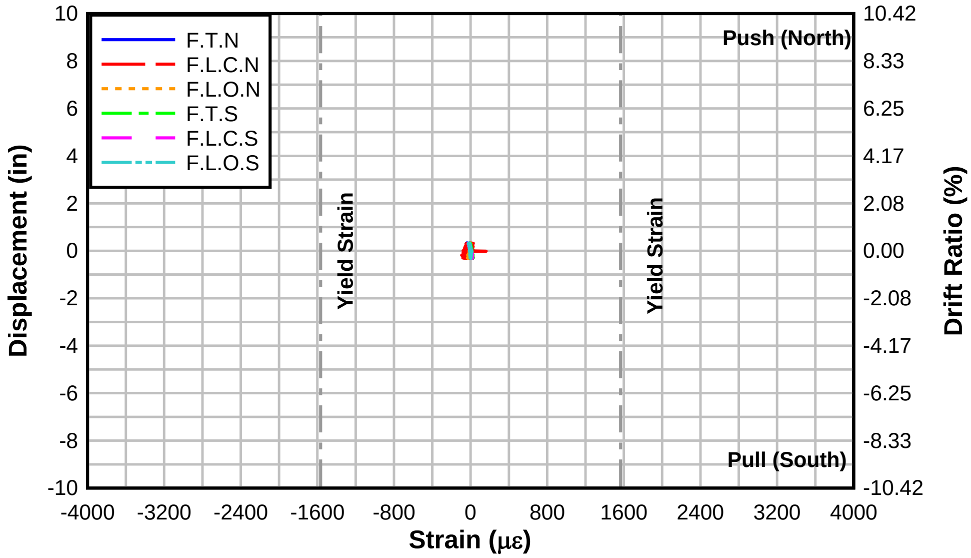

Figure C.8.15 – Footing Bar Strains Pre-failure – Test 8.

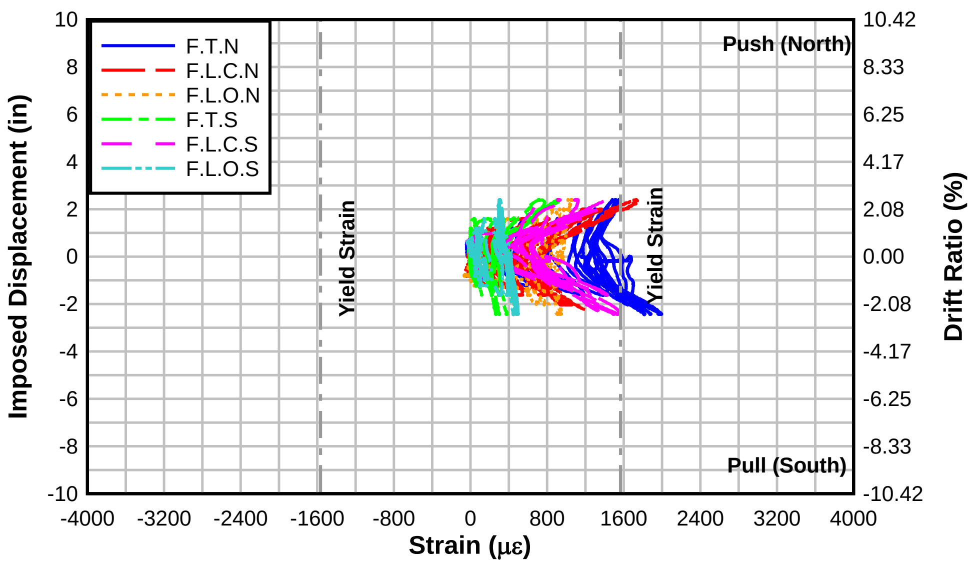

Figure C.8.16 – Footing Bar Strains Post-Failure – Test 8.

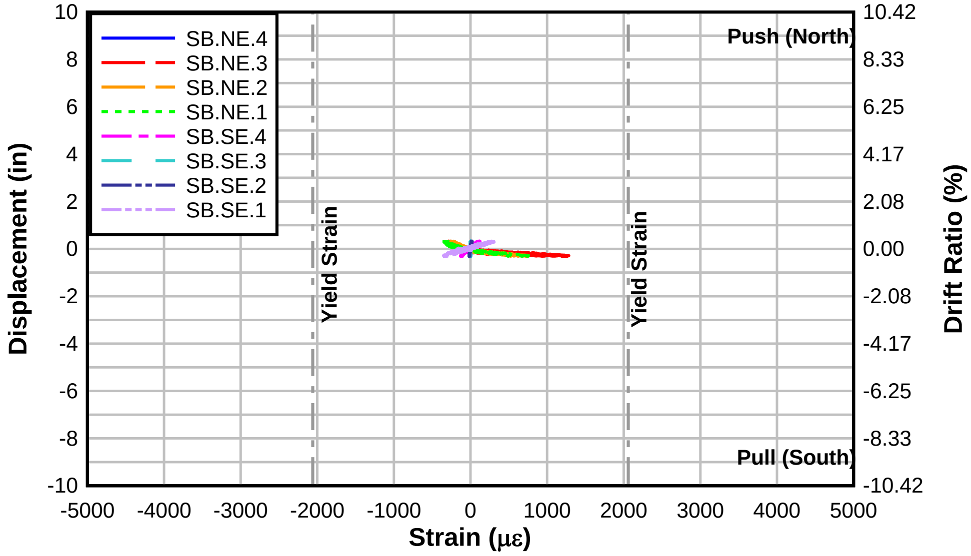

Figure C.8.17 – Starter Bar Strains Pre-failure – Test 8.

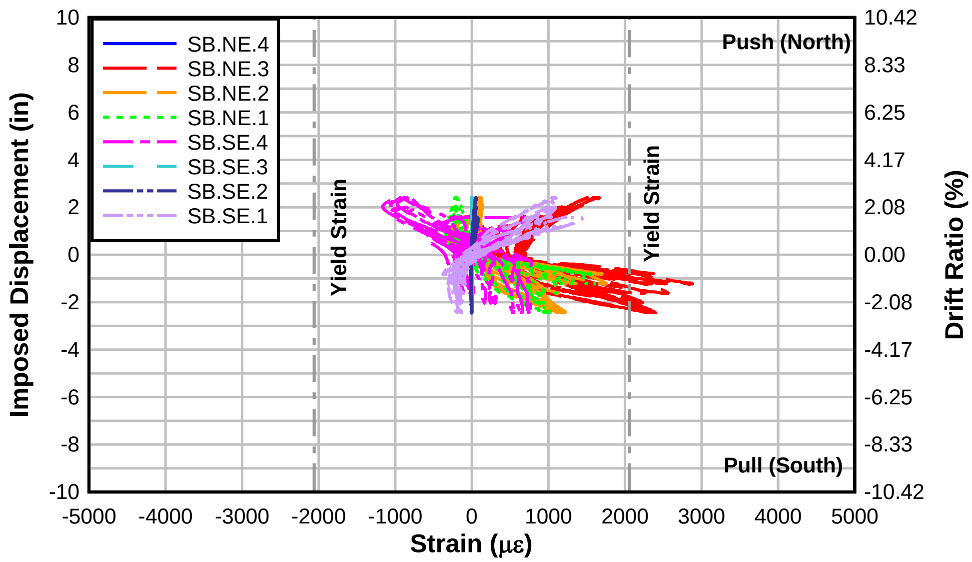

Figure C.8.18 – Starter Bar Strains Post-failure – Test 8.

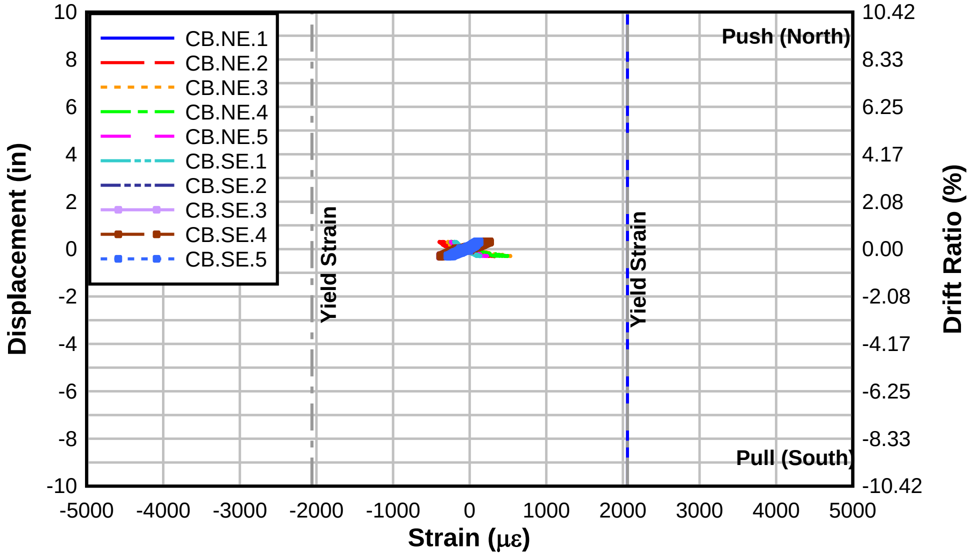

Figure C.8.19 – Column Bar Strain Pre-failure – Test 8.

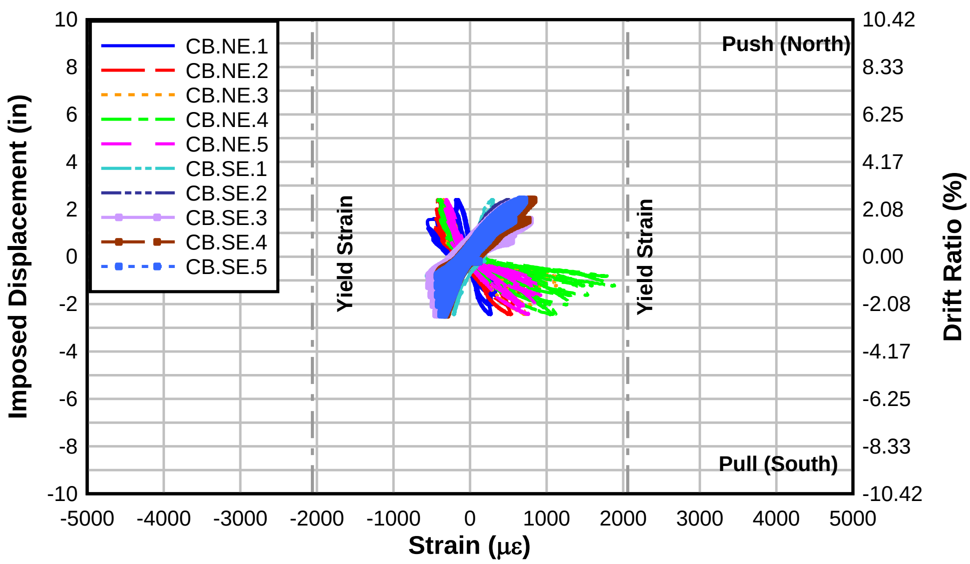

Figure C.8.20 – Column Bar Strain Post-failure – Test 8.

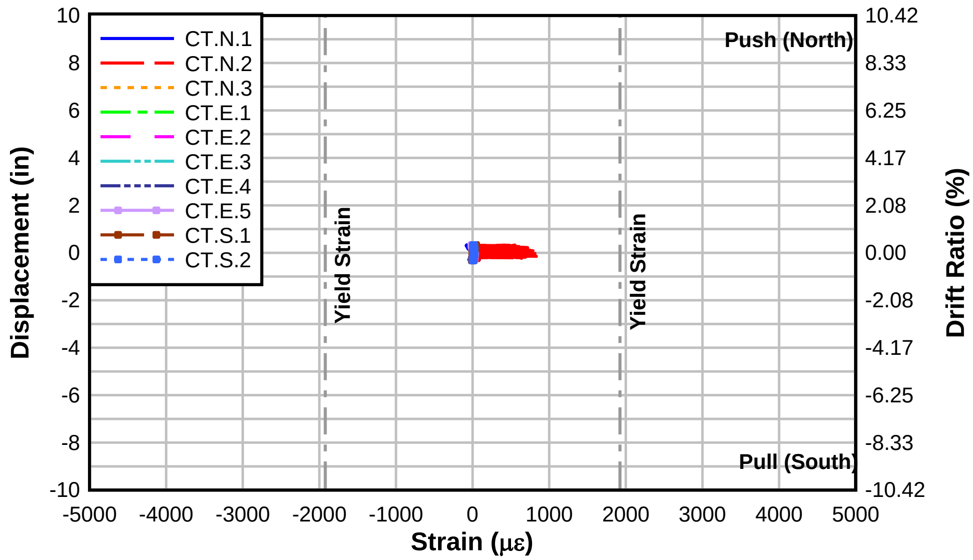

Figure C.8.21 – Column Tie Strains Pre-failure – Test 8.

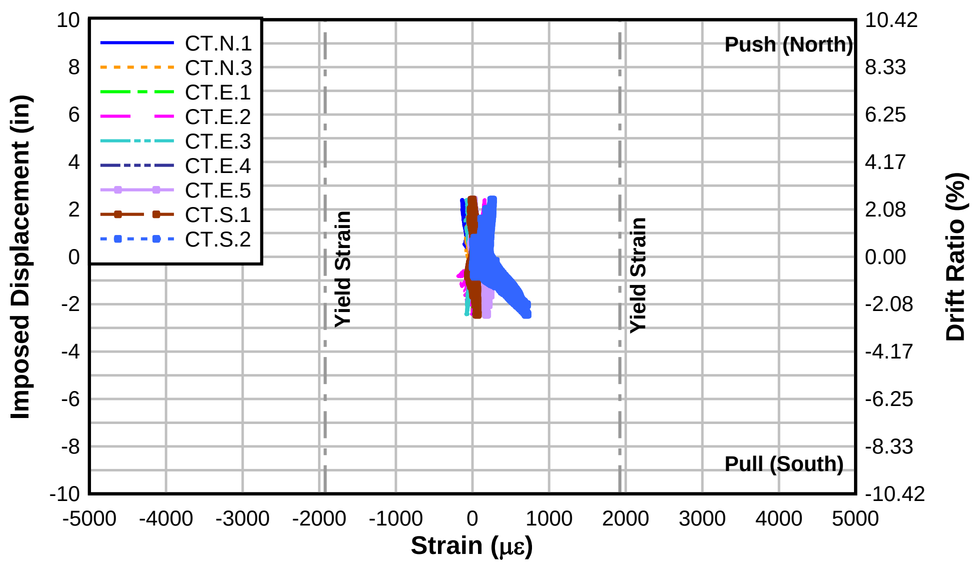

Figure C.8.22 – Column Tie Strains Post-failure – Test 8.

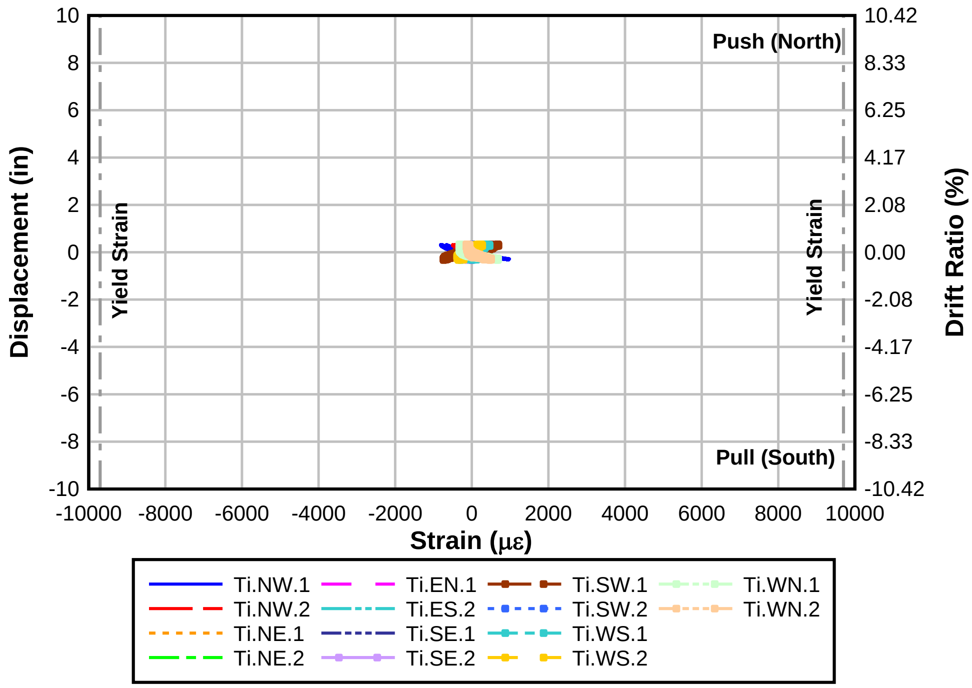

Figure C.8.23 – TiAB Ligament Strains Pre-failure – Test 8.

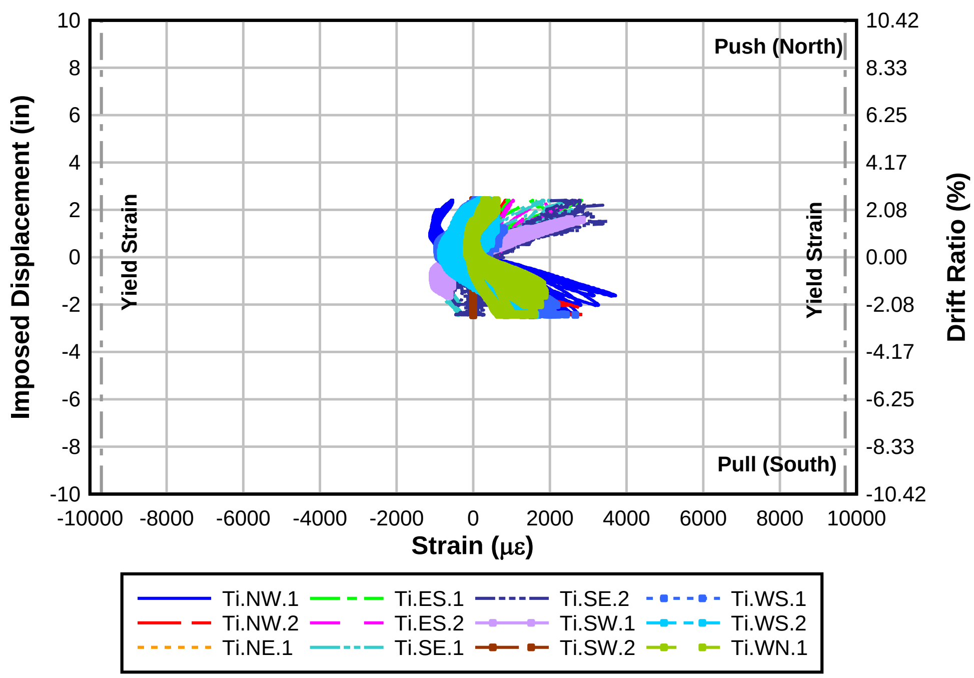

Figure C.8.24 – TiAB Ligament Strains Post-failure – Test 8.

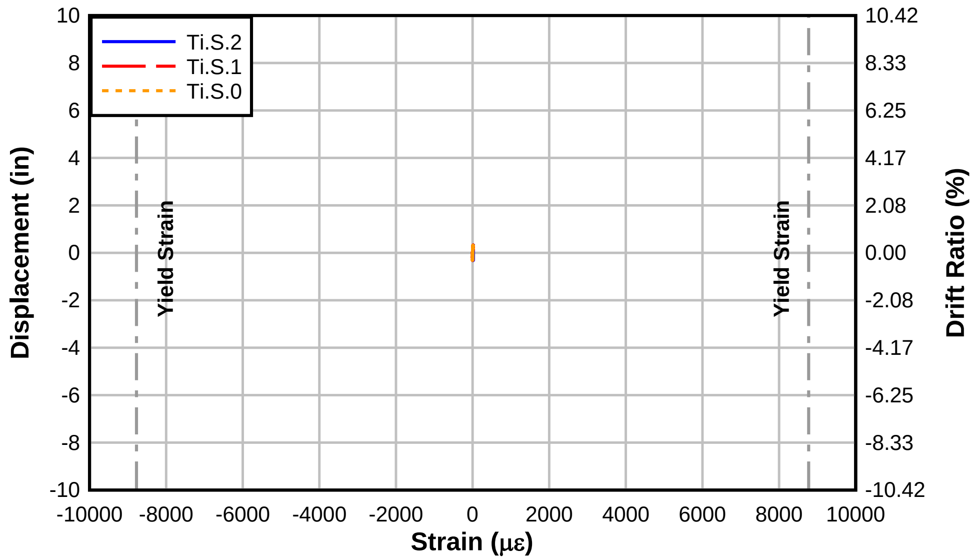

Figure C.8.25 – TiAB Spiral Strains Pre-failure – Test 8.

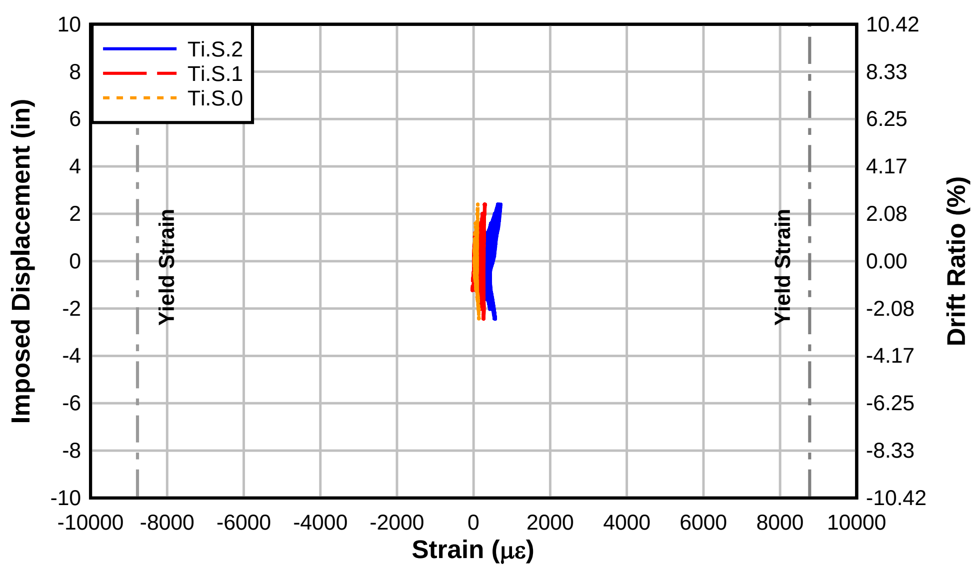

Figure C.8.26 – TiAB Spiral Strains Post-failure – Test 8.

C.9 Comparison Plots

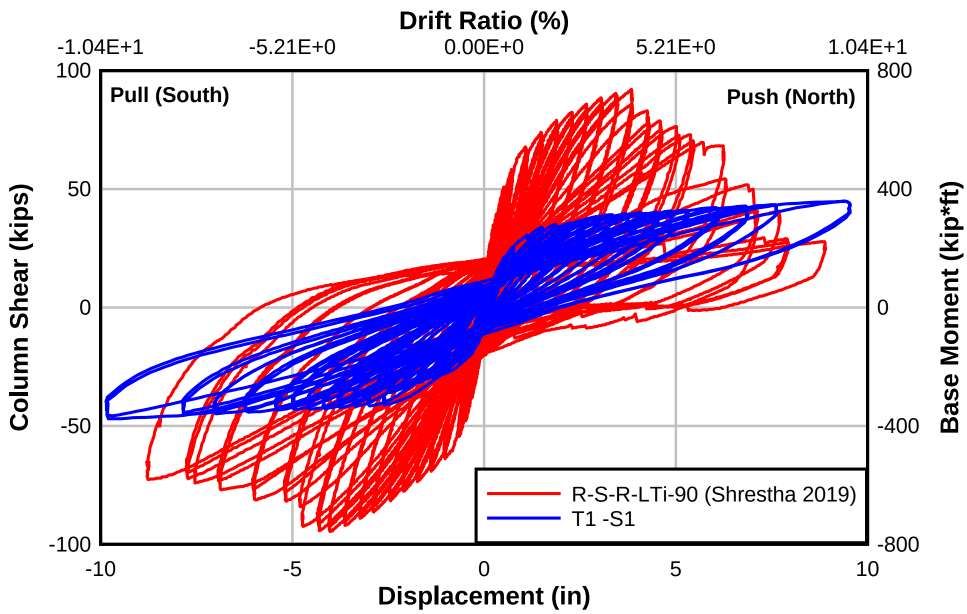

Figure C.9.1 – Comparison of Complete Retrofit SSI.

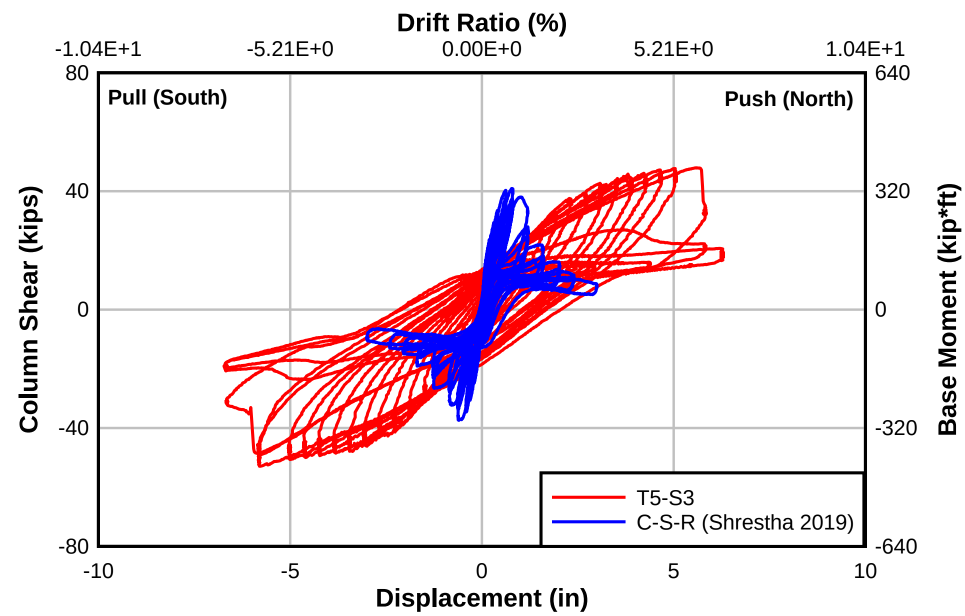

Figure C.9.2 – Comparison of Vintage Column SSI.

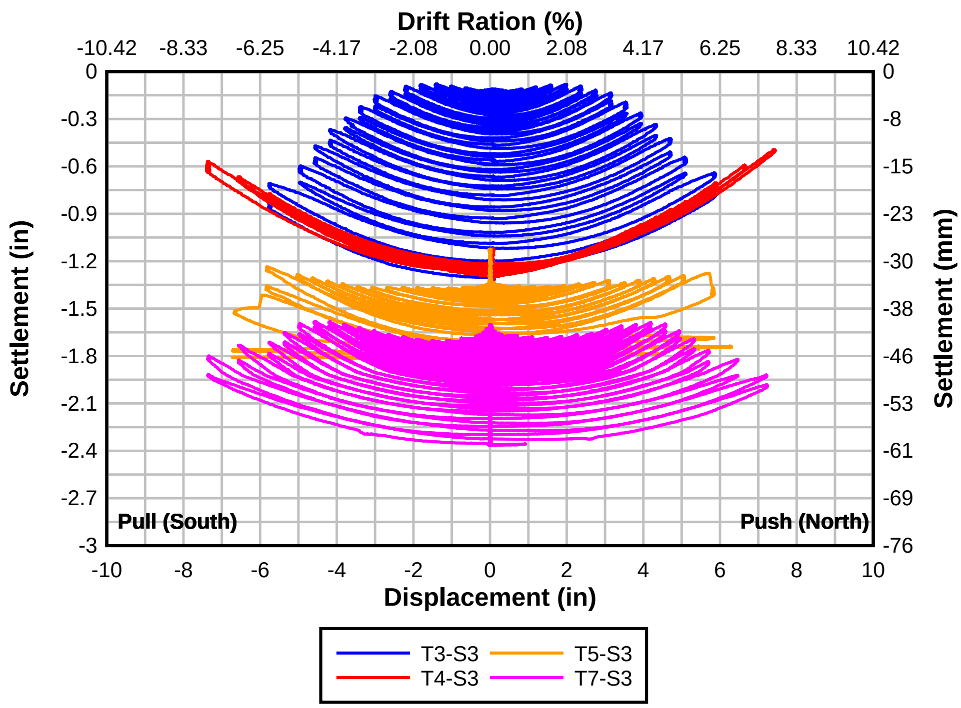

Figure C.9.3 – Subsequent Settlement Comparison.

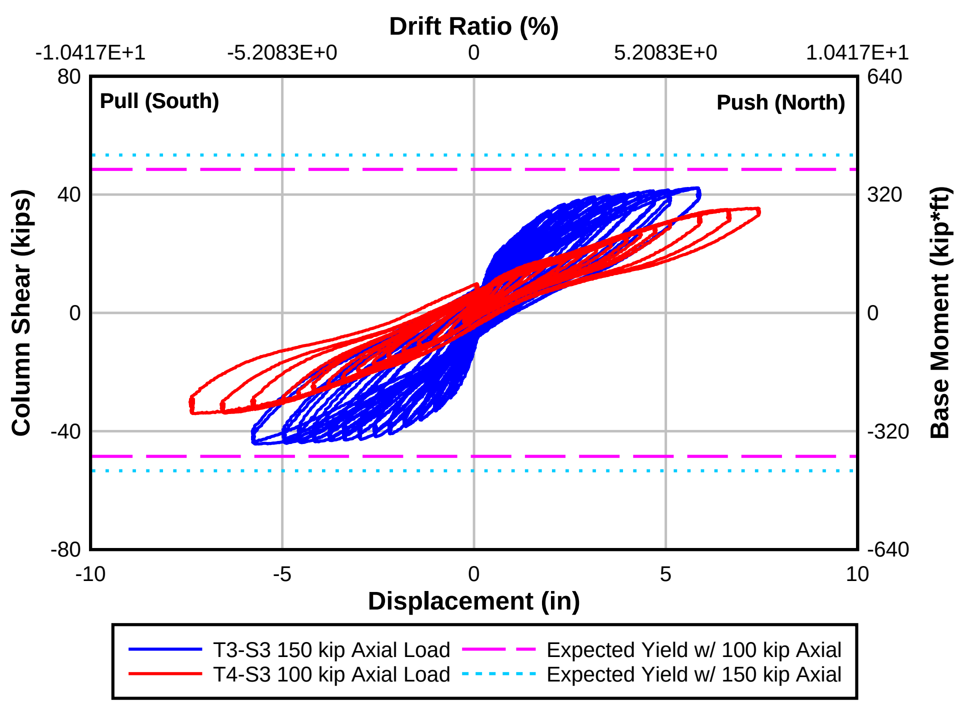

Figure C.9.4 – Effect of Axial Load.

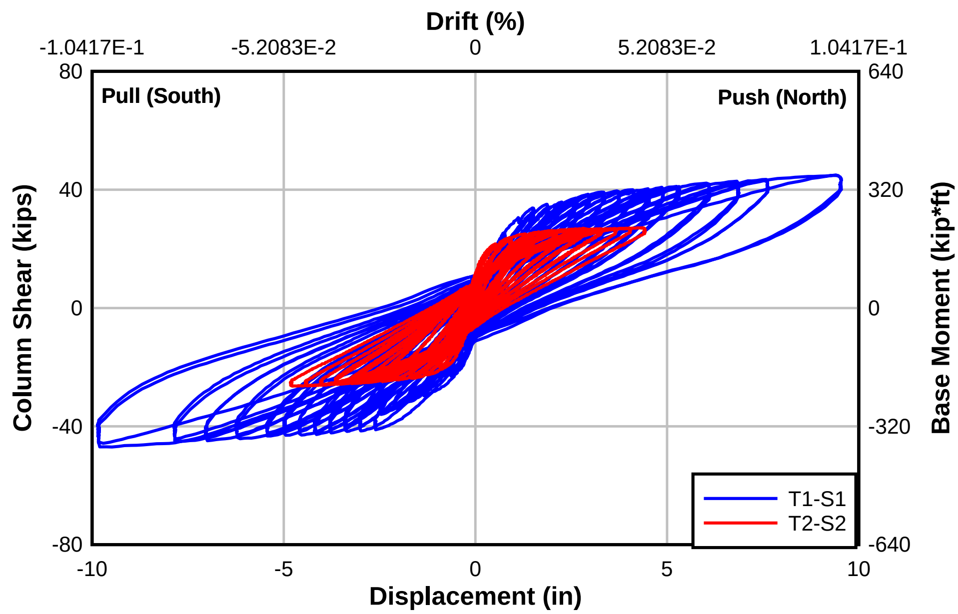

Figure C.9.5 – Effect of Embedment.

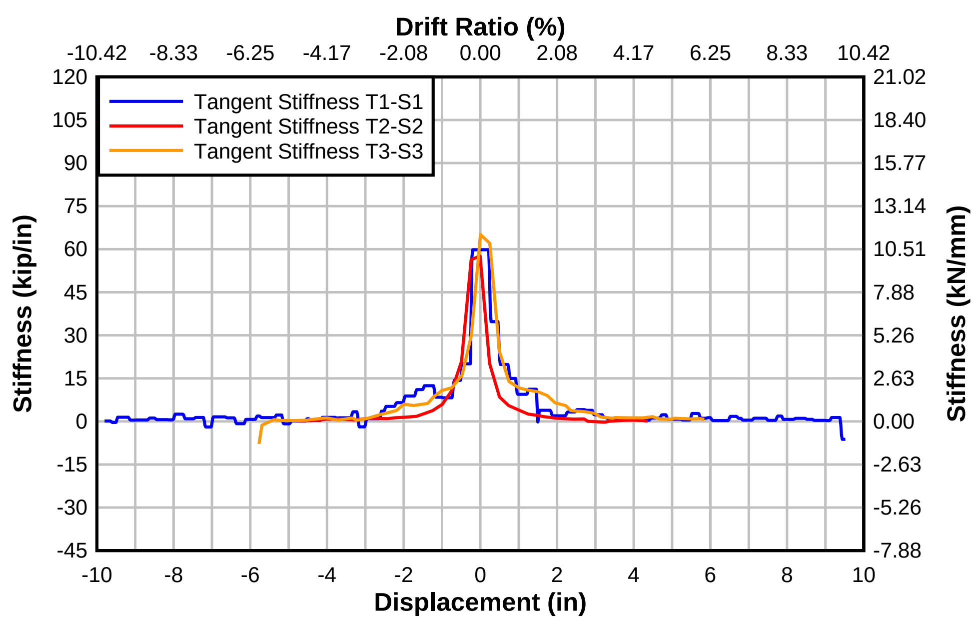

Figure C.9.6 – Tangent Stiffness Virgin Soil Simulant.

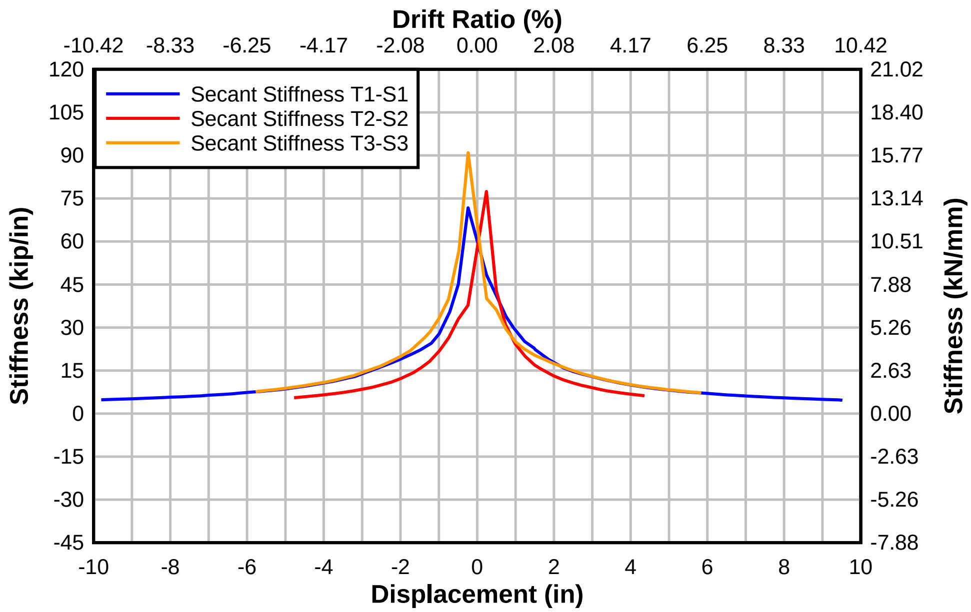

Figure C.9.7 – Secant Stiffness Virgin Soil Simulant.

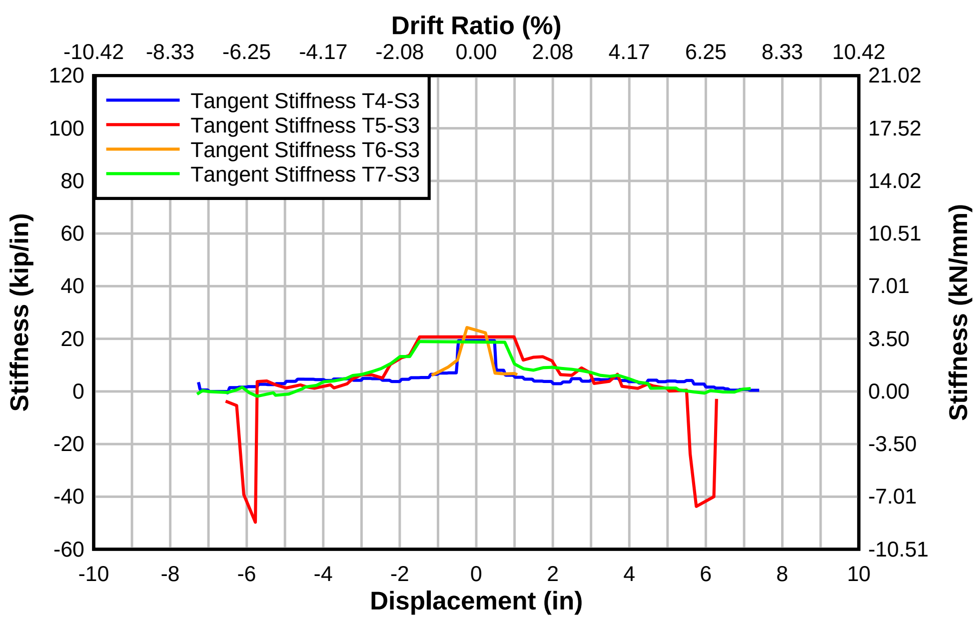

Figure C.9.8 – Tangent Stiffness of Failed Soil Simulant.

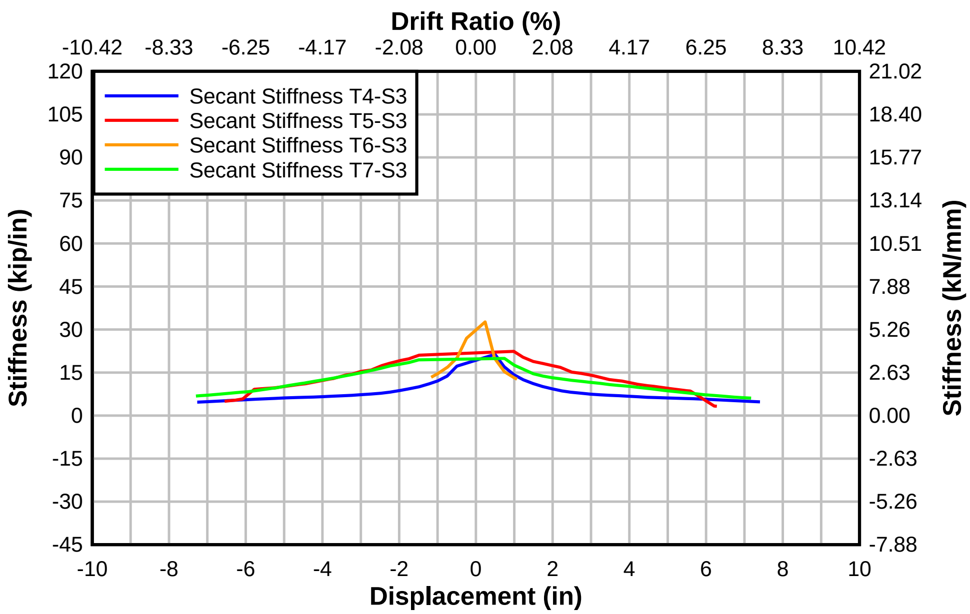

Figure C.9.9 – Secant Stiffness of Failed Soil Simulant.

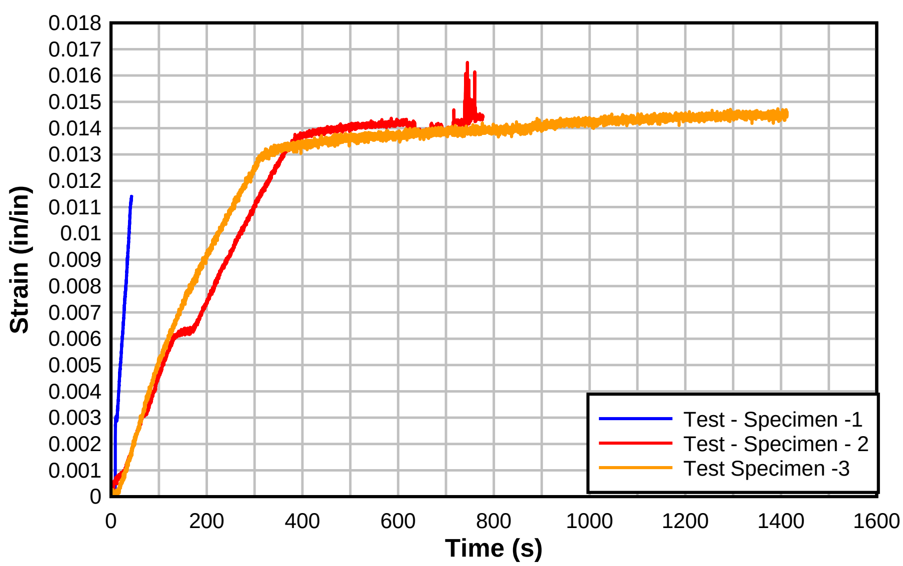

Figure C.9.10 – Strain Rate on Virgin Soil Simulant.

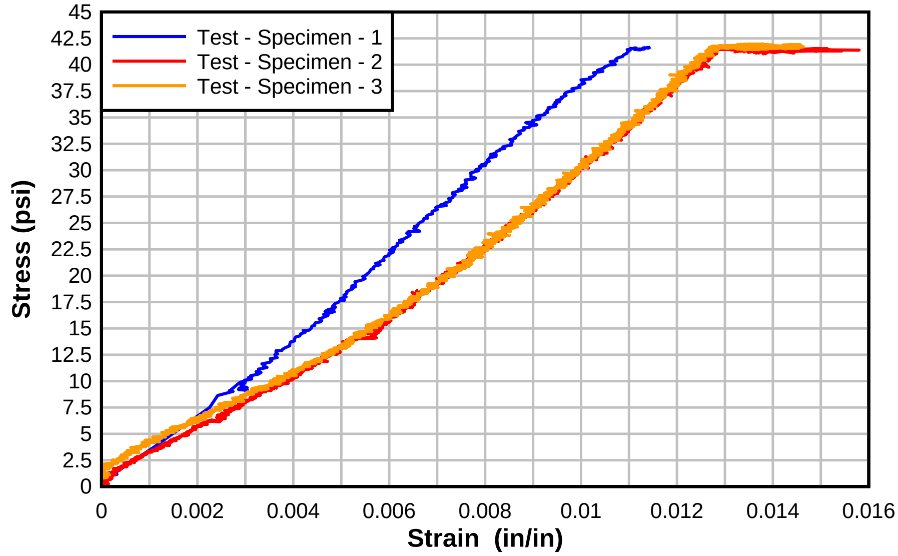

Figure C.9.11 – Bulk Engineering Stress-Strain Relationship on Virgin Soil.

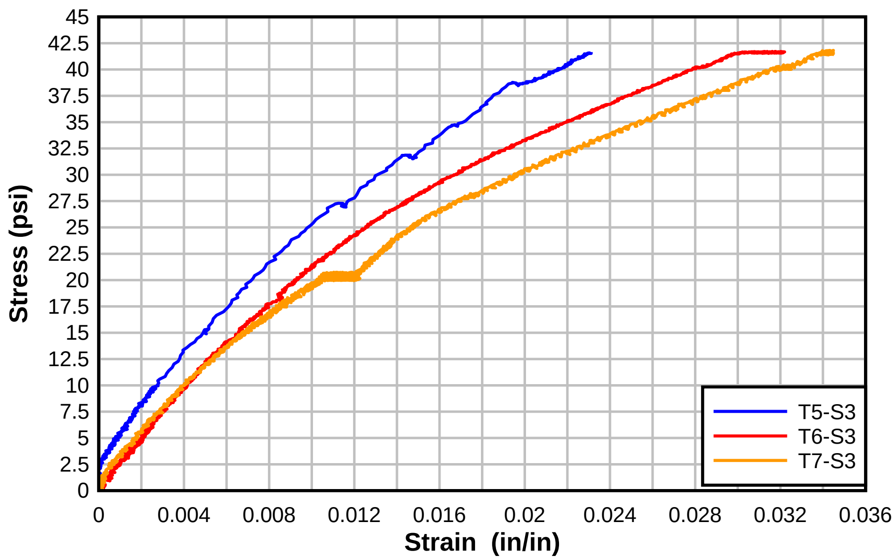

Figure C.9.12 – Bulk Average Engineering Stress-Strain Relationship on Failed Soil Simulant.

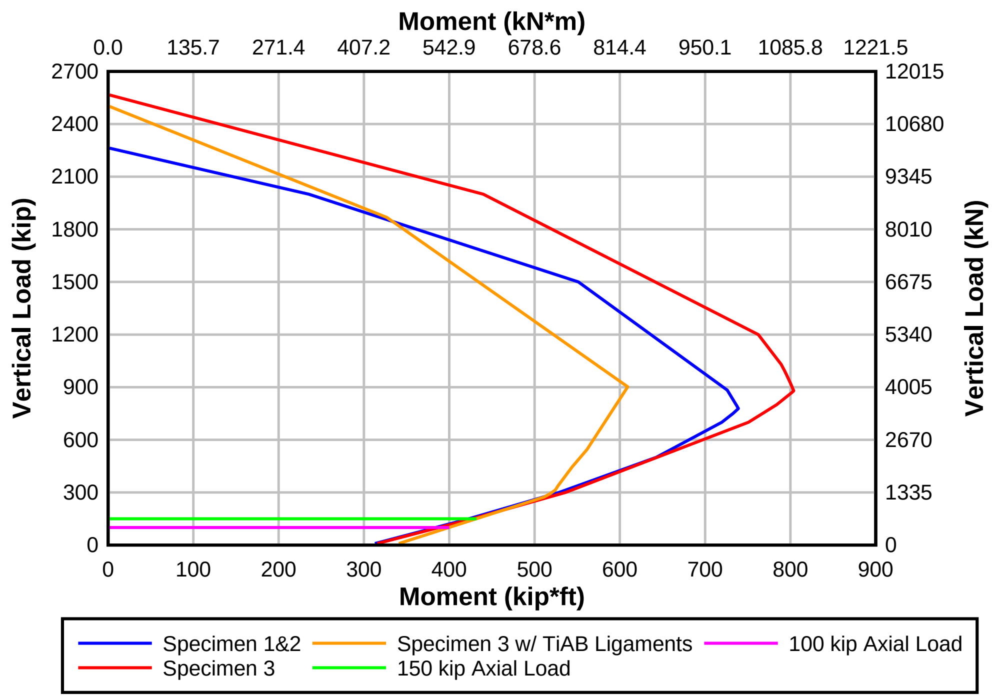

Figure C.9.13 – P-M Interaction Diagrams with As-Built Vintage Column Details.

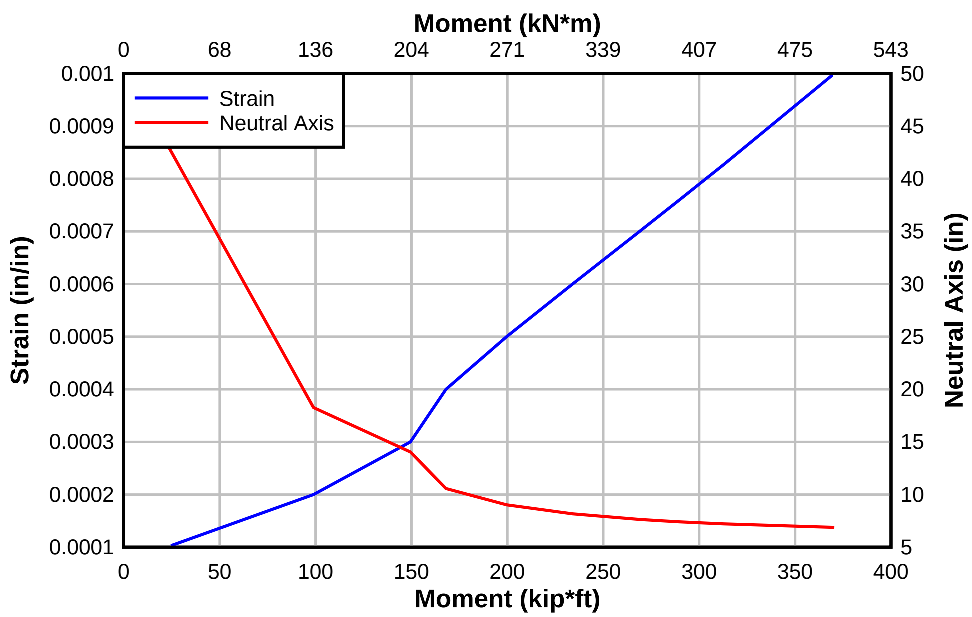

Figure C.9.14 – Expected moment strain as neutral axis varies.